When shape is enough:

from colloidal spheres to twisted polyhedra, from icosahedral to chiral order

On the cover: Computer-simulated cholesteric phase of colloidal twisted triangular prisms. The particle shape alone is enough to obtain the chiral liquid-crystalline order.

PhD thesis, Utrecht University, the Netherlands, June 2016.

ISBN: 978-90-393-6572-4

Printed by Gildeprint.

The work described in this thesis was performed in the Soft Condensed Matter group, part of the Debye Institute for Nanomaterials Science, at Utrecht University.

A digital version of this thesis is available at http://www.colloid.nl

When shape is enough:
from colloidal spheres to twisted polyhedra, from icosahedral to chiral order

---

Wanneer de vorm voldoende is:
van colloïdale bollen naar gedraaide polyhedra,
van icosahedrische naar chirale orde

(met een samenvatting in het Nederlands)

Proefschrift

ter verkrijging van de graad van doctor aan de Universiteit Utrecht op gezag van de rector magnificus, prof. dr. G. J. van der Zwaan, ingevolge het besluit van het college voor promoties in het openbaar te verdedigen op maandag 27 juni 2016 des ochtends te 10.30 uur

door

Simone Dussi

geboren op 12 februari 1987 te Rome (Italië).

Promotor: Prof. dr. ir. M. Dijkstra

This research was supported by an NWO-ECHO grant.

Contents

1

Introduction

1.1 Colloidal suspensions and self-assembly

The study of *colloidal suspensions* represents a peculiar example of how research can be driven by very fundamental questions or by very practical applications. It also serves as an example of how physics and chemistry meet, and how a synergy between physicists and chemists, but also engineers, mathematicians, biologists, computer scientists, as well as theory, computer simulations, experiments can lead to scientific progress. Clearly, the motivation in spending time in performing research in such an interdisciplinary and wide field can be different.

For what we discuss in this thesis, the first relevant aspect to consider is that colloids self-assemble due to Brownian motion.

The term "colloids" usually identifies particles with dimensions between 1 nm and 1 μm [1]. It comes from the Greek word $\kappa o\lambda\lambda\alpha$ (glue) since it was introduced in 1860 by Thomas Graham to describe sticky particles that were stuck on a semipermeable membrane [2]. Colloids are (more) interesting when dispersed in another medium. Examples of colloidal particles of different materials dispersed in media of different nature are available everywhere around us: toothpaste, creams, milk, butter, mayonnaise, paints etc...
When the suspended insoluble particles are in the colloidal size range, they constantly experience collisions with the smaller solvent particles (e.g. molecules) that are in constant motion because of thermal agitation. As a result, colloids have a random component in their trajectories. The first observation of this erratic motion is commonly attributed to Robert Brown, who studied in 1827 the behaviour of grains of pollen suspended in water [3]. A theoretical explanation of his observations was provided by William Sutherland [4] and by Albert Einstein [5]. Jean Baptiste Perrin provided further evidences of the so-called Brownian motion of colloidal particles with his sedimentation experiments on colloids [6, 7], and in 1926 he was awarded the Nobel Prize "for his work on the discontinuous structure of matter". Einstein and Perrin are just the last protagonists that proved for once and for all that matter is composed of "atoms", an idea that can even be dated back to the Greek philosopher Democritus (∼400 BC). As a consequence, also kinetic theory and statistical mechanics, that provide the link between the microscopic description of particles (e.g. atoms) and the macroscopic physical behaviour of matter, were finally accepted.

We have seen that the discovery of Brownian motion, in which colloids played a crucial role, represented a great advancement in the physics of condensed matter. The fact that colloids exhibit such a spontaneous motion is still largely exploited in nowadays research. Colloids exhibiting Brownian motion are able to move around in the suspension and can interact with each other or with the solvent molecules. Therefore, they are in principle able to explore all the possible configurations in which the system (colloids+solvent) can be. In statistical mechanics, this corresponds to the ergodic hypothesis, which is the central assumption of this theoretical framework. Its development had taken place during the 19th century, with Ludwing Boltzmann (1844-1906) as one of the main contributors, and represents nowadays one of the most important tools to study colloidal suspensions, whereas vice versa studies on colloids can be used to test and refine theoretical predictions. More practically, the (effective) interactions between colloids can lead to the formation of a great variety of structures (e.g. gas, liquids, crystals, liquid-crystals, glasses) that directly depend on both colloidal and solvent properties. Therefore, colloids can be considered as big brothers of atoms and molecules since they can exhibit the same behaviour, but at much larger length scales and longer time scales giving rise to several advantages that will be explained below. Since the colloidal self-organization occurs autonomously without *direct* human intervention, we describe this process as *self-assembly* of colloids, irrespective if they form finite-size structures (e.g. clusters) or thermodynamically stable bulk phase (e.g. crystals), or irrespective if this occurs with or without external field (e.g. gravity or confinement) [8]. "The concept of self-assembly is increasingly used in many disciplines, with a different flavor and emphasis in each" and therefore we refer to Ref. [8] for a more precise classification.

The study of colloidal suspensions can reflect the desire of answering fundamental questions such as "What are the microscopic properties needed to form a particular structure? Under which conditions will this structure form? What is the precise particle arrangement? How does the structure affect the macroscopic physical properties?" and so on. This is indeed the main motivation behind this thesis.

A second aspect, not to be overlooked, is the opportunity of addressing these questions by using very different approaches (e.g. experiments, theory and simulations) and achieving a complete understanding when all these approaches lead to the same answer.

From this point of view, the study of colloidal suspensions is currently in an exquisite position with respect to other fields of research. The existence of a well developed theoretical framework has been already highlighted and allows for a variety of theoretical formulations of problems under consideration. "Colloidal systems are also the simulator's dream", as many model systems and predictions have been later realized and verified in the laboratory [9]. On the other hand, computer simulations often provide a clear interpretation to a given experiment. In general, computer simulations are a valuable tool to study the behaviour of colloidal suspensions, often quicker and in many respects more controlled than experiments. Feasible simulations require simple models that yet can capture the main underlying physics of the experimental systems. Computer simulations can then be used both as a final validation of a given theory or as a "computer experiment" to explore new territories (see for example the introduction of Ref. [10]). From an experimental point of view, significant advancements have been recently made in preparing colloidal suspensions and tuning their properties (e.g. chemical synthesis) [11], therefore

increasing our possibility of manipulating these systems [12]. Moreover, because of their typical size, colloids are well suited to be imaged in real space and, because of their slow dynamics, in real time, by using light microscopy. Again, thanks to recent developments, e.g. confocal laser scanning microscopy, the self-assembly of colloids can be nowadays quantitatively studied in real-time and in real-space, on a single-particle level, and in 3D [13]. Something that is not yet possible for atoms, as they are too small and too fast. Computer simulations are the central tool of investigation in this thesis, but results for the experimental counterpart are also shown in chapters 2, 3, 4, and theoretical predictions are often made throughout this work.

Finally, the self-assembly of colloidal particles holds a great promise of structuring matter in three dimensions, at different length-scales, in a bottom-up, affordable and sustainable fashion. The design of materials with novel properties like materials with a photonic band gap or with a negative refractive index, is a clear goal [14–18]. To achieve this, a combination of theoretical, simulations and experimental studies are needed to identify the key features in the self-assembly processes. In this respect, the results of this thesis can be also interpreted as part of this joint effort of identifying design rules for the materials of the future. Colloids are also used in other applications not related to materials science, that ranges from biomedical applications to products for daily uses (cosmetics, paints, food), which however are not directly related to the content of this thesis.

1.2 Entropy and order

In order to reach the equilibrium state, a system minimizes its (Helmotz) free energy

$$F = U - TS\,, \tag{1.1}$$

where U is the internal energy of the system, T its temperature and S is the system entropy. A consequence of this fact is that upon changing some conditions (temperature, density etc..), phase transitions between different states of matter, e.g. formation of a crystal from a liquid, occur. Naively, it is tempting to always associate these transitions from a disordered to a more ordered state to the attractions between the particles. Indeed, this would be consistent with a decrease of the internal energy U. However, analogous transitions between disorder and order can be obtained by only increasing the entropy S [19]. The concept of entropy was first introduced by Clausius [20], who postulated the second law of thermodynamics, and later by Boltzmann, Gibbs and Planck, who gave a microscopic interpretation of entropy that is summarized in the following formula:

$$S = k_B \ln W\,. \tag{1.2}$$

This formula is usually attributed to Boltzmann, and it can be even found on Boltzmann's gravestone, but it was actually written in this form by Planck [21, 22]. It states that the entropy S (of an isolated system with fixed number of particles, volume and energy) is proportional (via Boltzmann's constant k_B) to the logarithm of the number W of the possible microscopic realizations of the system. It means that in the so called entropy-driven phase transitions the system moves towards phases for which more configurations

are accessible. Quoting Daan Frenkel: "the idea of entropy-driven phase transitions is an old one. However, it has only become clear during the past few years that such phase transformations may not be interesting exceptions, but the rule!" [19]. Here, we give two paramount examples of entropy-driven phase transitions, whereas we will briefly discuss some more recent studies at the end of this chapter.

In 1957, Alder and Wainwright [23], and Wood and Jacobson [24], reported computer simulation results indicating a transition from a fluid to a crystal phase upon compressing a system of hard spheres. Hard spheres are spherical particles that simply cannot overlap, they have infinite repulsion at contact but otherwise they do not interact. The freezing transition in hard spheres was also predicted a few years earlier by Kirkwood [25]. It can be understood recalling the microscopic definition of entropy. In this case the number of states accessible for the system is determined by the free volume of each particle, i.e., the volume in which the particle can move around without bumping onto another one. Upon increasing the system density, hard spheres spontaneously order in a crystal lattice to not lose their free volume, and therefore to increase their entropy. However, the possibility of having an ordered crystal phase in absence of attractions was received with huge scepticism. During a workshop in 1957 there was even a vote by a panel of experts that was evenly split "against" the simulation evidences [21, 26]. Nowadays, this transition is widely accepted, especially thanks to the experimental studies performed on colloidal suspensions [27–29]. Nevertheless, we will show in chapter 2 that, almost 60 years later, hard spheres are still a source of unexpected behaviour, since they can form stable icosahedral clusters under spherical confinement.

The earliest entropy-driven transition was actually predicted in 1949 by Lars Onsager for a system of thin hard rods [30]. On compression, the system undergoes a transition from an isotropic disordered state, in which the rods are uniformly distributed in space and have random orientations, to a partially ordered state, called *nematic* phase, in which the rods are on average aligned, still maintaining a homogeneous distribution in space of their centres of mass. In this case, there are different contributions to the entropy, one associated with the translational and one with the orientational particle degrees of freedom. The transition occurs because when rods align, despite losing orientational entropy, they decrease their excluded volume, and therefore gain translation entropy. This trade-off becomes crucial beyond a certain density, that is the one at which the transition occurs, and therefore to increase the total entropy, rods have to form a nematic phase. In the 1980s, Frenkel *et al.* provided computer simulation evidences not only for an entropy-stabilized nematic phase [31] but also for more complex liquid crystal phases, such as smectic [32] and columnar [33] phases, for which was thought, once more, that attractions were necessary [34]. Liquid crystal phases have an important role in this thesis and therefore the next section is dedicated to briefly introduce this peculiar state of matter.

1.3 Liquid crystals

Liquid crystals are an intermediate state of matter featuring properties in between those of conventional liquids and those of (solid) crystals, as the name suggests. For example, in

terms of mechanical properties, molecular liquid crystals flow, like a liquid, but have also elastic responses, like a crystal. A more rigorous definition can be formulated in terms of the microscopic arrangement of the particles: liquid crystals have long-range orientational order but no, or only partial, positional order [35]. Several liquid crystal phases have been discovered or predicted. In some cases, the naming of a given phase is associated to a peculiar property noticed at the moment of discovery, e.g. *nematic* comes from the Greek word $\nu\eta\mu\alpha$ that means threads, because of the presence of thread-like topological defects (called disclinations) that are clearly visible under cross-polarizers. In other cases, the name comes from the system in which the phase was first observed, e.g. *cholesteric* phases from cholesterol or *discotic* phases from disk-like molecules. However, these phases are not necessarily specific of a particular system and a general classification can be actually obtained in terms of phase symmetry, i.e. based on the microscopic arrangement of the particles. *Nematic* phases have only orientational order, i.e., particles are on average aligned along a common direction; *smectic* phases have an additional 1D positional order, i.e. particles form layers; *columnar* phases feature a 2D positional order, i.e. particles form columns, which are arranged on a 2D lattice. Nematic phases can be further divided into (i) prolate (or calamitic) uniaxial, (ii) oblate (or discotic) uniaxial and (iii) biaxial phases, depending if the long-range orientational order of the phase is associated to (i) the long, (ii) the short or (iii) both particle axes. Furthermore, in case of chiral particles, i.e., particles lacking mirror symmetry, the nematic organisation is usually chiral as well, i.e., the direction along which the particles are on average oriented twists in an helical fashion, and the phase is named cholesteric. Such phases were also simply termed as chiral nematic but this is now source of ambiguity since other nematic phases different from the cholesteric phase feature chiral arrangement, e.g. twist-bend nematics [36] and screw-like nematics [37]. Analogously, smectic phases are also often distinguished (according to a less descriptive naming) into smectic-A, smectic-B, smectic-C, and so on, until smectic-H, based on the type of positional order within the layers, the chiral nature of the phase and so on. Similar classification can be done for columnar phases. Some of these phases will be studied in detail in this thesis, and are only part of the multitude of liquid crystal phases observed or predicted, such as blue phases, chiral liquids in which defects could be arranged in a periodic fashion, and gyroid phases [38]. When systems exhibit long-range positional order but no orientational order, we refer to them as *plastic crystal* phases, or *rotator* phases, which are different kinds of mesophases, specular to liquid crystals. Liquid crystals can be distinguished into thermotropic and lyotropic, depending if the phase behaviour is mainly governed by temperature or by the system concentration, respectively. Thermotropics are usually composed of molecules and have found a widespread use in optoelectronic applications. Moderately dense suspensions of anisotropic colloids can also exhibit liquid crystalline behaviour. Examples range from organic rods, such as tobacco mosaic virus, fd-virus, DNA, to inorganic materials, like ferric oxyhydroxide rods, boehmite, vanadium pentoxide, gibbsite platelets, silica rods [39–50]. Comparisons between simulations and experiments on silica rods will be made in chapters 3 and 4.

Several theoretical frameworks have been proposed to describe the liquid crystalline behaviour, and can be roughly divided in microscopic or (more or less coarse-grained) phenomenological approaches, depending if the discrete nature of the constituent particles is explicitly taken into account or not. Microscopic approaches to describe the liquid

crystal order will be used in this thesis. Examples range from Onsager's theory and classical density functional theory, to particle-based computer simulations. Such techniques are valid for both thermotropic and lyotropic liquid crystals providing that the microscopic model, e.g. particle shape and interactions, captures the essential physics of the system. Ellipsoids interacting via Gay-Berne (and similar) potentials have been proven to be a simple model to reproduce the essential physical features of many thermotropic liquid crystals [51]. Hard bodies have been extensively used in theory and simulations [52] as models for colloidal systems, and will be used in this thesis as well. Other theories for liquid crystals do not explicitly consider the properties of the individual entities but rather coarse-grained (with different level of coarse-graining) properties such as, for example, the local averaged orientation of the particles (nematic director field) or the order parameter associated to a given symmetry. For example, the isotropic-nematic transition can be described by means of a phenomenological Landau-de Gennes theory, based on an expansion of the free energy in terms of the nematic order parameter, or the elastic distortions in a liquid crystal can be described by a continuum elastic theory, which is based on a change in free energy in terms of Frank elastic constants.

1.4 Methods

1.4.1 Monte Carlo computer simulations

In this thesis, we mostly employ Monte Carlo (MC) methods to study the self-assembly in many-body systems. MC simulations can be used to sample the phase space associated to the possible configurations in which the system can be. The evolution of the system is then based on trial moves that are rejected or accepted according to a given probability, that depends on the chosen statistical ensemble. The aim of this scheme is to efficiently sample the most relevant states. Such states are then used to calculate the equilibrium properties of the system.

Let us consider the simple case of N particles in a volume V at temperature T (canonical ensemble). Assuming that the particles interact via a pair potential $U(\mathbf{r})$, the Hamiltonian of the system is given by

$$H(\mathbf{r}^N, \mathbf{p}^N) = \sum_{i=1}^{N} \frac{\mathbf{p}_i^2}{2m} + \sum_{i<j} U(\mathbf{r}_{ij}) \,, \tag{1.3}$$

where $\mathbf{r}^N$ denotes the particles positions and $\mathbf{p}^N$ the particles momenta. The canonical partition function of such a system is given by

$$Z(N, V, T) = c \int d\mathbf{r}^N \exp(-\beta U(\mathbf{r}^N)) \,, \tag{1.4}$$

with c a normalization constant that also takes in account the fact that we have integrated out the degrees of freedom associated to the particle momenta (the kinetic part of the Hamiltonian), and $\beta = 1/k_B T$, with k_B the Boltzmann constant. The average of an observable $\mathcal{O}$ is therefore given by

$$\langle \mathcal{O} \rangle = \frac{\int d\mathbf{r}^N \mathcal{O} \exp(-\beta U(\mathbf{r}^N))}{\int d\mathbf{r}^N \exp(-\beta U(\mathbf{r}^N))} \,, \tag{1.5}$$

where we assume that $\mathcal{O}$ depends only on the particle coordinates. An efficient way of evaluating Eq. 1.5, that cannot be computed directly for a many-particle system, is to calculate $\mathcal{O}$ over a large number of relevant configurations that are obtained by a Metropolis algorithm. This sampling scheme consists of generating a sequence of random configurations, called Markov chain, that are accepted or rejected such that the configurations follow the Boltzmann distribution. In practice, starting from a given configuration of particles $\mathbf{r}^N_{old}$, a trial configuration $\mathbf{r}^N_{new}$ is obtained, for example, by randomly selecting a particle and randomly displacing it. The trial configuration is accepted with the probability

$$\mathrm{acc}(old \to new) = \min(1, \exp\{-\beta[U(\mathbf{r}^N_{new}) - U(\mathbf{r}^N_{old})]\}) \,. \tag{1.6}$$

In case of rejection the old configuration is kept. This procedure is repeated to generate a large number of configurations. For sufficiently long simulation times, the system should be able to reach equilibrium and the average over several equilibrium configurations can be performed. By implementing different moves and by varying the acceptance rules, systems can be simulated in different statistical ensembles. Trial moves need to obey specific balance rules to correctly produce the right set of configurations, but for example do not need to be physical, which can be exploited to speed-up the simulations. For a more comprehensive description of different MC techniques and their current use, see Ref. [10].

Simulating anisotropic hard particles

The focus of this thesis is on hard particles, i.e., particles that interact only via an hard-core potential. The basic ingredient for MC simulations is therefore to determine when particles overlap or not, and accordingly accept or not the trial configuration. In the simplest case of spherical particles with diameter σ the pair potential reads

$$U(r_{ij}) = \begin{cases} \infty & r_{ij} < \sigma \\ 0 & r_{ij} \geq \sigma \end{cases} \,, \tag{1.7}$$

where r_{ij} is the center-to-center distance between the two particles i and j that can be obviously calculated analytically. However, for anisotropic particles, the hard-core potential depends also on the orientations of the two particles:

$$U(\mathbf{x}_i, \mathbf{x}_j) = \begin{cases} \infty & d(\mathbf{x}_i, \mathbf{x}_j) < \sigma(\mathbf{x}_i, \mathbf{x}_j) \\ 0 & d(\mathbf{x}_i, \mathbf{x}_j) \geq \sigma(\mathbf{x}_i, \mathbf{x}_j) \end{cases} \,, \tag{1.8}$$

where $\mathbf{x}$ indicates the generalized coordinates (positions and orientations), $d(\mathbf{x}_i, \mathbf{x}_j)$ the center-to-center distance between particles i and j, and $\sigma(\mathbf{x}_i, \mathbf{x}_j)$ the "thickness" of the two hard bodies in that particular configuration. The orientation of the particles can be described by a unit vector in case of a uniaxial shape. For biaxial shapes, the use of a 3×3 rotation matrix (like in this thesis) or the use of quaternions are the most common choices. In some cases, the distance between anisotropic particles can be still efficiently computed numerically. For example, for two spherocylinders the *minimum* distance between two line segments in space $d(\mathbf{r}_{ij}, \hat{\mathbf{u}}_i, \hat{\mathbf{u}}_j)$, with $\hat{\mathbf{u}}$ the unit vector indicating the orientation of the main axis, is calculated by an efficient algorithm [53]. An overlap occurs when

$d(\mathbf{r}_{ij}, \hat{\mathbf{u}}_i, \hat{\mathbf{u}}_j) < D$, with D the diameter of the spherocylinders. A similar algorithm can be employed to determine the distance between a spherocylinder and a sphere (distance between a point and a line segment in 3D). However, in other cases, it is faster to directly check if the two shapes intersect, without calculating the minimum distance between the two particles. For convex shapes, possible choices are the intersection-detection algorithm based on the Separating Axes Theorem (SAT) [54] or the Gilbert-Johnson-Keerthi (GJK) algorithm [55, 56]. In case of non-convex shapes, a possibility (used in this thesis) is to decompose the surface of the particle in triangular faces and check for intersection between these triangles. This can be done efficiently by using the RAPID library [57]. Anyway, it is always possible to calculate the minimum distance between two shapes (e.g. based on GJK algorithm for convex particles or based on triangle-triangle distance for non-convex ones), that could be necessary for some types of analysis. To minimize the number of overlap checks, cell lists are often used in computer simulations [10, 58]. In case of (almost) spherical particles, a cubic cell list is a simple and efficient solution. For strongly anisotropic particles, i.e., very long or very flat shapes, different tricks can be implemented. Pre-checks based on embedded shapes for which the overlap algorithm is simple (e.g. circumscribed sphere, spherocylinder containing the entire particle) are convenient. It can be also advantageous to divide the long shapes in smaller parts, e.g. fully cover the particles with a set of (overlapping) spheres with a diameter larger than the particle diameter, and use these smaller parts to construct a cubic cell list (as in the case of simulations of simply spheres). These spheres are then used to identify the neighbours (overlaps are always checked in the proper way according to the algorithm suitable for the shape under consideration) and by keeping track of the pairs already checked this simple procedure could speed up substantially the simulation. More sophisticated implementation can be based on bounding boxes and other tricks, that can be found in literature. However, the efficiency of the simulation code always depends on the type of simulation, e.g. it can vary if the simulation is carried out in an NVT or NPT ensemble, where in the latter additional moves are used to change the volume of the simulation box, on the exact particle shape and on the exact implementation, and hence, the performance must be checked case by case. Finally, we highlight that for anisotropic particles, overlap checks must be performed also after an expansion of the system. For convex shapes, this is relevant only for anisotropic expansions (e.g. scaling only one side of the simulation box), whereas for non-convex shapes both isotropic and anisotropic expansions could introduce an overlap between particles.

1.4.2 Classical density functional theory

Some of our simulation results presented in this thesis are complemented with theoretical predictions based on classical density functional theory (DFT) [59]. DFT methods were originally developed to describe the properties (in particular the electronic structure) of quantum many-body systems by using appropriate functionals of the electron density. The classical analogue is also based on the relation between the single-particle density $\rho(\mathbf{x})$, with $\mathbf{x}$ a generalized coordinate, to the macroscopic properties of a given structure through an *intrinsic free-energy functional* $\mathcal{F}[\rho(\mathbf{x})]$. Such a functional contains all the information about the system and in general cannot be computed exactly. Once the free-energy

functional is defined, within some approximations, by following a variational principle it is possible to arrive at an explicit equation for the equilibrium single-particle density $\rho_{eq}(\mathbf{x})$. The latter contains information about the equilibrium microscopic organization of the particles and therefore can be used to obtain thermodynamic (e.g. free energy, pressure, chemical potential) and structural properties of the system. For a more precise introduction on the DFT framework, we refer to the existing literature (e.g. Refs. [59, 60]), while the specific approaches used in this thesis will be explained in detail in the respective sections. Onsager's theory [30], that is nowadays called a density functional theory within the second-virial approximation, is revisited in section 3.2. In chapter 5, Onsager's theory is tested against simulations of polyhedral rods and predictions based on another type of DFT. In chapter 6, we introduce a variation of a second-virial DFT to describe chiral nematic order. Such a DFT will be applied to different chiral models and in chapter 7 DFT results will be directly compared with simulation results. Upon increasing the complexity of the particle shape and symmetry of the thermodynamic phases, it becomes more evident that very efficient numerical approaches are required for the DFT calculations. Indeed, we use Monte Carlo methods to solve the multi-dimensional integrals (excluded-volume coefficients) in the DFT approach. Despite the intrinsic approximations of the DFT approaches, theoretical predictions are (often) quicker than simulations and can sometimes even access regimes which are inaccessible or hard to reach in computer simulations due to finite-size effects. On the other hand, the different approximations need to be tested against simulation results in order to refine the theoretical framework itself. Therefore, a frequent comparison between theory and simulation is desirable in order to provide valid insights and predictions on the phase behaviour of colloidal suspensions.

1.5 Scope of this thesis

In the context of self-assembly, *shape* is a subtle concept, as exquisitely pointed out in Ref. [61]. Here, we use the conventional definition that the shape of an object is given by the geometry of its surface. "This definition is familiar because it is appropriate to the macroscopic scale of our sense of touch and gives results that are consistent with the morphological characterization of an object: a nanocube will look like a nanocube in transmission electron microscopy, atomic force microscopy and optical microscopy" [61]. In this thesis, we mostly study hard particles, for which there is no ambiguity in defining what shape is, and we show that *shape is enough* to form several and different structures. Such a concept has been pioneered by Onsager [30] and many others have employed hard-particle models to study different thermodynamic phases (for example in Refs. [31, 32, 62–67]). In this respect, this thesis should be seen as a personal journey in the modification of particle shape to shed new light on some, sometimes novel, entropy-driven phase transitions. Notice that such a journey is not told in a chronological order but rather with the spirit to rationalise the change in phase behaviour corresponding to a progressive loss of particle shape symmetry, as illustrated in Fig. 1.1. We remark that complex-shaped particles are not a merely abstraction for theorists and simulators anymore. Indeed, nowadays a variety of shapes can be synthesized in the colloidal domain [12, 68–70] and

therefore a full understanding of the effect of shape on the phase behaviour is of crucial importance also for future progress in exploiting anisotropy for materials design [12].

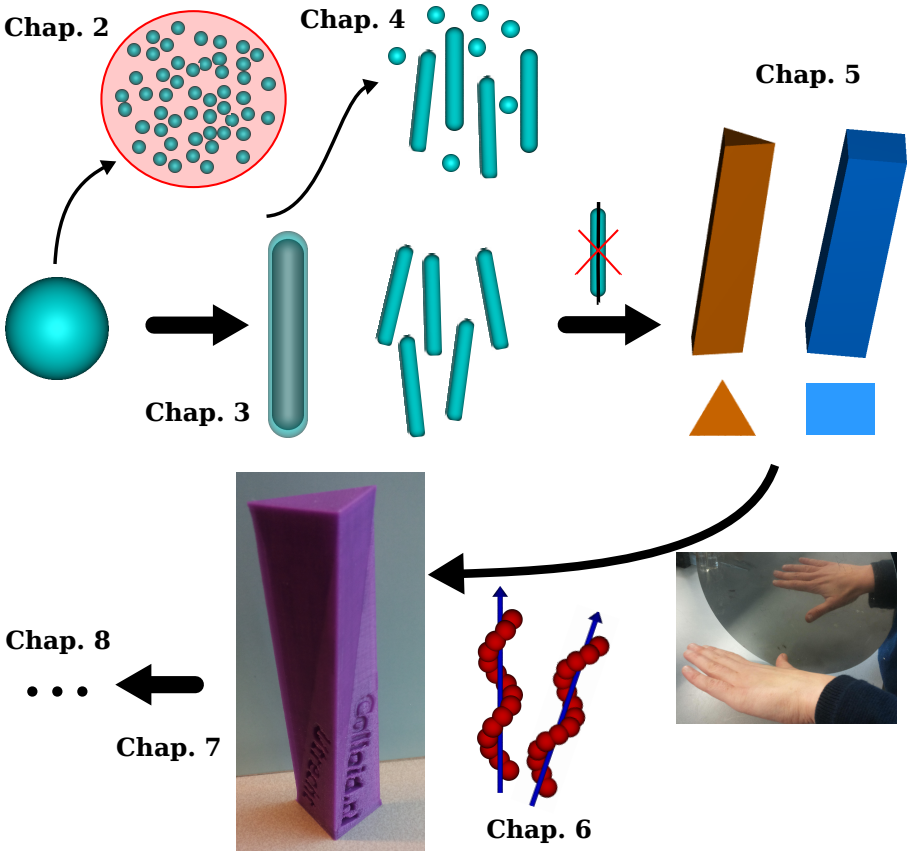

Figure 1.1: Graphical abstract of this thesis. We study the self-assembly of hard-particle systems, in which *shape* is the only relevant microscopic feature of the system. The simplest hard-particle model is a spherical particle that cannot overlap with any other object. The bulk phase behaviour of the hard-sphere system is briefly described in Sec. 1.2. However, a novel phase behaviour emerges when the system is spherically confined, as we show in Chap. 2. In Chap. 3, we introduce anisotropy in the particle shape and study the liquid-crystal behaviour of hard spherocylinders. Liquid crystals are introduced in Sec. 1.3. Experimentally, colloids with an "effective" spherocylindrical shape can be synthesised. In Chap. 4, we mix hard spheres and hard spherocylinders. In Chap. 5, the particles lose their uniaxial symmetry and we study the effect of biaxiality of polyhedral particles on the liquid-crystal behaviour. In Chap. 6, we consider chiral helical particles forming chiral nematic phases. Chiral objects, like our hands, lack of mirror symmetry. In Chap. 7, we study a novel hard chiral particle model system, namely twisted polyhedra (a macroscopic 3D-printed model is shown in the figure) and we show how the particle biaxiality and chirality are directly transmitted at a higher level into the nematic phases. The study is continued in Chap. 8, where we also conclude our journey by highlighting some open issues in the field of "hard" soft-condensed-matter.

2

Entropy-driven formation of icosahedral clusters of hard spheres under spherical confinement

Icosahedral symmetry, which is not compatible with truly long-range order, is readily found in many systems, e.g. liquids, glasses, atomic clusters, quasi-crystals, and virus-capsids. However, in all cases where more than tens of particles are arranged with a high degree of icosahedral order, attractions are considered essential. Here, we report that entropy and spherical confinement suffice to form icosahedral clusters consisting of up to almost 100000 particles. In particular, we show by computer simulations that tens of thousands of hard spheres, when compressed under spherical confinement, spontaneously crystallize into icosahedral clusters, which are thermodynamically favoured over the bulk equilibrium face-centered-cubic (FCC) crystal structure. Our results corroborate real-space measurements on evaporating emulsion droplets containing nano- and micron-sized colloids. Moreover, by elucidating the crystallization mechanism of the icosahedral structures, we provide new insights into the interplay between confinement and crystallization. We conclude the chapter by briefly exploring how spherical confinement can change the phase behaviour of different colloidal systems beyond single-component hard-sphere systems.

2.1 Introduction

More than half a century has passed since Sir Charles Frank first proposed that the most favorable local structures in simple liquids have icosahedral symmetry [71]. Such ordering occurs when 12 particles are arranged around a central particle at the vertices of an icosahedron. This icosahedron tends to maximize the short-ranged (Lennard-Jones-like) attractions typically present in atomic systems, and has been shown to be entropically favorable as well [72, 73]. However, its five-fold symmetry is incommensurate with long-range positional order, thereby acting as an obstacle for the formation of crystals on a larger scale. So, even though a typical liquid often contains many local icosahedral centers [71, 74–76], they rarely grow out into a crystal [77]. In the case of hard spheres, which do not attract and instead interact solely by excluded volume, (distorted) icosahedral order has been observed in the fluid phase [77], in glasses [78] and in growing crystal nuclei during crystallization [79]. On the other hand, the bulk thermodynamically stable crystalline phase for hard spheres is the face-centered-cubic (FCC) crystal, which maximizes the entropy at high densities [27, 80]. This arrangement of spheres has the densest possible packing ($\eta = 0.74$) at infinite pressure, and does not display any five-fold symmetry [27, 80]. The incompatibility of the locally favorable icosahedral symmetry with long-range three-dimensional order raises immediately the question over what length scales icosahedral order can be extended.

A dense non-crystalline packing of spheres featuring global icosahedral order was theoretically proposed by Mackay in 1962 [81]. The Mackay structure (that will be described in more detail later) has been observed and studied theoretically for atomic and molecular clusters [82–85] and clusters of nanoparticles [86–89]. In these cases, the formation of icosahedral structures is mainly attributed to energetic interactions [86, 90, 91] in conjunction with kinetic effects [87], hierarchical self-assembly [84], or intricate growth mechanisms [88, 89]. Additionally, Mackay clusters of Lennard-Jones particles have been shown to correspond to minima in the free-energy landscape [92]. In contrast, in hard-sphere systems attractions are not present and finite-size clusters can be obtained by means of confinement. It is known from theory, simulations, and experiments that confinement can change the equilibrium crystal structure of colloidal spheres from that in the bulk [93, 94]. However, predicting by first principles how dramatic and on what length scales this change can occur is not trivial.

In this chapter, we show by computer simulations that spherical confinement gives rise to purely entropy-driven icosahedral symmetry in the equilibrium phase of very large numbers of hard spheres. Our results are in agreement with experiments on colloidal particles confined within evaporating emulsion droplets and confirm that attractions in these systems are not needed to obtain equilibrium icosahedral clusters. In particular, after obtaining the icosahedral clusters by molecular dynamics simulations, we confirm their stability by performing Monte Carlo free-energy calculations. Moreover, we study the crystallization mechanism of the (Mackay and anti-Mackay) icosahedral structures. We conclude our study by briefly exploring the roles of particle-interface and particle-particle interactions in single-component and binary systems, speculating on how spherical confinement can be used to reliably control the phase behaviour in several colloidal systems.

2.2 Methods

2.2.1 Molecular dynamics simulations

In this chapter, we first perform event-driven molecular dynamics (EDMD) simulations of hard spheres with a diameter σ confined in a spherical cavity. The spherical particles interact only via a purely repulsive (excluded-volume) potential:

$$\beta U(r_{ij}) = \begin{cases} \infty & r_{ij} < \sigma \\ 0 & r_{ij} \geq \sigma \end{cases} \tag{2.1}$$

where r_{ij} is the distance between the centers of the spheres i and j, and $\beta = 1/k_B T$, with k_B Boltzmann constant and T the temperature. The particles follow Newton's law of motion, and the system is evolved according to an event calendar that keeps track of the time at which a particular event (e.g. collision between particles) occurs. Therefore, differently from traditional time-driven MD simulations, where the time is advanced in fixed steps, in EDMD simulations, which are suitable for discontinuous potentials, the time jumps from event to event. Clearly, EDMD simulations are not used to describe the (Brownian) motion of true colloids (for which hydrodynamics interactions could also play an important role) but rather represent a different way of sampling the phase space, in full analogy with Monte Carlo methods described in Sec. 1.4.1. For details on the technique and its implementation see for example Refs. [95, 96].
To mimic the solvent evaporation of the emulsion droplets, the radius of the spherical cavity is slowly reduced at a constant compression speed v that is expressed in units of σ/τ, where $\tau = \sqrt{m\sigma^2/k_B T}$ is the EDMD time unit. To keep the temperature of the system constant during the simulations, an Andersen thermostat has been implemented. This consists of choosing randomly, at fixed intervals, a given number of particles and assign them a new random velocity drawn from a Boltzmann distribution of velocities corresponding to the imposed temperature. In addition, we also perform EDMD simulations at fixed density, in which both the number of particles N and the cavity volume V are kept fixed, in order to investigate possible kinetic effects due to the compression. To model the spherical confinement, we use three types of external potentials that act on the hard spheres: (i) an impenetrable hard spherical wall, (ii) a short-ranged soft repulsive wall-particle potential, and (iii) an attractive wall-particle potential with an interaction range of σ. In the first case, we treat the confinement as an impenetrable hard spherical wall of radius R, described by the following potential

$$\beta U_{p-w}(r) = \begin{cases} \infty & r > R - \sigma/2 \\ 0 & r \leq R - \sigma/2 \end{cases} \tag{2.2}$$

with r the center-of-mass distance of the particle with respect to the center of the cavity. In the second case, we used a soft repulsive wall-particle potential with a functional form $1/|R - r|^n$, with $n \geq 2$ and interaction range $r_{soft} \leq 2\sigma$. In particular, the continuous potential is approximated by 30 concentric spherical interfaces, that are evenly spaced at distance R_i from the center, ranging from the outermost shell at distance R (that still acts as a hard cavity) to the innermost shell that is at distance $R - r_{soft}$, see also Ref. [95]

for further details. Finally, in Sec. 2.6 we consider a longer-ranged repulsive confinement, and binary systems of hard spheres or particles interacting via a square-well potential, that are straightforward extensions of the EDMD simulations described here.

2.2.2 Free-energy calculations

In this chapter, we calculate the absolute free energy associated to the structures that are observed in simulations and experiments, by means of a 3-step thermodynamic integration [10], based on the method proposed by Schilling and Schmid [97, 98]. In general, it is possible to calculate the free-energy difference between the system of interest and a reference system, for which the free energy F_{ref} is known. To this end, we introduce a potential energy function $U(\lambda)$ that depends on a coupling constant λ, which allows us to connect the system of interest at $\lambda = 0$ to the reference system at $\lambda = \lambda_{max}$ by an appropriate thermodynamic path. The free-energy difference is given by

$$F(\lambda = \lambda_{max}) - F(\lambda = 0) = \int_{\lambda=0}^{\lambda=\lambda_{max}} d\lambda \left\langle \frac{\partial U(\lambda)}{\partial \lambda} \right\rangle_{\lambda} , \tag{2.3}$$

where $\langle . \rangle_{\lambda}$ indicates an average over several configurations obtained by Monte Carlo simulations at fixed λ. The coupling constant λ is therefore increased in a series of simulations until the reference system is reached at $\lambda = \lambda_{max}$.

The method proposed by Schilling and Schmid [97] assumes that in the reference system the particles are ideal (do not interact with each other) and are pinned to their own wells via a linear potential:

$$u_{well}(x, \epsilon) = \begin{cases} -\epsilon(x-1) & x < 1 \\ 0 & x \geq 1 \end{cases} , \tag{2.4}$$

where $x = |\mathbf{r}_i - \mathbf{r}_i^{(0)}|/r_c$, with $\mathbf{r}_i$ the position of particle i, $\mathbf{r}_i^{(0)}$ the position of the corresponding well i, and r_c the cut-off radius of the well interaction, chosen to be $r_c = 2\sigma$ (but this is not crucial [97]), with σ the sphere diameter. Therefore, the free energy of the reference system F_{ref} reads [97–99]:

$$\frac{\beta F_{ref}(\epsilon)}{N} = \ln\left(\frac{N\Lambda^3}{V}\right) - 1 - \ln\left[1 + \frac{(4/3)\pi r_c^3}{V} g(\beta\epsilon)\right] , \tag{2.5}$$

where N is the number of particles, V the volume, Λ the thermal wavelength, and

$$g(\beta\epsilon) = \frac{3}{(\beta\epsilon)^3}\left(e^{\beta\epsilon} - 1 - (\beta\epsilon) - \frac{(\beta\epsilon)^2}{2} - \frac{(\beta\epsilon)^3}{6}\right) . \tag{2.6}$$

To reach the ideal reference state from our system, we need three separate integration steps with three different potentials $U_{well}(\mathbf{r}^N; \epsilon)$, $U_{p-p}(\mathbf{r}^N; \gamma)$, $U_{p-w}(\mathbf{r}^N, R; \alpha)$, in order (i) to pin the particles to their own wells based on their position $\mathbf{r}_i^{(0)}$ in a typical configuration, (ii) to switch off the interaction between the particles, (iii) to switch off the interaction

between the particles and the confining spherical wall of radius R, respectively. $\mathbf{r}^N$ indicates the positions of the N particles and ϵ, γ, α are the three coupling constants. The first potential clearly reads

$$U_{well}(\mathbf{r}^N; \epsilon) = \sum_{i=1}^{N} u_{well}(x, \epsilon)\,. \tag{2.7}$$

To switch off the hard-core interactions in our system we used the potential proposed in Ref. [100]. In particular, for two spheres i and j of diameter σ at distance r_{ij} we use

$$u_{p-p}(r_{ij}; \gamma) = \begin{cases} \gamma \left[1 - 0.9\left(\frac{r_{ij}}{\sigma}\right)^2\right] & r_{ij} < \sigma \\ 0 & r_{ij} \geq \sigma \end{cases}\,, \tag{2.8}$$

whereas for a sphere at distance r_i from the center of a cavity of radius R we use

$$u_{p-w}(r_i, R; \alpha) = \begin{cases} \alpha \left[1 - 0.9\left(\frac{R - r_i}{\sigma}\right)^2\right] & r_i > R - \sigma/2 \\ 0 & r_i \leq R - \sigma/2 \end{cases}\,. \tag{2.9}$$

Therefore $U_{p-p}(\mathbf{r}^N\,;\,\gamma) = \sum_{i<j} u_{p-p}(r_{ij}\,;\,\gamma)$ and $U_{p-w}(\mathbf{r}^N\,;\,\alpha) = \sum_i u_{p-w}(r_i, R\,;\,\alpha)$ and the free energy $\beta F(N, V, T)$ obtained by the complete thermodynamic integration reads

$$\begin{aligned} \beta F(N, V, T) = \beta F_{ref}(\epsilon_{max}) - \int_0^{\epsilon_{max}} d\epsilon \left\langle \frac{\partial \beta U_{well}}{\partial \epsilon} \right\rangle_\epsilon + \\ + \int_0^{\gamma_{max}} d\gamma \left\langle \frac{\partial \beta U_{p-p}}{\partial \gamma} \right\rangle_\gamma + \int_0^{\alpha_{max}} d\alpha \left\langle \frac{\partial \beta U_{p-w}}{\partial \alpha} \right\rangle_\alpha\,. \end{aligned} \tag{2.10}$$

We remark that the integration associated to the first step is particularly challenging and it is important to accurately sample the region at moderate ϵ, that largely contributes to the absolute free energy, and also correctly capture the decay for large ϵ. For this reason, we sample more than 300 values of the coupling constant ϵ and use $\epsilon_{max} > 1000$. Furthermore, the results are fitted with an Akima spline before performing the numerical integration. The other two integration steps are performed using a standard 20-points Gauss-Legendre integration scheme. In the first integration step we also implement ordinary swap moves consisting in randomly selecting a pair of particles and swapping their identities (see Ref. [97] for additional moves to speed up equilibration). Finally, to get an estimate of the error in our free energies, we repeated our calculations on five independent initial configurations displaying the desired symmetry. The free-energy difference between the different symmetries are then calculated to identify the thermodynamically stable structure.

2.2.3 Identifying crystalline domains

In order to identify the crystalline domains and the cluster symmetry, we use a local bond orientational order parameter based on spherical harmonics $Y_{l,m}$ to identify the solid-like

particles, i.e. particles with a solid-like environment, as introduced in [75]. In particular, for each particle i, we calculate

$$q_{lm}(i) = \frac{1}{N_b^i} \sum_{j=1}^{N_b^i} Y_{l,m}(\mathbf{r}_{ij}),$$

where N_b^i is the number of neighbours of particle i, i.e. all particles j with a center-of-mass distance $|r_{ij}| < 1.4\sigma$ with respect to particle i, and σ is the particle diameter. We set $l = 6$ and use a cluster algorithm [101] to discriminate different crystalline domains. The correlation between two particles i and j is quantified by:

$$d_6(i,j) = \frac{\sum_{m=-6}^{+6} q_{6m}(i) q_{6m}^*(j)}{\left(\sum_{m=-6}^{+6} |q_{6m}(i)|^2 \right)^{1/2} \left(\sum_{m=-6}^{+6} |q_{6m}(j)|^2 \right)^{1/2}},$$

and for each particle the number of connections is evaluated via

$$n_{con}(i) = \sum_{j=1}^{N_b^i} \mathcal{H}(d_6(i,j) - d_c),$$

where $\mathcal{H}$ is the (Heaviside) step function, and where we fix the correlation threshold $d_c = 0.6$. A particle i is defined as solid-like if $n_{con}(i) \geq 7$.
Different crystal domains are then identified by using an additional constraint to our criterion, reflecting the fact that the local environment of two neighbouring solid-like particles should display more similarity if they belong to the same crystalline domain than if they are part of different ones. According to this criterion we add particle j (already qualified as a solid-like particle) to the same crystalline domain of particle i if $d_6(i,j) \geq 0.9$.
Furthermore, we employ the cone algorithm described in Ref. [83] to discriminate between particles belonging to different layers (surface, different sublayers and the interior) of the spherical clusters. This analysis is needed to unveil the crystallization mechanism.

2.3 Crystallization of hard spheres in spherical confinement

We perform event-driven molecular dynamics simulations of hard spheres in a slowly shrinking hard spherical confinement. In the next section, we will see that these simulations mimic the evaporation process of droplets containing colloidal or nanoparticles that effectively interact as hard spheres. It is known that hard spheres in bulk exhibit a freezing transition from a fluid to a crystal phase [23, 24, 27], for which the stable crystal symmetry is the face-centered-cubic (FCC) [80]. The freezing and melting packing fractions associated to this first-order transition are $\eta \simeq 0.494$ and $\eta \simeq 0.545$, respectively [102]. Here, we first check if hard spheres confined in a shrinking cavity exhibit

crystalline order. In Fig. 2.1(a), we plot the fraction of crystalline particles as a function of packing fraction η. Note that the packing fraction increases with time during the simulations, so an increase in packing fraction can also be considered as moving forward in time. For a low compression rate v, we clearly observe that a large number of particles crystallize. Furthermore, we observe that our results do not alter upon changing the compression speed of the spherical confinement, provided the compression is sufficiently slow ($v \leq 10^4\sigma/\tau$) such that the system remains in quasi-equilibrium during the self-assembly process. In addition, we study the fraction of crystalline particles as a function of packing fraction for various system sizes, and present the results in Fig. 2.1(b). We see that the fraction of crystalline particles depends on the total number of particles contained in the cavity. In particular, for small number of particles the final crystalline assemblies present less ordered particles. This is not due to kinetic effects (compression speed $v = 10^4\sigma/\tau$) but it is an effect of the stronger frustration induced by the spherical cavity. Indeed, as reported in the inset of Fig. 2.1(b), when only $N = 500$ spheres are spherically confined a non-monotonic behaviour of the fraction of crystalline particles as a function of η is observed, even for simulations at fixed density (the radius of the cavity is fixed). As a consequence of this strong frustration, the final structure obtained at the end of a compression run for $N = 500$ appears quite disorderd. However, already for $N = 1000$ there is no such an effect and therefore the final structure exhibits a large degree of crystallinity.

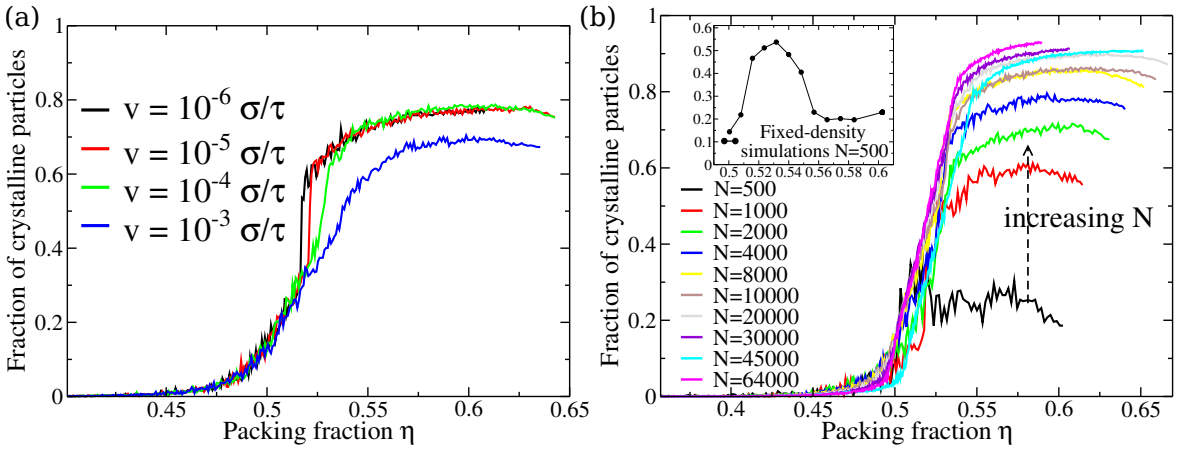

Figure 2.1: **(a)** Fraction of crystalline particles as a function of packing fraction η for different compression speed v, as indicated in the legend, for $N = 4000$ hard spheres confined in a shrinking spherical hard cavity. **(b)** Fraction of crystalline particles as a function of η for different N in a spherical hard cavity shrinking at a rate $v = 10^{-4}\sigma/\tau$. Inset: Fraction of crystalline particles as a function of η for $N = 500$ in a hard spherical cavity at fixed volume.

We now focus on the resulting crystalline clusters. We observe that in most of the clusters, despite the frustration of the hard spherical boundary that prevents a complete crystallization of the outer layers, most of the particles are arranged in wedge-shaped domains pointing towards the center of the assemblies. In particular, when the system size is relatively small, the clusters exhibit icosahedral symmetry, as shown in Fig. 2.2(a) for $N = 2000$ hard spheres. Such a structure is reminiscent of the icosahedral packing of spheres proposed by Mackay [81]. As it will be evident below (see Fig. 2.7), it consists

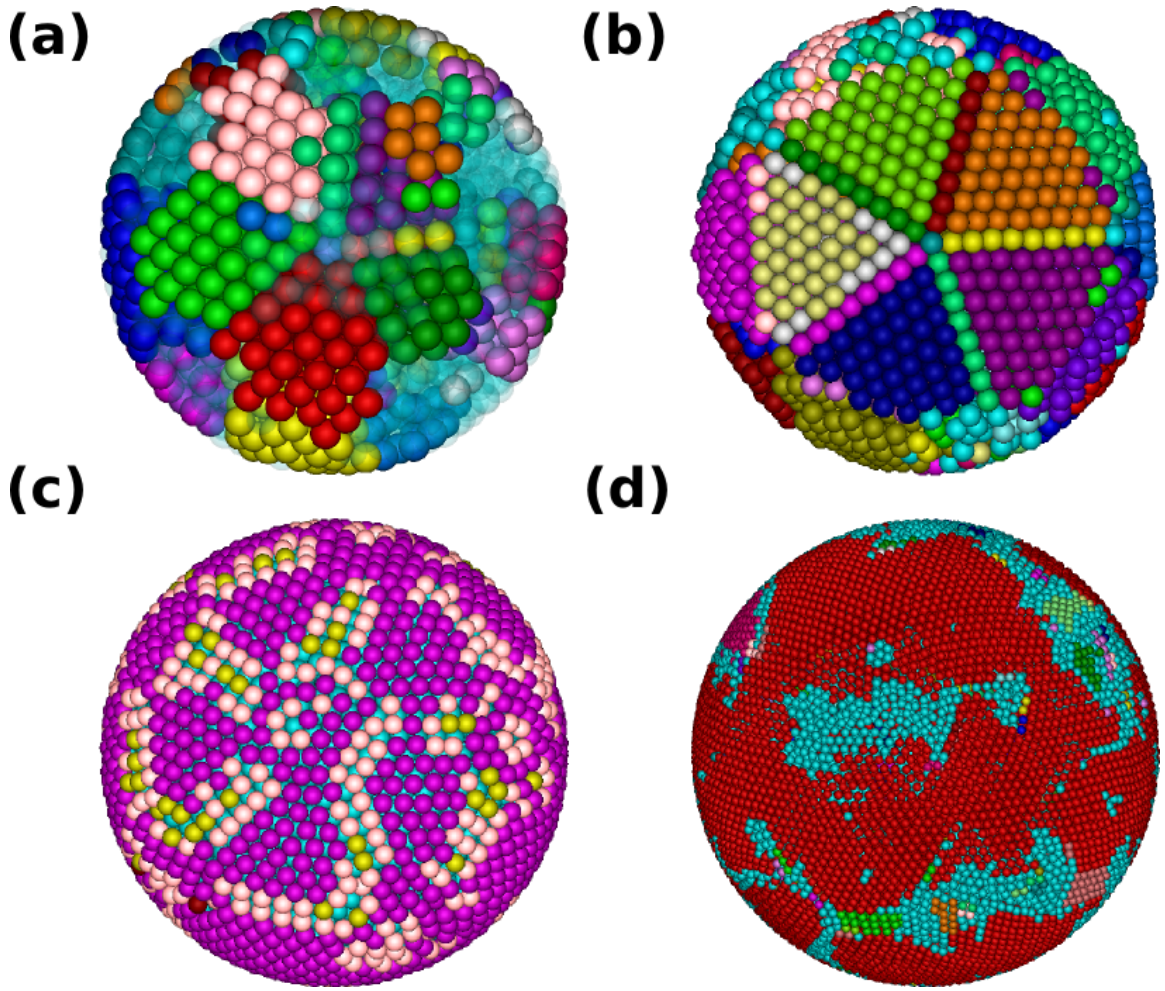

Figure 2.2: **(a)** Final configuration of $N = 2000$ hard spheres confined in a shrinking hard spherical cavity ($v = 10^{-5}\sigma/\tau$) obtained from EDMD simulations. Different colors indicate different domains. Fluid-like particles are light blue and transparent. The typical five-fold symmetry of an icosahedral arrangement is readily visible. **(b)** $N = 8000$ hard spheres confined in a hard shrinking spherical cavity ($v = 10^{-5}\sigma/\tau$). The three outer layers have been removed such that the icosahedral core is visible. **(c)** Surface order in a cluster composed of $N = 8000$ hard spheres. Particles are colored according to the number of neighbouring spheres in a Delaunay triangulation. Purple particles have 6 nearest neighbours on the surface, yellow have 4, pink 5, dark red 7. The surface resembles rhombicosidodecahedral order. **(d)** Outside view of a typical configuration in a system of $N = 64000$ hard spheres compressed in a hard spherical cavity ($v = 10^{-4}\sigma/\tau$). A large crystalline domain (red particles) spans the entire cluster. A cut through the middle of the cluster is shown in Fig. 2.3.

of twenty deformed FCC ordered tetrahedral domains that share a particle in the center, such that the (111) adjacent tetrahedral faces form twinning planes. The resulting cluster is a multiply twinned crystal with five-fold symmetry and has the shape of an icosahedron with 20 triangular (111) facets at the surface. Also for slightly larger systems, for example for $N = 8000$ as shown in Fig. 2.2(b), the icosahedral arrangement is still present in the

core of the cluster. However, the surface particles display a peculiar order, as can be observed in Fig. 2.2(c) that shows the number of neighbours for each particle at the surface. Such an arrangement resembles a rhombicosidodecahedral geometry consisting of twelve pentagonal faces, twenty triangular faces and thirty rectangular faces (cfr. Fig. 2.7). More precisely, this type of clusters belongs to the class of surface-reconstructed icosahedral structures, also known as anti-Mackay icosahedra. Indeed, they have a Mackay icosahedral core but a different surface termination, as the triangular facets meet yet another set of twinning planes near the surface [90]. Finally, for even larger cluster sizes, we observe that the wedge-shaped domains disappear in favour of larger domains that span the entire clusters, as shown in Fig. 2.2(d) for $N = 64000$ hard spheres. In this case, almost all the crystalline particles belong to a single FCC domain, except for some defects (cfr. also bottom left panel in Fig. 2.3), as expected for systems approaching the bulk limit.

These structural transitions between Mackay to anti-Mackay to FCC ordering clearly depend on the cluster size. To support this, we show in Fig. 2.3 cuts through the middle of the resulting clusters for several different system sizes. We observe that the typical wedge domains and the twinning planes observed in smaller system sizes slowly disappear upon increasing the system size. Analogously, the outer crystalline layers and the associated surface terminations are present only for intermediate size range. For very large clusters, the number of different crystalline domains drastically reduces until almost only one single FCC domain is present in the cluster.

Furthermore, we observe that adding a short-ranged ($\leq 2\sigma$) repulsion between the spheres and the confining wall, to model possible surface tension effects, gives rise to more faceted supraparticles, but does not affect the icosahedral symmetry of the core. In the right panels of Fig. 2.3, we show typical configurations obtained by using a potential of the form $\epsilon/|R-r|^n$, with r the distance between a particle and the center of the cavity of radius R, and with $n = 2$, interaction range $r_{soft} = 1\sigma$, and interaction strength $\epsilon = 1k_BT$. We indeed note that the clusters obtained in a soft repulsive spherical confinement have a higher fraction of crystalline particles and a more pronounced icosahedral symmetry than the clusters confined in a hard cavity as the geometrical confinement is less severe for the particles close to the surface. Similarly, the anti-Mackay surface termination is also more evident in the case of a soft confinement. Nevertheless, our simulations show clearly that icosahedral ordering arises spontaneously for hard spheres in both a hard and a soft repulsive spherical confinement.

Finally, we perform simulations with a short-ranged (1σ) square-well (maximum depth $\sim 10k_BT$) attractive potential between interface and particles. A typical resulting structure for $N = 8000$ hard spheres is shown in Fig. 2.4 and still exhibits an icosahedral core. We can conclude that the type of interface (repulsive or attractive) does not play a vital role in the stabilization of icosahedral symmetry. As we will show in Fig. 2.8, our simulations reveal striking agreement with the experimentally observed structures.

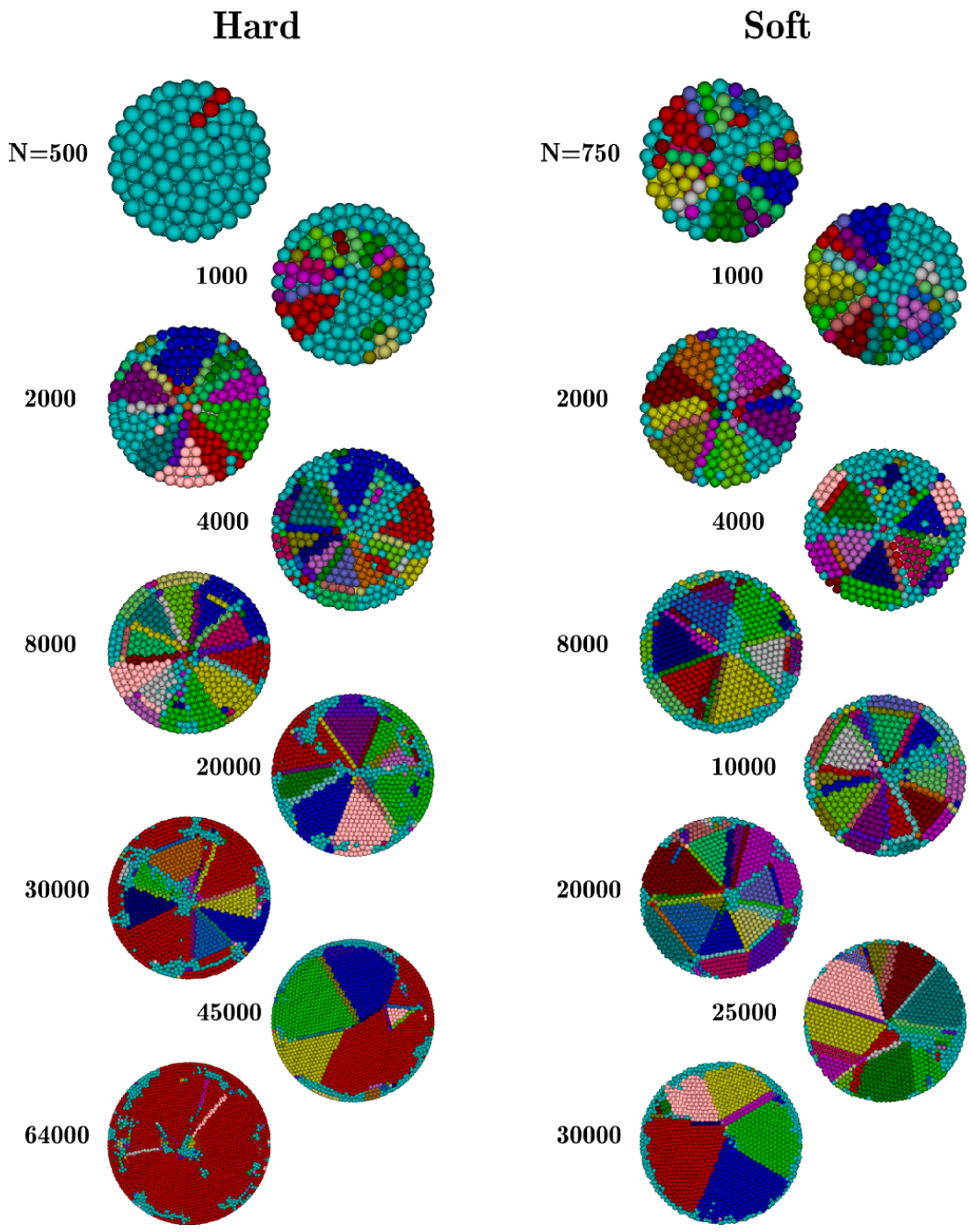

Figure 2.3: Size-dependence of the crystal morphology observed in computer simulations. A cut through the middle of the cluster is shown for different system sizes (N is the total number of particles). Different colors indicate different crystalline domains. Light blue particles are fluid-like particles. **Left:** A hard spherical confinement. **Right:** A soft repulsive spherical confinement. (See text for details on the potential).

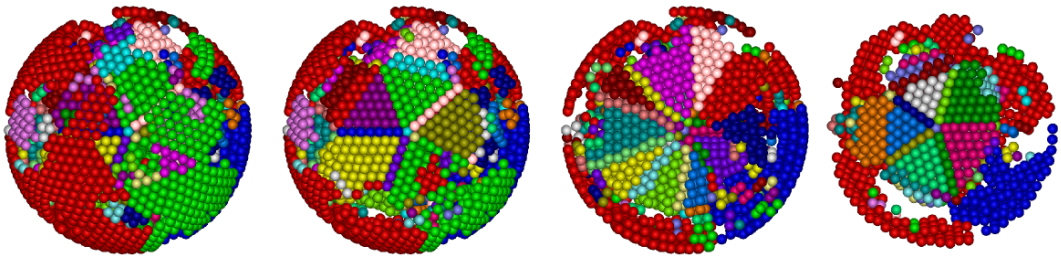

Figure 2.4: Clusters from EDMD simulations with an attractive wall. Snapshots of a cluster of $N = 8000$ particles in a system where the wall-particle interaction was modeled by a short-ranged attractive potential. The image on the left shows the outside of the cluster, while the next three images show progressively deeper cuts through the cluster, where 5, 10, and 5 tetrahedra are intersected, respectively. Particles identified as non-crystalline are not shown. Similar results were observed in smaller clusters ($N = 4000$).

The evolution of the crystal structure, and thus the nucleation and growth mechanism, can also be studied directly in the simulations. In Fig. 2.5 we examine the evolution of a system which forms an anti-Mackay rhombicosidodecahedron. Using the cone algorithm [83], we determine the fraction of crystalline particles in the surface layer near the confining wall, the first three sublayers from the surface, and the inner part of the cavity as a function of packing fraction. As already mentioned above, the packing fraction increases as the spherical cavity shrinks over time. We clearly see that the crystallization starts near the spherical interface, initially forming approximately two or three layers. When the packing fraction reaches approximately $\eta = 0.52$, part of the interior starts to crystallize, growing on the already present crystalline domains in the surface layers and proceeding inwards. Additionally, as the interior starts to crystallize, the surface layer becomes less crystalline (the decrease of the red curve in Fig. 2.5). Between volume fractions $\eta = 0.52$ and $\eta = 0.53$ the interior completely crystallizes, forming the tetrahedral domains associated with the Mackay icosahedron. It is worth noting that this process is very dynamic as the domains can crystallize and melt several times before the system fully crystallizes into 20 tetrahedral FCC units. Upon further increase of the packing fraction, the surface layers recrystallize into the anti-Mackay surface termination. This crystallization process is reminiscent of the nucleation of hard spheres near hard spherical seeds described by Cacciuto *et al.* [103]. In particular, they observed that crystal nucleation started on the surface of the seed, which then grew out into the bulk, while the crystal near the surface melted. In contrast, our simulations of smaller numbers of confined hard spheres which self-assemble into Mackay icosahedra, did not exhibit this final melting or recrystallization part. To illustrate that, we show in Fig. 2.6 results for the formation of a Mackay icosahedral cluster of 2000 hard spheres in a hard spherical confinement. Also in the case of clusters with a final FCC configuration, the nucleation starts at the wall but the crystal grows inside the cavity in a smooth way, as expected since the final structure does not present any wedge-shaped domains.

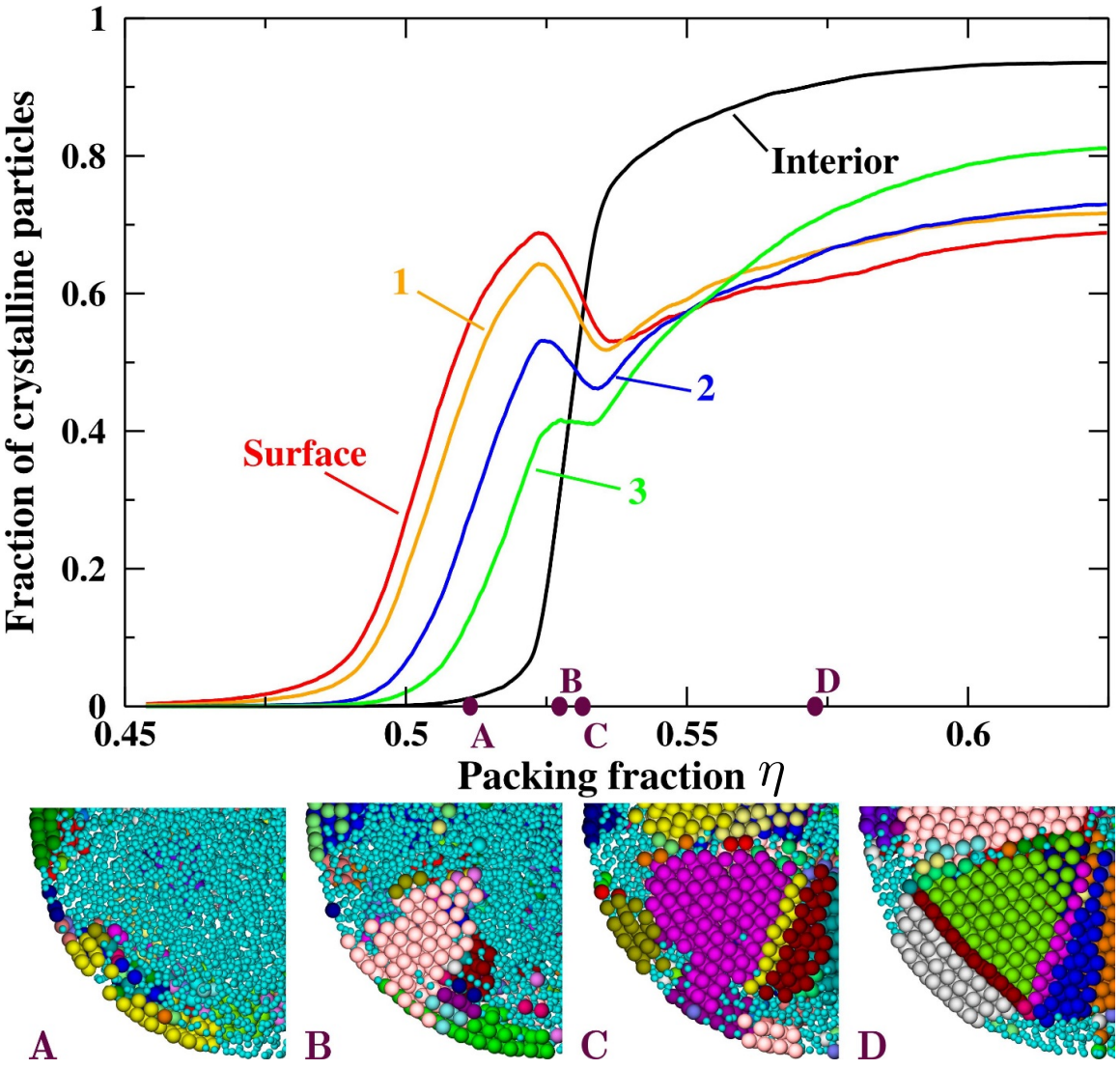

Figure 2.5: Crystallization process of 16000 hard spheres in a shrinking spherical confinement forming an anti-Mackay rhombicosidodecahedral cluster. **Top**: fraction of crystalline particles in the surface layer, the first three layers and the interior as a function of the packing fraction. Note that due to the shrinking confinement, the packing fraction slowly increases over time. **Bottom (A, B, C, D)**: typical configurations from simulations at different packing fractions ($\eta_A \approx 0.511$, $\eta_B \approx 0.527$, $\eta_C \approx 0.531$, $\eta_D \approx 0.572$) as indicated on the graph. Crystalline domains are indicated with different colors. Fluid-like particles are displayed with a smaller diameter and are coloured light blue.

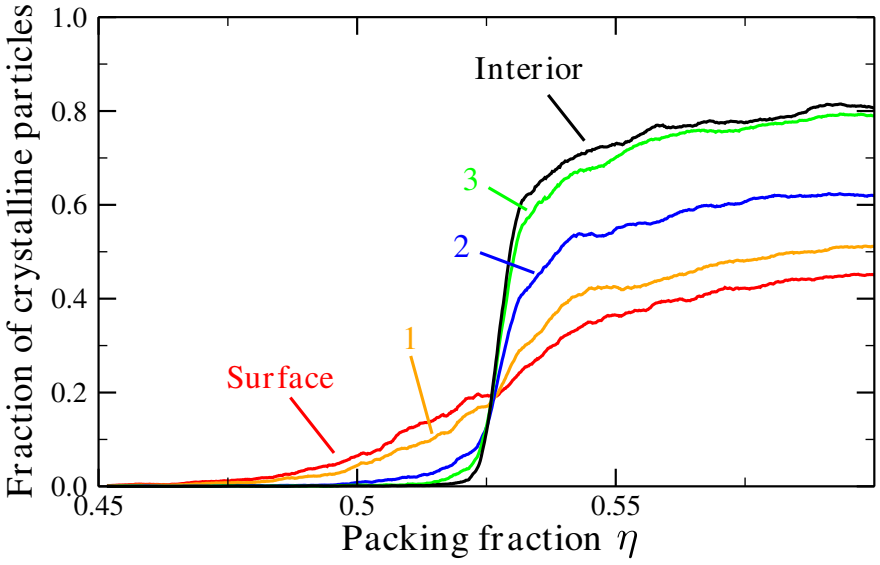

Figure 2.6: Crystallization process of 2000 hard spheres in a hard spherical confinement that slowly shrinks in time forming a Mackay icosahedral cluster. Fraction of crystalline particles in the surface layer, the first three sub-layers and the interior as a function of the packing fraction η.

2.4 Comparison with experiments

The behaviour of colloidal spheres in spherical confinement has also been studied experimentally in our group [104, 105]. Cobalt iron oxide nanoparticles with a core diameter of 6.0 ± 0.29 nm (9 nm effective diameter due to interdigitating oleic acid ligands and an effective polydispersity of 3.2 %) were synthesized [106] and dispersed in a suitable (apolar) solvent. This dispersion was emulsified into an oil-in-water emulsion. Subsequently, the evaporation of the solvent in the suspended emulsion droplets led to a slow increase in the packing fraction of the nanoparticles in the droplets, which eventually caused crystallization of the nanoparticles. The same process was used for fluorescently labelled micron-sized core-shell silica colloids [107], with a diameter of 1.32 ± 0.039 μm (and a polydispersity of 1.7 %), as well as for core-shell semiconductor nanoparticles with a core diameter of 12.4 ± 1.0 nm (14.5 nm effective and an effective polydispersity of 6.9 %). The colloids were dispersed in a water-in-oil emulsion instead of an oil-in-water emulsion. In all cases, the evaporation times were much longer than the diffusional equilibration time of the colloidal systems. Examples of the resulting self-assembled clusters, also denoted as "supraparticles", are shown in Fig. 2.7(a)-(b)-(c). Remarkably, we observe three different types of crystalline packings depending on the cluster size, in analogy with the simulation results. In particular, Fig. 2.7(a) shows a 105 nm diameter supraparticle that exhibits Mackay icosahedral symmetry, analogous to the clusters of gold nanoparticles formed by a similar process in Ref. [86]. For larger supraparticles, the surface resembles the (anti-Mackay) rhombicosidodecahedral geometry, as shown in Fig. 2.7(b), where a 216 nm supraparticle is depicted. Anti-Mackay icosahedra were also found for instance in clusters of argon [108] and lead [82] atoms, as well as in clusters of gold nanoparticles [86]. Finally, for sufficiently large cluster sizes, the supraparticles consist of a single FCC domain of nanoparticles. Fig. 2.7(c) shows an example of such a non-icosahedral FCC supraparticle with a diameter of 734 nm. In this case the surface presents the typical step edges of an FCC crystal confined to a sphere.

To study the size dependence of the cluster symmetry in more detail, 121 supraparticles containing between approximately 430 and 500000 nanoparticles (with a resulting supraparticle diameter between 75 nm and 785 nm) were examined. The cluster structure was determined from the secondary electron scanning transmission electron microscopy (SE-STEM) images of the particles at the surface. In the estimation of the number of nanoparticles, it was assumed that the volume fraction within each supraparticle corresponded to that of hard spheres at close packing ($\eta \approx 0.74$). As shown in Fig. 2.7(d), the transition from a Mackay icosahedron to an anti-Mackay rhombicosidodecahedron was found to be between 1000 and 3000 nanoparticles per supraparticle, and the transition to purely FCC ordering occurred between 25000 and 90000 nanoparticles. Clusters with more than 90000 nanoparticles exhibited solely FCC ordering. The same three structures were found for micron-sized colloids and the core-shell semiconductor nanoparticles. The transitions from Mackay to anti-Mackay to FCC ordering found by computer simulations approximately matched the ones observed in the experimental systems.

Furthermore, in order to confirm that the internal structure of our clusters corresponds to (anti-)Mackay icosahedra, the 3D-coordinates of the individual particles in several clusters were obtained. In particular the nanoparticles positions were extracted from

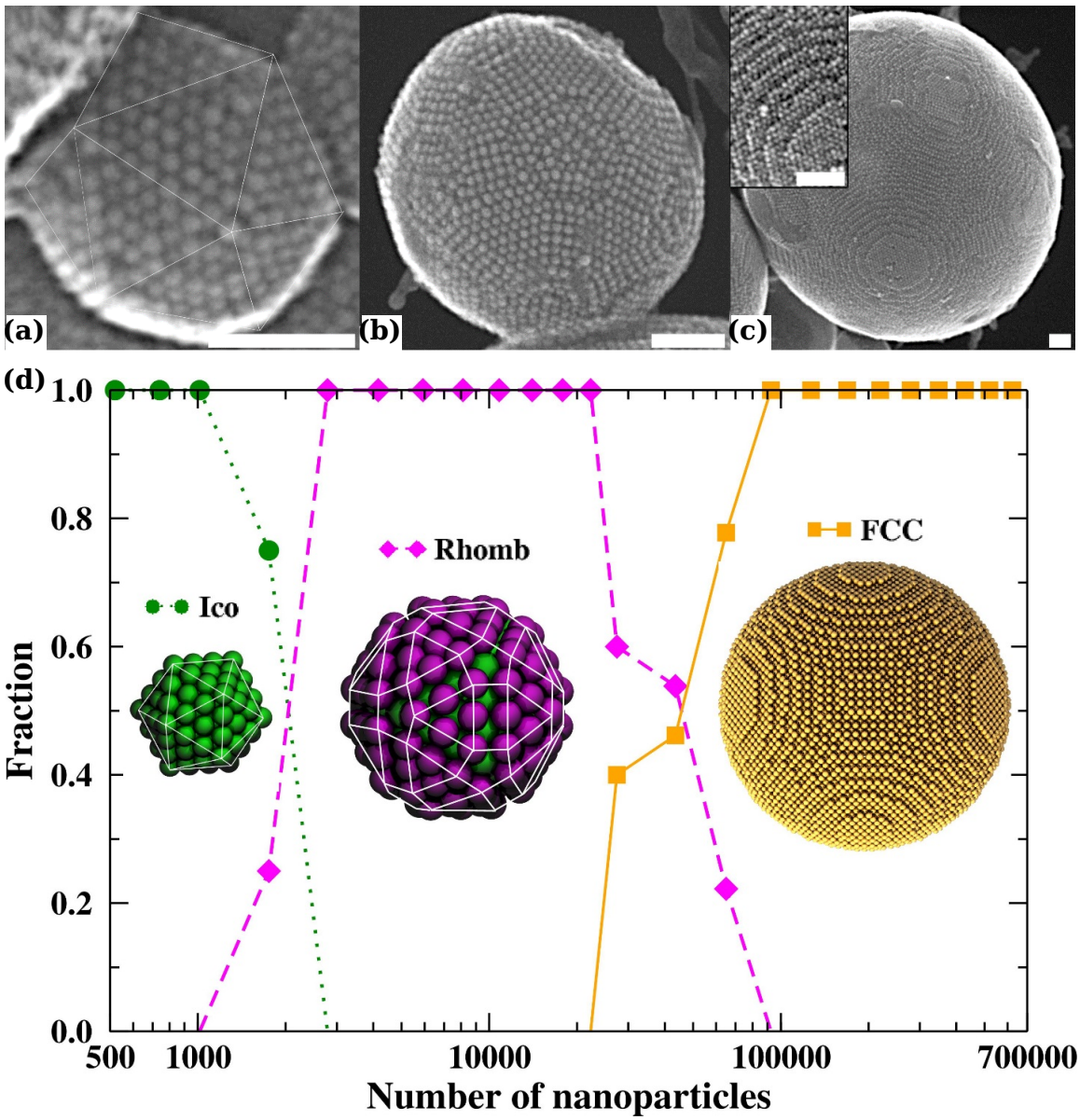

Figure 2.7: **(a)-(b)-(c)** Secondary electron scanning transmission electron microscopy (SE-STEM) images of typical supraparticles containing cobalt iron oxide nanoparticles. **(a)** Supraparticle with a diameter of 105 nm with Mackay icosahedral symmetry as indicated by the thin lines. **(b)** 216 nm supraparticle with anti-Mackay rhombicosidodecahedral structure. **(c)** 734 nm supraparticle consisting of a single face-centered-cubic (FCC) crystal domain. Inset: a magnified view of the step edges of the FCC supraparticle. All scale bars are 50 nm. **(d)** Size dependence of the cluster structure. Structural transition from a Mackay icosahedron (Ico) to an anti-Mackay rhombicosidodecahedron (Rhomb) to a face-centered-cubic (FCC) cluster as observed for supraparticles consisting of nanoparticles. The fraction of structures, based on 121 supraparticles, is plotted as a function of the number of nanoparticles per supraparticle. 14 icosahedra, 63 rhombicosidodecahedra and 44 FCC clusters were observed.

electron tomography images [109], and the colloids positions from confocal microscopy images [110], using particle tracking software. Figure 2.8 shows the structure of typical clusters displaying icosahedral symmetry formed from both nanoparticles and colloids, with different colors indicating different crystal domains as identified by a bond-orientational order parameter [75]. The characteristic five-fold symmetries of Mackay icosahedra are clearly visible in the interior of all clusters (top row of Fig. 2.8). The larger supraparticles additionally showed anti-Mackay icosahedral surface terminations (bottom row of Fig. 2.8). Note that the assemblies made from the colloids resulted in only partially ordered clusters, where roughly half of the cluster resembled a Mackay or an anti-Mackay icosahedron, and the other half consisted of disordered colloidal particles. This was observed in all the colloidal clusters examined and it is almost certainly due to gravitational sedimentation of the colloids within their emulsion droplets, as well as the sedimentation and deformation of the droplets themselves. Typical configurations obtained from simulations are also shown for comparison in Fig. 2.8. The clear emergence of icosahedral symmetry in these fairly different experimental systems and the agreement with computer simulations of hard spheres strongly indicates that this behaviour is not interaction specific, and confirm that the formation of icosahedral clusters can be purely entropy-driven. Finally, we notice that simulations with (slightly) softer boundaries capture better the order of the experimental cluster surface, consistently with the fact that some degree of softness in the confining cavity is expected, but this is not crucial for the internal icosahedral order.

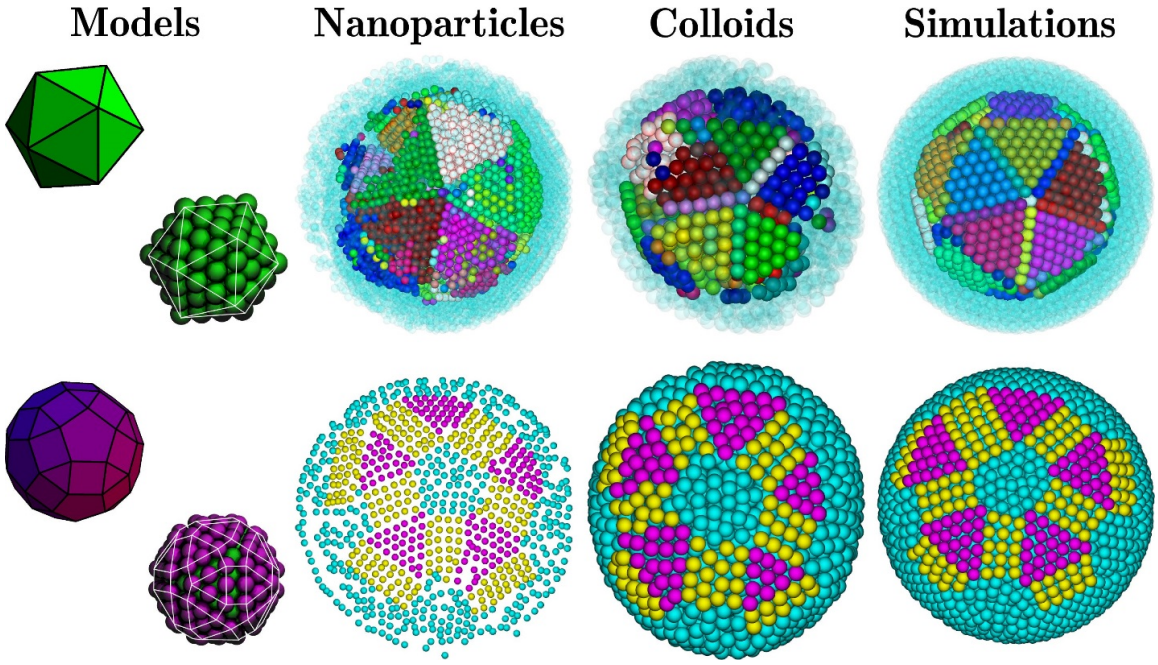

Figure 2.8: Core **(top)** and the surface termination **(bottom)** of large icosahedral supraparticles resulting from the self-assembly of spherically confined colloidal spheres. The first column depicts models of the corresponding polyhedra and their associated ideal sphere packings. The other columns contain typical examples of clusters in (from left to right) experimental systems of nanoparticles ($N \approx 12000$), experimental systems of micron-sized colloids ($N \approx 3000$), and simulations of hard spheres ($N = 6000$). Note that in the top row, particles belonging to the outer layers are plotted transparent so that the core, that displays Mackay icosahedral symmetry, is readily visible, and the crystalline domains are indicated by different colors. In the bottom row, the particles are colored as a guide to the eye to highlight the anti-Mackay rhombicosidodecahedral symmetry of the clusters.

2.5 Thermodynamic stability of icosahedral clusters

To examine the thermodynamic stability of the icosahedral clusters, we perform free-energy calculations [97] on all the structures that were observed in experiments and simulations, i.e., FCC and Mackay icosahedral clusters. We use a 3-step thermodynamic integration method proposed by Schilling and Schmid [97] and described in Sec. 2.2.2. In particular, this method allows us to calculate the free-energy difference between our system, e.g. spherically confined hard spheres, and a reference system for which the free energy is known exactly. The reference system we use consists of non-interacting particles attached, via a linear well potential, to lattice sites. The lattice sites are taken from representative configurations of the system featuring the desired cluster symmetry, see Fig. 2.9. To create these configurations, we first compress a system with a fixed number of particles to the desired volume starting from a configuration that displays the chosen symmetry. In a second stage, simulations at fixed volume were performed to evolve the system. We notice that also in almost ideal configuration not all particles display crystalline order, and defects in the structures can affect the final free energy. Therefore an accurate calculation of the absolute free-energy for icosahedral and FCC clusters is extremely challenging. To obtain a reliable error on the final value 5 independent but equivalent configurations were taken into account.

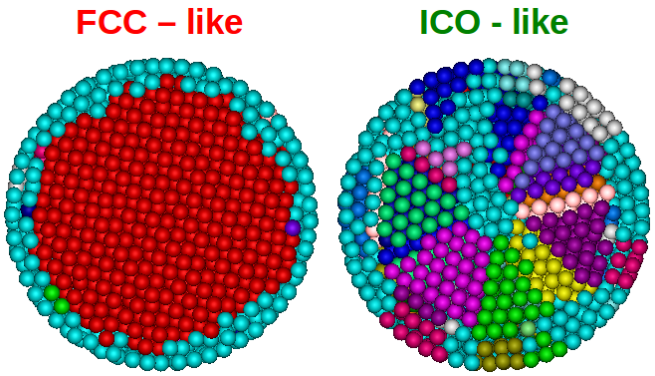

Figure 2.9: Examples of reference configurations for the free-energy calculations. Crystalline domains are indicated with different colors. Light blue particles represent fluid-like particles. Configurations were obtained by first placing particles in the desired lattice at a given packing fraction and then by letting the system evolves through simulations by keeping the volume fixed.

We compare the free energy of the two types of clusters (ico-like and fcc-like) containing between 1500 and 4000 particles. We find the icosahedral cluster to be more stable than FCC for packing fractions close to melting with free-energy differences of $0.03 \pm 0.01\ k_B T$ per particle (see Table 2.1). Hence, we conclude that the presence of icosahedral ordering observed is purely entropy-driven, and is not simply a kinetic, but rather a genuine equilibrium effect which explains the high reproducibility of the icosahedral clusters in both simulations and experiments. In addition, we remark that the free-energy differences due to entropy as reported in Table 2.1 is of the same order as the potential-energy difference between icosahedral and FCC Lennard-Jones clusters [85]. Our results thus show that

entropy could play an important role in determining the cluster structure even in cases where the clusters are stabilized by energetic interactions.

N	η	$\Delta F = F_{\mathrm{FCC}} - F_{ico}\ [k_B T/N]$
1500	0.551	0.026 ± 0.020
1500	0.571	0.036 ± 0.012
3000	0.554	0.036 ± 0.006
4000	0.537	0.030 ± 0.006
4000	0.558	0.038 ± 0.009
4000	0.572	0.034 ± 0.007

Table 2.1: Free-energy difference between FCC-like and icosahedral-like arrangements of N hard spheres confined in a hard spherical cavity. Clusters with a global icosahedral symmetry are thermodynamically more stable than FCC clusters for the cluster sizes and packing fractions that are reported here.

Furthermore, we note that even for small clusters the FCC structure should become stable for sufficiently high densities as the maximum packing fraction of icosahedral clusters is $\eta \approx 0.69$, which is significantly lower than that of a close-packed FCC cluster [81]. This has been also confirmed by repeating the free-energy calculations for the two different structures at higher packing fraction. Some results are reported in Fig. 2.10, together with a tentative state diagram of hard spheres under spherical confinement based on the following observations. Our free-energy calculations reveal a stable region for the icosahedral clusters in the state diagram. We observe both in experiments and simulations a Mackay to anti-Mackay structural transition upon increasing the number of particles. In the limit of $N \to \infty$, the system reduces to a bulk system of hard spheres, for which the phase behaviour is well-known. The maximum packing fraction of hard spheres in a spherical cavity depends in a non-trivial way on the total number of particles and is always smaller than the closest-packing in bulk. Based on these (very limited) observations (that also ruled out the possibility of other stable structures) we "sketch" in Fig. 2.10(b) a tentative state diagram of hard spheres in spherical confinement.

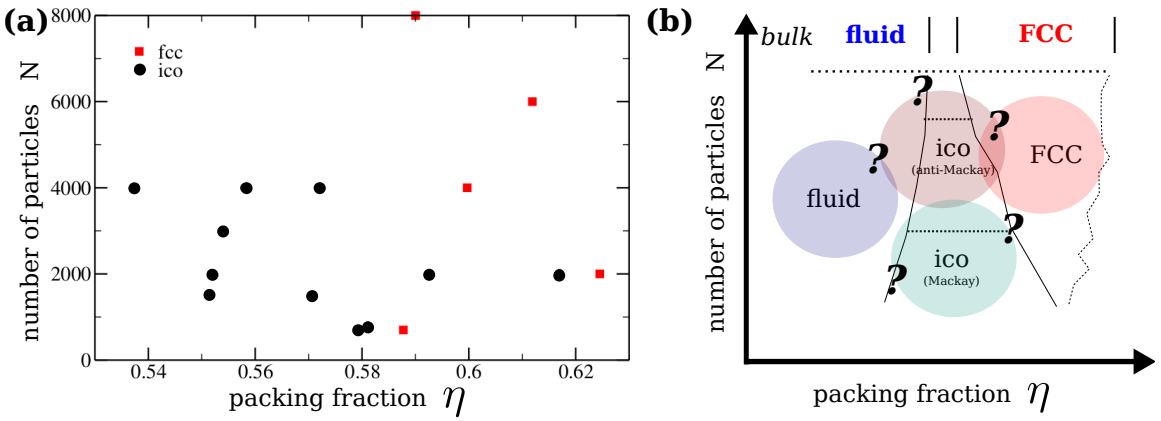

Figure 2.10: **(a)** Stability of FCC (red squares) and icosahedral (black circles) clusters for N hard spheres at packing fraction η confined within a hard spherical cavity obtained by free-energy calculations. **(b)** Tentative state diagram of hard spheres in a spherical confinement.

2.6 Outlook

From short-ranged to longer-ranged confinement

In summary, we have shown that the experimental behaviour of (some) evaporating droplets is well captured by our simple model, and that the interaction between particles and interface (modelled either as hard-core interaction or as a short-range interaction) does not qualitatively change the structures formed. However, we expect that in different experiments different interactions between particles and interface could lead to a qualitatively different structural organization in the supraparticles. To explore this possibility, we perform EDMD simulations of hard spheres within a shrinking spherical cavity interacting via a longer-ranged potential. We report two examples. In Fig. 2.11(a), we show the final cluster for $N = 4000$ hard spheres interacting with the spherical interface via a truly long-range repulsive potential $U_{p-w}(r) \propto 1/|R - r|$ that acts until the center of the cavity (of radius R). In this case, we observe that the nucleation does not start at the surface, i.e., heterogeneous nucleation, but in the middle of the cavity, i.e., homogeneous nucleation as what happens in the bulk. Moreover, the final crystalline structure does not contain any wedge-shaped domains but striped ones that span the entire cluster. In Fig. 2.11(b), we show the final cluster for a much smaller system ($N = 750$) and a "short-ranged" particle-interface potential $U_{p-w}(r) \propto 1/|r - R|^2$, as previously, but with interaction range $r_{soft} = 3\sigma$ that almost reach the center of the cavity for this system size. In this case, the five-fold symmetry is still evident but the overall structure does not resemble an icosahedron but a pentagonal prism. We thus conclude that the structural behaviour of hard spheres in spherical confinement can be changed drastically by the interaction range of the particle-interface potential.

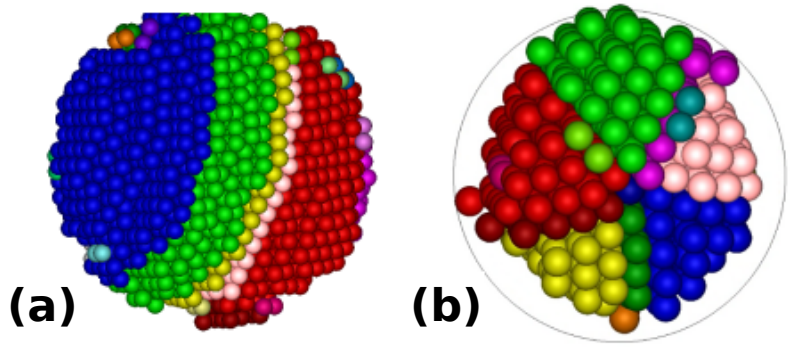

Figure 2.11: **(a)** Final cluster configuration of $N = 4000$ hard spheres obtained by shrinking a spherical cavity with a long-ranged repulsive wall-particle interaction potential $\beta U_{p-w} \propto 1/r$ and compression rate $v = 10^{-4}\sigma/\tau$. Different crystalline domains are depicted with different colors. Only particles belonging to crystal domains are shown. Stripes of crystalline domains span the entire cluster. **(b)** Final cluster configuration of $N = 750$ hard spheres obtained by shrinking a spherical cavity with a wall-particle interaction potential $U_{p-w} \propto |r - R|^2$ and interaction range $r_{soft} = 3\sigma$, which is of the order of the radius of the final cluster. Different crystalline domains are denoted by different colors. Only particles belonging to crystal domains are shown. The structure resembles a pentagonal prism.

From pure hard spheres to binary mixtures of spheres

Binary mixtures of (semiconductor) nanoparticles can form various types of structures, such as binary superlattice structures [111], core-shell supraparticles and Janus supraparticles, when confined in a shrinking emulsion droplet [112]. Clearly, the corresponding parameter space increases drastically, as not only the total number of particles N but also the composition N_L/N (with N_L the number of large spheres) and size ratio σ_S/σ_L (with σ_L the diameter of the large spheres and σ_S the diameter of the small spheres) play a crucial role. Furthermore, only under particular conditions semiconductor nanoparticles can be effectively described as hard spheres [111], and (subtle) changes, as different surface coverages of the ligands on the particles, can introduce attractive interactions. Therefore, a systematic study of all these effects is barely feasible at present.
Nevertheless, we perform several simulations on binary mixtures of hard spheres starting from a dilute state and slowly shrinking the hard spherical cavity. However, we never found a large degree of crystallinity in the resulting structures in contrast to the single-component case, which is perhaps not surprising as the spontaneous formation of binary crystals is notoriously difficult to observe also in bulk simulations. For instance, when we confine an equimolar mixture of large and small hard spheres with size ratio $\sigma_S/\sigma_L = 0.333$ and a total number of particles $N = 4000$ in a spherical cavity, only a very small part of the surface displays crystalline order, as shown in Fig. 2.12(a). However, the particles in the core of the cluster do not show any crystalline order. The stable bulk crystal structure for binary hard-sphere mixtures with a size ratio $\sigma_S/\sigma_L = 0.3$ is either the interstitial solid solution with the pure FCC crystal of large spheres and the NaCl structure the two limiting cases, or the LS_6 crystal structure [113]. It is interesting

to investigate under which conditions an interstitial solid solution with the large spheres arranged in an icosahedral cluster can become stable. On the other hand, for binary hard-sphere systems with a less-asymmetric size ratio, for example $\sigma_S/\sigma_L = 0.75$ and a total number of particles $N = 2000$, we only observe completely disordered clusters as shown in Fig. 2.12(b). This also raises the question if the binary crystal structures that are stable in the bulk are compatible with a (strong) spherical confinement. Indeed, one effect that the spherical confinement could induce is a radial dependence of the system composition.

An extreme limit of that would be the formation of a core-shell supraparticle, in which one of the species is prevalently close to the spherical interface while the other species resides in the core of the cavity. For highly asymmetric binary hard-sphere mixtures, it is tempting to speculate on the basis of Fig. 2.12(a) that the small spheres prefer to be close to the surface, but this does not seem the case for less asymmetric mixtures. We therefore expect that a core-shell cluster can only be formed due to a demixing transition of the two species, e.g., in the case of highly asymmetric binary hard-sphere mixtures [114], or due to enthalpic interactions that favor demixing. In order to examine this, we study a binary mixture of spheres with a size ratio of $\sigma_S/\sigma_L = 0.75$, composition $N_L/N = 0.2$, and a total number of particles $N = 2000$ in a spherical cavity with hard-sphere interactions between the small particles, between small and large spheres, hard-wall interactions with both particle species, but an attractive square-well interaction between the large hard spheres with a interaction range 1.4 σ_L and a well depth of $1k_BT$. We clearly observe the formation of a core-shell supraparticle as shown in Fig. 2.12(c), in which the large particles tend to maximize the number of bonds with the other large spheres in order to minimize the energy, and hence they reside in the middle of the core-shell supraparticle. Clearly, by varying the particle-interface interaction it is also possible to modify the structure of the supraparticle. In Fig. 2.12(d), we show that in the case of a binary hard-sphere mixture with only a very short-ranged attraction between the large hard spheres and the spherical interface (square-well potential with a depth of $1k_BT$ and an interaction range of $0.5\sigma_L$), the large spheres tend to occupy the surface. However, the outer single layer of large particles cannot act as a template for the formation of more layers and the thickness of the shell of large particles is therefore directly determined by the interaction range of the particle-interface potential.

In conclusion, we show that it is not trivial to find the right conditions for the formation of a supraparticle with a binary superlattice structure using a binary mixture of spheres in a spherical confinement. In addition, we find that a demixing transition due to enthalpic interaction can lead to the formation of core-shell supraparticles in spherical confinement.

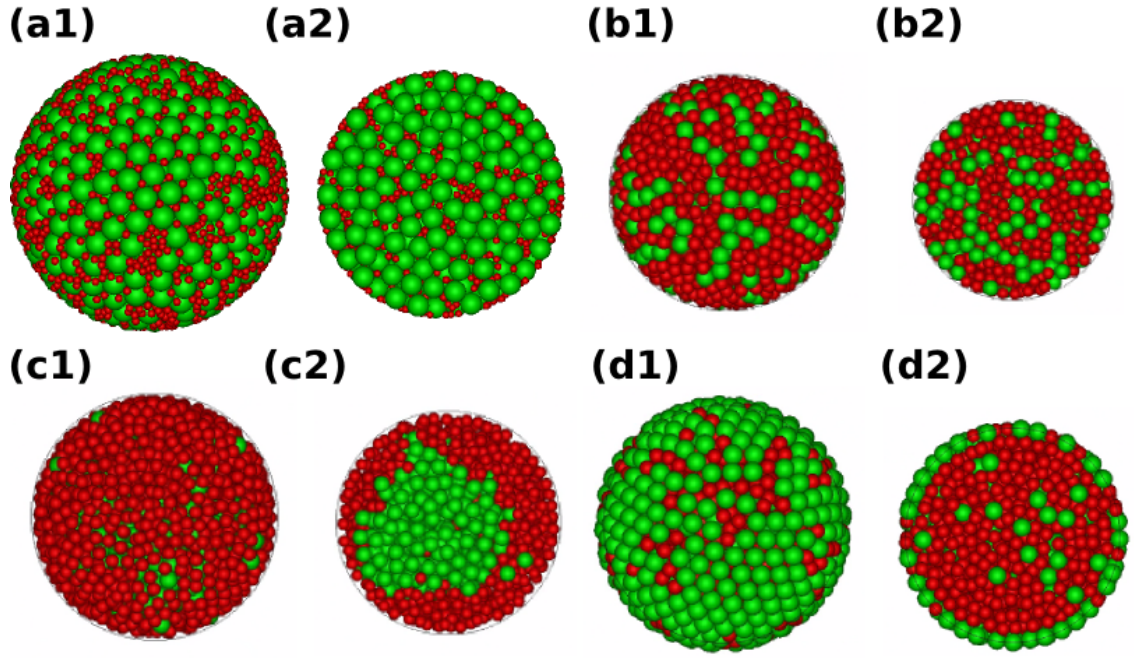

Figure 2.12: **(a)** Binary mixture of hard spheres with a size ratio $\sigma_S/\sigma_L = 0.333$, composition $N_L/N = 0.25$, and $N = 4000$, confined in a slowly shrinking hard spherical cavity. An outside view (a1) and a cut through the middle (a2) of the final cluster are shown. **(b)** Binary mixture of hard spheres with a size ratio $\sigma_S/\sigma_L = 0.75$, composition $N_L/N = 0.2$, and $N = 2000$, confined in a slowly shrinking hard spherical cavity. An outside view (b1) and a cut through the middle (b2) of the final cluster are shown. **(c)** Binary mixture of spherical particles ($\sigma_S/\sigma_L = 0.75$, $N_L/N = 0.2$, $N = 2000$) in which the interaction between the large particles is attractive (square-well with interaction range $1.4\sigma_L$ and depth $1k_BT$) while the other interactions (large-small, small-small, particle-wall) are hard-core. An outside view (c1) and a cut through the middle (c2) of the final cluster are shown. **(d)** Binary mixture of hard spheres with a size ratio $\sigma_S/\sigma_L = 0.75$, composition $N_L/N = 0.25$, and $N = 2000$, confined in a shrinking cavity that has a short-range ($r_{soft} = 0.5\sigma_L$) square-well (depth $1k_BT$) attractive interaction with the large particles (while the potential between the small particles and the wall is hard-core). An outside view (d1) and a cut through the middle (d2) of the final cluster are shown.

2.7 Conclusions

In conclusion, we have shown that entropy and spherical confinement alone are sufficient for the formation of stable icosahedral clusters. Our simulations clearly demonstrate that energetic interactions between the particles are not required for icosahedral order. Interestingly, this also provides new insights regarding the results reported in Ref. [86]: while the authors of that study attributed the formation of icosahedral clusters of gold nanoparticles to energetic interactions, it is now clear that entropic contributions should not be overlooked. Additionally, as already argued in Ref. [86], we clearly find that the interaction between the particles and the interface, at least for the experiments described in Sec. 2.4, does not appear to play a crucial role in this self-assembly process. In fact, our simulations show similar results regardless of whether the interface-particle interaction is attractive, hard, or repulsive. Our results also provide an interesting contrast to the icosahedral order observed in much smaller ($N = 13$) clusters of particles observed by Manoharan *et al.* [115]. In such systems, it was argued that the structure of the clusters was mainly determined by capillary forces during the final stages of the evaporation process, resulting in clusters that minimized the second moment of the mass distribution [116]. Here, we find that the spherical confinement provided by the surface tension of emulsion droplets is sufficient for the formation of large icosahedral clusters that minimize the free energy.

The fact that spherical confinement can stabilize structures that are fully incommensurate with that of the bulk, suggests new ways of designing small crystals with unusual symmetries that may be beneficial for optical or other applications. This opens up a new avenue for the self-assembly of novel structures by combining the vast array of currently available colloidal building blocks (e.g. rods, platelets, dumbbells), and mixtures thereof. Furthermore, the resulting supraparticles themselves can in turn self-assemble [117], resulting in hierarchical structures with new functionalities added at different length scales, e.g. with plasmonic properties at the nanoscale and photonic properties at the micron-scale.

It remains for future work to carefully analyse to what extent the entropy contributes in stabilizing clusters of particles with long-ranged attractions, if it is possible to increase the size range of equilibrium icosahedral supraparticles using particles with long-range interactions, and how the present study can be extended to binary systems. We already briefly showed that computer simulations can be used to explore these new directions and guide experiments, that are currently possible to perform.

Acknowledgements

Some of the results presented in this chapter are part of a collaboration with Bart de Nijs, who performed the experimental work described here under the supervision of Arnout Imhof and Alfons van Blaaderen, Frank Smallenburg, who initiated the computer simulations, and Laura Filion, who supervised part of the simulation work. Frank Smallenburg is acknowledged for providing the EDMD code in the initial stage of the project. Bart de Nijs is thanked for providing the beautiful experimental images. I want to express my sincere gratitude to Frank, Bart and Laura for many useful discussions. Furthermore, I want to thank John Edison for fruitful discussions and Da Wang for insights on the experiments on binary systems.

3

Hard spherocylinders: the exemplar case of liquid crystals formed by colloidal rods

This chapter is dedicated to the study of liquid crystal phases formed by anisotropic hard particles with a spherocylindrical shape. We use this system as an example to introduce Onsager theory that will be used throughout this thesis. Furthermore, we introduce a set of global and local order parameters to describe liquid crystalline order that will be used in this and in the following chapters both on simulation and experimental data. The ultimate goal of this chapter is to map the experimental behaviour of colloidal silica rods on that of hard spherocylinders. To achieve this, two important aspects need to be considered: the determination of the effective dimensions of the experimental particles and the effect of size polydispersity on the phase behaviour. For the latter, we perform computer simulations both in bulk and under gravity and see how the equation of state and the order parameters are affected by different size distributions with a small degree of polydispersity. After estimating the particle effective dimensions by mapping the jump of the nematic order parameter at the transition and the equation of state, we compare our simulation results with experiments. Qualitative agreement is obtained for the overall phase behaviour and quantitative agreement for packing fractions up to 40%.

3.1 Introduction

In this section, we focus on a simple model for anisotropic particles, namely hard spherocylinders, which form liquid crystal phases (see Sec. 1.3). The use of hard particles to study the liquid crystal behaviour has been quite extensive in theory and simulations [52]. Systems of hard ellipsoids were the first studied in 1984 by computer simulations to show a purely entropy-driven isotropic-nematic transition [31], as already theoretically predicted by Onsager in 1949 [30]. However, the drawback of such a model is that a smectic phase of hard ellipsoids is not stable. Hard spherocylinders have been introduced and studied by computer simulations in 1988 to overcome this limitation [32]. This study showed that smectic phases, as the ones that were observed in several colloidal systems [39, 44], can be stabilized by entropy alone. Since then, hard spherocylinders have been widely used in computer simulations, not only to study their liquid crystal phase behaviour [118, 119] but also, for example, to unveil the kinetic pathways and the nucleation process of nematic, smectic and crystal phases [120, 121], the particle dynamics in smectic phases [122], and as a model system to study the interfacial and wetting behaviour of liquid crystals at surfaces [123].

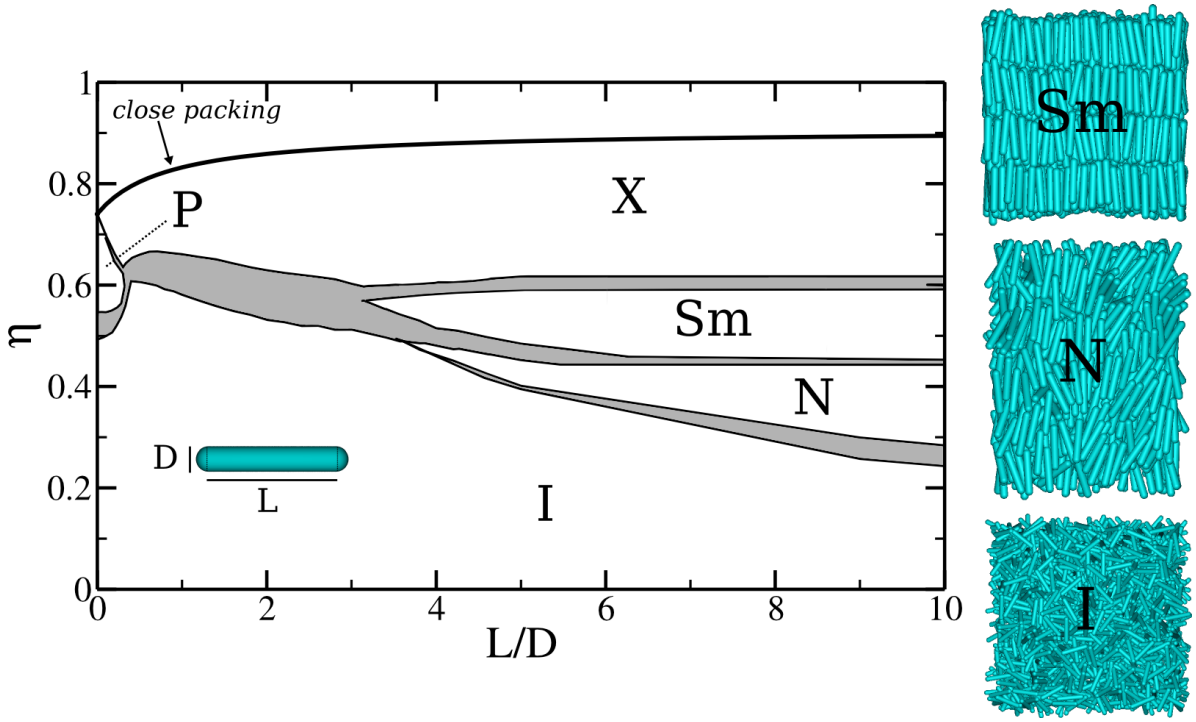

Figure 3.1: Phase diagram of hard spherocylinders (cartoon in the inset) in the packing fraction η - aspect ratio L/D plane, adapted from Bolhuis and Frenkel [118]. Shown are the regions where isotropic (I), nematic (N), smectic (Sm), crystal (X) and plastic crystal (P) phases are stable. Representative snapshots for I, N and Sm obtained from computer simulations are shown on the right. Solid line at the top denotes the maximum packing fraction η of the rods (close packing).

The sequence of thermodynamically stable phases in systems of hard spherocylinders depends on the aspect ratio L/D (see Fig. 3.1 adapted from Ref. [118]). For all L/D

at small packing fraction η an isotropic phase (I) with no long-range order neither in particle positions nor in particle orientations, is present. For very large η, a crystal phase (X) with long-range positional and orientational order is formed. The stacking (ABC or AAA) of the layers of rods in this phase depends on L/D [118]. At intermediate densities, so called mesophases can be stabilized. For short rods, plastic crystal phases (P) with positional order but no orientational order, are formed. For sufficiently long rods ($L/D > 3.1$) a smectic-A phase (Sm) occurs and if $L/D > 3.7$ also a nematic phase (N) is stabilized between the I and Sm phase. In this chapter, we first introduce Onsager theory to explain the I-N transition (Sec. 3.2) and describe theoretically how a uniaxial nematic phase can be elastically deformed (Sec. 3.3). These aspects will be relevant for the remainder of the thesis. In Sec. 3.4 we introduce a set of order parameters that will be used to distinguish the different thermodynamic phases. In Sec. 3.5 we calculate these order parameters for bulk configurations obtained by computer simulations, and we also study the effect of a small degree of size polydispersity on the liquid-crystal behaviour. In Sec. 3.6 we describe how sedimentation can be used to probe the phase behaviour and thermodynamics of a system over a wide range of parameters in just a single simulation and we present computer simulation results of polydisperse systems. Finally, in Sec. 3.7 we apply the order parameter analysis of an equilibrium sedimentation profile of colloidal silica rods and we compare the equation of state as obtained from simulations with the experimental data. We end with some concluding remarks in Sec. 3.8.

3.2 Revisiting Onsager theory: isotropic-nematic transition

In this section, we revisit Onsager theory [30] within the framework of classical density functional theory (DFT) [59], in the simple case of anisotropic rod-like colloids of diameter D and length L (see inset of Fig. 3.1).

The center-of-mass position of a particle with cylindrical symmetry can be described by a three-dimensional vector $\mathbf{r} = (x, y, z) \in V$, with V the volume of the system, whereas a unit vector $\hat{\mathbf{u}} = (\sin\theta\cos\phi, \sin\theta\sin\phi, \cos\theta)$ represents the particle orientation. Here $\theta \in [0, \pi)$ and $\phi \in [0, 2\pi)$ are the polar and the azimuthal angle with respect to $\hat{\mathbf{n}}$, the nematic director, that identifies the direction along which the particles are on averaged aligned (see inset in Fig. 3.2(a)). The single-particle density $\rho(\mathbf{r}, \hat{\mathbf{u}})$ of a generic phase depends on the single-particle degrees of freedom and satisfies the normalization condition

$$\int_V d\mathbf{r} \oint d\hat{\mathbf{u}}\, \rho(\mathbf{r}, \hat{\mathbf{u}}) = N, \tag{3.1}$$

where N is the total number of particles and the rotation-invariant measure is $d\hat{\mathbf{u}} = d\phi\, d\cos\theta$. The free energy is a functional of the single-particle density and can be written as a sum of ideal and excess contributions, $\mathcal{F}[\rho(\mathbf{r}, \hat{\mathbf{u}})] = \mathcal{F}_{id}[\rho] + \mathcal{F}_{ex}[\rho]$. The ideal term reads

$$\beta\mathcal{F}_{id}[\rho] = \int_V d\mathbf{r} \oint d\hat{\mathbf{u}}\, \rho(\mathbf{r}, \hat{\mathbf{u}}) \left[\log \mathcal{V}\rho(\mathbf{r}, \hat{\mathbf{u}}) - 1\right], \tag{3.2}$$

where $\beta = 1/k_B T$, with k_B the Boltzmann constant and T the temperature, and $\mathcal{V}$ is an (irrelevant) constant thermal volume. For the excess part we consider the second-order

truncation of the virial expansion (second-virial approximation):

$$\beta\mathcal{F}_{ex}[\rho] = -\frac{1}{2}\int_V d\mathbf{r}\, d\mathbf{r}' \oint d\hat{\mathbf{u}}\, d\hat{\mathbf{u}}' f(\mathbf{r}-\mathbf{r}', \hat{\mathbf{u}}, \hat{\mathbf{u}}')\rho(\mathbf{r}, \hat{\mathbf{u}})\rho(\mathbf{r}', \hat{\mathbf{u}}'), \tag{3.3}$$

where the interactions between particles are contained in the Mayer function

$$f(\mathbf{r}-\mathbf{r}', \hat{\mathbf{u}}, \hat{\mathbf{u}}') = e^{-\beta U(\mathbf{r}-\mathbf{r}', \hat{\mathbf{u}}, \hat{\mathbf{u}}')} - 1, \tag{3.4}$$

where $U(\mathbf{r}-\mathbf{r}', \hat{\mathbf{u}}, \hat{\mathbf{u}}')$ is the pair potential.

In a nematic phase, the positions of the particles are homogeneously distributed throughout the system and the single-particle density can be rewritten as $\rho(\mathbf{r}, \hat{\mathbf{u}}) = n\psi(\hat{\mathbf{u}})$, where $n = N/V$ is the average number density and $\psi(\hat{\mathbf{u}})$ is the orientation distribution function (ODF). Since the nematic director is the symmetry axis for global rotations, the ODF is independent of the azimuthal angle ϕ and depends only on the polar angle: $\psi(\hat{\mathbf{u}}) = \psi(\theta)$. Inserting this into $\mathcal{F}$ and integrating out the spatial and azimuthal degrees of freedom we obtain

$$\frac{\beta\mathcal{F}[\psi]}{V} = n(\log \mathcal{V}n - 1) + 2\pi n \int_{-1}^{1} d\cos\theta\, \psi(\theta)\, \log\psi(\theta) + \frac{n^2}{2}\int d\cos\theta\, d\cos\theta'\, E(\theta, \theta')\, \psi(\theta)\, \psi(\theta'), \tag{3.5}$$

where we identify the three terms associated to translational entropy, orientational entropy and excess contributions related to the excluded volume

$$E(\theta, \theta') = -\int d\phi\, d\phi'\, d\mathbf{r}\, f(\mathbf{r}, \hat{\mathbf{u}}, \hat{\mathbf{u}}'). \tag{3.6}$$

Eq. (3.5) is an exact expression for the bulk free energy of the nematic phase of infinitely long (aspect ratio $L/D \to \infty$) hard rods, as derived by Onsager [30]. Subsequently, Parsons and Lee [124, 125] used the same approach to describe nematics of rods with finite L/D, by mapping the system free energy to that of hard spheres at the same packing fraction $\eta = nv_0$, with $v_0 = \frac{\pi}{4}LD^2 + \frac{\pi}{6}D^3$ being the single-particle volume. This correction introduces a density-dependent prefactor

$$G(\eta) = \frac{(1 - \frac{3}{4}\eta)}{(1-\eta)^2} \tag{3.7}$$

in front of $\mathcal{F}_{ex}$. Following the DFT recipe [59], once the free-energy functional is defined, the next step consists of minimizing $\mathcal{F}[\psi]$ with respect to $\psi(\theta)$, subject to the normalization condition $\int d\hat{\mathbf{u}}\psi(\hat{\mathbf{u}}) = 1$. In the case of (Parsons-Lee-)Onsager theory, the resulting non-linear equation for $\psi(\theta)$ reads:

$$\psi(\theta) = \frac{1}{Z}\exp\left(-n\, G(\eta)\int_{-1}^{1} d\cos\theta'\, \frac{E(\theta, \theta')}{2\pi}\, \psi(\theta')\right), \tag{3.8}$$

where Z is a normalization constant such that $2\pi\int_0^\pi d\theta \sin\theta\psi(\theta) = 1$. Eq. (3.8) can be solved *self-consistently* at fixed n and $E(\theta, \theta')$. An example on how to solve it numerically

by using a discrete grid for the polar angle θ in the case of hard rods, can be found in Ref. [126]. The resulting (equilibrium) ODF can be used to calculate all relevant thermodynamic quantities (e.g. free energy, pressure, chemical potential) that can be used to determine phase boundaries, and to calculate structural properties such as the nematic order parameter:

$$S = \int d\theta \, \mathcal{P}_2(\cos\theta)\psi(\theta) = \int d\theta \left[\frac{3}{2}\cos^2(\theta) - \frac{1}{2}\right]\psi(\theta) \tag{3.9}$$

where $\mathcal{P}_2$ is the second-order Legendre polynomial.

In Fig. 3.2(a), we plot the orientation distribution function $\psi(\theta)$ obtained by solving Onsager theory with a Parsons-Lee correction for spherocylinders with $L/D = 5$ and at varying packing fractions η ranging from $\eta = 0.40$ to $\eta = 0.60$ (in steps of 0.01). We clearly observe that the ODFs become more peaked at higher η. By equating the chemical potential and the pressure of the isotropic and nematic phase, we find that the I-N coexistence region is given by $\eta \in [0.4 - 0.42]$ for $L/D = 5$. We plot the nematic order parameter S as a function of η in Fig. 3.2(b) for varying aspect ratios, from $L/D = 4.0$ to $L/D = 7.0$. The isotropic-nematic transition, as displayed by the jump in the nematic order parameter value S, shifts to higher η upon increasing L/D. In chapters 5, 6, 7, 8 we will show that Onsager theory can be extended to different particle models, where the excluded-volume term can be calculated using Monte Carlo integrations and a suitable overlap algorithm for the particle shapes.

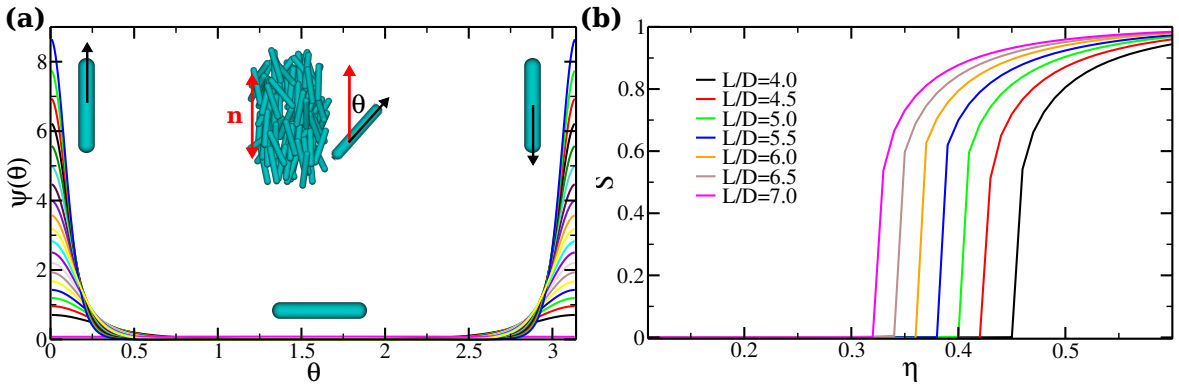

Figure 3.2: **(a)** Orientation distribution functions (ODFs) $\psi(\theta)$ obtained by solving numerically Onsager theory (with Parsons-Lee correction) for hard spherocylinders with $L/D = 5$ at different packing fractions ranging from $\eta = 0.4$ to $\eta = 0.6$. θ is the angle between particle orientation and the nematic director $\mathbf{n}$, as indicated in the cartoons. Upon increasing the packing fraction the ODFs become more peaked. **(b)** Nematic order parameter S (see Eq. 3.9) as a function of packing fraction η for different particle aspect ratio L/D. The isotropic-nematic transition, as witnessed by the jump in the nematic order parameter S, shifts towards larger η upon increasing L/D.

3.3 Elastic deformations in a uniaxial nematic phase

In a continuum description of a bulk uniaxial nematic phase [127], the ground state is represented by a uniform nematic director field $\hat{\mathbf{n}}(\mathbf{r})$. However, there are three possible elastic deformations that can occur (because of thermal fluctuations or external fields), namely bend, twist and splay. A schematic representation of how $\hat{\mathbf{n}}$ changes upon these deformations is depicted in Fig. 3.3. The free energy cost associated to these deformations reads [127]:

$$\mathcal{F}_d = \frac{1}{2}\int d\mathbf{r}\, K_1(\nabla\cdot\hat{\mathbf{n}}(\mathbf{r}))^2 + K_2(\hat{\mathbf{n}}(\mathbf{r})\cdot(\nabla\times\hat{\mathbf{n}}(\mathbf{r})))^2 + K_3(\hat{\mathbf{n}}(\mathbf{r})\times(\nabla\times\hat{\mathbf{n}}(\mathbf{r})))^2 \quad (3.10)$$

where K_1 (bend), K_2 (twist) and K_3 (splay) are called (Frank) elastic constants. These quantities can be measured in experiments or calculated for a particular particle model by using a suitable microscopic theory [128–131] or by using computer simulations [132, 133]. Assuming $\hat{\mathbf{n}} \parallel \hat{z}$, we can write general expressions for the calculations of the elastic constants within a DFT framework [128]:

$$K_1 = -\frac{n^2}{2\beta}\int d\mathbf{r}\, d\hat{\mathbf{u}}\, d\hat{\mathbf{u}}'\, c^{(2)}(\mathbf{r},\hat{\mathbf{u}},\hat{\mathbf{u}}')\dot{\psi}(\theta)\dot{\psi}(\theta')x^2u_xu_x' \quad (3.11)$$

$$K_2 = -\frac{n^2}{2\beta}\int d\mathbf{r}\, d\hat{\mathbf{u}}\, d\hat{\mathbf{u}}'\, c^{(2)}(\mathbf{r},\hat{\mathbf{u}},\hat{\mathbf{u}}')\dot{\psi}(\theta)\dot{\psi}(\theta')x^2u_yu_y' \quad (3.12)$$

$$K_3 = -\frac{n^2}{2\beta}\int d\mathbf{r}\, d\hat{\mathbf{u}}\, d\hat{\mathbf{u}}'\, c^{(2)}(\mathbf{r},\hat{\mathbf{u}},\hat{\mathbf{u}}')\dot{\psi}(\theta)\dot{\psi}(\theta')z^2u_xu_x' \quad (3.13)$$

where n is the number density, $\beta = 1/k_BT$, $c^{(2)}(\mathbf{r},\hat{\mathbf{u}},\hat{\mathbf{u}}')$ is the function describing the direct correlation between two particles [134], and $\dot{\psi}$ is the derivative of the ODF. Depending on the theoretical approximations, general relations can be obtained. For example within mean-field theory [135] for rod-like particles, one obtains $K_3 > K_1 > K_2$. Within the second-virial approximation, $c^{(2)}(\mathbf{r},\hat{\mathbf{u}},\hat{\mathbf{u}}')$ is replaced by the Mayer function $f(\mathbf{r},\hat{\mathbf{u}},\hat{\mathbf{u}}')$, defined in Eq. 3.4. By employing the derivative of the ODF obtained from the procedure described in the previous section, the elastic constants K_i can be computed numerically by performing Monte Carlo integration. To this end, we generate typically $\geq 10^{10}$ random pairs of particles, i.e., random positions and orientations for the two particles, and we calculate the quantities appearing in the integrands of Eqs. (3.11)-(3.12)-(3.13). In Fig. 3.3, we show the three elastic constants as a function of packing fraction for hard spherocylinders with aspect ratio $L/D = 5$ together with some literature results. We see that our results are consistent with the literature, in particular the density-dependence is well captured. Quantitatively, our approach resembles most the one from Poniewierski *et al.* [128], that is based on a weighted-density functional and represents an improvement over the second-virial theory proposed by Lee [130]. Identifying the most suitable DFT to describe the elasticity of the nematic phase of hard spherocylinders and a quantitative comparison with more recent computer simulations, are still topics of research [131].

The MC integration approach described here will also be extensively used in the remainder of this thesis, for example when the second-virial DFT presented in the previous section will be extended to cholesteric phases (Chap. 6). In that case, we consider chiral

particles for which the nematic ground state is a twisted state and K_2 is related to the cholesteric pitch. In Sec. 8.3 we explore the possibility of a negative twist elastic constant K_2, implying that the uniaxial nematic phase is metastable with respect to a twist deformation.

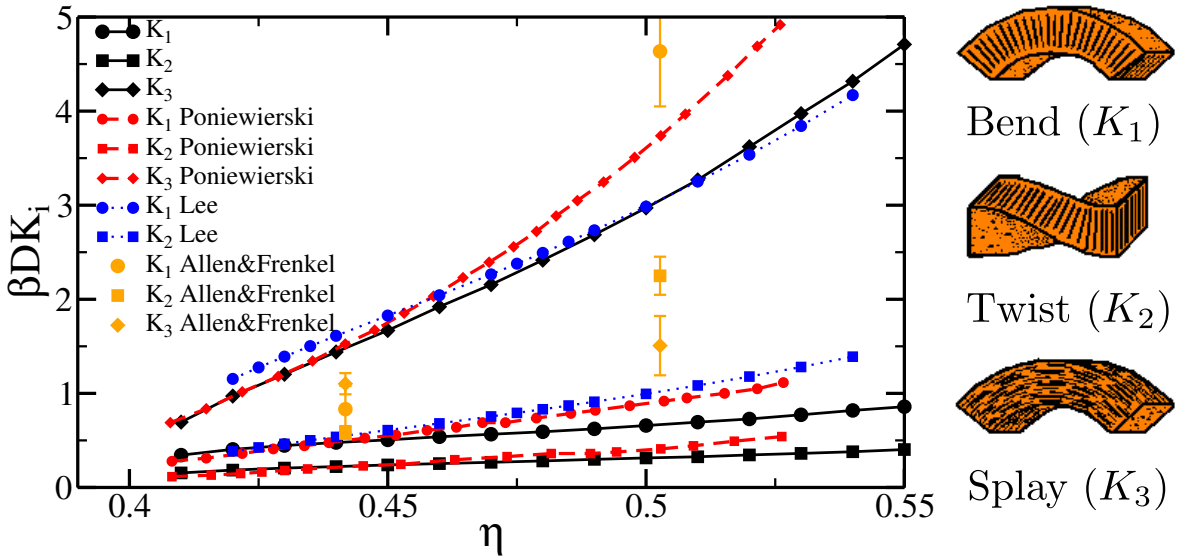

Figure 3.3: Elastic constants K_i for a nematic phase of hard spherocylinders with aspect ratio $L/D = 5$. K_1 (circles) is the elastic constant associated to a bend deformation, K_2 (square) to a twist deformation, and K_3 (diamond) to a splay deformation (see cartoons on the side). Black solid curves (and symbols) represent the results using the method of this section (second-virial DFT combined with MC integration). Red dashed lines are results from Poniewierski *et al.* [128] where a DFT based on a weighted-density approximation was used. Blue dotted lines are earlier results from Lee [130] within a second-virial DFT (K_3 is not shown as the values are beyond the scale of this figure). Yellow symbols are results from earlier computer simulations (1988) of small systems ($N = 576$) of hard spherocylinders by Allen and Frenkel [132].

3.4 Order parameters for colloidal rods

To distinguish between the isotropic and the various liquid crystalline phases, we employ global order parameters as well as order parameters that are defined locally. As the naming suggests, global order parameters quantify the long-range nature of some kind of order that develops in the system. The order can also be measured without using direct (real-space) information on the particle positions and orientations, e.g. by performing scattering experiments. On the other hand, local order parameters quantify the order in the local environment of a given particle, i.e., it depends on positions and orientations of the neighbouring particles. A local analysis is also relevant, for example, to identify defects in a given structure [136] or to study the nucleation of a given phase [137]. In Sec. 2.2.3 we showed an example of a local order parameter for spherical particles. In this section, we introduce a set of order parameters for colloidal rods that we will use throughout this thesis. It is worth to stress that an order parameter analysis can be performed both on simulation and experimental data of colloidal systems, in the case that the particles can be imaged and the positions and orientations can be tracked.
The well-known global nematic order parameter (the same as defined in Eq. 3.9) is obtained by diagonalizing the nematic order parameter tensor

$$\mathcal{Q}_{\alpha\beta} = \frac{1}{N}\sum_{i=1}^{N}\left[\frac{3}{2}\mathbf{u}_{i\alpha}\mathbf{u}_{i\beta} - \frac{\delta_{\alpha\beta}}{2}\right], \tag{3.14}$$

where $\mathbf{u}_{i\alpha}$ is the α-th component of the unit vector describing the orientation of the long axis of rod i, N is the number of particles, and $\delta_{\alpha\beta}$ the Kronecker delta. The global nematic order parameter S is defined as the largest eigenvalue of $\mathcal{Q}$ and the corresponding eigenvector is the nematic director $\mathbf{n}$. S ranges from -0.5 to 1. The error on S that arises from the diagonalization of $\mathcal{Q}$ is on the order of $1/\sqrt{N}$, yielding inaccurate results when small systems are considered. In addition, we define as introduced in Ref. [120] the local nematic order parameter S_i of particle i as

$$S_i = \frac{1}{n_i}\sum_{j=1}^{n_i}\left[\frac{3}{2}(\mathbf{u}_i \cdot \mathbf{u}_j)^2 - \frac{1}{2}\right], \tag{3.15}$$

with n_i the number of neighbours of particle i, where two particles are considered neighbours if $\rho_{ij} < \rho_{ij}^{cut} = 1.0D$, with ρ_{ij} the surface-to-surface distance. S_i also ranges from -0.5 (particle transverse to its neighbours) to 1 (perfect alignment). A cluster criterion based on this order parameter has been successfully developed to study the nucleation in simulated suspensions of colloidal hard rods [121].
The global smectic order can be probed by calculating the following order parameter [35, 138–140]:

$$\tau = \max_{l}\left|\sum_{j=1}^{N} e^{2\pi i \mathbf{r}_j \cdot \mathbf{n}/l}\right|, \tag{3.16}$$

where the value of $l \in \mathbb{R}$ that maximizes the above expression is identified as the layer spacing d. However, when the number of particles considered is small or when the smectic layers are highly fluctuating, the error associated to τ can be large. In particular, in case

of confocal data, where the statistics is limited, we often observed that τ does not capture well the smectic order in the system.
We therefore introduce a novel order parameter to quantify the *local* tendency of the particles to form (single) smectic or crystalline layers and we use it as a local smectic order parameter. We first calculate the shift h_{ij} of the center of mass of particle i with respect to its neighbouring particles j projected on a common axis (we pick the main orientation $\mathbf{u}_i$ of particle i but another direction such as the local nematic director would give similar results). We then normalize it and define:

$$\Delta_i = 1 - \frac{1}{m_i} \sum_{j=1}^{m_i} \frac{h_{ij}}{r_{cut}} = 1 - \frac{1}{m_i} \sum_{j=1}^{m_i} \frac{\mathbf{r}_{ij} \cdot \mathbf{u}_i}{r_{cut}} \,, \tag{3.17}$$

where $r_{cut} = (L_i + D_i)/2$ and m_i is the number of neighbours of particle i satisfying $r_{ij} < r_{cut}$, with r_{ij} the center-to-center distance between the rods. $\Delta_i = 1$ corresponds to the orthogonality condition between r_{ij} and the common axis (in this case u_i). However, such a condition can be obtained both for perfectly aligned rods and in the case of transverse order (Fig. 3.4). Notice that transverse rods are anyway expected in the smectic phase due to thermal fluctuations but we want to consider them as defects in a perfectly layered structure. In order to discriminate between these two configurations Δ_i is then multiplied by S_i. In conclusion, we define

$$\tau_i \equiv S_i \Delta_i \tag{3.18}$$

to quantify the layer structure locally and we call it the local smectic order parameter. Using τ_i we are able to distinguish (locally) between the smectic order (high values of τ_i) from the isotropic, nematic, as well as columnar order for which we expect low values of τ_i. Note that the neighbour definition in Δ_i and τ_i is different and that the precise threshold value of the cut-off distance yields some degree of arbitrariness in the use of these order parameters to define the different phases. Furthermore, other approaches to define a local smectic order parameter are in principle possible, for example by considering

$$\tau_i{}' = \max_l \left| \sum_{j=1}^{n_i} e^{2\pi i \mathbf{r}_{ij} \cdot \mathbf{u}_i / l} \right| , \tag{3.19}$$

with $\mathbf{r}_{ij}$ the center-to-center distance between particle i and its neighbours j, defined as particles that have a minimum surface-to-surface distance $\rho_{ij} < 1.0D$ (as for S_i). However, to avoid misidentification a large number of neighbours n_i are needed, otherwise even particles in the isotropic phase could have a large value of such an order parameter. When imposing this kind of threshold on the number of neighbours, we found similar results as using $\tau_i \equiv S_i \Delta_i$.

In order to distinguish the smectic-B and crystal phase from the smectic-A phase, we have to quantify the local hexagonal order. To this end, we first calculate for each particle i the local nematic director $\mathbf{n}_i$ based on the set of neighbouring particles j with a minimum surface-to-surface distance $\rho_{ij} < \rho_{ij}^{cut} = 1.0D$, and we define the plane $\mathcal{P}_i$ perpendicular to $\mathbf{n}_i$. The local hexagonal order is then quantified through the following order parameter:

$$\psi_{6i} = \left| \frac{1}{n_i^{2D}} \sum_{j=1}^{n_i^{2D}} \exp(\mathrm{i}6\theta_{ij}) \right| , \tag{3.20}$$

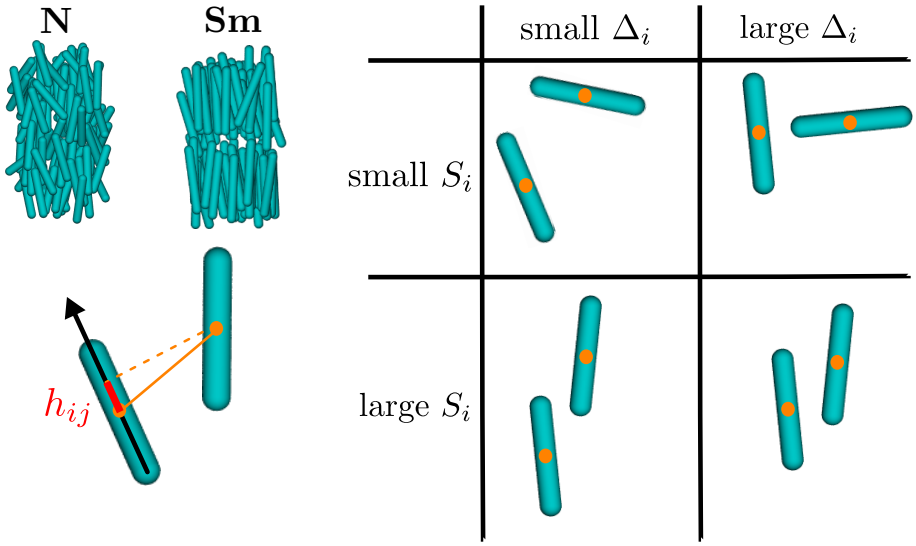

Figure 3.4: Schematic of the smectic local order parameter $\tau_i = S_i \cdot \Delta_i$. By combining the projected displacement between the rods center-of-mass h_{ij} and the tendency of alignment (quantified by the local nematic order parameter S_i), it is possible to quantify the tendency of layering and therefore distinguish locally between smectic and nematic order.

with θ_{ij} the angle between the center-to-center distance r_{ij} and the reference axis in the plane $\mathcal{P}_i$, and n_i^{2D} the number of neighbouring particles with $r_{ij} < 2.0D$. A similar approach has been used to identify stacking faults in sediments of hard spheres [141]. In order to identify the hexagonal order in the case of Smectic-B or crystalline phases of rod-like particles, we also multiply ψ_{6i} by the local nematic order parameter:

$$\mathrm{hex}_i \equiv S_i \psi_{6i} \,. \tag{3.21}$$

We wish to remark that all of these criteria based on order parameters to distinguish the different phases depend on the cut-off distance used for the identifications of the neighbours. The cut-off distance should be optimized for the specific system (particle shapes, pair interaction) and phenomenon (nucleation, interfacial behaviour, wetting). The order parameters for anisotropic particles based on the local environment of a specific particle can be then refined in many different ways, in analogy with the modifications made to the bond orientational order parameters that describe the local symmetry of crystals made of spherical particles [75, 142].

3.5 Computer simulations

In this section we perform Monte Carlo (MC) simulations on bulk systems of hard spherocylinders with length L and diameter D, and compare our simulation results with Onsager theory. In addition, we use these simulations to test our criteria based on local and global order parameters to distinguish the liquid-crystalline phases. We perform MC simulations in the NPT ensemble of thousands of spherocylinders and employ standard periodic boundary conditions. Particles interact only via an excluded-volume potential:

$$U(r_{ij}) = \begin{cases} \infty & d_{ij}(\mathbf{r}_{ij}, \mathbf{u}_i, \mathbf{u}_j) < D \\ 0 & d_{ij}(\mathbf{r}_{ij}, \mathbf{u}_i, \mathbf{u}_j) \geq D \end{cases} \tag{3.22}$$

where $d_{ij}(\mathbf{r}_{ij}, \mathbf{u}_i, \mathbf{u}_j)$ is the shortest distance between particles i and j, calculated according to Ref. [53]. We measure the averaged packing fraction η at fixed pressure P, and present the equation of state for rods with $L/D = 4.5$ in Fig. 3.5(a) along with results obtained from Onsager theory with the Parsons-Lee correction (see Sec. 3.2). For this aspect ratio the isotropic-nematic (I-N) transition is weakly first order (the jump in density is barely visible), whereas the N-Sm transition (still first order) is more pronounced, as expected [118, 119]. In general, Onsager-Parsons-Lee theory (that in this formulation describes only the I-N transition) only slightly underestimates the packing fraction η at which the transition occurs and a very good agreement is obtained for larger aspect ratios, as can be observed from Fig. 3.5(b) where the global nematic order parameter S is also plotted versus η. In addition, we test the local order parameters as introduced in Sec. 3.4 to identify the different liquid-crystal phases for varying particle aspect ratio. To this end, we calculate the averaged (over all the particles in the system) local nematic $\langle S_i \rangle$ and smectic $\langle \tau_i \rangle$ order parameters for bulk configurations obtained at different packing fraction η. We plot them together with the traditional global nematic S and smectic τ order parameters in Fig. 3.5(c)-(d) for rods with $L/D = 4.5$ and $L/D = 3.82$, respectively. We observe that the I-N transition is equally well captured by S and $\langle S_i \rangle$, despite the latter has a less abrupt jump. Analogously, the transition to the smectic phase is identified by a jump in τ and in $\langle \tau_i \rangle$, where the latter changes more gradually at the transition. In particular, for longer rods ($L/D = 4.5$, Fig. 3.5(c)) pre-smectic fluctuations, i.e., the appearance and disappearance of small metastable smectic domains, are expected before the Sm is thermodynamically stable. As a consequence, the local smectic order increases before long-range order is established in the system, and this causes higher values for $\langle \tau_i \rangle$ than τ before the N-Sm transition occurs. In case of $L/D = 3.82$ the region where the nematic phase is expected to be stable is very narrow [118] and more simulation runs should be performed at several pressures closer to the transition to observe the I-N and N-Sm phase transitions separately, instead of a single I-Sm transition as observed in Fig. 3.5(d). However, this does not affect our comments on the local order parameters.

It is also possible to measure the probability distribution of the local order parameters by considering the values associated to the particles over several independent configurations. In Fig. 3.6 we report the probability distributions for S_i and τ_i in different thermodynamic phases of rods with $L/D = 4.5$. The average values of such distributions have been plotted before in Fig. 3.5(c) and the jumps in their values correspond to the

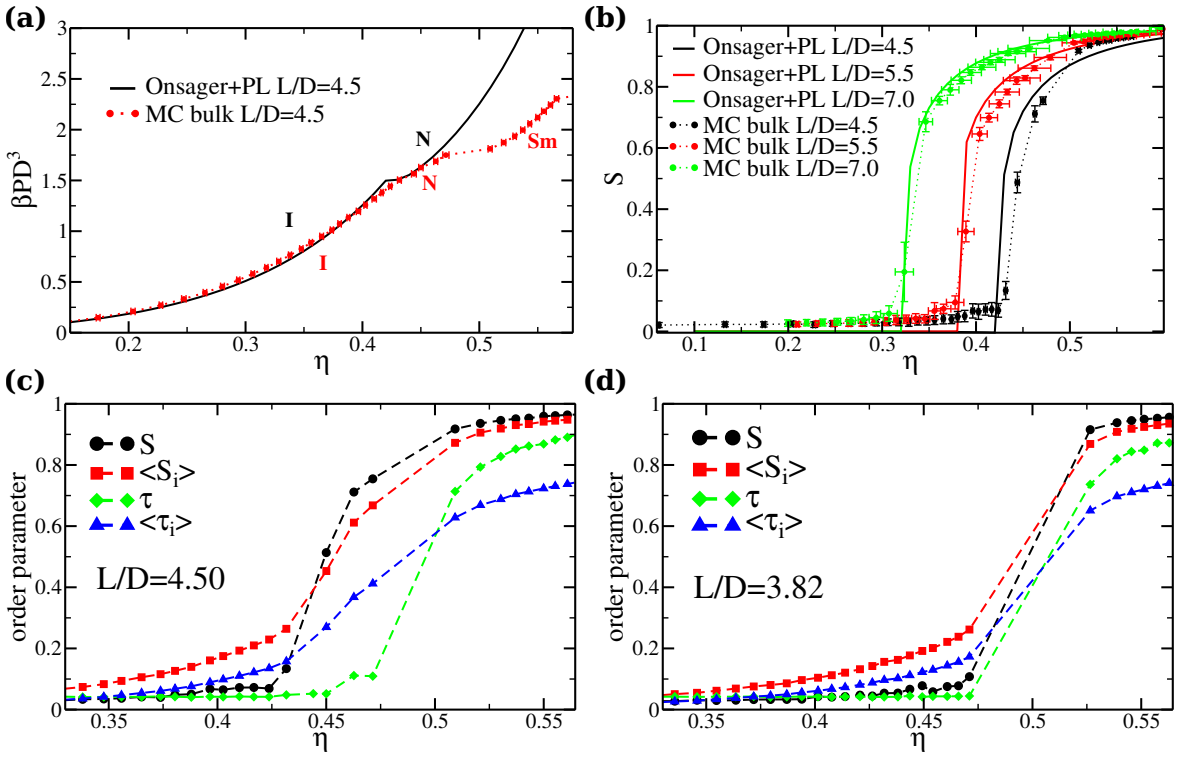

Figure 3.5: **(a)** Equation of state (pressure P versus packing fraction η) obtained from Onsager theory with Parsons-Lee (PL) correction (solid black line) and from MC-NPT bulk simulations of hard spherocylinders with aspect ratio $L/D = 4.5$. **(b)** Global nematic order parameter S versus packing fraction η obtained by theory (Eq. 3.9, solid lines) and simulations (symbols and dashed lines) for different particle aspect ratio L/D. **(c)** Global nematic S, averaged local nematic $\langle S_i \rangle$, global smectic τ and averaged local smectic $\langle \tau_i \rangle$ order parameters as a function of packing fraction η obtained from MC-NPT simulations of hard spherocylinders with aspect ratio $L/D = 4.5$ **(d)** Same order parameters for shorter rods $L/D = 3.82$.

different phase transitions. Indeed, also by observing the full distribution upon increasing pressure/packing fraction we can clearly see the shift towards larger values. The probability distribution of the local nematic order parameter S_i, as shown in Fig. 3.6(a), is particularly broad close to the I-N transition (red and green curves), and becomes more peaked when the nematic phase becomes more dense and eventually transforms into a smectic phase. In the latter (see magenta curve), despite a very high peak at large values, indicating a strong particle alignment, a left-shoulder is evident (broadening of the distribution at low values). Moreover, a small peak around $\tau_i = -0.5$ (barely visible in the graph) occurs, indicating the presence of rods with transverse orientations with respect to the local alignment. Such transverse particles (see green particle in the bottom right snapshot of Fig. 3.6(b)) have already been the focus of previous research [143]. Their presence reduces the S_i of the neighbouring particles and this contributes to the shoulder in the distribution of S_i together with the less ordered particles that hop between the smectic layers. The local smectic τ_i probability distribution (Fig. 3.6(c) and representative snapshots in (d)) displays the same features but more smoothed out (compare magenta curve in Fig. 3.6(a) and blue curve in Fig. 3.6(c)). Moreover, it captures well the increase

in the smectic order since the distribution becomes more peaked and shifts towards higher values upon increasing system density. We remark that τ_i could in principle distinguish between smectic and columnar order, in contrast with S_i.

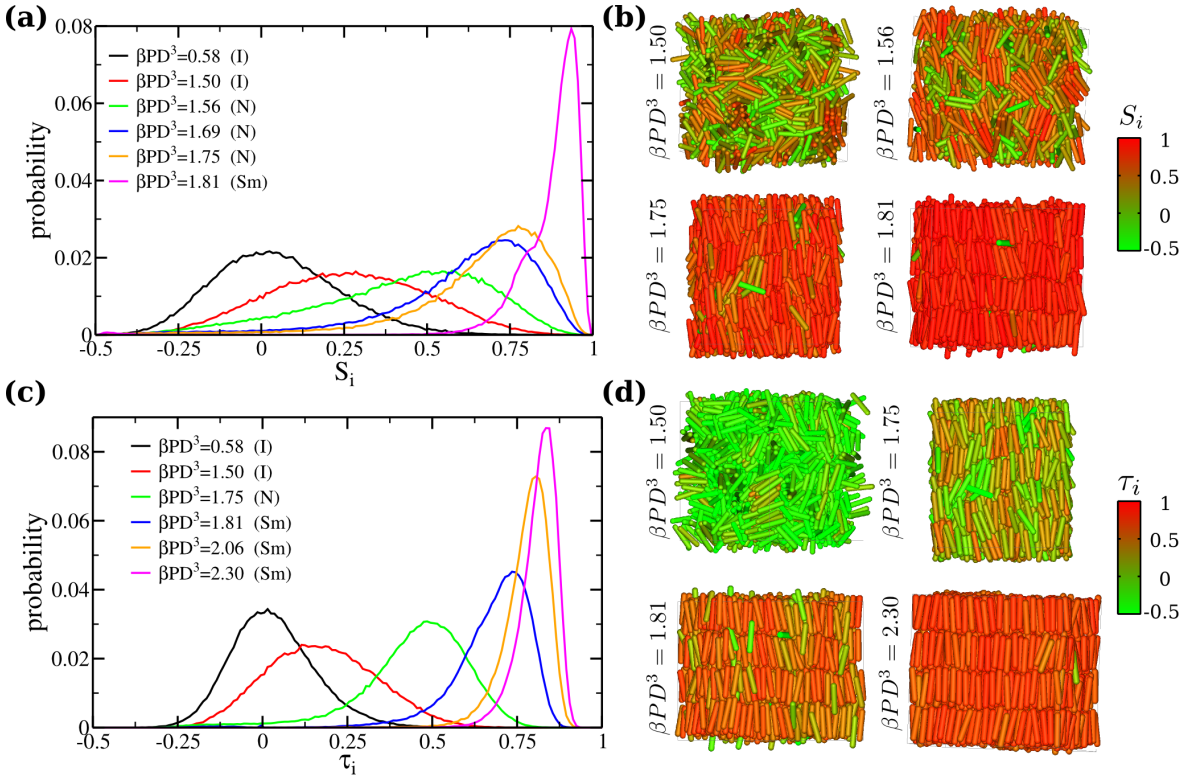

Figure 3.6: **(a)** Probability distribution of the local nematic order parameter S_i for rods with $L/D = 4.5$ at different thermodynamic states. The pressure and the stable phase formed are indicated in the legend. Data are averaged over hundreds of independent configurations obtained by NPT-MC simulations. **(b)** Typical snapshots at different pressures as indicated in the legend, and particles colored according to S_i. **(c)** Probability distribution of the local smectic order parameter τ_i obtained from NPT-MC simulations of rods with $L/D = 4.5$. **(d)** Typical snapshots with particles colored according to τ_i.

We now focus on the effect of small size polydispersity in the system on the equation of state and order parameters. We perform NPT-MC simulations starting from initial configurations in which the rods have different lengths L_i and diameters D_i that are drawn from a given particle size distribution. The size distribution does not change during the simulations, or in other words the system composition is fixed. In addition to the standard Monte Carlo moves (single-particle translations, rotations and changes in the volume of the simulation box), also swap moves between particles (selecting randomly two particles and switching their identities) have been implemented. However, for the bulk simulations presented in this section, these moves are not relevant (they are important for simulations on systems subjected to a gravitational field as presented in the next section). The degree of size polydispersity δ (sometimes expressed in percentages) is defined as the relative

standard deviation of a given distribution:

$$\delta_x = \frac{\sqrt{\langle x^2 \rangle - \langle x \rangle^2}}{\langle x \rangle} \tag{3.23}$$

where x can be the particle diameter D or particle length L, and $\langle . \rangle$ denotes an average. It is known that polydispersity can influence several phenomena typical of colloidal systems, such as equilibrium phase behaviour, nucleation, gelation, and glass transition, as extensively studied in systems of spherical colloids [144–149]. The effects of polydispersity on liquid crystal behaviour have also been studied experimentally, e.g. in Ref. [150], theoretically, e.g. in Ref. [151] (see also section 3.5.2 in Ref. [52] for a recent review) and by computer simulations, e.g. for infinitely-thin hard platelets [152] and for infinitely-long hard rods [153]. Here, we perform simulations on finite-size rods and consider only distributions with small δ_L and δ_D typical of the experimental colloidal systems of silica rods used for the self-assembly experiments, as will be described in Sec. 3.7.

In Fig. 3.7 we compare results obtained by NPT-MC simulations of systems with different particle size distributions: either Gaussian or uniform (also known as top-hat distribution), but with the same averaged diameter $\langle D \rangle$, same averaged length $\langle L \rangle$ and same degree of polydispersity δ_D, δ_L (when present). For a uniform distribution of $x_i \in [x - \Delta x/2, x + \Delta x/2]$ the average value is given by $\langle x \rangle = x$, whereas $\delta_x = \Delta x/(\sqrt{12}\langle x \rangle)$. In particular, we fix $\langle L/D \rangle = 4.55$, $\delta_D = 8.8\%$ and $\delta_L = 9.3\%$, that are values similar of the experimental system studied in Sec. 3.7, and we consider systems of $N = 2880$ particles with lengths L_i and diameter D_i chosen in six different ways: i) Gaussian distributed in only D_i ; ii) Gaussian in only L_i ; iii) Gaussian in both D_i and L_i; iv) uniformly distributed in only D_i ; v) uniformly in only L_i ; vi) uniformly distributed in both D_i and L_i. Five independent initial configurations for each case were then used to check the consistency of our results. In Fig. 3.7(a) we plot the equation of state for the different distributions and we compare the results with the equation of state of the corresponding pure (single-component) system. We observe that significant differences occur only at sufficiently large packing fraction $\eta > 0.45$, when the system is already approaching the N-Sm transition. In the case of a uniform size distribution the equation of state is more affected by the polydispersity than in the case of Gaussian distributions, despite the same degree of polydispersity. Such a difference is reflected also in the structure as evidenced by the order parameters shown in Fig. 3.7(b). We observe that the isotropic-nematic transition (both packing fraction and values of the order parameters) seems to be not significantly affected by the polydispersity in the system. Also the location of the nematic-smectic transition does not change in case of the small polydispersity considered here. However, in case of a uniform size distribution (magenta curve) we find that the global smectic order parameter τ decreases at high packing fraction η, and becomes noisier. We now take a closer look at the smectic order by analysing the probability distribution of the local smectic order parameter τ_i. In Fig. 3.8 we plot such a distribution for a pure, a uniformly polydisperse and a Gaussian polydisperse system at reduced pressure $\beta P \langle D \rangle^3 \simeq 2.075$ corresponding to a stable smectic phase. We observe that for the Gaussian distribution, the probability distribution deviates only slightly with respect to the pure (single-component) case. On the contrary, for the uniform case the smectic phase is more disordered since the local τ_i distribution (green curve) shifts to lower values, becomes very broad and has a significant

tail at $\tau_i < 0$ corresponding to particles transversally oriented with respect to the (local) nematic director, as also evident from the snapshot in Fig. 3.8(c). The full particle size distribution is therefore important, especially for the smectic phase, and not only the degree of polydispersity, as also noticed earlier for example in the study of the glass transition of hard spheres [149]. To conclude, we have shown that a small degree of size polydispersity has a marginal effect on the bulk equation of state at low densities, which becomes more significant only at large packing fractions. In the next section we investigate the effect of size polydispersity on the sedimentation of colloidal hard rods.

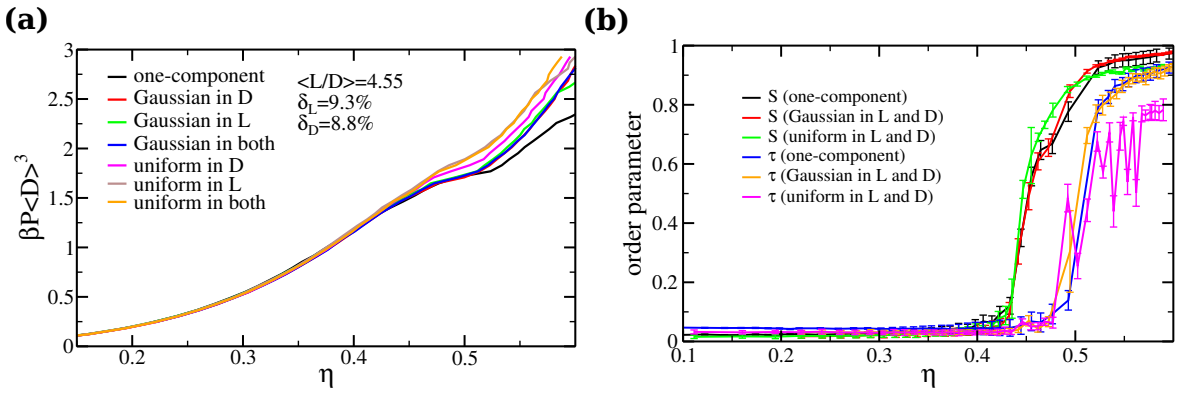

Figure 3.7: **(a)** Equation of state (reduced pressure $\beta P\langle D\rangle^3$ versus packing fraction $\eta = \sum_i v_{0i}/V$, with v_{0i} the volume of particle i and V the total volume), obtained by bulk NPT-MC simulations for $N = 2880$ spherocylinders with $\langle L/D\rangle = 4.55$ and different size distributions, as indicated in the legend, with polydispersity $\delta_L = 9.3\%$ and $\delta_D = 8.8\%$ (if present). **(b)** Global nematic S and smectic τ order parameter as a function of η for pure (single-component) and polydisperse system as indicated.

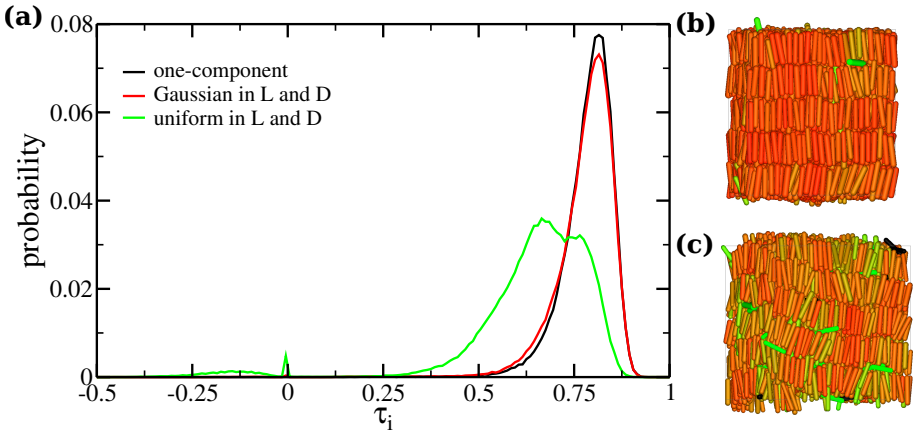

Figure 3.8: Probability distribution of the local smectic order parameter τ_i obtained by bulk NPT-MC simulations at $\beta P\langle D\rangle^3 \simeq 2.075$ for rods with $\langle L/D\rangle = 4.55$ and different polydispersity. The system with a uniform size distribution of the particles shows a less ordered smectic structure.

3.6 Sedimentation-diffusion equilibrium of colloidal rods

Gravity can often not be neglected in colloidal systems as the gravitational energy becomes comparable to the thermal energy for micron-sized particles. Hence, the system becomes spatially inhomogeneous due to the gravitational field, resulting in a density profile $\rho(z)$ that varies with the height z. However, sedimentation can also be exploited as it enables us to probe the phase behaviour and thermodynamics over a wide range of system parameters in a single experiment (as shown in the next section) or simulation.

We consider colloidal particles that are suspended in a structureless solvent and have a buoyant mass m. Following Archimedes' principle, m is related to the particle volume v_0 and to the difference in mass density between the colloids and the solvent $\Delta\rho_m$: $m = \Delta\rho_m v_0$. At equilibrium, the sedimentation profile of the colloidal suspensions $\rho(z)$ (assuming z the gravity direction) is a result of the balance between the osmotic pressure gradient and the gravitational contribution:

$$\frac{dP(z)}{dz} = -mg\rho(z)\,, \tag{3.24}$$

where P is the pressure and g the gravitational acceleration constant. Eq. 3.24 represents a macroscopic description of the sedimentation equilibrium ($dP(z)$ is the weight per unit area of all the particles in a layer with thickness dz at z) and it is only valid when the density profile does not vary too rapidly, i.e., is constant over length scales that are larger than the typical particle interaction range [29, 154]. If the previous condition holds, it is then possible to calculate the difference in pressure between two heights z_1 and z_2 of the sediment by integrating the density profile:

$$\beta[P(z_2) - P(z_1)] = -\frac{1}{l_g}\int_{z_1}^{z_2} \rho(z')dz'\,, \tag{3.25}$$

where we introduced the particle gravitational length $l_g = k_B T/mg$, with k_B Boltzmann's constant and T the temperature. The pressure $P(z)$ at any height z can be obtained in experiments or simulations in which the density profile $\rho(z)$ is measured. In case of oscillating profiles, for example when particle layering occurs, a coarse-grained profile can be used. Density functional theories can also reproduce the macroscopic description of sedimentation equilibrium when a local density approximation is used [154]. For a semi-infinite system, the top of the capillary/simulation box reaches a vanishing density $\rho(z \to \infty) = 0$ and therefore $P(z \to \infty) = 0$; whereas the pressure at the bottom wall is given by $P(z = 0) = mgN/A$, where A is the area of the capillary/simulation box and N the number of particles. By eliminating the z-dependence in both the pressure and the density profile, the equation of state $P(\rho)$ can be extracted. Vice versa, knowing the equation of state, one can calculate the sedimentation profile $\rho(z)$ [154]. Single-component systems of colloidal rods under gravity have been studied by computer simulations, for example in Ref. [155] where it has been shown that the bulk behaviour can be recovered by using the above procedure.

Simulations

We use MC simulations to study how a small degree of size polydispersity of the rods affects the equation of state of sedimenting hard rods. Each spherocylinder i is subjected to the gravitational external potential $\beta U^{ext}(z_i) = z_i/l_{gi}$, where l_{gi} is the gravitational length and z_i is the distance from the bottom wall, that is modelled as a hard planar and smooth surface, of rod i. No wall is present at the top of the simulation box that is effectively semi-infinite. We describe the size polydispersity of the rods by Gaussian distributions for the length and diameter that are correlated as shown in the inset of Fig. 3.9(b). Defining the Gaussian distribution for the variable x as

$$\mathcal{G}\left(x\,;\,\langle x\rangle,\sigma_x\right) = \frac{1}{\sqrt{2\pi}\sigma_x}\exp\left(-\frac{\left(x-\langle x\rangle\right)^2}{2{\sigma_x}^2}\right)\,, \tag{3.26}$$

where $\langle x\rangle$ is the mean value and $\sigma_x \equiv \delta_x\langle x\rangle$ is the standard deviation, with δ_x the degree of polydispersity as defined before; the distribution for the particle sizes is given by

$$\mathcal{P}(L_i,D_i) \propto \mathcal{G}\left(L\,;\,\langle L\rangle,\sigma_L\right)\;\mathcal{G}\left(D\,;\,\frac{L}{\langle L/D\rangle},\sigma_D\right)\,. \tag{3.27}$$

This distribution describes well the experimental system studied in the next section (cfr. Fig. 3.12(b)) for which the thicker rods are on average longer as well, due to the synthesis method. The aim of this study is a quantitative comparison with experiments on highly-screened charged silica rods, which interact as nearly hard particles but with a slightly larger effective dimensions. Therefore, despite the hard-core interactions are based on spherocylinder lengths L_i and diameters D_i, the gravitational lengths l_{gi} are based on the bare particle volume $v_{0i} = \pi L_i(D_i-\lambda)^2/4 + \pi(D_i-\lambda)^3/6$, with λ the layer to add to the bare dimensions. On the other hand, the effective particle volume $v^*_{0i} = \pi L_i D_i^2 + \pi D_i^3/6$ is used to calculate the packing fraction of the system $\eta = \sum_i v^*_{0i}/V$. A more precise investigation on the effective dimensions of silica rods is reported in the next section.

To speed up the equilibration, particles are initially placed close to the bottom wall and aligned perpendicularly to the gravity direction. We implement MC moves that attempt to re-scale the sides of the simulation box in the x and y directions while keeping the area fixed. This procedure is usually adopted in bulk simulations to allow the simulation box to be commensurate with the system equilibrium structure. However, since the pressure varies along the sediment, different equilibrium structures are obtained at different heights in a single simulation, meaning that the system cannot be commensurate at all heights. Rescaling the simulation box is then probably advantageous only for the denser structures and should still result in a better equilibration of the system. Furthermore, we implement swap moves that consist in randomly selecting a pair of particles and swapping their identities according to the usual Metropolis rule based on overlap checking and the difference in gravitational energy. Equilibration is reached within a few million MC steps and a typical snapshot is depicted in Fig. 3.9(a). We measure the density profile $\rho(z)$ in the simulation and obtain the equation of state from Eq. 3.25 by replacing l_g with the averaged value $\langle l_g\rangle$.

We report the main result of this section in Fig. 3.9(b), where we plot the equation of state for a one-component system and for a polydisperse system under gravity with

particle size distribution according to Eq. 3.27 and with a mean aspect ratio $\langle L/D \rangle = 4.5$ and polydispersity $\delta_L = 10$ % and $\delta_D = 5$ %. Pressure and number density are rescaled with the averaged (effective) diameter $\langle D \rangle$. We observe that the effect of gravity on a polydisperse system is quite appreciable, especially if compared with bulk simulations of a system with the same polydispersity in which the equation of state does not differ much from the single-component case (cfr. Fig. 3.7(a)). We observe that the two curves in Fig. 3.9(b) intersect around $\rho \langle D \rangle^3 \simeq 0.11$, approximately where the isotropic-nematic transition occurs. At lower density, the sedimenting polydisperse system has a lower pressure than the pure bulk one. On the other hand, at larger densities the pressure increases steadily. Finally, the appearance of layering at large densities, that corresponds to the smectic phase, is evident in the equation of state obtained by integrating the density profile.

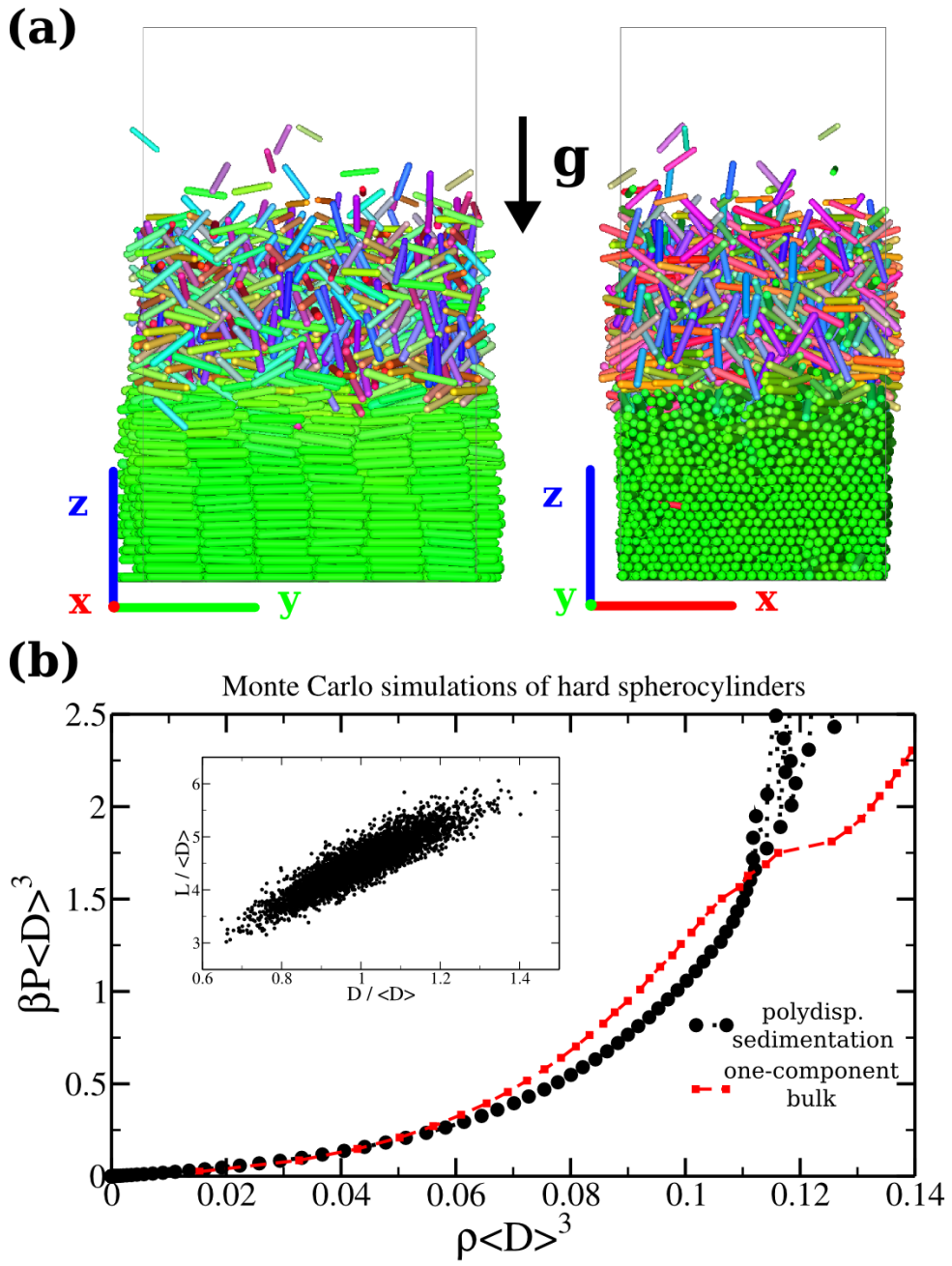

Figure 3.9: **(a)** Sediment of $N = 4800$ hard spherocylinders with a small degree of polydispersity in their particle dimensions obtained by MC simulations (side views). Particles are colored according to their orientations. **(b)** Equation of state (reduced pressure $\beta P\langle D\rangle^3$, with $\langle D\rangle$ the averaged diameter, versus reduced number density) obtained by integrating the density profile $\rho(z)$ for a polydisperse system (black) and the one obtained for the corresponding one-component bulk system (red). The particle size distribution, shown in the inset, was generated according to two coupled Gaussians for D and L (Eq. 3.27) with $\langle L/D\rangle = 4.5$ and polydispersity $\delta_L \simeq 10\%$ and $\delta_D \simeq 5\%$, and we assumed an additional layer of $\lambda = 60$ nm for the particle effective dimensions and an averaged gravitational length $\langle l_g\rangle = 550$ nm (see text for details).

3.7 Comparison with experiments

Experiments on silica rods have been performed in our research group and full details can be found in Refs. [156, 157]. The silica rod synthesis is based on the method developed by Kuijk *et al.* [49, 158]. At the end of the synthesis procedure, the fluorescent silica rods are fully coated with additional silica layers such that they obtain a spherocylindrical shape as shown in Fig. 3.10(a). The colloidal particles are then dispersed in a solvent and they are let to sediment for long times (several weeks) in order to reach the sedimentation-diffusion equilibrium. The fluorescent labelling allows real-space and real-time imaging of the experimental sample by using scanning confocal laser microscopy. An example of a confocal image of part of a rod sediment is shown in Fig. 3.10(b). For this sample, we estimate the average bare rod diameter $\langle D \rangle \simeq 624$ nm ($\delta_D \simeq 8\%$) and average bare rod length $\langle L^{end-end} \rangle \simeq 3.73$ μm ($\delta_L \simeq 9\%$) from TEM images as shown in Fig. 3.10(a) yielding an $\langle L^{end-end}/D \rangle \simeq 5.97$. By applying state-of-the-art particle tracking algorithms [157, 159], rod lengths, positions and orientations are identified. The experimental sample is then rendered by using the spherocylinder model and quantitative analysis is performed. Here we analyse only the top part of the sediment, neglecting the layers close to the bottom wall. In Fig. 3.10(c), the silica rods are colored according to their orientation, whereas in (d)-(e)-(f) they are colored according to the local nematic, smectic, hexagonal order parameter. Such an order parameter analysis at a single-particle level enables us to identify defects in a dense structure, for example notice the transverse (green) particles in panel (d) and how these particles influence the local order around them. The different thermodynamic phases formed by the silica rods can be then distinguished by analysing how the order parameters vary as a function of the sediment height z. The experimental data were first divided in equally spaced slabs of $0.5D_{TEM}$ along the gravity direction. The analysis was carried out for each slab and averaged over different equilibrium configurations. Notice that the analysis of the local order parameters was based on the lengths of the rods obtained by the particle tracking procedure. Such an analysis is reported in Fig. 3.11(a). The wall is located well below $z = 0$ and does not influence the behaviour of the sample part analysed here. The transition from an isotropic phase to an aligned phase is evidently captured by the jump in the order parameters. In particular, the global nematic S and smectic τ order parameters show jumps at different heights, confirming the expected I-N-Sm sequence, even though the nematic layer is only a few particle diameters thick (as expected for this range of aspect ratios and the averaged gravitational length of the silica rods $\langle l_g \rangle = 0.55$ μm). However, due to the limited statistics (small number of layers) and fluctuations in their positions, we obtained not very large values of τ (smaller than what you would expect after visual inspection of the sample) and a rather noisy trend of τ as a function of z. Nematic and smectic phases can be identified by using the local order parameters as well. However, as observed for the simulation data (Fig. 3.5(c)), the jumps are usually smoother and the local smectic τ_i tends to jump earlier than when the smectic phase is thermodynamically stable. Nevertheless, in contrast with the global τ, the local τ_i has a constant (large) value in the smectic region, suggesting that it is able to identify the layering even in the presence of limited and possibly noisy data. Finally, we observe a high degree of local hexagonal order and future studies could be dedicated to characterize the positional order within the smectic layers and in the crystal phases of

silica rods. Same analysis, reported in Fig. 3.11(b), was carried out for a similar sample of silica rods (that will be used in the next chapter) and analogous conclusions can be drawn also in this case.

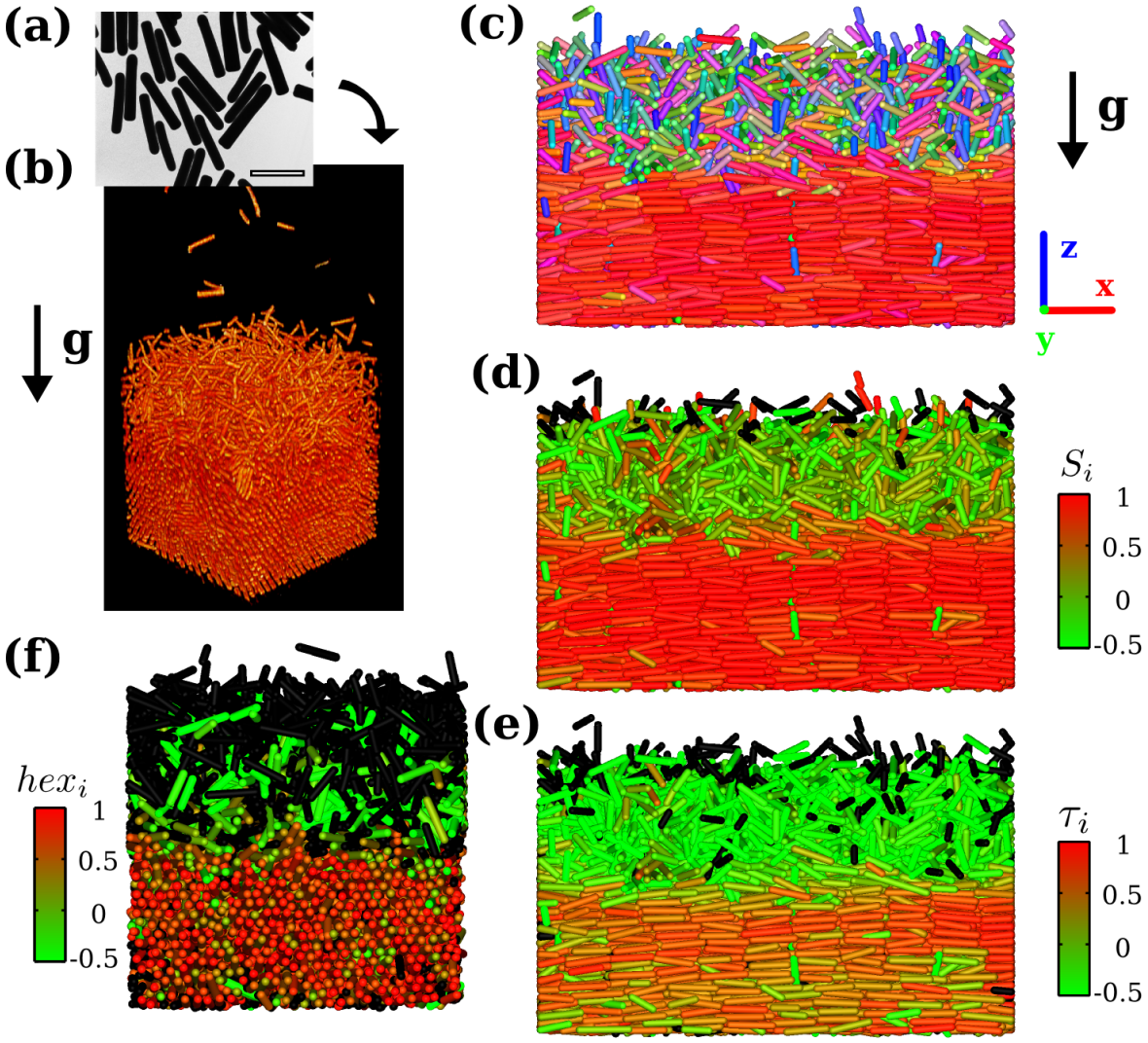

Figure 3.10: **(a)** TEM images of (fully coated) silica rods with $\langle L^{end-end} \rangle \simeq 3.7\mu$m ($\delta_L \simeq 9\%$) and $\langle D \rangle \simeq 624$ nm ($\delta_D \simeq 8\%$) (see Fig. 3.12 for full particle size distribution). Scale bar is 3 μm. **(b)** Confocal image of a part of an equilibrated sediment of silica rods. **(c)** Computer reconstruction of the sediment after using particle tracking algorithms that identify particle lengths, positions and orientations. Particles are colored according to their orientation. The same configuration is also shown with particles colored according to the **(d)** local nematic order parameter S_i , **(e)** local smectic order parameter τ_i , **(f)** local hexagonal order parameter hex_i. Black particles do not have neighbours according to the cut-off chosen ($\rho_{ij}^{cut} = 0.5D$ for the surface-to-surface distance ρ_{ij}, whereas for the center-of-mass distance $r_{ij}^{cut} = (L_i + D)/2$ for τ_i, and $r_{ij}^{cut} = 1.0D$ for hex_i). See Sec. 3.4 for definition of the order parameters.

We have confirmed the qualitative phase behaviour of silica rods, and probed how quantitatively the order parameter varies. To further continue our quantitative analy-

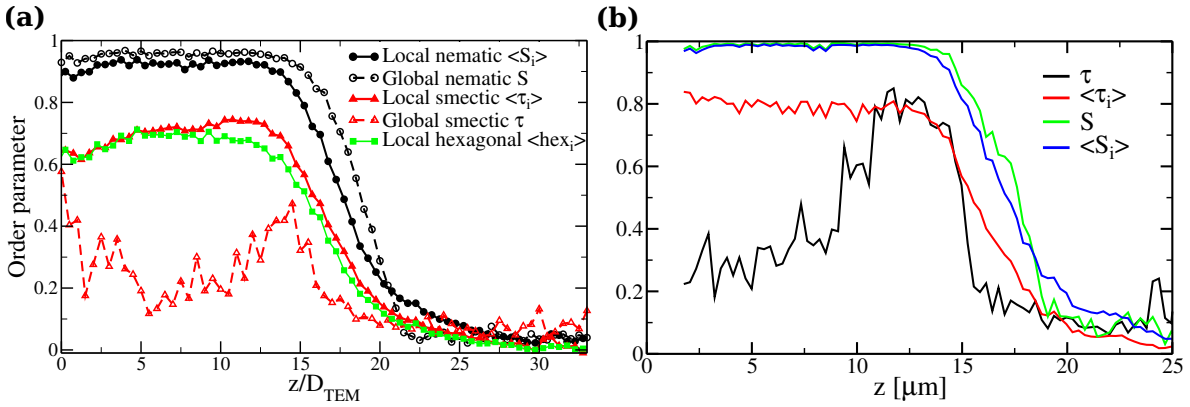

Figure 3.11: **(a)** Order parameter analysis for the sediment of Fig. 3.10. The values of the different order parameters (as indicated in the legend) are plotted as a function of height z, in units of bare averaged particle diameter obtained by TEM ($D_{TEM} = 624$ nm). **(b)** Same analysis for a different sample of silica rods with $\langle L^{end-end} \rangle \simeq 3.6$ μm, $\delta_L \simeq 18\%$, $\langle D \rangle \simeq 590$ nm, $\delta_D \simeq 10\%$, that has been also used in the experiments presented in the next chapter.

sis, i.e., extracting the equation of state, we need more information on the particle size distribution. Indeed, polydispersity is an inevitable outcome of the colloidal synthesis procedure, and even if it is reduced by several centrifugation steps, the final sample always presents rods with (slightly) different lengths and diameters. In Fig. 3.12(a) we plot the lengths and diameters of 110 particles measured by TEM images. A strong correlation between particle length and diameter is evident due to the synthesis method. As it can be observed from Fig. 3.12(b), a simple distribution that well captures the experimental one is obtained by two Gaussian distributions for the length and diameter that are correlated (Eq. 3.27), with mean aspect ratio $\langle (L/D)_{TEM} \rangle = 4.97$ and size polydispersity $\delta_L \simeq 10$ % and $\delta_D \simeq 5$ %. It is important to note that the separate distributions of diameter, lengths or aspect ratio (panels (b)-(c)-(d)) contain only partial information that could give misleading indications on the sample polydispersity (e.g. the polydispersity associated to the aspect ratio is only 5.1 %). Moreover, despite the fact that the polydispersity in particle dimensions is relatively small, the polydispersity in particle volume (or equivalently mass) is significant (30%), which could yield size fractionation in the overall sediment.

The second crucial step to map the experimental behaviour onto that of hard spherocylinders is to identify the contribution of the electrostatic screening, namely identify the particle effective dimensions $D_{eff} = D_{TEM} + \lambda$. Indeed, silica rods are dispersed in a mixture of DMSO/water with a reflective index that matches that of colloids and therefore (almost) cancels the van der Waals interactions. However, silica colloids have a charged surface yielding Coulombic interactions, that can be screened by salt addition to the solvent. The small but non-negligible Debye screening length is estimated to be around 10 nm, yielding $\lambda_{Debye} \geq 20$ nm, for the experiments considered here [157]. To identify the additional layer λ, we rely on the nematic order parameter and try to rescale experimental data such that the isotropic-nematic transition matches the one obtained by computer simulations of rods with the same effective dimensions. In Fig. 3.13, we compare both the global S (panel (a)) and the local $\langle S_i \rangle$ (panel (b)) nematic order parameter as

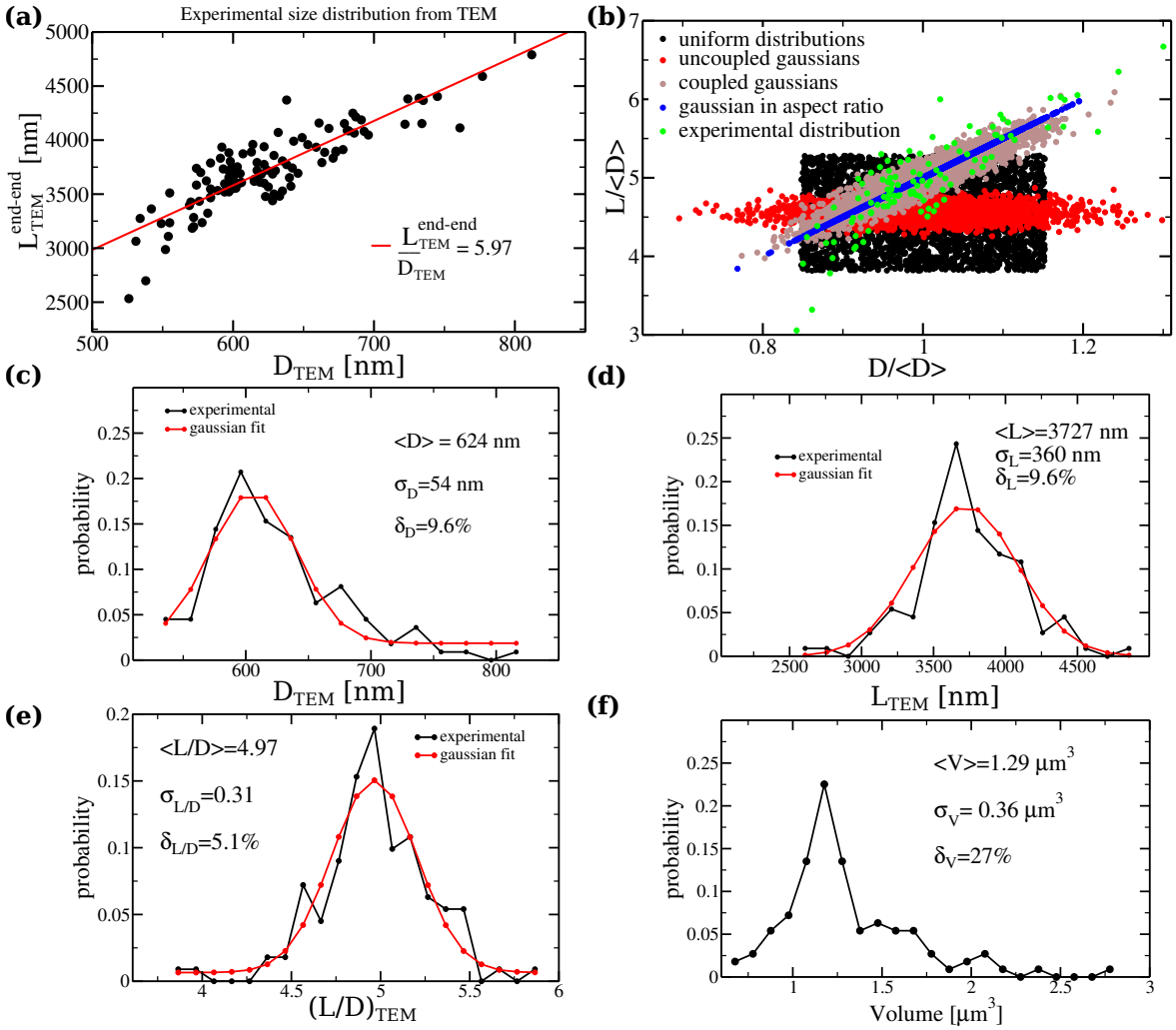

Figure 3.12: Particle size distribution of the experimental sample of silica rods studied here. **(a)** Particle dimensions in the length-diameter plane. **(b)** Matching the experimental distribution with different particle size distributions. Distributions in only **(c)** diameter, **(d)** length, **(e)** aspect ratio, **(f)** particle volume of the experimental system shown together with the indication of the average value $\langle . \rangle$, standard deviation σ and polydispersity δ. Gaussian fits are plotted in red for comparison.

a function of the reduced density, where the brackets denote an average over all particles in the bulk simulations and over all particles within a slab in the case of sedimentation experiments and simulations. In principle, $\langle S_i \rangle$ could suffer from errors associated to particle tracking, whereas only orientations and not particle dimensions are needed for S. However, both analyses seem comparable and suggest that λ is in the range between 40 nm to 80 nm, i.e., from 2 to 4 times the estimated Debye screening layer. Finally, in Fig. 3.14 we compare the equation of state obtained by integrating the density profile (as described in Sec. 3.6), using the averaged gravitational length $\langle l_g \rangle$, with the simulation results. In Fig. 3.14(a) the equation of state is plotted with the pressure rescaled with the effective particle volume as a function of packing fraction η. The theoretical Carnahan-

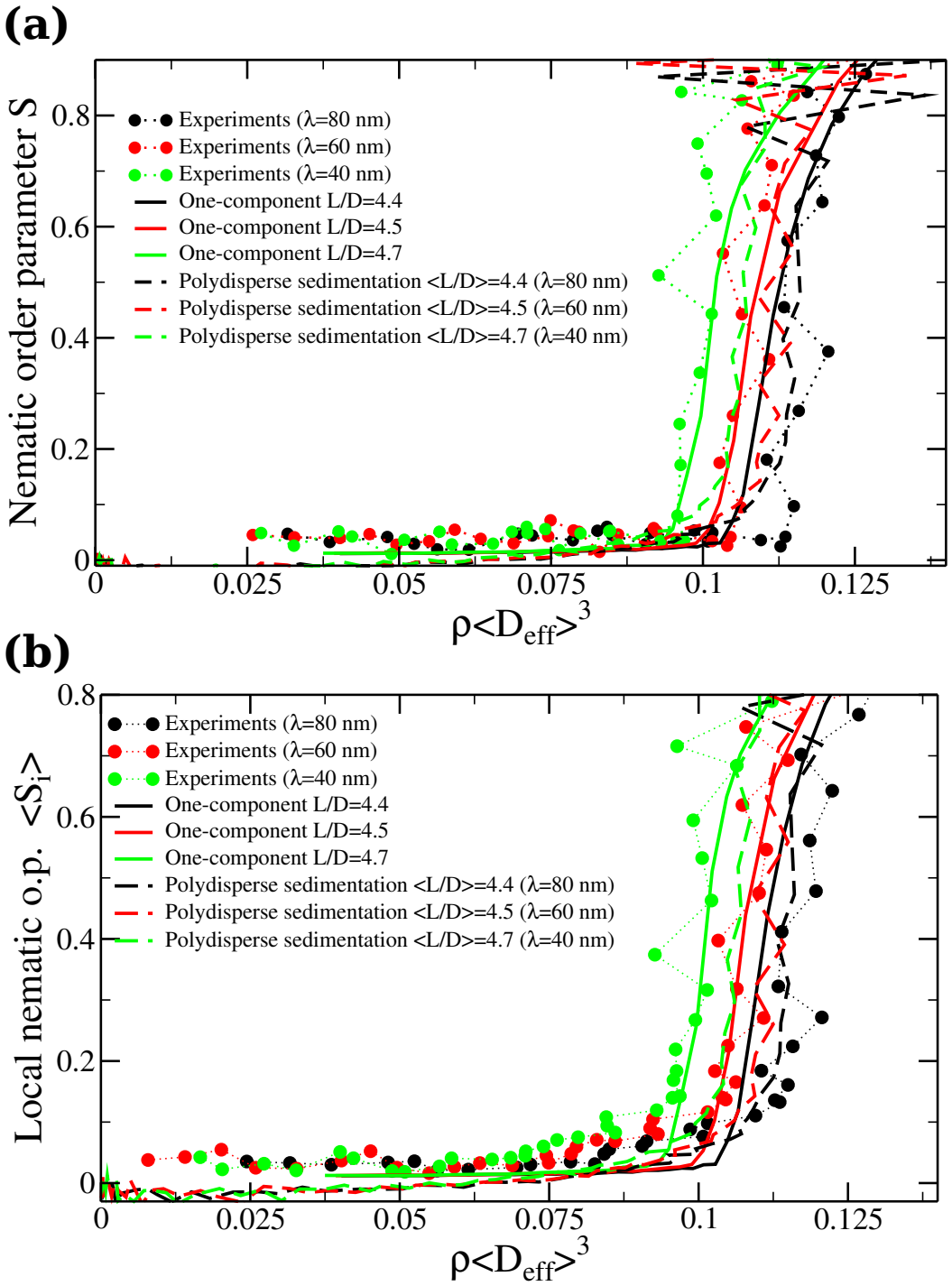

Figure 3.13: Identification of the effective dimensions of the silica rods by mapping **(a)** the global nematic order parameter S or **(b)** the local nematic order parameter $\langle S_i \rangle$ on the results obtained by MC computer simulations of hard spherocylinders, either in the bulk pure system or under gravity for an experimental-like polydisperse system. The density ρ is rescaled with the averaged effective diameter $\langle D_{eff} \rangle = \langle D_{TEM} \rangle + \lambda$, with λ the additional layer (values indicated in the legend). Same colors correspond to the same particle dimensions.

Starling equation of state for hard spheres is plotted as well for reference. We observe that the differences between the equation of state of rods with different aspect ratios obtained by computer simulations either for bulk single-component systems (solid lines) or for sedimenting polydisperse systems (dashed lines), are barely visible for this range of L/D. However, we observe that the choice of λ significantly influences the equation of state for silica rods. We find that the best match is obtained when $\lambda \simeq 80$ nm, for which we are able to match the equation of state up to 35% packing fraction, if we consider the effect of polydispersity and gravity (cfr. Fig. 3.14(b)). Around 40% packing fraction the difference in pressure is quite significant. It seems unlikely that even with a better tuning of λ and particle size distribution, the equations of state can quantitatively match. We also have to remark that both the experimental data analysis and the simulation procedure contain some sources of uncertainties that could propagate on the final values of pressure and density. In particular, we integrated the density profile, as obtained from both experiments as well as simulations, assuming an averaged gravitational length for all the particles. This simplification could have significant effect on the equation of state in the presence of size segregation throughout the capillary. Swap moves have been employed in computer simulations to take into account this phenomenon, but yet the overall particle size distribution is fixed at the beginning of the simulation and finite size effects could be important. From an experimental point of view, the possibility of missing particles during the tracking procedure has clear consequences on the measurement of the density profile. Finally, it is possible that at this already quite large density the experimental sample is not able to reach the equilibrium structure.

Nevertheless, we can conclude that silica rods, under particular conditions, can behave quantitatively as (nearly) hard spherocylinders.

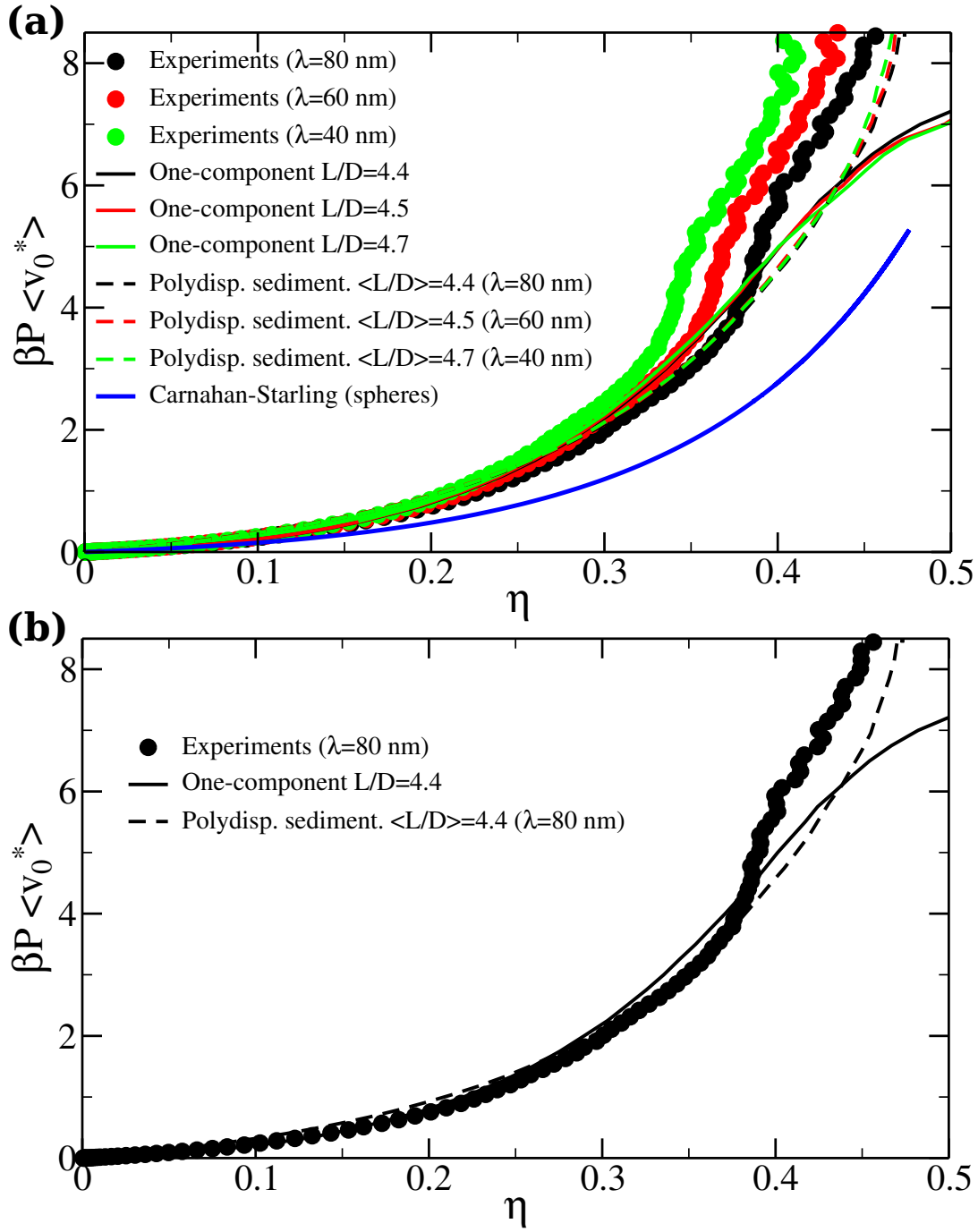

Figure 3.14: Comparison between the experimental equation of state of silica rods and that of hard spherocylinders obtained by MC simulations. Same colors correspond to same particle dimensions. **(a)** Equations of state in which the pressure is rescaled with the averaged particle effective volume $\langle v_0^* \rangle$ and as a function of (effective) packing fraction η. **(b)** Same as panel (a) with only one set of curves.

3.8 Discussion and conclusions

In this chapter we have revisited the well-known phase behaviour of hard spherocylinders, being a paramount system to describe microscopically the order of a wide class of (colloidal) liquid crystals. After reviewing Onsager theory, that is widely used in literature and will be applied in several places in this thesis, we have focused on mapping the phase behaviour observed in experiments on silica rods onto that of hard spherocylinders, obtained by computer simulations. This correspondence was already observed qualitatively [156], and here we performed a quantitative study. Indeed, the possibility of imaging a 3D sample in real space and tracking particle positions, orientations and lengths, allows for a comprehensive analysis on the order developed in the system. Such analysis has been carried out by using a set of global and local order parameters, some introduced specifically for this study, both on experimental and simulation data. On a more general point of view, the accessibility of information at a single-particle level for systems of anisotropic colloids allows for studies that go beyond the phase behaviour and include for example nucleation, glassy dynamics, defects re-arrangement, that so far have been investigated mostly in system of spherical particles.

From a simulation point of view, several aspects have been taken into account in this chapter to meet the experimental conditions as close as possible. Indeed, we examined how the exact particle size distribution influences the phase behaviour and the effect of gravity on a system with a small degree of size polydispersity. We have identified the effective dimensions for which the experimental rods can be indeed considered hard particles. By rescaling the rod dimensions and by comparing the occurrence of the first phase transition (isotropic-nematic) with that of a simulated system of hard spherocylinders with corresponding aspect ratio, we have found that an additional layer of a few times the Debye screening length must be added to the bare particle diameter. The use of effective dimensions allows us to match quantitatively the equation of state as obtained from sedimentation experiments up to almost 40% of packing fraction for the particular sample studied. In summary, we have shown that silica rods can indeed be the ultimate experimental realization of (nearly) hard spherocylinders. Furthermore, the overall procedure described here seems promising for further investigation on the phase behaviour of anisotropic silica particles and mixtures thereof, as we will describe in the next chapter.

Acknowledgments

Some of the results presented in this chapter are part of collaborations with Thijs Besseling, Chris Kennedy, and Henriëtte Bakker, who performed experiments on silica rods under the supervision of Arnout Imhof and Alfons van Blaaderen. I would like to thank Thijs, Chris, Henriëtte for providing confocal images, TEM images, experimental data, and for many useful discussions.

4

Binary liquid crystals of hard rods and hard spheres

In this chapter we study liquid crystal phases formed by binary mixtures of colloidal rods and spheres, focusing in particular on the binary smectic Sm_2 phase. First, we present a quantitative real-space analysis on an experimental binary mixture of silica rods and spheres that serves as motivation for our simulation study. By determining the local order and by extracting the equation of state of the sedimented suspensions, the liquid-crystal behaviour of the experimental mixture has been mapped out. After determining the effective dimensions of the particles, we perform isothermal-isobaric Monte Carlo (NPT-MC) computer simulations of a mixture composed of hard spherocylinders and hard spheres and we verify that the Sm_2 phase observed experimentally can be stabilized by entropy alone. The fact that the Sm_2 phase is accessible by particle shape alone, opens up the possibility of combining new materials properties at different length scales, without the need to finely tune inter-particle attractions.

4.1 Introduction

The self-assembly of multiple different components typically corresponds to an increase in the number of possible stable structures and in their complexity, that in turn could expand and strengthen our ability of tuning several structure properties [16]. For example, colloidal binary systems of spherical particles could be used to obtain a photonic crystal with a band gap in the visible region [14], or three-dimensional superlattices with tunable optical and magnetic properties [17]. Moreover, shape-anisotropic particles may self-assemble in intermediate thermodynamic phases, such as liquid-crystalline phases that display various degrees of positional and orientational order [160].

Colloidal binary liquid crystals have hardly been investigated experimentally [161–163], despite the existence of a significantly larger number of theoretical and simulation studies [164–180]. Rod and sphere mixtures with a highly asymmetric size ratio between the particles were studied before, in the limit where the smaller particles induced so-called depletion interactions between the bigger components (see e.g. Ref. [181]). Here, we focus on the phase behaviour of anisotropic and spherical colloids that are comparable in size and form a binary smectic phase Sm_2 (see Fig. 4.1(c)) featuring long-range orientational order and long-range one-dimensional positional order. Indeed, the Sm_2 phase consists of alternating layers of rods and layers of spheres. The first experimental Sm_2 phase was observed by Adams *et al.* [161] in a mixture of *fd*-viruses (of aspect ratio $L/D \sim 100$) and polymer spheres, and was named lamellar phase in analogy with biological systems. However, since the smectic organisation arises in a two-component system, differently from the common lamellar order that occurs in single-component systems, we prefer to use the notation Sm_2. This phase has been predicted theoretically for binary mixtures of hard spherocylinders with equal diameter when (i) at least one of the two species has an aspect ratio large enough to form a smectic phase, (ii) the asymmetry in the aspect ratio is sufficiently large to promote micro-phase separation, i.e., the two species prefer to be in different layers (Sm_2) rather than sharing the same layers (Sm) [167], (iii) the size asymmetry is not large enough to induce global phase separation, e.g. two phases rich in only one of the two species (e.g. isotropic-nematic, nematic-nematic demixing [170]). The stabilization mechanism of the Sm_2 phase in a mixture of *fd*-viruses and polymer spheres was already explained in terms of excluded volume interactions [161]. However, despite the fact that under particular conditions *fd*-viruses can effectively be considered hard particles [182], chirality and flexibility play an important role in their phase behaviour. For example, the existence of a columnar phase between the smectic and the crystal phase in single-component suspensions of *fd*-viruses [182] cannot be mapped on the phase behaviour of achiral rigid rods since the columnar phase is unstable in a system of hard spherocylinders [118]. Furthermore, the origin of a phase consisting of columns of spheres perpendicular to the smectic-like layers of rods observed in mixtures of *fd*-viruses and spheres [161] remains still puzzling. Here, we consider mixtures of achiral rigid silica rods and silica spheres, that can be imaged in real-space by using confocal microscopy. In contrast with *fd*-virus systems, it is possible to track all particle positions and orientations and to perform a quantitative analysis that is compared with simulations of hard particles. Real-space imaging, but not a quantitative 3D analysis, has been also recently performed on self-assembled systems of semiconductor nanorods and nanospheres [183]. The rods

considered were too short ($L/D < 3$) to form liquid-crystalline phases based on entropic interactions alone, as concluded from computer simulations of attractive particles [183].

Silica rods with bare end-to-end length $L_{TEM} = 3.6$ μm (polydispersity $\delta_L \simeq 18\%$) and bare diameter $D_{TEM} = 0.59$ μm ($\delta_D \simeq 10\%$) were synthesized [49, 158] in our group (see Fig. 4.1(a)), as well as silica spheres with an average diameter of $\sigma_{TEM} = 385$ nm (polydispersity $\delta_\sigma \simeq 9\%$) [184] (see Fig. 4.1(b)). The colloidal rods and spheres were mixed and dispersed in a refractive-index matched glycerol-water solvent mixture and left to sediment. In order to provide charge screening around the particles LiCl was added to the medium, yielding a Debye screening length of $\kappa^{-1} = 10$ nm. Hence, the particles act as nearly hard particles with slightly larger effective dimensions. The samples were analysed using quantitative confocal microscopy and particle fitting algorithms were used [159]. For single-particle fitting, the dispersion was left to sediment for at least four weeks.

The silica rods and spheres are not density-matched with the solvent mixture. Hence, the sedimentation-diffusion equilibrium profile is not homogeneous, and most of the rods ($l_g = 0.64$ μm) reside at the bottom of the sediment and most of the spheres ($l_g = 17.65$ μm) at the top (Fig. 4.1(d)) due to a difference in gravitational length (l_g) between the particles. However, at intermediate heights, both species were present and for appropriate pressure and composition (as we will see below) the Sm_2 phase was formed (Fig. 4.1(c)). In most of the samples, the Sm_2-phase was not present as one single large domain and an ac-electric field was applied to align the sample and to form a large Sm_2 phase. At the same time, this proves the ability of the system to respond to the electric field that is usually important for applications. After switching off the electric field, the binary smectic order persisted in the system suggesting that it is indeed the equilibrium structure. To characterize the quality of order in the aligned Sm_2-phase, Fast Fourier Transform (FFT) images were made and confirmed the long-range nature of the binary assemblies. Furthermore, the system can be imaged by using confocal microscopy and after deconvolution of the confocal images, single-particle identification were used to obtain all particle positions and orientations [159]. This information can then be used to quantitatively characterize the system as a function of the sample height z (see Fig. 4.1(e)), in analogy with the procedure presented in Chap. 3. In particular, we divided the system in equally spaced slabs of $0.5D_{TEM}$ (with D_{TEM} the averaged bare diameter obtained by TEM images) along the gravity axis and determined the number density profile $\rho_{rod}(z)$ and $\rho_{sph}(z)$ of the rods and spheres, respectively, and the system composition $x_{sph}(z)$, with $x_{sph} = N_s/N$. Using not only the positions but also the orientations of the rods allows us to determine the average local nematic $\langle S_i \rangle(z)$ and smectic $\langle \tau_i \rangle(z)$ order parameter profiles as a function of z, where the brackets denote an average over all particles in the slab at z. In Fig. 4.1(e), we plot both the composition x_{sph} as well as the order parameters as a function of z. For comparison, the deconvolved confocal xyz-stack is presented in Fig. 4.1(d). We clearly observe a smectic phase with high nematic order $\langle S_i \rangle > 0.9$ and a high smectic order $\langle \tau_i \rangle > 0.6$, which is rich in rods, i.e., $x_{sph} \simeq 0.4$, at the bottom of the sample, whereas an isotropic sphere-rich phase with $x_{sph} \sim 1$ and low nematic and smectic order is observed at the top. The transition between the isotropic and Sm_2 phase occured at a height ~ 14 μm. In order to distinguish the different phases, we did not use the positions of the spheres in the order parameter analysis, as the order of the spheres is dictated by that of the rods and is less pronounced. Next, during imaging it has been

observed that the spheres could diffuse freely within the sheets of spheres in the Sm_2 phase.

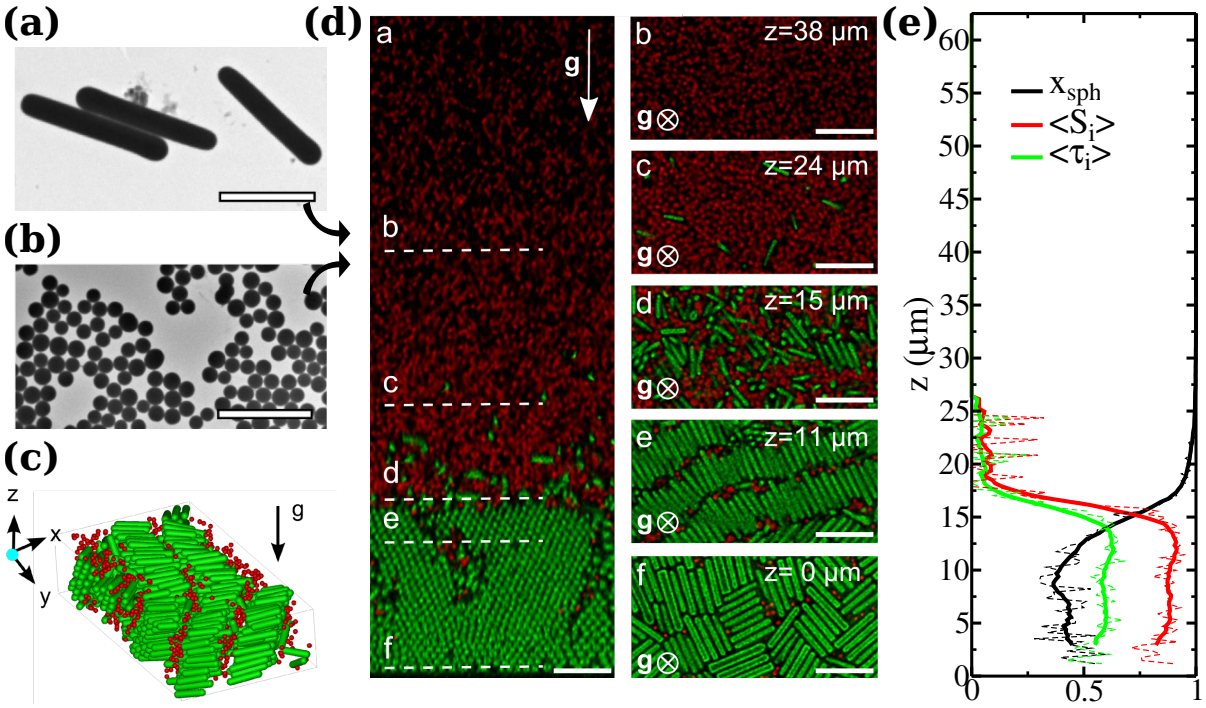

Figure 4.1: Experimental system: binary mixture of silica rods and spheres. **(a-b)** TEM images of **(a)** silica spheres with diameter $\sigma_{TEM} = 385$ nm (polydispersity $\delta_\sigma \simeq 9\%$) and **(b)** silica rods with end-to-end length $L_{TEM} = 3.6$ μm ($\delta_L \simeq 18\%$) and diameter $D_{TEM} = 0.59$ μm ($\delta_D \simeq 10\%$), scale bars 2.5 μm. **(c)** 3D reconstruction of part of confocal data stack showing a Sm_2 phase. **(d)** Deconvolved confocal microscopy images of a sediment of rods and spheres. Images are shown parallel (left) and perpendicular (right) to the gravity direction. Dashed lines and letters indicate the height at which the images perpendicular to the gravity direction (panels on the right) are acquired. All scale bars are 5 μm. The height of the total sediment was 120 μm, of which only the bottom 62.5 μm are shown. **(e)** Quantitative analysis of the local structure of the sediment in **(d)**. Composition $x_{sph} = N_{sph}/N$, averaged local nematic order parameter $< S_i >$ and averaged local smectic order parameter $< \tau_i >$ are shown as a function of the sample height z. See Sec. 3.4 for the definition of the order parameters. Thin dashed lines represent the raw data and the thick solid lines are data smoothed by convolution using a top-hat function of $5D_{TEM}$ width.

4.2 Estimating the experimental phase diagram

As pointed out in Sec. 3.7, the crucial step towards the interpretation of the experimental phase behaviour in terms of purely entropy-driven phase transitions, is to identify the effective dimensions for which the colloidal particles act as hard particles. The effective diameter of the silica spheres $\sigma_{eff} = \sigma_{TEM} + \lambda_s$ was obtained by mapping the equation of state as obtained from integrating the density profile of the top part of an equilibrated sample, corresponding to a fluid phase of only spheres, to the Carnahan-Starling equation of state. We obtained $\lambda_s = 80$ nm. The procedure to identify the effective dimensions of the rods, namely $D_{eff} = D_{TEM} + \lambda_r$, is the same as in Sec. 3.7 (see also Fig. 3.13). In Fig. 4.2(a) we map the I-N transition as identified by the jump in the global nematic order parameter S in an equilibrated sample of only silica rods, to the transition as obtained from NPT-MC simulations of thousands of hard spherocylinders. We observe that the best agreement is obtained for $\lambda_r = 120$ nm. Notice that $\lambda_s \neq \lambda_r$ since the rods and spheres have different charges. Additionally, we observe that the equation of state (EOS), shown in Fig. 4.2(b), does not agree with the corresponding EOS of a one-component system of hard spherocylinders when $\lambda_r = 120$ nm. Rather, it would be tempting to match as much as possible the low density branch and assume $\lambda_r = 80$ nm. However, as discussed in Chap. 3, we ascribed the difference in EOS to the polydispersity in the system, that in this sample is also (slightly) larger than in the one considered in Chap. 3. Once again, we prefer to rely on the use of the jump of S that is less sensitive to small polydispersity. In general, it is worth to stress that to find the particle effective dimensions (both for spheres and for rods) discrepancies can also arise from particles missed in the tracking and segregation effects.

In order to map out the experimental phase diagram in the pressure P - composition x_{sph} representation, many samples with different initial volume fractions and compositions were prepared and analysed using the same procedure described above. The pressure P at height z was also obtained by integrating the density profiles of both species to obtain the weight of all particles above it. The pressure changes as a function of height z in the sediment and depends solely on the local densities of the spheres $\rho_{sph}(z)$ and rods $\rho_{rods}(z)$, yielding the equation of state. In Fig. 4.3(a), we project the sedimentation path onto a two-dimensional $P - x_{sph}$ plane. From the top of the sediment down, each path shows an initial increase in pressure at large x_{sph}, followed by a nearly horizontal portion in the $P(x_{sph})$ curve suggestive of a broad coexistence between a low density phase and a Sm_2 phase. Finally, in the Sm_2 phase the pressure rises, while x_{sph} decreases only slowly. Each path presented the expected sequence isotropic I - (nematic N) - binary smectic Sm_2 that was identified by employing the average nematic and smectic local order parameters. In particular, we used the following threshold values to determine the different phases: isotropic if $\langle S_i \rangle < 0.5$ and $\langle \tau_i \rangle < 0.35$, nematic if $\langle S_i \rangle > 0.5$ and $\langle \tau_i \rangle < 0.35$, Sm_2 if $\langle S_i \rangle > 0.5$ and $\langle \tau_i \rangle > 0.35$. Whereas the choice of the threshold values of the order parameters at which we define the transitions can influence the identification of the different phases (cfr. Fig. 4.3(b)), we chose values corresponding to the inflection points observed in the trend of the local order parameters, as shown in Fig. 4.3(c)-(d). We thus find a stable Sm_2 phase in our experimental phase diagram for sufficiently high pressures $\beta P D_{eff}^3 > 3$ and compositions $0 < x_{sph} \leq 0.8$ in binary silica rod-sphere

mixtures. In order to explore the possibility that the Sm_2-phase coexists with a low-density phase and to investigate if the Sm_2-phase can be stabilized by entropy alone, we perform Monte Carlo simulation that are described in the next section.

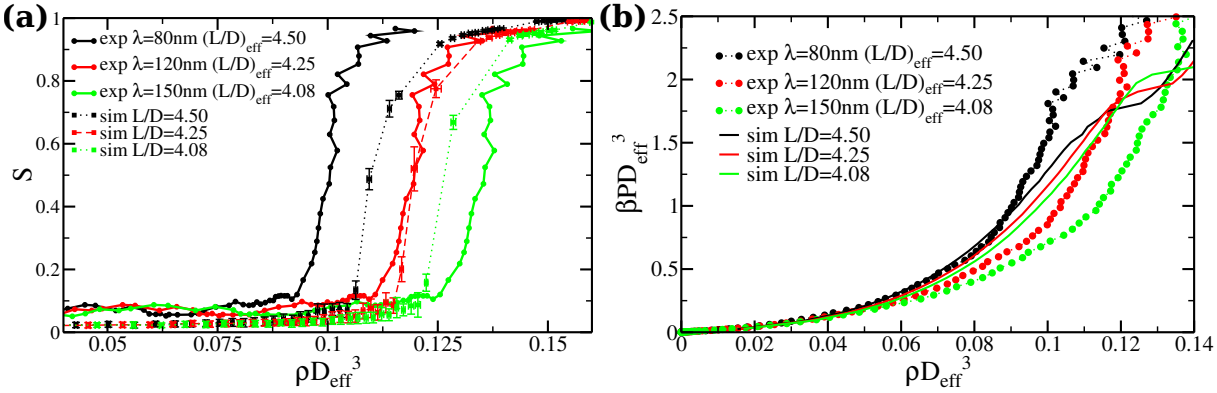

Figure 4.2: Determining the effective dimensions of silica rods. **(a)** Global nematic order parameter S as a function of the reduced density ρD_{eff}^3, where $D_{eff} = D_{TEM} + \lambda$, for different values of the additional layer λ. Experimental data (solid lines) are compared with simulations of one-component systems of hard spherocylinders with same aspect ratio. We observe that the best agreement is obtained for $\lambda = 120$ nm. **(b)** Same comparison for the equation of state: reduced pressure $\beta P D_{eff}^3$ versus reduced density ρD_{eff}^3. As detailed in the text, the equation of state with $\lambda = 120$ nm does not match properly (only close to $\rho D_{eff}^3 \sim 0.12$ where the I-N transition occurs) because of polydispersity in the system. See also Figs. 3.9 and 3.14.

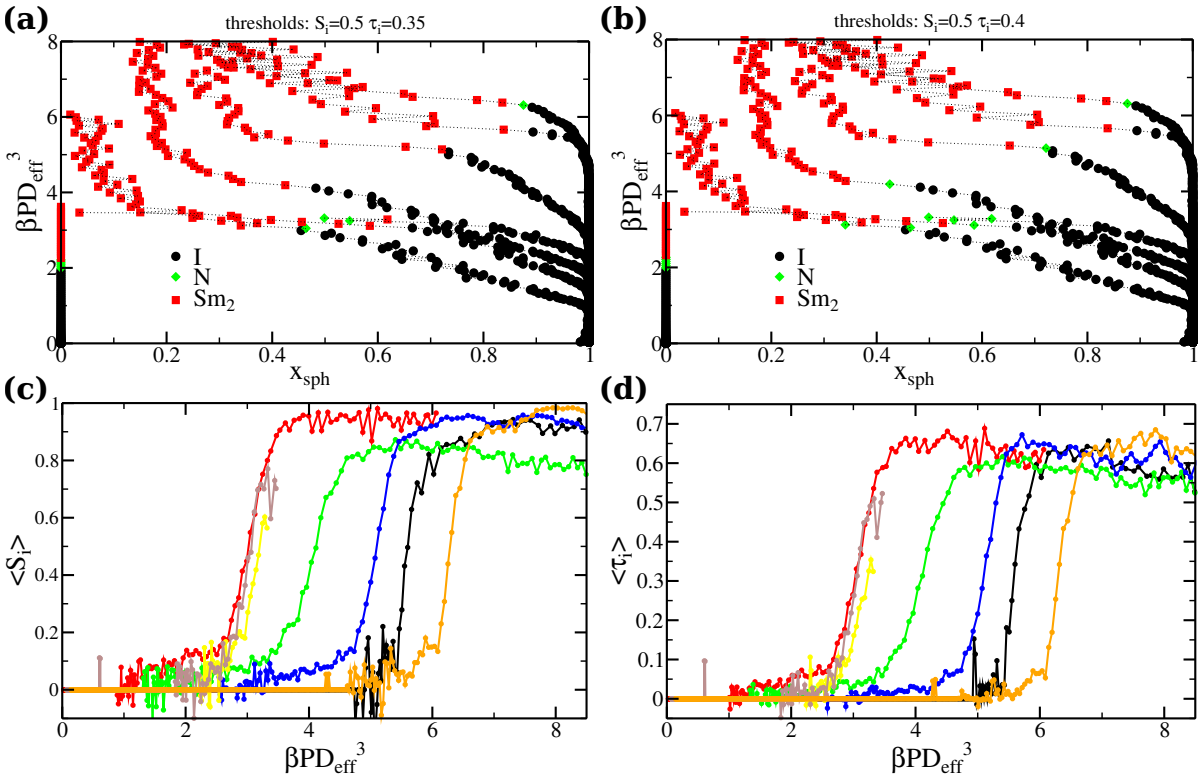

Figure 4.3: Experimental state diagram and order parameters for a binary mixture of silica rods and spheres. **(a)** Experimental state diagram for the mixture studied here. **(b)** Different choice of the threshold for the local smectic order parameter τ_i. **(c)** Local nematic order parameter S_i as a function of reduced pressure βPD^3_{eff} for different sediments. **(d)** Local smectic order parameter τ_i for different sediments.

4.3 Mapping out the bulk phase diagram of binary rod-sphere mixtures using computer simulations

We simulate $N = N_{sph} + N_{rods} = 3125$ hard spheres of diameter σ and hard spherocylinders (length $L = 6.46\sigma$ and diameter $D = 1.52\sigma$, $L/D \simeq 4.25$), based on the effective dimensions determined for the colloidal silica particles (see Sec. 4.2). Particles interact via a purely excluded-volume potential: $U = \infty$ if two particles overlap, $U = 0$ otherwise. We perform NPT simulations at many different state points and analyse the phase behaviour by employing local and global nematic and smectic order parameters. Each simulation consists of several millions of MC steps, where one step is defined as N moves randomly chosen between sphere translation, rod translation, rod rotation, plus one (either isotropic or anisotropic) attempt of changing the simulation box volume. Initial configurations at a given composition x are obtained from an equilibrated configuration at lower x by replacing an appropriate number of rods with spheres.

According to theoretical predictions based on a second-virial density functional theory applied to a rod-sphere mixture with similar sizes ($L/\sigma = 7$, $D = \sigma$), we expect stable isotropic (I), nematic (N) and binary-smectic (Sm_2) liquid crystal phases [167]. In our study, we do not take into account the possible crystalline (hexagonal) order, neither within a single layer nor between different layers, and therefore we do not distinguish between (binary) Smectic-A and (binary) Smectic-B and (binary) crystal phases, even though we (often) observe hexagonal arrangements of rods, both in experiments and in simulations (see Fig. 4.4). Notice that in case of binary crystals also the spheres should have (hexagonal) long-range order. Such phase is not observed in experiments, mainly because of relatively high polydispersity ($\delta_\sigma \sim 9$ %) that is known to prevent crystallization [146].

Since for the short rods considered here both the I-N and the N-Sm transitions are weakly first order [118, 119], and a particularly broad I-Sm_2 coexistence region is expected when such rods are mixed with hard spheres [167], an accurate identification of the phase boundaries is clearly challenging. Nevertheless, we use both global and local order parameters to discriminate between the different liquid crystalline structures for a large number of state points (for which x_{sph} and P are imposed) and to map out the state diagram of the rod-sphere mixture for which experiments have been performed (see Fig. 4.5(a)). In particular, in the isotropic phase (see Fig. 4.5(b)) all the order parameters are vanishing. The nematic phase (see Fig. 4.5(c)) is characterized by a large value of the nematic order parameter (both the global S and the local S_i) but not of the smectic ones, since neither the rods nor the spheres form layers. We observe that the I-N shifts towards higher pressure upon increasing composition x_{sph} until a (triple) point (around $x_{sph} \simeq 0.6$) beyond which the nematic phase is no more stable. In the Sm_2 phase (see Fig. 4.5(d)) the rods locally form layers resulting in a large value of the local smectic order parameter τ_i. The structure is clearly long-range and this is confirmed by the (ordinary) global smectic order parameter τ. The binary character of the smectic phase is confirmed by the fact that also the spheres are arranged in layers, as clearly evident from the snapshot in Fig. 4.5(d). The layering can also be quantified by a global smectic order parameter for the spheres, calculated along the nematic director of the rods $\mathbf{n}$ (that coincides with the layer normal),

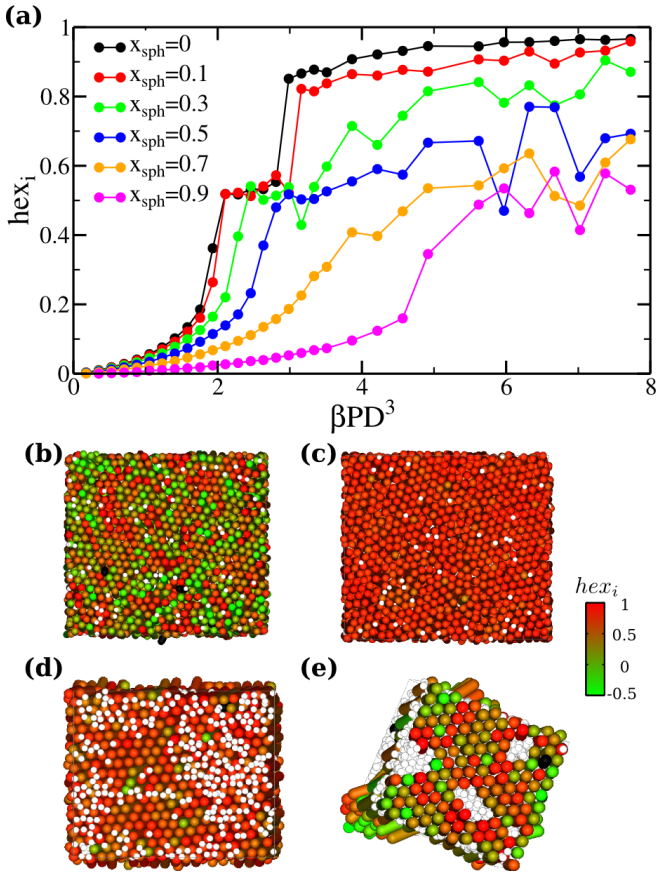

Figure 4.4: **(a)** Local hexagonal order parameter hex_i as a function of reduced pressure (βPD^3) for several compositions as indicated in the legend. Representative snapshots with particles colored according to hex_i are shown in **(b)** for $x_{sph} = 0.1$ and $\beta PD^3 = 2.81$; **(c)** $x_{sph} = 0.1$ and $\beta PD^3 = 2.98$ **(d)**; $x_{sph} = 0.5$ and $\beta PD^3 = 6.32$; **(e)** $x_{sph} = 0.9$ and $\beta PD^3 = 7.37$.

in full analogy with the one for the rods (see Sec. 3.4):

$$\tau_{sph} = \max_{l} \left| \sum_{j=1}^{N} e^{2\pi i \mathbf{r}_j \cdot \mathbf{n}/l} \right|, \tag{4.1}$$

where $\mathbf{r}_j$ is the position of sphere j and l is a real number. The value of l that maximizes the above expression coincides with the layer spacing. Both the smectic order parameter values of τ_{sph} and the corresponding spacing between layers of spheres are consistent with the values of τ (for only rods) and the spacing between the smectic layers of rods, as expected for the Sm_2 phase. However, for small x_{sph} and high pressures P (see Fig. 4.5(e)-(f)), the spheres do not form layers but are expelled from the layers of rods and organised in linear aggregates. This structure is not a novel thermodynamically stable phase but should be considered as an indication of the underlying phase separation in a sphere-rich isotropic phase and rod-rich (binary) smectic phase (or a crystal phase of rods at sufficiently high pressures, as evident from Fig. 4.5(e)). Indeed, since the system cannot really demix because of the finite size nature of the simulations, the spheres have to act as a substitute of rods to minimize the overall system free volume. It is important

to remark that this columnar arrangement of spheres is not related with the columnar phase observed in a mixture of colloidal spheres and fd-viruses [161], since in that case the columns of spheres were perpendicular to the direction of the layers of rods. The possibility of forming that structure with only hard-core interactions and its thermodynamic stability are still open questions.
The transition from a stable Sm_2 phase to this kinetically trapped structure, that is an evidence of I-Sm_2 demixing, is often associated to a drop in τ_{sph} as reported in Fig. 4.6(f). As can be seen from Fig. 4.5(f), the formation of columns of spheres occurs also when most of the spheres are still arranged in layers, therefore yielding to a somehow arbitrary definition of the upper bound of the Sm_2 stability region. Different simulation techniques should be employed to accurately determine this boundary.
For larger values of x_{sph}, the I-Sm_2 demixing is more evident as can be appreciated from Fig. 4.5(g)-(h) in which a number of smectic layers (depending on x_{sph}) is in coexistence with an isotropic phase richer in spheres. This behaviour is also captured by the probability distribution of rods having a certain value of the local smectic order parameter τ_i (some examples are reported in Fig. 4.6(a)). Indeed, for state points inside the I-Sm_2 regions two populations of particles (one with $|\tau_i| \sim 0$ and one with τ_i bigger than a given threshold) are often evident. However, extracting the equilibrium composition of the two coexisting phases based on the amount of particles in the two populations seemed to be not an easy task due to the limited system size of our simulations and the sensibility on the choice of the threshold value. By examining the state diagram obtained, we notice that compositions around $x_{sph} = 0.6$ show a peculiar *re-entrant* sequence upon increasing the pressure, going from an isotropic to I-Sm_2 region to a pure Sm_2 to a demixed region again. Representative snapshots at this composition, along with a quantitative analysis, are reported in Fig. 4.6. Finally, we notice that the topology of the phase diagram here reported is consistent with theoretical predictions [167], including the re-entrant behaviour of the Sm_2 region.

We have to remark that the use of NPT ensemble is not always suitable to study demixing in binary mixtures since the composition (x_{sph}) is fixed and large system sizes are needed to observe phase coexistence between different thermodynamic states (this analysis would not be reliable for smaller systems than studied here). Indeed, a standard procedure to trace the phase diagram of a mixture would require simulations in the grand-canonical ensemble that are, however, not feasible for short rods (only the insertion/removal of the small spheres would be possible). Recently, the use of hard walls in computer simulations of rod-sphere systems composed of similar numbers of particles as used here and similar particle dimensions, have been employed as an alternative to determine slightly more accurately the variation in composition of the isotropic-nematic transition but limiting the study to a small region in the $x_{sph} - P$ plane [166]. However, at the densities where the binary smectic phase is observed, the effect of walls would be still quite pronounced for ordinary system sizes. Ultimately, an accurate study of the equilibrium phase behaviour should be based on (computationally expensive) free-energy calculations.

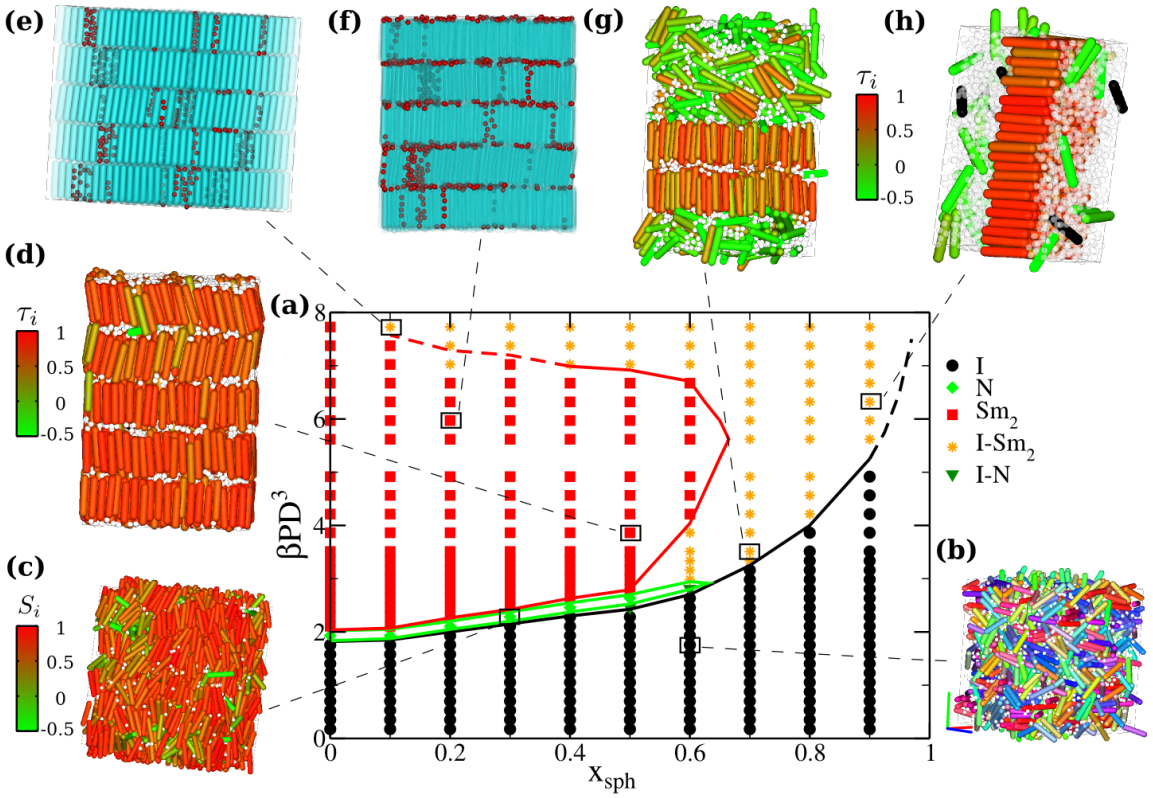

Figure 4.5: **(a)** State diagram from bulk MC-NPT simulations. Representative snapshots for **(b)** isotropic phase (I) with $x_{sph} = 0.6$ and $\beta PD^3 = 1.93$, rods are colored according their orientations (axis colors indicated in the snapshot); **(c)** nematic phase (N) $x_{sph} = 0.3$ and $\beta PD^3 = 2.28$ with rods colored according to the local nematic order parameter S_i; **(d)** binary smectic phase (Sm_2) $x_{sph} = 0.5$ and $\beta PD^3 = 3.86$ with rods colored according to the local smectic order parameter τ_i; **(e)** Formation of columnar aggregates of hard spheres as indication of demixing between a smectic (or crystal) phase rich in rods and an isotropic phase rich in spheres. $x_{sph} = 0.1$ and $\beta PD^3 = 7.73$; **(f)** Columns of spheres start to appear in a Sm_2 phase (most of the spheres are still arranged in layers) $x_{sph} = 0.2$ and $\beta PD^3 = 5.97$; **(g)** Coexistence between I and Sm_2 phase, $x_{sph} = 0.7$ and $\beta PD^3 = 3.86$, rods colored according to τ_i ; **(h)** Single layer of rods in coexistence with a sphere-rich isotropic phase, $x_{sph} = 0.9$ and $\beta PD^3 = 6.32$, rods are colored according to τ_i.

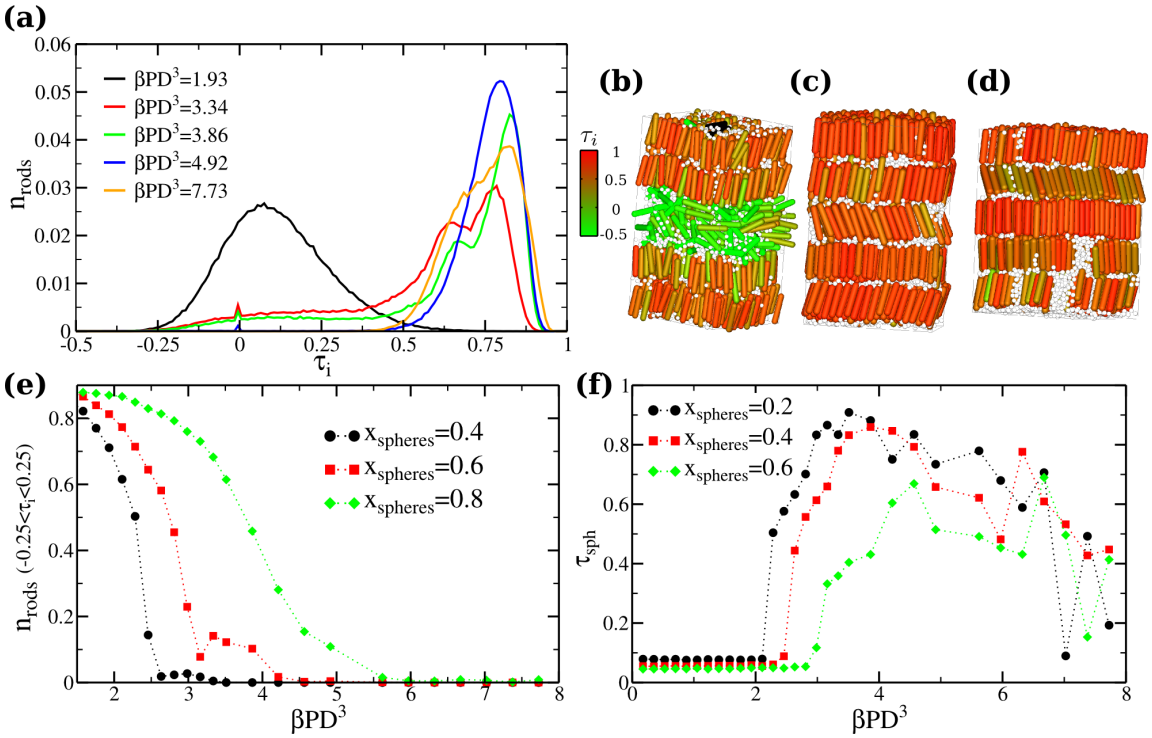

Figure 4.6: Identifying coexistence between isotropic and binary smectic phase.**(a)** Fraction of rods n_{rods} with a given value of the local smectic order parameter τ_i for state points with $x_{sph} = 0.6$ and reduced pressures βPD^3 as indicated in the legend. $\beta PD^3 = 1.93$ corresponds to an isotropic state (representative snapshot in Fig. 4.5(b)). $\beta PD^3 = 3.34$ corresponds to an I-Sm_2 state (typical snapshot in panel **(b)**), a small peak at $\tau_i \sim 0$ is evident. $\beta PD^3 = 4.92$ corresponds to a Sm_2 state (snapshot in panel **(c)**). $\beta PD^3 = 7.73$ corresponds to a I-Sm_2 state (snapshot in panel **(d)**). In this case the probability distribution of τ_i is not useful to identify the state point but the low value of τ_{sph} (see panel **(f)**) indicates that the spheres are not arranged in layers. In all the snapshots the rods are colored from green (low) to red (high) according to the value of τ_i. Rods that are colored black do not have nearby neighbours and therefore have $\tau_i = 0$. Peaks around zero (panel **(a)**) are evidences of demixing between I and Sm_2. Tracking the number of rods with small values of τ_i could help in identifying the state point. In panel **(e)** the fraction of rods n_{rods} with a small τ_i (arbitrarily chosen such that $|\tau_i| < 0.25$) are plotted as a function of the reduced pressure βPD^3 for different composition x_{sph}. For $x_{sph} = 0.6$ the non-monotonic behaviour of n_{rods} could be used to identify the re-entrant behaviour of the Sm_2 region, even if it is admittedly somehow arbitrary. In panel **(f)** the smectic order parameter associated to layers of spheres τ_{sph} (see text for the definition) is plotted against the pressure for different composition. The different arrangement of spheres, either in layers or in columns/random aggregates (these are indications of I-Sm_2 demixing) is associated to a large or small value of τ_{sph}, respectively.

4.4 Comparison with experiments and conclusions

In Fig. 4.7 the experimental sedimentation paths are superimposed on the state diagram obtained using computer simulations of hard spherocylinders and hard spheres in bulk without a gravitational field using the effective dimensions of the experimental particles, as described in the previous section. The topology of the phase diagram is consistent with previous theoretical studies [167] and shows a large isotropic-binary smectic (I-Sm_2) coexistence region. Sedimentation paths going through such demixing regions look mostly flat (pressure is constant) for a good part, even though a clear identification of the coexistence points remains a clear challenge. Nevertheless, an overall qualitative agreement is obtained. Hence, the phase behaviour of silica rods and spheres is predominantly entropy-driven, so mostly dominated by the particle shape. This was expected because the van der Waals interactions were reduced by refractive index-matching solvent and colloids, and because the length of the charge repulsion was also reduced by the addition of salt to the medium. In summary, the liquid crystal behaviour of the experimental system is in agreement with simulations and it can be well described by using a second-virial theory [167].

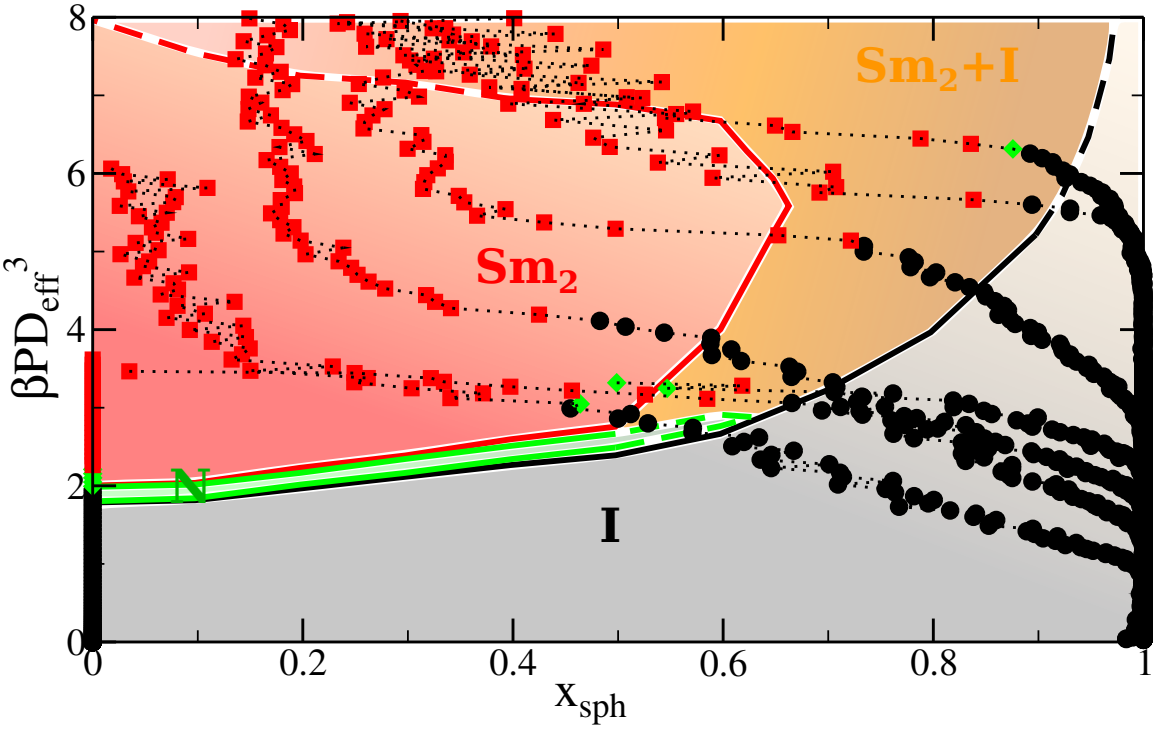

Figure 4.7: Mapping of experimental data (symbols) on bulk state diagram from Monte Carlo simulations. The regions where the phases are expected to be thermodynamically stable were roughly identified by MC bulk simulations of mixtures of hard rods and hard spheres. Experimental equations of state (pressure βPD^3 versus composition $x = N_s/N$) obtained from different sediments of rods and spheres (symbols). We used the following thresholds to determine in the experimental system the different phases; isotropic (I) if $\langle S_i \rangle < 0.5$ and $\langle \tau_i \rangle < 0.35$ (black spheres), nematic (N) if $\langle S_i \rangle > 0.5$ and $\langle \tau_i \rangle < 0.35$ (green diamonds), Sm_2 if $\langle S_i \rangle > 0.5$ and $\langle \tau_i \rangle > 0.35$ (red squares).

Due to the relatively high polydispersity (in rod length $\delta_L \simeq 18\%$ and diameter $\delta_D \simeq 10\%$, and in sphere diameter $\delta_\sigma \simeq 9\%$), no long-range positional order was found in the sample, i.e., no binary crystal phases was obtained. By decreasing the polydispersity in the sample (δ_L and $\delta_D < 5\%$ is currently achievable), we expect to find crystalline structure at higher pressures, possibly the same binary crystal phase observed for nanorods and nanospheres [183]. However, the fact that computer simulations at high pressure show a strong tendency to phase separation between a crystal phase with almost only rods poses some doubts on the possibility of forming a binary crystal at intermediate compositions for this particular diameter ratio ($D/\sigma = 1.52$). The influence of large and small spheres on the stability of layered phases have been investigated theoretically [169] and partially experimentally [161]. Futures studies combining experiments using silica colloids and simulations could address the stability of binary crystal phases in a systematic way.

In conclusion, we demonstrated that Sm_2 phases of rods and spheres can be formed by shape alone. This allows the possibility of realizing these intriguing phases with a broad class of systems over several lengths scales and profit from the combined benefits of both binary systems and the tunability of liquid crystal phases. For instance, realizing an aligned Sm_2 phase of gold nanorods and spherical semiconductor particles using a small electric field is of great interest. Spherical semiconductor particles would self-assemble at the gold nanorod tips. At these positions there will be very strong plasmon enhanced electromagnetic fields, that will enhance the luminescence of semiconductor particles. However, the use of different materials could clearly change the interparticle potential that in turn could change the equilibrium structure. For example, it has been shown that in two-dimensional assemblies of semiconductor nanorods and gold nanospheres when the rod-sphere attractions are dominant the favored structure consists in a certain number of spheres aligned linearly (in parallel) between two neighbouring rods [163]. Finally, mixtures of colloidal rods and spheres are a valuable model system to study the particle dynamics and the nucleation of binary systems in real-time and in real-space. Quantitative analysis based on order parameters such as the ones used in this chapter will be useful for this purpose.

Acknowledgments

This work was done in collaboration with Henriëtte Bakker who performed the experimental part of the project under the supervision of Arnout Imhof and Alfons van Blaaderen. Henriëtte is sincerely thanked for providing images, experimental data and for stimulating discussions.

5

Moving away from spherocylinders: polyhedral hard rods and biaxial nematic phases

In this chapter we study the liquid-crystal behaviour of biaxial hard rod-like particles with a polyhedral shape. We perform computer simulations of hard equilateral triangular prisms and we find isotropic, uniaxial nematic and smectic phases. Theoretical predictions based on fundamental measure theory are in agreement with the simulation results. Furthermore, we observe that triangular prisms exhibit liquid-crystal phases at slightly lower densities and slightly lower particle aspect ratios with respect to spherocylinders, a feature that can be attributed to the presence of flat faces. By changing the angle of the (isosceles) triangular base of the prisms, we also observe the formation of oblate and biaxial nematic phases by computer simulations. Our state diagram indicates that the general liquid-crystal behaviour can be predicted on the basis of a shape parameter that depends on the difference between the ratios of the particle axes, as already pointed out in the literature. In particular, biaxial nematic phases of triangular prisms are found when such a shape parameter is close to zero, i.e., the "dual" shape. This shape parameter criterium is further confirmed by computer simulations of hard cuboidal particles. However, biaxial nematic phases are only observed when the particles are sufficiently elongated, which is equivalent to sufficiently thin for dual-shaped particles, in order to stabilize both prolate and oblate order. This additional criterium depends sensitively on the exact particle shape, i.e., the threshold value on the particle length becomes more extreme going from spheroplatelets to triangular prisms to cuboids.

5.1 Introduction

Recent advances in colloidal synthesis techniques allow the preparation of colloids and nanoparticles with a large number of distinct polyhedral shapes and sizes ranging from the nanometer to the micrometer [68–70]. The sheer number of available polyhedral colloids with distinct shapes and the prospect of even more shapes synthesized in the near future demands efficient theories or computer simulations to guide future synthesis efforts. In particular, it is of clear interest to understand what is the effect of the particle facets on the liquid crystal phase behaviour of such rod-like nano-polyhedra and what shape parameters can be used to rationalize the observed phase behaviour. In the first part of this chapter, we assess the accuracy of density functional theory (DFT), in particular fundamental measure theory (FMT), in describing the liquid-crystal behaviour of polyhedral rods. To this end, we perform computer simulations of hard equilateral triangular prisms forming liquid crystal phases. We compare our results with FMT predictions and we highlight the difference with respect to the (uniaxial) spherocylindrical model.

In the second part, we investigate the formation of biaxial nematic phases in systems of hard elongated polyhedral particles by using computer simulations. Biaxial nematic phases have three distinct optical axes in contrast with the (simpler) uniaxial nematic phase, which has a single preferred axis. Biaxial nematic phases have been the focus of several theoretical works [62, 151, 185, 186], they have been long searched and debated in experimental thermotropic liquid crystals [187–190] and investigated by computer simulations based on attractive particle models (see for example Refs. [191, 192]). Biaxial nematics have also been observed in colloidal systems [193] and hard-particle models have been employed in simulations to shed new light into the biaxial nematic phases stabilized by entropy alone [194, 195]. As theoretically predicted [62, 185], biaxial nematics can appear in systems composed of particles that have a particular ratio of their molecular axes, quantified by a shape parameter ν. The first evidence of an entropy-driven transition to a biaxial nematic phase was provided by simulations on biaxial ellipsoids [194], which do not exhibit a smectic phase that can destabilize the biaxial nematic phase. More recently, computer simulations of hard spheroplatelets [195, 196] showed that it is still possible to obtain a biaxial phase before the formation of a smectic phase in a very narrow shape parameter regime where $\nu \sim 0$, providing that also the ratio between the long and the short particle axis is greater than a given threshold (which is 9 for this specific particle model). Here, we consider two different models: hard elongated triangular prisms with an isosceles triangular base and hard cuboidal (brick-like) particles. In both cases we find regions in which biaxial nematic phases are stable, for particles with $\nu \sim 0$. However, consistently with the literature, we observe that additional, strongly shape-dependent, conditions need to be satisfied as well.

5.2 Models and methods

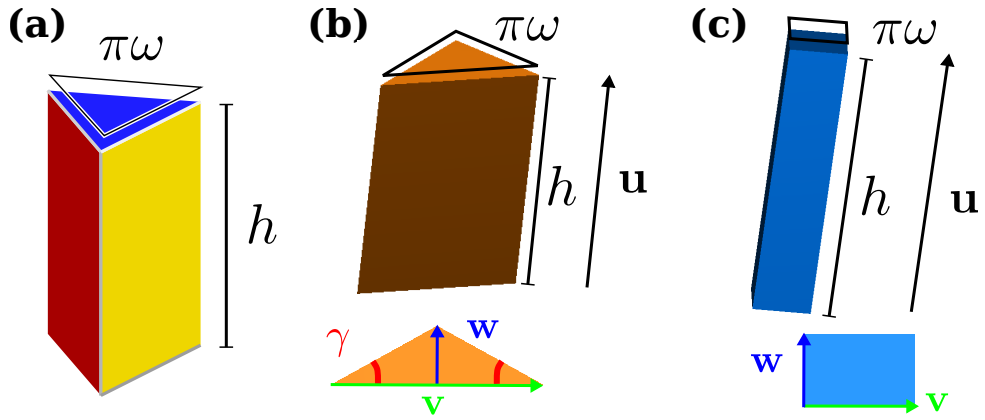

Figure 5.1: Triangular prism (TP) with an **(a)** equilateral or **(b)** isosceles base. The height of the particle is h, whereas the width is ω and is defined such that the base perimeter is $\pi\omega$. The isosceles base (panel (b)) is defined by the angle γ. The particle orientation can be described by the unit vector $\hat{\mathbf{u}}$, $\hat{\mathbf{v}}$ and $\hat{\mathbf{w}}$. **(c)** Cuboidal (brick-like) particle of height h, width ω, such that the base perimeter is $\pi\omega$. The orientation of the long, medium and short axis is described by $\hat{\mathbf{u}}$, $\hat{\mathbf{v}}$ and $\hat{\mathbf{w}}$, respectively. The particle dimensions are in all cases defined by the length of the vectors $|\hat{\mathbf{u}}|$, $|\hat{\mathbf{v}}|$, and $|\hat{\mathbf{w}}|$.

The first particle model we consider is a hard triangular prism (TP) of height h with an equilateral base, as shown in Fig. 5.1(a). The width ω of the particle is defined such that the base perimeter is $\pi\omega$. According to this definition, when the number of the sides of the base tends to infinity, so in the limit that the particle becomes a cylinder, ω coincides with the particle diameter. Therefore h/ω is the particle aspect ratio. This particle model is clearly biaxial and the shape can be further tuned by varying the triangular base. In particular, we consider TPs with an isosceles triangular base defined by the angle γ, as shown in Fig. 5.1(b). Clearly, the equilateral case is obtained when $\gamma = \pi/3 \simeq 1.04719$. The particle orientation is described by three unit vectors $\hat{\mathbf{u}}$, $\hat{\mathbf{v}}$ and $\hat{\mathbf{w}}$ associated to the main particle axes, as shown in Fig. 5.1(b). By introducing the vectors $\mathbf{u}$, $\mathbf{v}$, and $\mathbf{w}$, we are also able to define the particle dimensions of the TP by using their length $|\mathbf{u}|$, $|\mathbf{v}|$, and $|\mathbf{w}|$. For the TPs studied here, $|\mathbf{u}|$ always represents the long axis, which coincides with the height h, whereas $|\mathbf{v}|$ and $|\mathbf{w}|$ are the medium and short axis, that depend on the angle γ. For $\gamma \lesssim 1.10715$, the length of the short axis is $|\mathbf{w}| = (\pi \sin\gamma)/(2 + 2\cos\gamma)$ and the length of the medium axis is $|\mathbf{v}| = (\pi\cos\gamma)/(1+\cos\gamma)$. On the contrary, for $\gamma \gtrsim 1.10715$, $|\mathbf{w}| > |\mathbf{v}|$, and in particular $|\mathbf{w}| = (\pi\cos\gamma)/(1+\cos\gamma)$ and $|\mathbf{v}| = (\pi\sin\gamma)/(2+2\cos\gamma)$.

The shape parameter ν is defined as the difference between the ratio of the long and medium axis and the ratio of the medium and the short axis. For $\gamma \lesssim 1.10715$, it yields

$$\nu = \frac{|\mathbf{u}|}{|\mathbf{v}|} - \frac{|\mathbf{v}|}{|\mathbf{w}|} = \frac{h(1+\cos\gamma)}{\pi\cos\gamma} - \frac{2}{\tan\gamma}\,, \tag{5.1}$$

and a similar expression can be obtained when $\gamma \gtrsim 1.10715$.

At the end of this chapter we also study the liquid crystal behaviour of hard cuboidal (brick-like) particles. Similar definitions also hold for this particle model, which is shown

in Fig. 5.1(c). The particle height is $h = |\mathbf{u}|$ and the particle width is ω such that the base perimeter is $\pi\omega = 2|\mathbf{v}|+2|\mathbf{w}|$. We assume, without loss of generality, that $|\mathbf{u}| \geq |\mathbf{v}| \geq |\mathbf{w}|$, such that the shape parameter $\nu = |\mathbf{u}|/|\mathbf{v}| - |\mathbf{v}|/|\mathbf{w}|$.

Computer simulations and order parameters

To study the phase behaviour of polyhedral hard rods we employ standard Monte Carlo (MC) simulations either in the NPT or NVT ensemble [10]. System sizes range from $N \simeq 1000$ to $N \simeq 3000$ particles and several millions of MC steps are performed for typical runs. For NVT-MC simulations, each MC step consists on average of $N/2$ attempts of translating a random particle and $N/2$ attempts of rotating a random particle. For NPT-MC simulations, an additional attempt to either scale isotropically the volume or to change only one edge of the cuboidal simulation box is tried at each MC step. The particles interact via an hard-core potential only. To detect overlaps between particles, we use an algorithm, based on the RAPID library [57], that consists in detecting the intersections between the (triangular or rectangular) faces of the polyhedral particles.

To quantify the orientational and positional order in the system we use several order parameters. First, we extend the nematic order parameter used for uniaxial particles (cfr. Sec. 3.4) to the biaxial particle models considered here. In particular, we construct the following tensors

$$\mathcal{Q}^{\hat{\mathbf{a}}}_{\alpha\beta} = \frac{1}{N}\sum_{i=1}^{N}\left[\frac{3}{2}\hat{\mathbf{a}}_{i\alpha}\hat{\mathbf{a}}_{i\beta} - \frac{\delta_{\alpha\beta}}{2}\right], \tag{5.2}$$

where $\alpha, \beta = x, y, z$ component and $\hat{\mathbf{a}} = \hat{\mathbf{u}}, \hat{\mathbf{v}}, \hat{\mathbf{w}}$ denotes the three symmetry axes of the particle. N is the number of particles and $\delta_{\alpha\beta}$ the Kronecker delta. By diagonalizing each of these tensors we obtain three eigenvalues $\lambda^+_a \geq \lambda^0_a \geq \lambda^-_a$. We identify the (scalar) order parameter associated to the nematic order of the axis $\hat{\mathbf{a}}$ as the maximum of these eigenvalues: $S^{\hat{\mathbf{a}}} \equiv \lambda^+_a$. The corresponding eigenvector is the nematic director $\hat{\mathbf{n}}_{\hat{\mathbf{a}}}$. In Secs. 5.4 and 5.5 we use these order parameters to distinguish between oblate, prolate and biaxial nematic phases.

It is also possible to quantify the degree of (macroscopic) biaxial alignment of a nematic phase by defining an additional order parameter, that we call $\mathcal{B}$. Different notations are used to identify such a parameter [197] and slightly different approaches are employed to calculate it in computer simulations [192, 194, 196]. We follow the procedure in Refs. [194, 198] that consists in first identifying an appropriate orthonormal basis for the laboratory reference frame that is aligned with the two main directions of the biaxial phase. For each configuration, we identify the largest $S^{\hat{\mathbf{a}}}$ and we define the z-axis of the laboratory reference frame as $\hat{\mathbf{Z}} \equiv \hat{\mathbf{n}}_{\hat{\mathbf{a}}}$, with $\hat{\mathbf{a}}$ the principle main axis of the particle. Then, we identify the second largest nematic order parameter $S^{\hat{\mathbf{b}}}$ and we define the second axis of the laboratory reference frame as $\hat{\mathbf{Y}} \equiv \hat{\mathbf{n}}_{\hat{\mathbf{b}}} - (\hat{\mathbf{n}}_{\hat{\mathbf{b}}} \cdot \hat{\mathbf{Z}})\hat{\mathbf{Z}} \simeq \hat{\mathbf{n}}_{\hat{\mathbf{b}}}$. Analogously, we define the third axis of the laboratory frame by orthogonalizing the third nematic director: $\hat{\mathbf{X}} \equiv \hat{\mathbf{n}}_{\hat{\mathbf{c}}} - (\hat{\mathbf{n}}_{\hat{\mathbf{c}}} \cdot \hat{\mathbf{Z}})\hat{\mathbf{Z}} - (\hat{\mathbf{n}}_{\hat{\mathbf{c}}} \cdot \hat{\mathbf{Y}})\hat{\mathbf{Y}}$, with $\hat{\mathbf{c}}$ the third symmetry axis of the particle. Finally, we compute

$$\mathcal{B} = \frac{1}{3}\left(\hat{\mathbf{Y}} \cdot \mathcal{Q}^{\hat{\mathbf{b}}} \cdot \hat{\mathbf{Y}} + \hat{\mathbf{X}} \cdot \mathcal{Q}^{\hat{\mathbf{c}}} \cdot \hat{\mathbf{X}} - \hat{\mathbf{Y}} \cdot \mathcal{Q}^{\hat{\mathbf{c}}} \cdot \hat{\mathbf{Y}} - \hat{\mathbf{X}} \cdot \mathcal{Q}^{\hat{\mathbf{b}}} \cdot \hat{\mathbf{X}}\right). \tag{5.3}$$

$\mathcal{B}$ is normalized such that it ranges from 0 to 1. Low values of $\mathcal{B}$ correspond to an isotropic phase or to a uniaxial phase and high values to a biaxial phase.

To identify the phase transition to a smectic phase, more precisely to a prolate smectic-A phase, we use the same order parameter as introduced for spherocylinders (cfr. Sec. 3.4):

$$\tau = \max_{l \in \mathbb{R}} \left| \sum_{j=1}^{N} \exp\left(\frac{2\pi}{l} i \mathbf{r}_j \cdot \hat{\mathbf{n}}_{\hat{\mathbf{a}}} \right) \right| , \tag{5.4}$$

where $\mathbf{r}_j$ denotes the position of particle j.

Density functional theories

For the equilateral TPs, we compare our simulation results with the theoretical predictions based on different types of density functional theory (DFT). First, to describe the isotropic-nematic transition we use the second-virial Onsager theory with Parsons-Lee (PL) correction, already described in Sec. 3.2. We do not explicitly consider the biaxial nature of the particle shape in the description of the nematic order. In particular, we assume that the orientation distribution function ψ depends only on the polar angle θ between $\hat{\mathbf{u}}$, that is the orientation of the long axis of the particle (see Fig. 5.1) and the nematic director $\hat{\mathbf{n}}_{\hat{\mathbf{u}}}$. In other words, we assume $\psi(\mathcal{R}) = \psi(\theta)$, where $\mathcal{R}$ is the 3×3 rotation matrix describing the particle orientation. In analogy with Eq. 3.6, the excluded volume between two particles is given by :

$$E(\theta, \theta') = -\int d\phi \, d\phi' \, d\chi \, d\chi' d\mathbf{r} \, f(\mathbf{r}, \mathcal{R}, \mathcal{R}') \, , \tag{5.5}$$

with $f(\mathbf{r}, \mathcal{R}, \mathcal{R}')$ the Mayer function (see Eq. 3.4), ϕ the azimuthal angle with respect to $\hat{\mathbf{n}}_{\hat{\mathbf{u}}}$, and χ the particle internal angle. In practice, the excluded volume is computed by performing MC integration over many randomly generated pairs of particles. This procedure has been already outlined in Sec. 3.2 and is described extensively in Sec. 6.2.4 for chiral nematic phases (the uniaxial achiral nematic state is recovered by assuming no twist). In summary, the excluded volume used as input for Onsager-PL theory is an average over the particle internal angle.

Calculations based on a more sophisticated DFT, namely fundamental measure theory (FMT) [199–203], performed by M. Marechal (Universität Erlangen-Nürnberg), are also reported in this chapter and compared with our simulation results. Contrary to Onsager-PL theory (in the version used here), FMT is based on the full single-particle distribution $\rho(\mathbf{r}, \mathcal{R})$, i.e., it takes into account explicitly all the orientational degrees of freedom and the positional degrees of freedom. In this way, it is possible to distinguish between isotropic, nematic and smectic phases and to investigate also the biaxial order and the smectic layer structure. FMT was recently applied to polyhedral particles [204]. Results from two different flavours of FMT are reported, and are denoted as 0D-FMT and TR-FMT. 0D-FMT was derived by considering a quasi-zero dimensional system, i.e., a cavity that contains at most one particle [205, 206]. 0D-FMT should work well for strongly layered systems and long particles. TR-FMT was obtained by Tarazona and Rosenfeld [205] from 0D-FMT for spheres by an expansion and subsequent rescaling to get the correct third virial coefficient for the bulk fluid of hard spheres. The rescaling should improve the results for the isotropic phase of shorter particles.

5.3 Liquid crystals of equilateral triangular prisms

The liquid crystal behaviour of hard equilateral TPs (model shown in Fig. 5.1(a)) is studied by performing MC simulations of $N = 2000$ particles with different aspect ratios $h/\omega \in [3.0, 6.0]$. The equation of state is obtained after long equilibration runs in the NPT ensemble, typically expanding from close-packed configurations, and averaging the density over equilibrated configurations generated in the last $\sim 10^6$ MC steps. In Fig. 5.2(a), we plot the reduced pressure $\beta P\omega^3$, with $\beta = 1/k_BT$, T the temperature and k_B the Boltzmann constant, as a function of the packing fraction η for some of the systems studied. We find an isotropic (I) phase at low densities and a crystal (X) phase at high densities for all the aspect ratios h/ω studied. For $h/\omega = 3$, we observe a clear jump in the density that corresponds to a first-order transition from I to a smectic (Sm) phase. In case of longer particles, a nematic (N) phase is also observed, and the jumps in densities associated to the I-N and N-Sm transitions are barely visible.

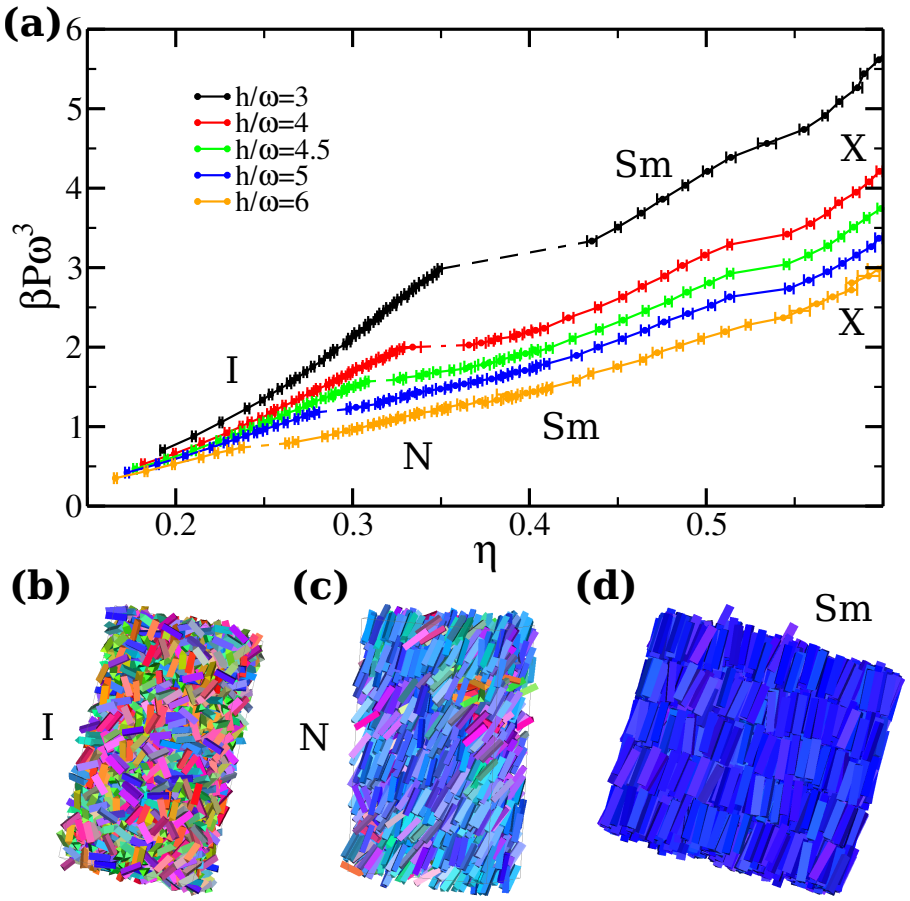

Figure 5.2: **(a)** Equations of state (reduced pressure $\beta P\omega^3$ versus packing fraction η) obtained by MC-NPT simulations for TPs with different aspect ratio h/ω along with representative snapshots of **(b)** an isotropic (I) phase, **(c)** a nematic (N) phase and **(d)** a smectic (Sm) phase. Particles are colored according to the orientation of their long axis **u**. At high densities the TPs form a crystal phase (X).

Both in the nematic phase and in the smectic phase, only the long particle axis $\hat{\mathbf{u}}$ exhibits long-range orientational order, as evident from visual inspection of typical configurations, shown in Fig. 5.2(c)-(d), and further confirmed by the order parameter analysis. The liquid crystal behaviour is therefore qualitatively similar to that of spherocylinders (uniaxial rod-like particles) with comparable aspect ratio. This is expected since equilateral TPs in this aspect ratio range have a shape parameter ν significantly larger than zero, for which a prolate (or calamitic) nematic phase is predicted. The phase transitions can be determined by identifying the jumps of the nematic order parameters $S \equiv S^{\hat{\mathbf{u}}}$ and the smectic order parameter τ as a function of the packing fraction η, as shown in Fig. 5.3. For $h/\omega = 3$, we can clearly identify an I-Sm transition since both S and τ simultaneously jump in correspondence of the large density jump. A direct transition from I to Sm can be also observed for $h/\omega = 4$, despite the smectic order parameter τ displays a less abrupt jump. Beyond this aspect ratio, a N phase appears in between the I and the Sm phase. A weakly first order N-Sm transition is observed for TPs with $h/\omega = 4.1$ and $h/\omega = 4.3$, since τ displays a jump at larger η than S, and this is further confirmed by visual inspection of the configurations. Longer TPs exhibit more pronounced jumps of the order parameters. We can conclude that TPs with $h/\omega \gtrsim 4$ self-assemble into a N phase. For larger h/ω, the I-N transition clearly shifts towards smaller η whereas the location of the N-Sm is less sensitive to h/ω.

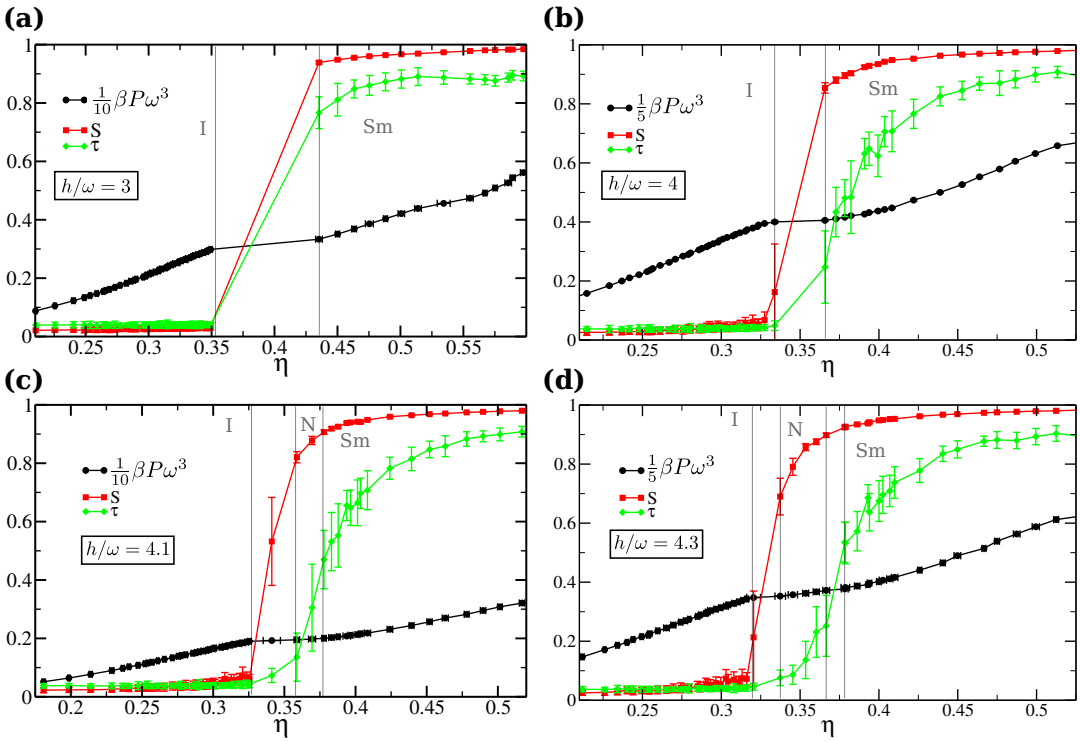

Figure 5.3: Reduced pressure $\beta P\omega^3$, nematic order parameter S and smectic order parameter τ versus packing fraction η for TPs with **(a)** $h/\omega = 3$, **(b)** $h/\omega = 4$, **(c)** $h/\omega = 4.1$, and **(d)** $h/\omega = 4.3$. Vertical lines are guides-to-the-eye to locate the jumps in the order parameters and therefore estimate the phase transitions.

The order parameter analysis is repeated in the NVT ensemble and the previous observations are confirmed. In Fig. 5.4, we compare the dependence of the nematic order parameter S on the packing fraction η as obtained by computer simulations, by Onsager-PL theory and by FMT, for TPs with different h/ω. We observe that Onsager-PL theory largely overestimates the packing fraction at which the I-N transition occurs, confirming the known drawback of such a theory. On the other hand, FMT predictions for the jump of S match well the simulation results for TPs with $h/\omega = 3$, for which only the I-Sm transition occurs. On the other hand, as soon as the N phase becomes stable, e.g. for $h/\omega = 4.3$, the FMT underestimates the packing fraction associated to the jump of S. However, upon increasing aspect ratio h/ω, the discrepancy diminishes and already for $h/\omega = 6$ a good agreement for the I-N transition is obtained.

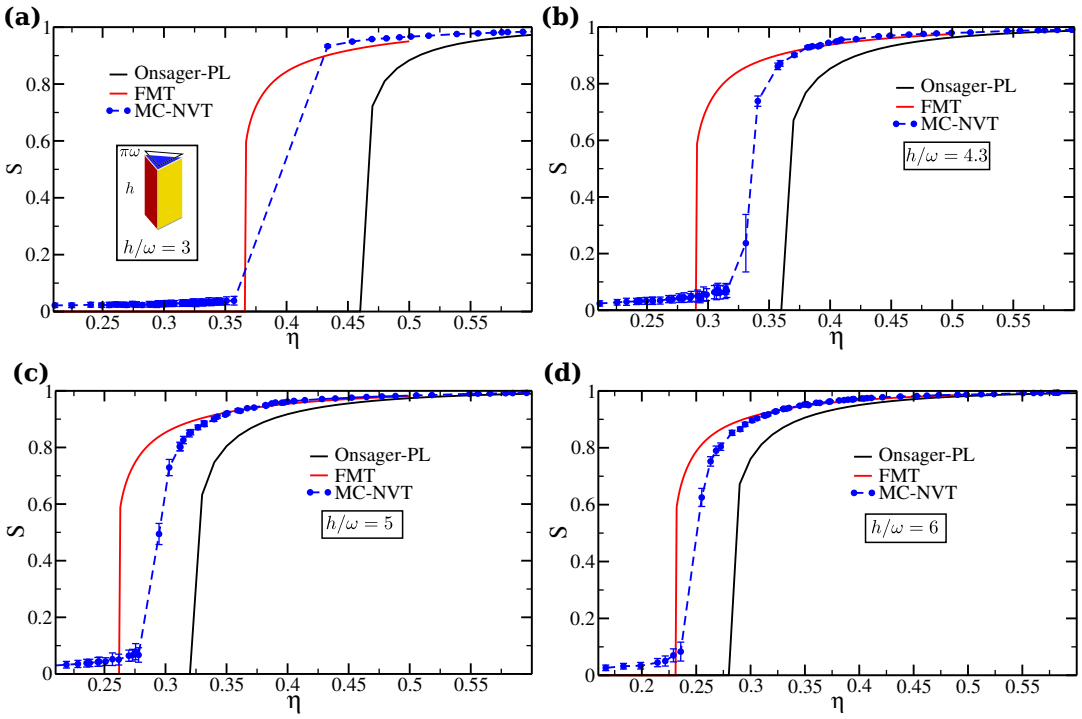

Figure 5.4: Nematic order parameter S versus packing fraction η as obtained by MC-NVT simulations, by Onsager theory with Parsons-Lee (PL) correction, and by FMT, for TPs with **(a)** $h/\omega = 3$, **(b)** $h/\omega = 4.3$, **(c)** $h/\omega = 5$, and **(d)** $h/\omega = 6$.

In Fig. 5.5 we plot the equation of state of TPs with $h/\omega = 3$ and $h/\omega = 6$ obtained by computer simulations with that calculated by using two versions of FMT. We observe a very good agreement between the simulation results and the 0D-FMT predictions in the case of short particles, especially for the isotropic branch of the equation of state. On the other hand, the TR-FMT seems to capture better the equation of state of longer particles. This is in line with the expectations and the assumptions based on the different versions of the FMT. Finally, we superimpose the simulation results in Fig. 5.6 together with the phase diagram obtained by the FMT in the aspect ratio h/ω - packing fraction η representation. For the simulation results, we estimate the phase boundaries based on the order parameters and by considering the upper and lower packing fraction at which a

given phase is observed. We estimate the degree of uncertainty in the identification of the phase boundaries, and plot the coexisting densities in η with the estimated error bar of 0.01 in Fig. 5.6. We confirm once more that the overall qualitative liquid-crystal behaviour of TPs is well captured by FMT, that also predicts a stable nematic phase for TPs with $h/\omega > 4.0$. No biaxial order was observed in simulations or predicted by FMT, neither for the nematic nor the smectic phase. As expected, the liquid-crystal phase behaviour of hard TPs closely resembles that of hard spherocylinders (SCs) (cfr. Fig. 3.1). Despite the two particle models have different shapes we can try to compare their phase behaviour assuming that TPs with $h/\omega = h^*$ behave similar to SCs with $(L + D)/D = h^*$, with L the cylinder length and D the particle diameter (which coincides with the diameter of the two hemispherical caps). If this analogy holds, we observe that a nematic phase is stabilized for TPs with $h^* \gtrsim 4$ and for SCs with $h^* > 4.7$. Furthermore, in this range of h^* the smectic phase can be stabilized at lower packing fraction η in the case of TPs ($\eta \lesssim 0.4$) than for SCs ($\eta \gtrsim 0.45$). We thus conclude that the flat facets of TPs promote order at lower aspect ratios and lower packing fraction with respect to the rounded shape of SCs.

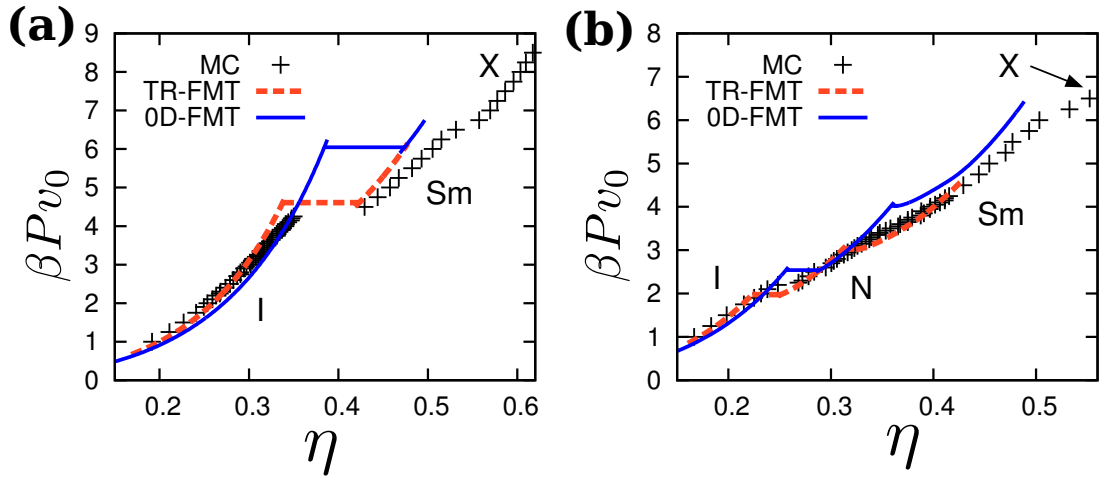

Figure 5.5: Equation of state (reduced pressure $\beta P v_0$, with v_0 the particle volume, versus packing fraction η) for TPs with **(a)** $h/\omega = 3$ and **(b)** $h/\omega = 6$ obtained by MC simulations and by two versions of FMT.

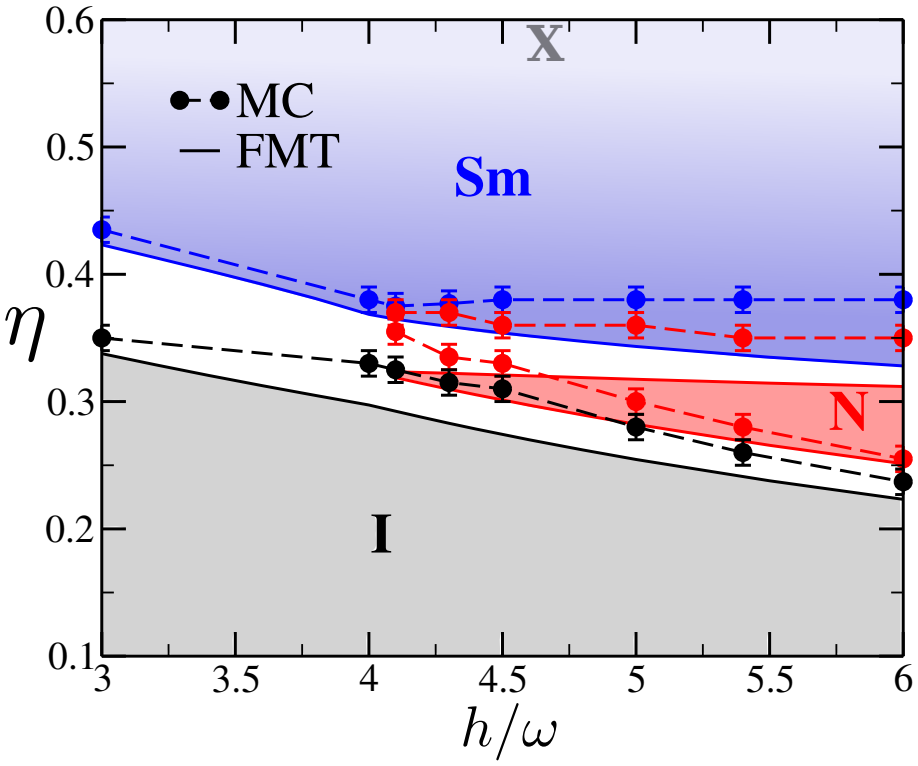

Figure 5.6: Phase diagram obtained by FMT (solid lines) compared with simulation results (symbols) in the aspect ratio h/ω - packing fraction η representation. Isotropic (I) stability region is colored grey, nematic (N) red, smectic (Sm) blue, and coexistence regions white. The boundaries for the crystal phase (X) are not calculated explicitly.

5.4 Biaxial order in nematic phases of isosceles triangular prisms

In this section, by changing the base angle γ in the TP particle model, we study if TPs can stabilize a biaxial nematic phase and if their liquid-crystal behaviour can be rationalized in terms of the shape parameter ν defined in Eq. 5.1. We consider TPs with a fixed $h/\omega = 5$ and by varying the base angle γ we change the shape parameter ν. Notice that a biaxial nematic phase can be predicted when $\nu = 0$, a condition that is obtained for two values of γ, namely $\gamma^* \simeq 0.527458 < \pi/3$ and $\gamma^{**} \simeq 1.43462 > \pi/3$.

In Figs. 5.7 and 5.8, we report the equation of state and the order parameters obtained by MC-NPT simulations of 2400 TPs with $\gamma = 0.5$ ($\nu \simeq -0.258$) starting from a dilute configuration. We first study the orientational order developed in the system by evaluating the eigenvalues $\lambda_a^{+,0,-}$ of the nematic order tensors $\mathcal{Q}^{\hat{\mathbf{a}}}$, with $\hat{\mathbf{a}} = \hat{\mathbf{u}}, \hat{\mathbf{v}}, \hat{\mathbf{w}}$, as defined in Eq. 5.2, which are shown in Fig. 5.7(a) as a function of the packing fraction η. We observe that at low η in the isotropic phase $\lambda_{a,b,c}^{+} \simeq \lambda_{a,b,c}^{0} \simeq \lambda_{a,b,c}^{-} \simeq 0$ for all the three axes. Upon increasing η, we observe that all the three maximum eigenvalues $\lambda_{a,b,c}^{+}$ display a jump, that is larger in the case of the eigenvalue associated to the short axis $\hat{\mathbf{w}}$. This is a signature of the formation of a (uniaxial) nematic phase, that we denote with N_-, in which the short axis features long-range orientational order. A representative snapshot of the N_- phase is shown in Fig. 5.7(b)-(c) in which the particles are either colored according to the orientation of the particle long axes $\hat{\mathbf{u}}$ or the particle short axes $\hat{\mathbf{w}}$. It is evident that the particle short axes $\hat{\mathbf{w}}$ are aligned along a common direction (panel (c)) whereas the particle long axes $\hat{\mathbf{u}}$ are not. The N_- phase is specular to the nematic phase observed for the equilateral TPs (cfr. Fig. 5.2(b)), that we now denote with N_+. In general for a uniaxial nematic phase (of biaxial particles), it holds that $\lambda_a^+ > \lambda_a^0 \simeq \lambda_a^-$ whereas $\lambda_{b,c}^+ \simeq \lambda_{b,c}^0 > \lambda_{b,c}^-$. Based on the largest eigenvalues, we distinguish between prolate (or calamitic) N_+ and oblate (or discotic) N_- nematic phase. Upon further increasing η, we observe that $\lambda_{u,v,w}^+ > \lambda_{u,v,w}^0 \simeq \lambda_{u,v,w}^-$ for all the three particle axes, suggesting the formation of a biaxial nematic phase N_b. Furthermore, we also observe a cross-over between λ_u^+ and λ_w^+. To better characterize the N_b phase we use the biaxial order parameter $\mathcal{B}$ defined in Eq. 5.3. We show $\mathcal{B}$ together with the nematic order parameters $S^{\hat{\mathbf{u}}}$ and $S^{\hat{\mathbf{w}}}$, and the smectic order parameter τ, as a function of the reduced pressure $\beta P \omega^3$, in Fig. 5.8. We observe that $\mathcal{B}$ exhibits a clear jump at $\beta P \omega^3 \simeq 1.5$ towards significantly large values and therefore confirms the formation of a N_b phase. We can further distinguish between a N_{b-} and a N_{b+} phase, that are both nematic phases with the same macroscopic biaxial symmetry but with the short or the long axis featuring a larger degree of orientational order. These phases have been already identified in simulations of hard spheroplatelets [195, 196]. Finally, we observe that at larger pressures the smectic order parameter τ displays a jump indicating the formation of a (prolate) smectic phase (Sm).

By performing extensive computer simulations in the NPT-ensemble of TPs with different base angle γ, we are able to roughly map out the liquid-crystal behaviour of TPs with $h/\omega = 5$ using the order parameter analysis as described above. We present our results in Fig. 5.9. Since a "very sluggish behaviour" [194] is observed when $\nu \sim 0$, con-

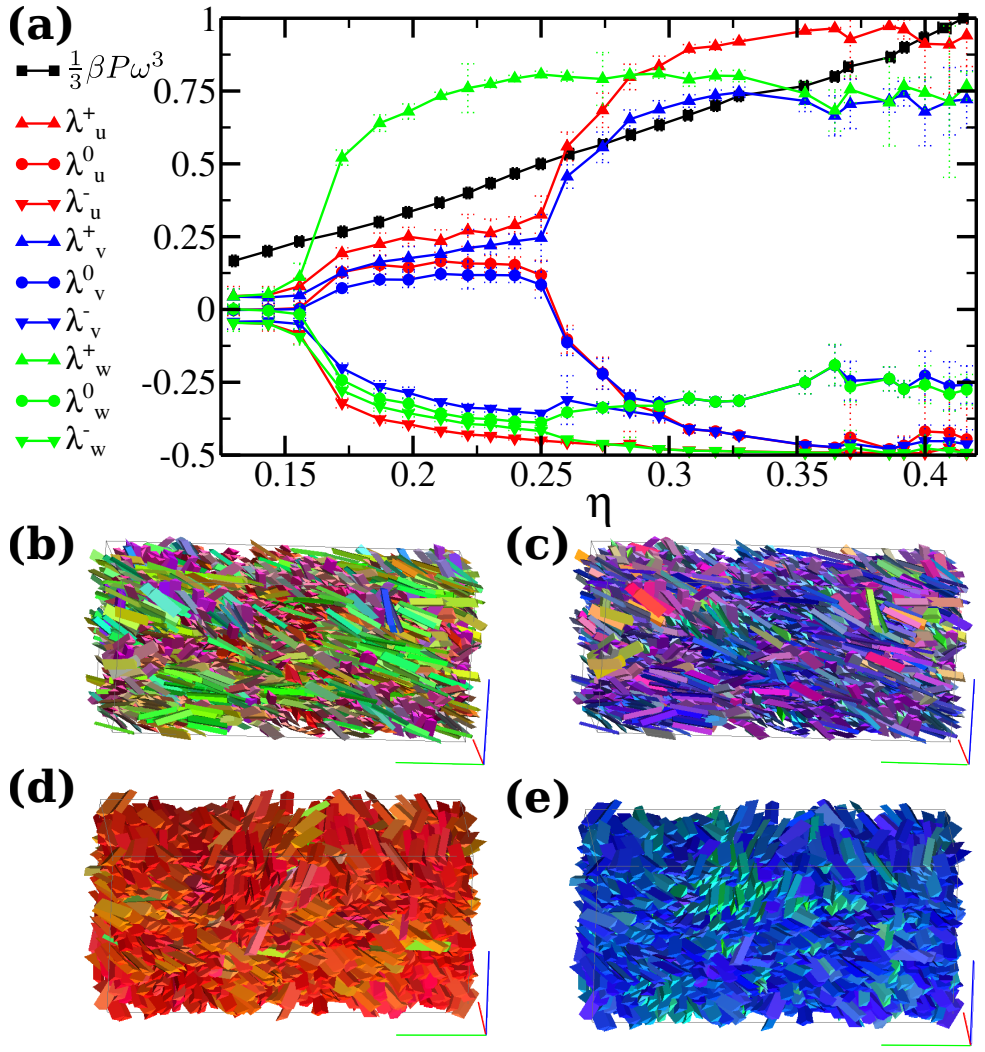

Figure 5.7: **(a)** Reduced pressure $\beta P\omega^3$ and eigenvalues $\lambda^{+,0,-}_{u,v,w}$ of the nematic order tensors $\mathcal{Q}^{\hat{\mathbf{u}}}$, $\mathcal{Q}^{\hat{\mathbf{v}}}$, $\mathcal{Q}^{\hat{\mathbf{w}}}$ (see Eq. 5.2) associated to the orientation of the long $\hat{\mathbf{u}}$, medium $\hat{\mathbf{v}}$, and short $\hat{\mathbf{w}}$ axis of TPs with $h/\omega = 5$ and $\gamma = 0.5$ (yielding a shape parameter $\nu \simeq -0.258$) as a function of packing fraction η. Data are obtained by MC-NPT simulations compressing from an isotropic phase. **(b)-(c)** Representative snapshot of an oblate nematic phase (N_-) of TPs with $h/\omega = 5$ and $\gamma = 0.5$ at $\beta P\omega^3 = 1.4$. In (b) particles are colored according to the orientation of the long axis $\hat{\mathbf{u}}$ and in (c) according to the orientation of the short axis $\hat{\mathbf{w}}$. **(d)-(e)** Representative snapshot of a biaxial nematic phase (N_b) of TPs with $h/\omega = 5$ and $\gamma = 0.5$ at $\beta P\omega^3 = 2.1$. In (d) particles are colored according to $\hat{\mathbf{u}}$ and in (e) according to $\hat{\mathbf{w}}$.

clusions should be carefully drawn from this state diagram. Nevertheless, from Fig. 5.9(a), where we plot the state points in the base angle γ - packing fraction η representation, we observe that close to the two values of γ^* and γ^{**} for which $\nu = 0$, as denoted by the vertical dashed lines, the N_b phase can be formed. From Fig. 5.9(b), where we plot the state points in the shape parameter ν - packing fraction η representation for TPs with $\gamma < \pi/3$, we observe that the region for which N_b is observed is asymmetric with respect to $\nu = 0$, since it extends more towards negative ν. This is in agreement with previous

studies [185, 194]. Furthermore, TPs with a small but positive value of ν, for which a prolate order is expected, surprisingly form an oblate nematic phase. In Fig. 5.9(c), together with the just discussed state points for TPs with $\gamma < \pi/3$ (filled symbols), we also plot the state points for TPs with $\gamma > \pi/3$ (empty symbols) in the ν-η representation. We notice that for similar values of ν the phase behaviour is not the same for the two sets of TPs. In particular, we notice that for $\gamma < \pi/3$ the N_b phase can be stabilized over a larger region of ν than in the case of TPs with $\gamma > \pi/3$. This asymmetry in the phase behaviour arises from the triangular shape of the prisms. Finally, we want to remark that we consider TPs with fixed $h/\omega = 5$ and different base angles γ that correspond to particles with different long-to-short axis ratio, which is $|\mathbf{u}|/|\mathbf{w}|$ for TPs with $\gamma < \pi/3$ and $|\mathbf{u}|/|\mathbf{v}|$ for TPs with $\gamma > \pi/3$. In Fig. 5.9(d), we plot the same results in the long-to-short axis ratio - packing fraction η representation. We observe that in this representation it is evident that the I-N transition shifts towards lower η whereas the N-Sm transition is less sensitive to the particle length, as already shown for equilateral TPs in Fig. 5.6. However, by just knowing the long-to-short axis ratio of the particle, it is not possible to predict the symmetry of the N phase. We conclude that in order to rationalize the behaviour of TPs, the knowledge of two independent parameters based on the particle dimensions is needed, as expected for biaxial particles, in addition with the value of the base angle γ, that is a requirement that directly comes from the intrinsic asymmetry of the triangular base.

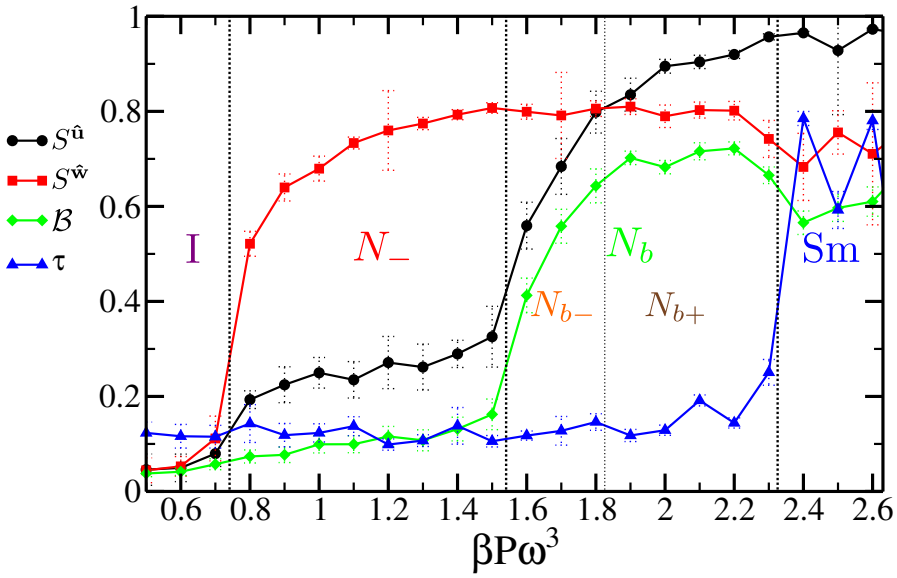

Figure 5.8: Nematic order parameters $S^{\hat{\mathbf{u}}}$ and $S^{\hat{\mathbf{w}}}$, biaxial order parameter $\mathcal{B}$ and smectic order parameter τ as a function of reduced pressure $\beta P\omega^3$ for TPs with $h/\omega = 5$ and $\gamma = 0.5$ ($\nu = -0.258$) obtained by MC-NPT simulations compressing from an isotropic phase. Dotted lines are guides-to-the-eye for the I-N_--N_b(N_{b-}-N_{b+})-Sm sequence.

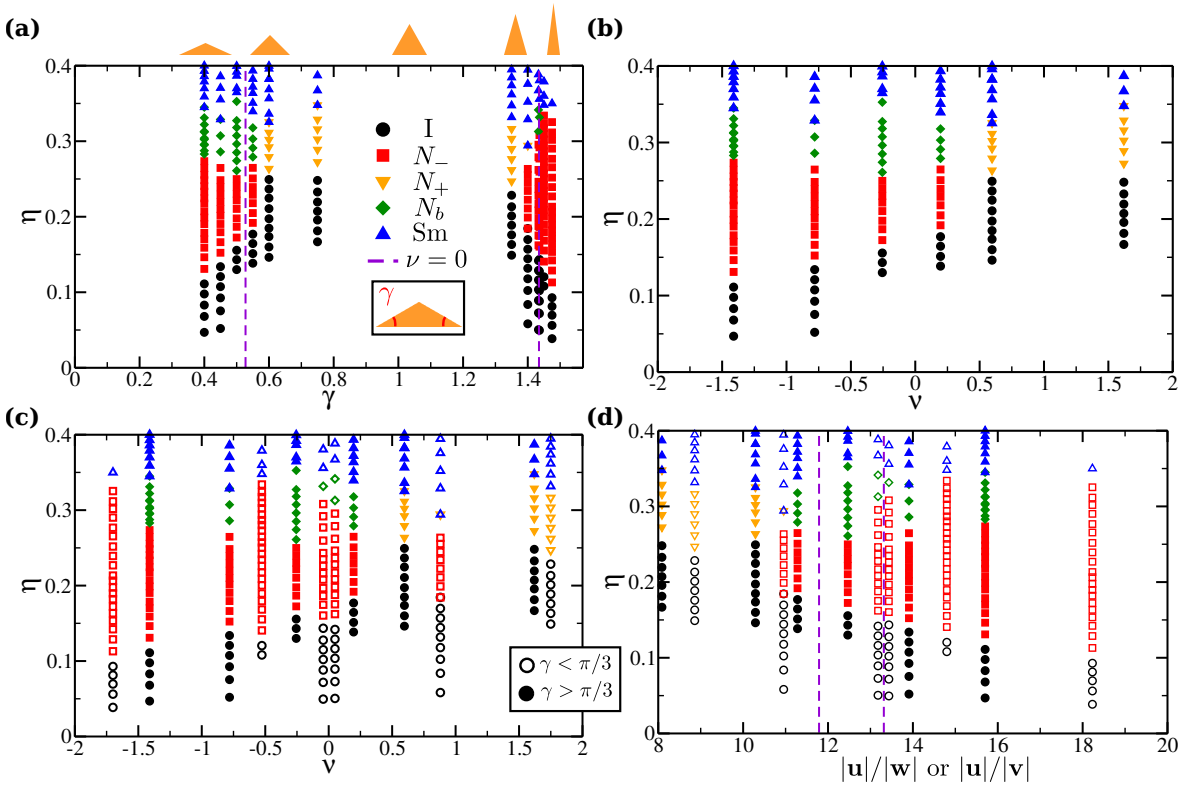

Figure 5.9: State diagram for TPs with $h/\omega = 5$. Each state point has been labelled according to the order parameter analysis described in the text. Legend of panel (a) is the same for each panel. **(a)** Base angle γ - packing fraction η representation. **(b)** Shape parameter ν - packing fraction η representation for TPs with $\gamma > \pi/3$. **(c)** Shape parameter ν - packing fraction η representation for all the TPs studied. **(d)** Long-short axis ratio ($|\mathbf{u}|/|\mathbf{w}|$ or $|\mathbf{u}|/|\mathbf{v}|$ depending on γ) - packing fraction η representation for all TPs studied. In (c) and (d) filled symbols indicate TPs with $\gamma < \pi/3$ and empty symbols TPs with $\gamma > \pi/3$.

5.5 Biaxial nematic phases of brick-like colloids

The study presented in the previous section can be repeated for cuboidal (brick-like) colloids (see Fig. 5.1(c)). This particle model was recently studied in Ref. [207] by computer simulations of particles with $|\mathbf{v}| = |\mathbf{w}|$, for which a biaxial nematic phase cannot be formed. The liquid-crystal behaviour of a similar board-like particle model, namely spheroplatelets, has been extensively studied by computer simulations in Refs. [195, 196]. Theoretical predictions expect the formation of a biaxial nematic phase when the particle shape parameter $\nu \simeq 0$ [62, 185]. One of the main results of the computer simulation study of Refs. [195, 196] was that biaxial nematic phases can be indeed obtained when the shape parameter $\nu \simeq 0$ but with the additional condition that the ratio between the long axis and the short axis should be at least 9 (compared to our model this reads $|\mathbf{u}|/|\mathbf{w}| \geq 9$). For shorter particles, the biaxial nematic phase is not observed and there is a direct transition between a uniaxial nematic phase and a smectic phase. Here, we highlight how the difference in shape between our cuboidal particles, that have sharp edges, sharp corners and flat faces, and the spheroplatelets, that have rounded edges, rounded corners and fewer flat faces, is reflected in the stabilization of a biaxial nematic phase N_b.

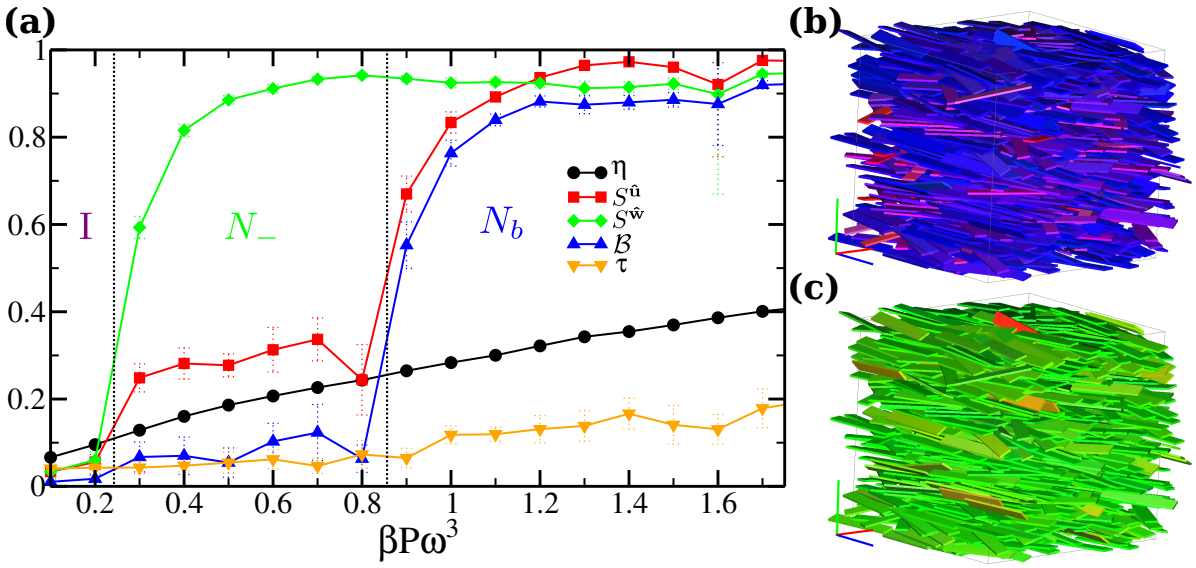

Figure 5.10: **(a)** Packing fraction η, nematic order parameters $S^{\hat{\mathbf{u}}}$ and $S^{\hat{\mathbf{w}}}$, biaxial order parameter $\mathcal{B}$ and smectic order parameter τ as a function of reduced pressure $\beta P\omega^3$ for hard brick-like colloids with $h/\omega = 8$ and $|\mathbf{v}| = 1.34475$ ($\nu \simeq 0$) obtained by MC-NPT simulations of $N = 1200$ particles compressing from a dilute configuration. Dotted lines are guides to the eye for the I-N_--N_b-Sm sequence. **(b)-(c)** Representative snapshot of a biaxial nematic phase (N_b) obtained at $\beta P\omega^3 = 1.0$ with particles colored according to the orientation of the long axis $\hat{\mathbf{u}}$ in (b) and according to the orientation of the short axis $\hat{\mathbf{w}}$ in (c).

We first study extremely long particles with an aspect ratio $h/\omega = 8$ and $|\mathbf{v}| = 1.34475$ such that $\nu \simeq 0$ (notice that this corresponds to $|\mathbf{u}|/|\mathbf{w}| \simeq 35$). We show in Fig. 5.10(a) the packing fraction η, the nematic order parameters $S^{\hat{\mathbf{u}}}$ and $S^{\hat{\mathbf{w}}}$, the biaxial order parameter $\mathcal{B}$ and the smectic order parameter τ, as a function of the reduced pressure $\beta P\omega^3$, as obtained by MC-NPT simulations of $N = 1200$ particles starting from a dilute configuration. We

clearly observe a I-N_--N_b phase sequence, and the N_b is also evident by visual inspection of typical configurations, as shown in Fig. 5.10(b)-(c). However, by reducing the aspect ratio to $h/\omega = 6$ we do not observe the N_b phase, as reported in the state diagram of Fig. 5.11(a), with the exception of a single state point for particles with $h/\omega = 6$ and $|\mathbf{v}| = 1.29$ ($\nu \simeq 0.057$ and $|\mathbf{u}|/|\mathbf{w}| \simeq 21$). However we are not able to clearly identify this state point as N_b since the value of the biaxial order parameter $\mathcal{B}$ is very small and prone to large fluctuations. A simulation run expanding from a smectic phase shows a strong hysterisis around that pressure and indicates that the identification of the N_b is particularly difficult when its stability region is very narrow, since the transition between an oblate N_- to a prolate Sm implies a re-arrangement of both particle axes. Analogously with the case of TPs, we observe an asymmetry with respect to $\nu = 0$ and it seems that the cross-over between particles forming N_- phases and particles forming N_+ phases occurs for a positive value of ν. Notice that in the regions close to the N_--N_+ transition, we observe that $\mathcal{B}$ assumes small and highly fluctuating values. All these observations need to be confirmed with additional studies, perhaps based also on the density functional theories described above. Upon further decreasing the particle aspect ratio to $h/\omega = 5$, for which the state diagram is reported in Fig. 5.11(b), the doubts on the absence of a N_b phase vanishes. Indeed, we do not observe any evidence of a N_b phase even in the case of brick-like colloids with $h/\omega = 5$ and $|\mathbf{v}| = 1.26$, yielding $\nu \simeq -0.086$ and $|\mathbf{u}|/|\mathbf{w}| \simeq 16$. For completeness, in Fig. 5.11(c)-(d) we report the state diagrams for brick-like colloids in the long-to-short axis ratio $|\mathbf{u}|/|\mathbf{w}|$ - packing fraction η representation. In summary, despite we are not able at this stage to pinpoint exactly when the N_b becomes unstable in systems of sharp brick-like colloids, we can conclude that N_b does not form when $h/\omega \leq 5$, or alternatively when $|\mathbf{u}|/|\mathbf{w}| \lesssim 16$.

5.6 Conclusions

In conclusion, we have found a biaxial nematic phases for TPs with $h/\omega = 5$ and $\gamma = 0.5$, corresponding to $\nu \simeq -0.258$ and $|\mathbf{u}|/|\mathbf{w}| \simeq 12.5$, but not for brick-like colloids with $|\mathbf{u}|/|\mathbf{w}| \lesssim 16$. Furthermore, Refs. [195, 196] reported N_b phases for spheroplatelets with $|\mathbf{u}|/|\mathbf{w}| \geq 9$. It is therefore evident that the roundness of the particle shape and the number of flat facets play an important role in the stabilization of the N_b phase. Furthermore, we have shown that by a fine tuning of the particle shape it is possible to obtain uniaxial and biaxial nematic phases, as well as smectic phases, and to change the phase sequence between them. This is consistent with previous studies and indicates that the liquid-crystal phase behaviour can be generally predicted on the basis of the ratios between the main particle axes. However, we have also highlighted that the exact shape matters. For example, to rationalize the liquid-crystal behaviour of TPs, the knowledge of ν, the long-to-short axis ratio and the angle γ are needed. The former two parameters are enough for cuboidal particles. Future studies could use these particle models and rely on the state diagrams provided here to thoroughly investigate how the different nematic phases and the transitions between them are influenced by (other) polyhedral particles. Finally, these particle-based simulations can be used to further refine the theoretical

descriptions of the phase behaviour of complex-shaped particles, as we showed in the first part of this chapter where we compared our simulation results against FMT predictions.

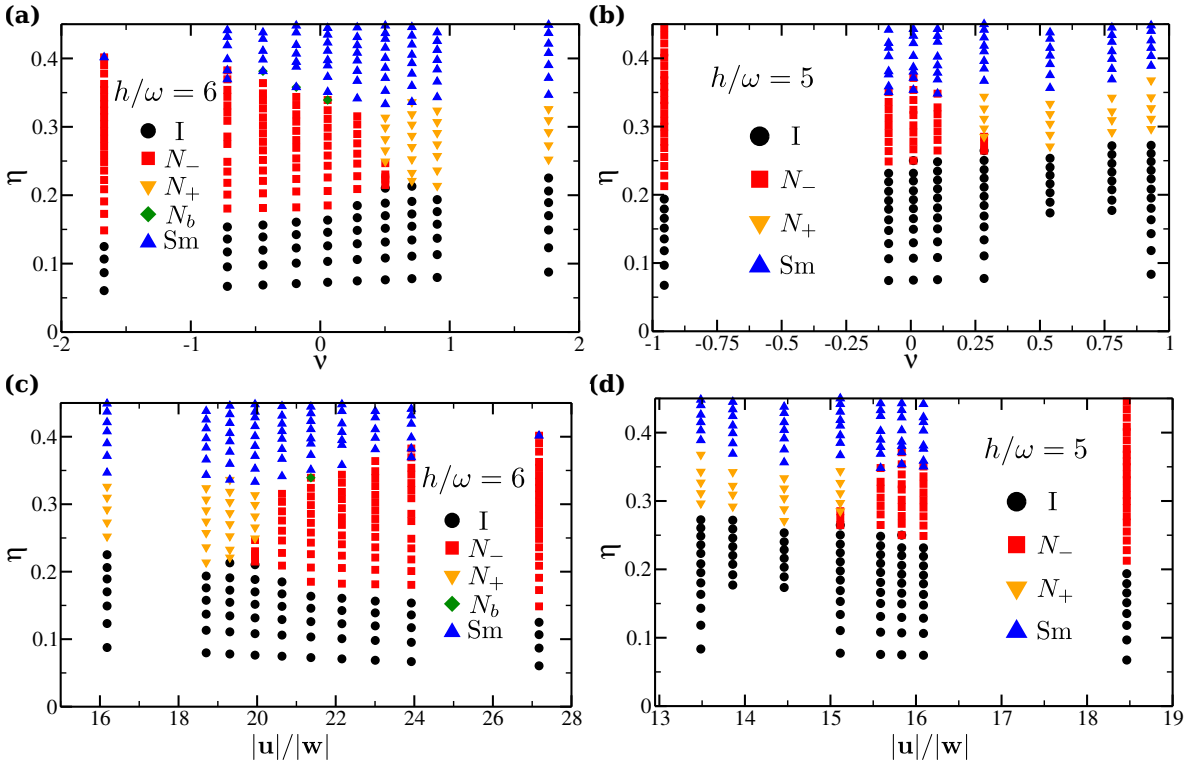

Figure 5.11: State diagram for hard brick-like colloids with **(a, c)** $h/\omega = 6$ and **(b, d)** $h/\omega = 5$. **(a, b)** Shape parameter ν - packing fraction η representation. **(c, d)** Long-to-short axis ratio $|\mathbf{u}|/|\mathbf{w}|$ - packing fraction η representation. Each state point has been labelled according to the order parameter analysis described in the text.

Acknowledgments

Matthieu Marechal (Institut für Theoretische Physik, Universität Erlangen-Nürnberg, Germany) is acknowledged for his work on the equilateral triangular prisms by means of the fundamental measure theory (FMT) presented in this chapter.

6

Cholesterics of colloidal helices: predicting the macroscopic pitch from the particle shape and thermodynamic state

Building a general theoretical framework to describe the microscopic origin of macroscopic chirality in (colloidal) liquid crystals is a long-standing challenge. Here, we combine classical density functional theory with Monte Carlo calculations of virial-type coefficients, to obtain the equilibrium cholesteric pitch as a function of thermodynamic state and microscopic details. Applying the theory to hard helices, we observe both right- and left-handed cholesteric phases that depend on a subtle combination of particle geometry and system density. In particular, we find that entropy alone can even lead to a (double) inversion in the cholesteric sense of twist upon changing the packing fraction. We show how the competition between single-particle properties (shape) and thermodynamics (local alignment) dictates the macroscopic chiral behaviour. Moreover, by expanding our free-energy functional we are able to assess, quantitatively, Straley's theory of weak chirality, used in several earlier studies. Furthermore, by extending our theory to different lyotropic and thermotropic liquid-crystal models, we analyse the effect of an additional soft interaction on the chiral behaviour of the helices. Our results provide new insights on the role of entropy in the microscopic origin of this state of matter.

6.1 Introduction

"What is the origin of chirality in the cholesteric phase of virus suspensions?" [208]. With such an intriguing question, which is to date unanswered, Eric Grelet and Seth Fraden titled their paper about a decade ago. The link between micro- and macro-chirality remains elusive not only in virus suspensions but in many systems exhibiting liquid crystal phases [35]. These thermodynamic states in between the disordered liquid phase and the (fully) ordered crystal phase, consist of anisotropic particles or molecules featuring long-range orientational order but no (or only partial) positional order. In this study, we focus on nematic phases, where the particles are preferentially aligned along a common direction, identified by a unit vector called nematic director $\hat{\mathbf{n}}$, while keeping their centers of mass homogeneously distributed in space. Whereas the nematic director of an ordinary (achiral and uniaxial) nematic phase is homogeneously distributed throughout the system (Fig. 6.1**(a)** and see Chap. 3), the cholesteric phase, often called chiral nematic, displays an helical arrangement of the director field (Fig. 6.1**(b)**). The typical length scale associated to this macroscopic chirality, that determines the periodicity of such an imaginary helix, is named cholesteric pitch P. Depending on the twist sense of the director field around the chiral director $\hat{\chi}$, the liquid crystal phase is denoted right- or left-handed.

Cholesterics are readily observed in both thermotropic molecular compounds and lyotropic colloidal suspensions [35]. The former class of liquid crystals, in which phase transitions are mainly governed by temperature, has found wide technological application in the opto-electronic industry due to the unique combination of rheological, electrical and optical properties conferred by the chiral structure [209–211]. Derivatives of cholesterol [212–214], the first liquid-crystal-forming systems experimentally observed [215, 216], belong to this class.

Several lyotropic systems, where the phase behaviour is density-driven [217], such as suspensions of colloidal particles or polymers, exhibit chiral order as well. Examples range from biological materials, such as DNA [43, 218, 219], filamentous viruses [42, 208, 220–223], cellulose and derivatives [224, 225], chiral micelles [226], to synthetic polymers, such as polyisocyanates [227, 228] and polysilanes [229]. Suspensions of filamentous viruses are among the most studied [42] colloidal systems in which chirality plays a major role in self-assembly processes at different levels, leading to fascinating phenomena [230, 231]. At the microscopic level, charged (protein) subunits self-assemble into supramolecular helical structures. However, whereas suspensions of fd virus particles exhibit chirality also at macroscopic scale, thereby stabilizing a cholesteric phase [42, 208, 220, 221], other virus particles, such as tobacco mosaic virus [232] and Pf1 virus [220] particles, with similar helical charge distributions, form only a uniaxial nematic phase, challenging the idea that molecular chirality is a guarantee for macroscopic chirality. Even though in the latter case the cholesteric pitch is expected to be too large to be directly observed in experiments, very subtle differences at the single-particle level can drastically change the macroscopic self-organization [221, 222]. Surprisingly, fd virus particles that are sterically stabilized with a polymer coat so thick that the electrostatic chiral interactions are proved to be fully masked, still exhibit a cholesteric phase [208]. These observations, together with a recent study aimed to map the fd-virus phase diagram onto that of hard rods [182], suggest that entropy alone could govern the phase behaviour of (some) virus suspensions,

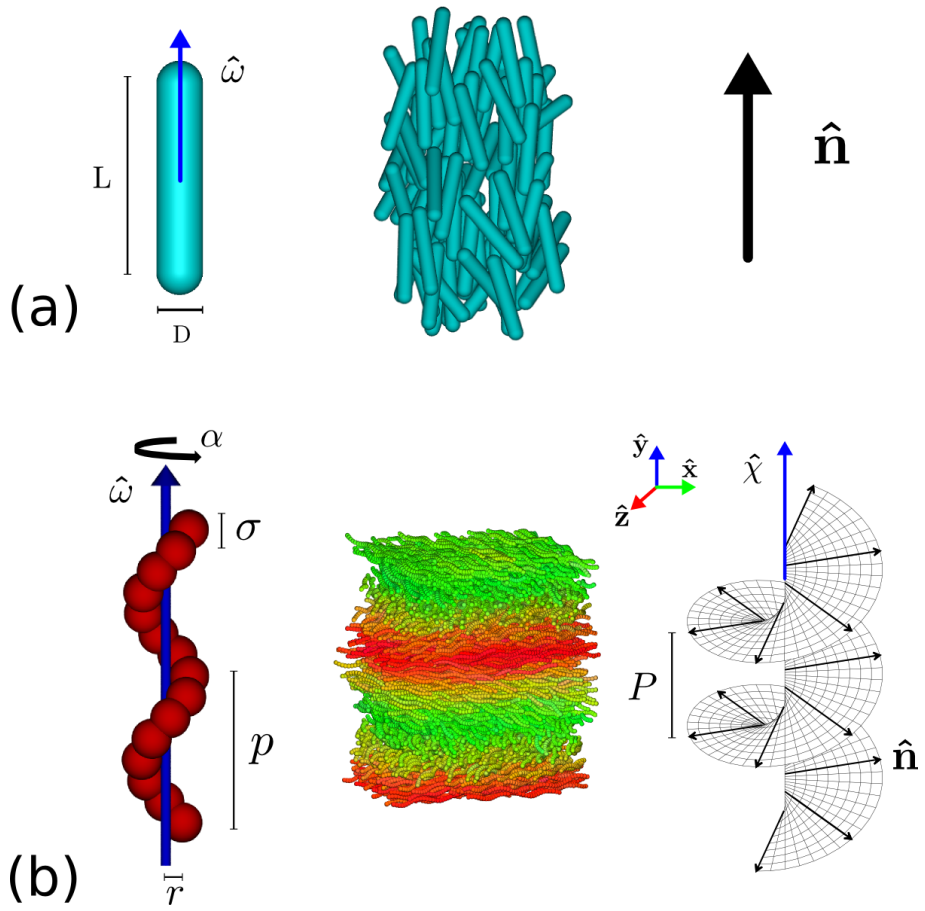

Figure 6.1: Microscopic particle model (left), macroscopic liquid crystalline phase (cartoon in the middle), and schematic of the nematic director field (right). **(a)** Achiral colloids are often modeled as spherocylinders of length L and diameter D, whose orientation is described by a unit vector $\hat{\omega}$. These rod-like particles give rise to a uniaxial and achiral nematic phase with a uniform nematic director $\hat{\mathbf{n}}$. Notice that both for the particle orientation and for the nematic director the up-down symmetry holds: $\hat{\omega} = -\hat{\omega}$ and $\hat{\mathbf{n}} = -\hat{\mathbf{n}}$. **(b)** The hard helix model consists of N_s hard spheres of diameter σ, rigidly fused together to form an helix with molecular pitch p and radius r. Particle orientation is described by a unit vector $\hat{\omega}$ and an internal angle α. Colloidal helices self-assemble into a cholesteric configuration. The nematic director field $\hat{\mathbf{n}}$ exhibits an helical arrangement along the chiral director $\hat{\chi}$, with periodicity given by the cholesteric pitch P.

including the stabilization of a cholesteric phase. However, whereas the phase diagram of the coated fd virus and the nematic order parameter were independent of ionic strength, the cholesteric pitch varied surprisingly strongly with ionic strength [208].

The underlying competition between steric and electrostatic interactions appears even more evident in the case of another charged filamentous virus suspension (M13), where a left-handed cholesteric phase was obtained by right-handed particles [223]. The observed sense of the macroscopic twist could not be correctly predicted by modeling the particles as hard bodies without taking into account a soft electrostatic contribution [223].

Cholesterics with opposite handedness with respect to that of the constituent particles were also observed in solutions of ultrashort DNA [219, 233]. Surprisingly, a peculiar type of DNA oligomers showed an inversion in the helical sense of the cholesteric phase upon changing system concentration, suggesting that packing arguments could explain in which sense these systems should twist. However, the cholesteric pitch seemed to be influenced by other factors as well, such as particle length and oligomer sequences, but not, for example, by particle flexibility. As a result, no simple rules could exhaustively explain the chiral behaviour [219]. Inversion in the cholesteric handedness has been reported in other studies as well, often concerning temperature-driven systems [213, 234]. The list of systems indicating that the connection between micro- and macro-chirality is far from trivial, is quite long [235], and difficult to rationalize due to the different interactions in place.

On the other hand, a recent study seemed to have succeeded in identifying a chiral system ruled by entropic effects only [236]. Indeed, interactions in suspensions of helical flagella extracted from bacteria can be finely tuned by modifying solvent properties. In particular conditions, these colloidal particles can be ultimately considered as hard helices, whose exact shape can be also precisely regulated [236, 237]. As expected, when helical flagella self-assemble, the chirality is transmitted to the liquid crystalline state. However, the formed chiral nematic phase has a different symmetry from the cholesteric phase and was identified as a conical phase [236, 238, 239]. Why such a phase should be thermodynamically more stable than the cholesteric is another question thickening the mystery of colloidal chirality. An even more complicated mechanism of chirality propagation from molecular to macroscopic scale has been observed in thermotropic bent-core liquid crystals [240]. In peculiar cases the intricate coupling between twisting and bending deformations stabilize another chiral nematic phase, named twist-bend nematics [241, 242]. In this instance the local nematic director $\hat{\mathbf{n}}$ is tilted with respect to the chiral director $\hat{\chi}$, resembling therefore the conical order.

In view of such a complex and sometimes controversial experimental scenario, it is not surprising that a unifying microscopic theory is still lacking. The attempt of incorporating all the interactions present in experiments in a suitable model for chiral particles, is often beyond the limits of current theoretical tools and computational resources. For this reason, despite very few exceptions [233], focus was separately given to the chiral behaviour arising from either purely hard-core repulsions [63, 243–245] or from soft electrostatic potentials only [245–248]. Even with this simplification, the complexity of a chiral interparticle potential is such that most of these studies resorted to coarse-grained potentials [245–250], in which the microscopic chiral features are masked into a single pseudo-scalar parameter [251]. By contrast, we decided to build our study in small steps [252], first improving our understanding of entropy-driven systems, and only at a later stage introducing further elements into the particle model.

Beside the particle model, an appropriate theoretical approach is crucial. Computer simulation methods are limited by the large number of particles required to accommodate a full rotation of the nematic director. Despite ad-hoc techniques that have been developed to try to overcome such an issue [253, 254], only few simulation studies, mainly using coarse-grained potentials tailored to decrease the cholesteric pitch lengths, have been dedicated to the investigation of cholesteric phases [246, 249, 250, 255–258]. Therefore,

to shed new light on the microscopic origin of the macroscopic chirality, we appeal to a suitable microscopic theory. A successful example of a microscopic theory, often used in soft matter, is due to Onsager, who was the first in 1949 to explain the role of entropy on the liquid-crystalline behaviour of anisotropic particles [30]. However, it took until 1976 to describe the cholesteric ordering, when Straley proposed his approach, based on Frank's theory of elastic deformations [63]. The seminal work of Straley has been extensively used in modern studies to predict the cholesteric pitch of several colloidal systems [233, 245, 247, 248, 259–262]. Only few exceptions presented alternative methods, limited, however, by severe analytical assumptions [243, 244]. Despite the undoubted relevance of Straley's pioneering work, his approach is based on two main assumptions. First, the theory is rigorously valid only in the limit of weak macroscopic chirality, a limit that is anyway usually not far from the experimental conditions. Second, the theory cannot be solved fully self-consistently, in the sense that the orientation distribution of the cholesteric phase equals that of the underlying uniaxial achiral nematic phase, thereby neglecting the differences in the local order between the latter and a cholesteric phase. Of course this second assumption is consistent with the perturbative treatment of chirality in Straley's theory. Additionally, Straley's approach has been used only for the description of cholesterics, and only very recently density functional theories have been developed to consider chiral nematics with different symmetries [36, 37].

We have recently introduced a novel approach to address these issues [252]. Our aim is twofold: by refreshing the theoretical description of chiral nematics within the density functional framework, we propose an additional tool to advance our understanding of this complex state of matter. At the same time, by applying our theory to hard helices, we provide new insights into the role of entropy in colloidal cholesterics. Indeed, such an apparently simple model exhibits a fairly rich and complex chiral behaviour [252, 260], that goes beyond simplified scenarios suggested in earlier studies [63, 263, 264]. Moreover, despite a thorough simulation study aimed to map out the entire phase diagram [37, 265, 266], leading to a newly observed chiral nematic (screw-like) phase, a question mark is still pending on the cholesteric phase and a definitive evidence from simulations is yet to come.

This chapter is organized as follows: we dedicate Sec. 6.2 to readers interested in technical details, where we describe extensively the theoretical framework used and its numerical implementation. In Sec. 6.3, we study the cholesteric order in systems of hard helices. In Sec. 6.4, we analyse the effect of an additional soft, short-range interaction on the macroscopic chiral behaviour, thereby providing an explicit example of how the theory can be applied to different particle models. We briefly analyse the extension of our theory to mixtures in Sec. 6.5. We conclude the chapter with some final remarks in Sec. 6.6, and present the first evidence from simulation for a cholesteric of hard helices in Sec. 6.7.

6.2 Theory

6.2.1 Density functional theory for chiral nematics

It is known that a chiral particle cannot be uniaxial [263, 264]. Biaxiality introduces an additional degree of freedom: the orientation of a generic rigid body is described by three scalar parameters, $(\theta, \phi, \alpha) \in [0, \pi) \times [0, 2\pi) \times [0, 2\pi)$, known as Euler angles, or alternatively by a 3×3 rotation matrix $\mathcal{R}$. The rotation matrix $\mathcal{R}$ can be parametrized in terms of the unit vector $\hat{\omega}$, representing the orientation of the main long axis, and the internal azimuthal angle α (cf. Fig. 6.1**(b)**). The single-particle density has to be modified for the extra degree of freedom and is now subjected to the following normalization condition

$$\int_V d\mathbf{r} \oint d\mathcal{R}\, \rho(\mathbf{r}, \mathcal{R}) = N, \tag{6.1}$$

with $d\mathcal{R} = d\alpha\, d\phi\, d\cos\theta$. Since the achiral nematic phase is a homogeneous phase with orientational order only, the corresponding single-particle density depends on the orientation variable only: $\rho(\mathbf{r}, \mathcal{R}) = n\psi(\mathcal{R})$, with $\int d\mathcal{R}\psi(\mathcal{R}) = 1$ and n the number density. In the most general case $\psi(\mathcal{R})$ describes a biaxial phase.

Let us now consider a chiral nematic phase of pitch P with the chiral director $\hat{\chi}$ aligned along the y axis (cf. Fig 6.1**(b)**). The cholesteric pitch P is related to the chiral wave vector q through $P = 2\pi/q$. The chiral structure implies that the orientation distribution function (ODF) at arbitrary y can be deduced from that at $y = 0$ by rotating by an angle $2\pi y/P = qy$ around the y-axis. Such a condition reads

$$\rho(\mathbf{r}, \mathcal{R}) = n\psi(\, \mathcal{T}_q(\mathbf{r})\, \mathcal{R}\,), \tag{6.2}$$

where

$$\mathcal{T}_q(\mathbf{r}) \equiv \mathcal{R}_{\hat{\chi}}(q\, \hat{\chi} \cdot \mathbf{r}) = \mathcal{R}_{\hat{\mathbf{y}}}(qy) \tag{6.3}$$

is a rotation around the chiral director $\hat{\chi}$ (that coincides with the y-axis) by an angle qy. From Eq. (6.2) we can immediately verify that chiral nematic phases are characterized by the inequality $\rho(\mathbf{r}, \mathcal{R}) \neq \rho(-\mathbf{r}, \mathcal{R})$. By explicitly imposing the parity symmetry $\rho(\mathbf{r}, \mathcal{R}) = \rho(-\mathbf{r}, -\mathcal{R})$, based on the assumption that the physics does not change by passing from a right-handed to a left-handed reference frame and vice versa, we can rewrite the previous as $\rho(\mathbf{r}, \mathcal{R}) \neq \rho(\mathbf{r}, -\mathcal{R})$. A necessary (not sufficient) condition for a system of particles to manifest chiral nematic ordering is that an inversion transformation, i.e., $\mathcal{R} \to -\mathcal{R}$, *does not* transform a particle into itself, as previously noticed [63, 263, 264]. It is also interesting to ask what kind of two-body interaction $U(\mathbf{r}, \mathcal{R}, \mathcal{R}')$ generates chiral nematic ordering. Again, a necessary condition for chirality is $U(-\mathbf{r}, \mathcal{R}, \mathcal{R}') \neq U(\mathbf{r}, \mathcal{R}, \mathcal{R}')$ or, alternatively, $U(\mathbf{r}, -\mathcal{R}, -\mathcal{R}') \neq U(\mathbf{r}, \mathcal{R}, \mathcal{R}')$.

Eq. (6.2) describes the functional dependence of the single-particle density of a chiral nematic phase. The corresponding density functional theory, already briefly outlined in our previous work [252], is based on three steps that will be described in detail here. First of all, we will insert the functional dependence of the chiral phase $\rho(\mathbf{r}, \mathcal{R}) = \rho(\mathcal{T}_q(\mathbf{r})\mathcal{R})$ into $\mathcal{F}[\rho(\mathbf{r}, \mathcal{R})]$. Secondly, we will rewrite $\mathcal{F}[\rho(\mathcal{T}_q(\mathbf{r})\mathcal{R})]$ in such a way that the dependence on q and $\rho(\mathcal{R})$ are disentangled. In other words, we will construct a functional $\mathcal{F}_q$ such that $\mathcal{F}_q[\rho(\mathcal{R})] = \mathcal{F}[\rho(\mathcal{T}_q(\mathbf{r})\mathcal{R})]$. Finally, we will minimize the density functional with

respect to $\psi(\mathcal{R})$ and q. Let $\rho^*(\mathcal{R})$ be the solution at given q and given number density n, such that $F_q(n) = \mathcal{F}_q[\rho^*(\mathcal{R})]$. The equilibrium value of q (and hence the equilibrium cholesteric pitch P) at number density n corresponds to the minimum in q of the free energy $F_q(n)$.

As a lemma, let us first see that the ideal part of the free-energy functional

$$\beta\mathcal{F}_{id}[\rho(\mathcal{T}_q(\mathbf{r})\mathcal{R})] = \int_V d\mathbf{r} \oint d\mathcal{R}\, \rho(\mathcal{T}_q(\mathbf{r})\mathcal{R}) \left[\log \mathcal{V}\rho(\mathcal{T}_q(\mathbf{r})\mathcal{R})) - 1\right] \tag{6.4}$$

does not contribute to the chiral ordering. By changing the orientation integration variable from $\mathcal{R}$ to $\mathcal{Q} = \mathcal{T}_q(\mathbf{r})\mathcal{R}$ (with unit Jacobian), we obtain

$$\beta\mathcal{F}_{id}[\rho(\mathcal{T}_q(\mathbf{r})\mathcal{R})] = \int_V d\mathbf{r} \oint d\mathcal{Q}\, \rho(\mathcal{Q}) \left[\log \mathcal{V}\rho(\mathcal{Q}) - 1\right] = V \oint d\mathcal{R}\, \rho(\mathcal{R}) \left[\log \mathcal{V}\rho(\mathcal{R}) - 1\right]. \tag{6.5}$$

We can therefore conclude that the ideal term is independent from q.

We now consider the excess free-energy term $\mathcal{F}_{ex}[\rho]$ and we describe an approach to minimize it exactly without recurring to the second-order q-expansion. The second-virial excess free-energy functional, with Parsons-Lee correction, for a chiral nematic phase reads

$$\beta\mathcal{F}_{ex}[\rho] = -\frac{G(\eta)}{2} \int_V d\mathbf{r}\, d\mathbf{r}' \oint d\mathcal{R}\, d\mathcal{R}' f(\mathbf{r}-\mathbf{r}', \mathcal{R}, \mathcal{R}')\, \rho(\mathcal{T}_q(\mathbf{r})\mathcal{R})\, \rho(\mathcal{T}_q(\mathbf{r}')\mathcal{R}'). \tag{6.6}$$

By transforming the particle position variables and performing a volume integration, we can rewrite the previous equation as

$$\frac{\beta\mathcal{F}_{ex}[\rho]}{V} = -\frac{G(\eta)}{2} \int_V d\mathbf{r} \oint d\mathcal{R}\, d\mathcal{R}' f(\mathbf{r}, \mathcal{R}, \mathcal{R}')\, \rho(\mathcal{T}_q(\mathbf{r})\mathcal{R})\, \rho(\mathcal{R}'). \tag{6.7}$$

To extract the q-dependence from the density distribution, we expand ρ in rotational invariants. For an *achiral* nematic phase the expansion is

$$\rho(\mathcal{R}) = \sum_{l=0}^{\infty} \sum_{m,n=-l}^{l} \rho^l_{mn} \mathcal{D}^l_{mn}(\mathcal{R}), \tag{6.8}$$

where $\mathcal{D}^l_{mn}(\mathcal{R})$ are Wigner matrices [267] and the expansion amplitudes read

$$\rho^l_{mn} = \frac{2l+1}{8\pi^2} \oint d\mathcal{R} \rho(\mathcal{R}) \mathcal{D}^l_{mn}(\mathcal{R}). \tag{6.9}$$

Similarly, for a chiral nematic phase we have

$$\rho(\mathcal{T}_q(\mathbf{r})\mathcal{R}) = \sum_{l=0}^{\infty} \sum_{m,n=-l}^{l} \rho^l_{mn} \mathcal{D}^l_{mn}(\mathcal{T}_q(\mathbf{r})\mathcal{R}). \tag{6.10}$$

By inserting Eq. (6.10) into $\mathcal{F}_{ex}$ of Eq. (6.7) we have

$$\frac{\beta\mathcal{F}_{ex}[\rho]}{V} = \frac{G(\eta)}{2} \sum_{l,m,n} \sum_{l',m',n'} E^{ll'}_{mm'nn'}(q) \rho^l_{mn} \rho^{l'}_{m'n'} \tag{6.11}$$

where we introduced the rotational-invariant q-dependent excluded-volume coefficients

$$E^{ll'}_{mm'nn'}(q) = -\int d\mathbf{r} \oint d\mathcal{R}\, d\mathcal{R}' f(\mathbf{r},\mathcal{R},\mathcal{R}')\mathcal{D}^{l}_{mn}(\mathcal{T}_q(\mathbf{r})\mathcal{R})\mathcal{D}^{l'}_{m'n'}(\mathcal{R}'). \tag{6.12}$$

Using Eq. (6.5) and Eq. (6.11), we have thus shown that the free-energy functional of a chiral nematic phase can in general be written as

$$\frac{\beta\mathcal{F}_q[\rho(\mathcal{R})]}{V} = \oint d\mathcal{R}\, \rho(\mathcal{R})[\log\rho(\mathcal{R})\mathcal{V} - 1] + \frac{G(\eta)}{2}\sum_{l,m,n}\sum_{l',m',n'} E^{ll'}_{mm'nn'}(q)\rho^{l}_{mn}\rho^{l'}_{m'n'}. \tag{6.13}$$

As a result, the q-dependence has been shifted from the ODF to the excluded volume coefficients. Minimizing with respect to ρ^l_{mn} and q would allow to obtain the equilibrium properties of a general chiral nematic phase.

6.2.2 Local uniaxiality

Let us now consider the simplest case of a chiral nematic phase: a phase which at $\mathbf{r} = 0$ is locally uniaxial along the z direction and is invariant to rotations around the main particle axis. In this case

$$\rho^{l}_{mn} = \sqrt{\frac{2l+1}{2}}\rho_l\delta_{m0}\delta_{n0}\,, \tag{6.14}$$

where the l-dependent factor is introduced for later convenience. The excess free energy of Eq. (6.7) can therefore be expressed as

$$\frac{\beta\mathcal{F}_{ex}[\rho]}{V} = \frac{G(\eta)}{2}\sum_{l,l'=0}^{\infty}\rho_l\rho_{l'}E_{ll'}(q)\,, \tag{6.15}$$

where $E_{ll'}(q) = \sqrt{\frac{2l+1}{2}}\sqrt{\frac{2l'+1}{2}}E^{ll'}_{0000}(q)$, which from Eq. (6.12) reads

$$E_{ll'}(q) = -\sqrt{\frac{2l+1}{2}}\sqrt{\frac{2l'+1}{2}}\int d\mathbf{r} \oint d\mathcal{R}\, d\mathcal{R}' f(\mathbf{r},\mathcal{R},\mathcal{R}')\mathcal{D}^{l}_{00}(\mathcal{T}_q(\mathbf{r})\mathcal{R})\,\mathcal{D}^{l'}_{00}(\mathcal{R}'). \tag{6.16}$$

We can rewrite the rotational invariants in terms of the (standard) normalized Legendre polynomial $\mathcal{P}_l(x)$ (with l the degree of the polynomial):

$$\mathcal{P}_l(\hat{\mathbf{n}}\cdot\hat{\omega}) = \sqrt{\frac{2l+1}{2}}\mathcal{D}^{l}_{00}(\mathcal{R}). \tag{6.17}$$

It follows that

$$\rho_l = \int_{-1}^{1} d(\hat{\mathbf{n}}\cdot\hat{\omega})\,\rho(\hat{\mathbf{n}}\cdot\hat{\omega})\mathcal{P}_l(\hat{\mathbf{n}}\cdot\hat{\omega}), \tag{6.18}$$

which allows us to write, for a chiral nematic phase,

$$\mathcal{P}_l(\hat{\mathbf{n}}_q(y)\cdot\hat{\omega}) = \sqrt{\frac{2l+1}{2}}\mathcal{D}^{l}_{00}(\mathcal{T}_q(\mathbf{r})\mathcal{R}). \tag{6.19}$$

In the case of a cholesteric phase, in which the chiral director $\hat{\chi} \perp \hat{\mathbf{n}}$ (and $\hat{\chi} \parallel \hat{\mathbf{y}}$ in our reference frame), we have

$$\hat{\mathbf{n}}_q(y) = \hat{\mathbf{x}} \sin qy + \hat{\mathbf{z}} \cos qy. \tag{6.20}$$

Therefore, we obtain

$$E_{ll'}(q) = -\int d\mathbf{r} \oint d\mathcal{R}\, d\mathcal{R}' f(\mathbf{r}, \mathcal{R}, \mathcal{R}') \mathcal{P}_l(\hat{\mathbf{n}}_q(y) \cdot \hat{\omega}) \mathcal{P}_{l'}(\hat{\mathbf{n}}_0 \cdot \hat{\omega}') \tag{6.21}$$

where $\hat{\mathbf{n}}_0 = \hat{\mathbf{n}}_q(0)$. The excluded volume coefficients of Eq. (6.21) can be directly calculated using numerical techniques, as we explain in Sec. 6.2.4.

In conclusion, starting from Eq. (6.13), valid for a generic chiral nematic phase, we have assumed local uniaxiality and independence of the distribution on rotations around the main particle axis, to obtain an explicit functional for the cholesteric phase, that we can rewrite as

$$\frac{\beta \mathcal{F}_q[\psi]}{V} = n(\log \mathcal{V} n - 1) + 4\pi^2 n \int_{-1}^{1} d\cos\theta\, \psi(\theta) \log \psi(\theta) + \frac{n^2 G(\eta)}{2} \sum_{l,l'=0}^{\infty} \psi_l \psi_{l'} E_{ll'}(q), \tag{6.22}$$

where, in analogy with the uniaxial case (cf. Eq. (3.5)), we kept only the dependence on the polar angle θ by defining the ODF $\psi(\theta) = \rho(\mathcal{R})/n$ and its expansion coefficients

$$\psi_l = \int_{-1}^{1} d\cos\theta\, \psi(\cos\theta) \mathcal{P}_l(\cos\theta)\,. \tag{6.23}$$

Once the excluded volume coefficients $E_{ll'}(q)$ defined by Eq. (6.21) are known, the equilibrium ODF is obtained, in complete analogy with Sec. 3.2, by solving the following equation

$$\psi(\cos\theta) = \frac{1}{Z} \exp\left\{ -n\, G(\eta) \sum_{l,l'=0}^{\infty} \frac{E_{ll'}(q)}{4\pi^2} \frac{1}{2} \left[\mathcal{P}_l(\cos\theta) \psi_{l'} + \mathcal{P}_{l'}(\cos\theta) \psi_l \right] \right\}, \tag{6.24}$$

with Z the normalization constant. Notice that the local uniaxiality approximation yields $E_{ll'}(q) = E_{l'l}(q)$ and the previous equation reduces to

$$\psi(\cos\theta) = \frac{1}{Z} \exp\left[-n\, G(\eta) \sum_{l,l'=0}^{\infty} \frac{E_{ll'}(q)}{4\pi^2} \mathcal{P}_l(\cos\theta) \psi_{l'} \right]. \tag{6.25}$$

The minimization procedure is performed by using a very fine grid for the angles θ to obtain the solution $\psi(\theta)$, at fixed number density n and fixed chiral wave vector q. For each density, the value of q that corresponds to the minimum value of the free energy is the equilibrium one and the corresponding equilibrium pitch of the cholesteric phase reads $P = 2\pi/q$.

6.2.3 Limit of weak chirality: Straley's theory

The expression obtained by Straley for the cholesteric pitch of weakly-chiral infinitely-long hard helices [63], can be easily assessed within our theoretical framework. Let us expand a general functional $\mathcal{F}[\rho(\mathcal{T}_q(y)\mathcal{R})]$ to second-order in q:

$$\frac{\mathcal{F}[\rho(\mathcal{T}_q(y)\mathcal{R})]}{V} = \frac{\mathcal{F}[\rho(\mathcal{R})]}{V} + K_T[\rho(\mathcal{R})] q + \frac{1}{2} K_2[\rho(\mathcal{R})] q^2 + \mathcal{O}(q^3), \tag{6.26}$$

where we introduced the constants

$$K_T[\rho(\mathcal{R})] = \frac{1}{V}\frac{d\mathcal{F}_{ex}[\rho(\mathcal{T}_q(y)\mathcal{R})]}{dq}\bigg|_{q=0}, \tag{6.27}$$

and

$$K_2[\rho(\mathcal{R})] = \frac{1}{V}\frac{d^2\mathcal{F}_{ex}[\rho(\mathcal{T}_q(y)\mathcal{R})]}{dq^2}\bigg|_{q=0}. \tag{6.28}$$

K_T is usually called the *chiral strength* since it must differ from zero to have macroscopic chiral order. K_2 is the twist elastic constant [35, 63] (see also Sec. 3.3). According to Straley's theory, the phase is homogeneous with respect to the internal angle, implying that the non-cylindrically-symmetric character of the particle is averaged out. The equilibrium cholesteric pitch is $P = 2\pi/q = -2\pi K_2/K_T$. Since in general $K_2 > 0$ (in Sec. 8.3 we will explore the possibility of having negative K_2), the handedness of the cholesteric phase depends on the sign of K_T. The explicit expression for K_T depends on the theoretical framework adopted, see for example Refs. [247, 260], and within the second-virial approximation it reads

$$K_T = -\frac{n^2}{2}\int d\mathbf{r} \oint d\hat{\omega}\, d\hat{\omega}' f(\mathbf{r},\hat{\omega},\hat{\omega}')\, y\, \omega_x\, \psi(\hat{\mathbf{n}}_0\cdot\hat{\omega})\, \dot{\psi}(\hat{\mathbf{n}}_0\cdot\hat{\omega}'), \tag{6.29}$$

where $\omega_x = \hat{\omega}\cdot\hat{\mathbf{x}}$ and $\dot{\psi}(x) = \partial\psi(x)/\partial x$ indicates the derivative with respect to the function argument. By using Eqs. (6.27) and (6.28), we will assess quantitatively Straley's approach for hard-helix systems. Moreover, we will compare our results with those presented in Ref. [260], where a sophisticated implementation of Straley's approach has been used.

6.2.4 Numerical procedure

As input for our theory, we need to evaluate the excluded-volume coefficients defined in Eq. (6.21). To perform these calculations, we use a Monte Carlo (MC) integration scheme that has several advantages. First of all, it is a very general approach suitable for several particle models [268–273]. Moreover, MC integration is a robust method for functions with discontinuities and for integration regions with complicated boundaries [274], as in this study where we integrate the Mayer function of complex shaped particles. In general, it is also computationally more efficient than standard quadrature methods for the evaluation of high-dimensional integrals and it is intrinsically parallelizable since it consists of uncorrelated calculations. Furthermore, by determining the associated statistical errors (that decay as $\sim 1/\sqrt{n_{MC}}$, with n_{MC} the number of MC steps), it is easy to control the accuracy of the calculations, as we will show below in Fig. 6.2**(b)**. Finally, we point out that we use the simplest brute-force method for now; the implementation of more sophisticated schemes could be beneficial [275–278] but this is left for future studies.

Assuming the first particle in the origin, the procedure consists of repeating n_{MC} times the following steps: **(i)** generate uniformly the random variables $\mathbf{r} = (x, y, z) \in V$, $\theta, \theta' \in [0, \pi)$ and $\phi, \phi', \alpha, \alpha' \in [0, 2\pi)$ to obtain a random two-particle configuration; **(ii)** compute the Mayer function $f(\mathbf{r}, \mathcal{R}, \mathcal{R}')$, that in case of hard bodies consists of checking for particle overlaps; **(iii)** for each l, l' and q under consideration, compute the Legendre

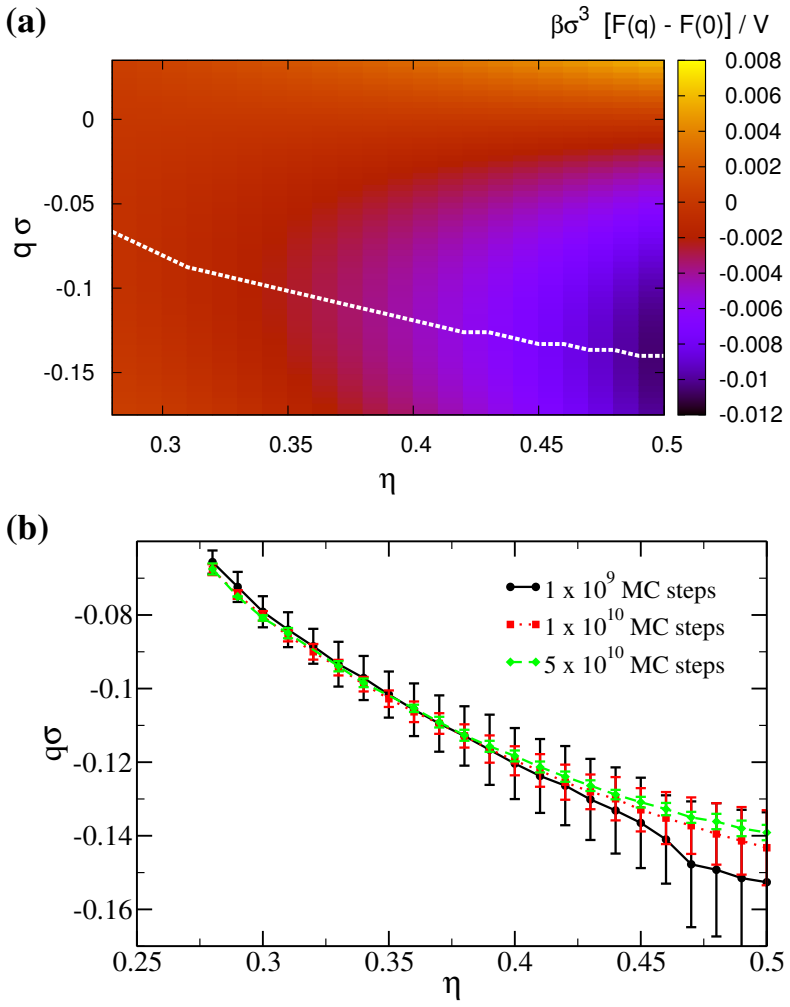

Figure 6.2: Example of typical output of the theory, applied to a system of hard helices with molecular pitch $p = 8\sigma$, outer radius $r = 0.4\sigma$, contour length $L_c = 10\sigma$, and number of beads (of diameter σ) $N_s = 15$ (see Fig. 6.1**(b)**). **(a)** Free-energy difference $F(\eta, q) - F(\eta, 0)$ between a cholesteric and an achiral nematic phase as a function of cholesteric wave vector q and packing fraction η. The white dashed line indicates the free-energy minimum, thereby identifying the equilibrium q for each η. **(b)** Density-dependence of the cholesteric wave vector q and associated statistical errors computed over 8 independent runs of $n_{MC} = 1 \times 10^9$ (black solid line), $n_{MC} = 1 \times 10^{10}$ (red dotted) and $n_{MC} = 5 \times 10^{10}$ (green dashed) MC steps. As expected, error bars are smaller for increasing number of integration steps n_{MC}.

polynomials $\mathcal{P}_l(\hat{\mathbf{n}}_q(y) \cdot \hat{\omega})$, $\mathcal{P}_{l'}(\cos\theta')$ and combine them with $f(\mathbf{r}, \mathcal{R}, \mathcal{R}')$ according to Eq. (6.21). The coefficients $E_{ll'}(q)$ are therefore calculated as

$$E_{ll'}(q) = -V_s \langle f(\mathbf{r}, \mathcal{R}, \mathcal{R}') \mathcal{P}_l(\hat{\mathbf{n}}_q(y) \cdot \hat{\omega}) \mathcal{P}_{l'}(\cos\theta') \sin\theta \sin\theta' \rangle_{MC} \tag{6.30}$$

where for hard bodies the MC average $\langle . \rangle_{MC}$ reduces to an average over overlapping configurations, and V_s is the sampling volume. For example, if positions are generated within a sphere of maximum radial distance r_{max}, we have $V_s = (4/3)\pi r_{max}^3 (16\pi^6)$. Coefficients

up to $l_{max} = 20$ are sufficient to ensure convergence, as also reported for spherocylinders [168]. Calculations are sped up by using recursive formulas for P_l and the number of coefficients $E_{ll'}$ can be reduced in case of additional symmetries. For example, up-down symmetric particles have only even coefficients $E_{2l2l'} \neq 0$. After evaluating $E_{ll'}(q)$, we can iteratively solve Eq. (6.25), at fixed number density n and chiral wave vector q, by using a discrete grid for the polar angles θ (cf. Ref. [126]). The resulting ODFs are used to obtain a full free-energy landscape in the (q, η) plane like the one shown in Fig. 6.2**(a)**. Locating the free-energy minimum among the q-values studied at every packing fraction η, allows us to calculate the density-dependence of the equilibrium cholesteric pitch P. Pressure and chemical potential are derived from the free energy, and coexistence between isotropic and nematic phases is located by imposing equal pressure and equal chemical potential conditions. The most significant source of numerical errors in this procedure is caused by the limited accuracy due to a low number of n_{MC} steps in evaluating the excluded-volume coefficients. However, by considering independent runs (that can subsequently be averaged to increase the accuracy) it is possible to carefully estimate the associated statistical errors. Fig. 6.2**(b)**, for instance, shows the equilibrium cholesteric wave vector q as a function of packing fraction η for a system of hard helices, determined after the numerical calculation of the excluded volume coefficients with different number of MC steps n_{MC}. As a general trend, upon increasing the packing fraction η, errors become bigger since excluded-volume coefficients are coupled with density (see Eq. (3.5) and Eq. (6.25)), with higher-l coefficients (with poorer statistics) becoming increasingly important for the stronger peaked distributions at higher η. However, n_{MC} can be increased in order to reach the desired accuracy. In the remainder of this chapter, we will show the error bars only in a few cases, when we need to quantify our statistical accuracy before drawing conclusions on the physics of the system. The main drawback of the procedure is that a fine grid in q-values is computationally expensive and it is advisable to perform a shorter run in advance to define the optimal q-mesh.

6.3 Results

6.3.1 Cholesterics of hard helices: handedness, (double) sense inversion, and length dependence

We study the cholesteric order arising in systems of colloidal hard helices. A hard helix is modeled as N_s hard spheres of diameter σ, rigidly fused together to form an helix of contour length L_c, microscopic pitch p and radius r (see Fig. 6.1**(b)** and Refs. [252, 265]). In Fig. 6.3**(a)**-**(c)**, we report the density dependence of the cholesteric pitch P for right-handed helices with $L_c = 10\sigma$ and $N_s = 15$. We focus on the range of packing fractions for which the nematic phase is stable with respect to the isotropic phase, and we choose an upper limit of $\eta = 0.5$ since at higher densities smectic phases are expected [37, 118, 265, 266]. Depending on the microscopic parameters r and p, we observe three different cases. In Fig. 6.3**(a)**, we report the pitch P of helices manifesting cholesteric phases with the same handedness of the constituent particles (positive pitch corresponds to right-handed twist). The magnitude of P varies from hundreds to thousands of sphere diameters σ,

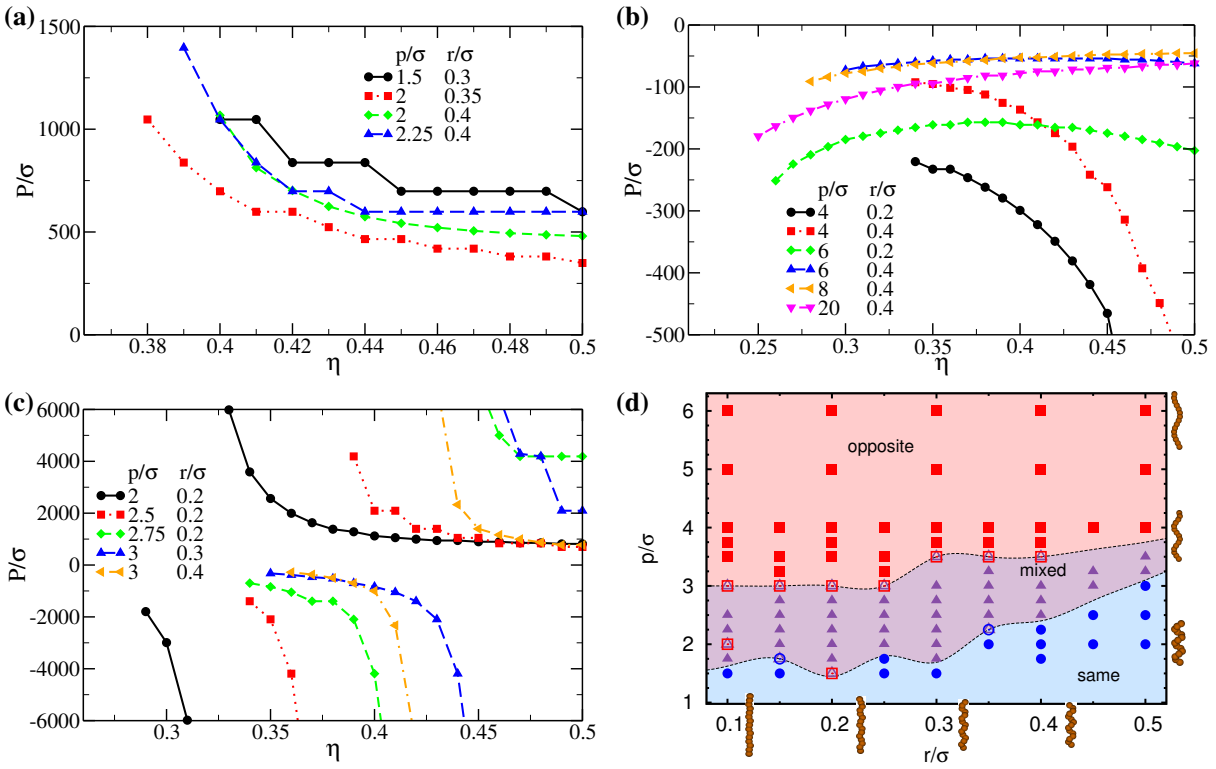

Figure 6.3: Cholesteric pitch P as a function of packing fraction η for right-handed helices consisting of $N_s = 15$ fused hard spheres with diameter σ, contour length $L_c = 10\sigma$ and varying microscopic pitch p and radius r as labelled, stabilizing cholesteric phases with same **(a)**, opposite **(b)** or both **(c)** handedness. **(d)** State diagram for helices with $L_c = 10\sigma$ and $N_s = 15$ in the $p - r$ representation. Open symbols indicate parameters for which statistics is not sufficient for an accurate classification. Boundary lines are guides-to-the-eye.

depending on particle shape and system density, and it is monotonically decreasing upon increasing η. The step-like feature is an artifact due to the use of a discrete mesh for the q-values (see Sec. 6.2.4) and a smooth curve would be obtained by decreasing mesh-size and increasing statistics. Fig. 6.3**(b)** shows helices developing cholesterics with opposite handedness. The density dependence of P appears to be more complex in this case but it is still possible to observe a few common trends. For instance, $|P|$ seems to exhibit a minimum for some η, and at fixed p, helices with a larger radius r lead to a shorter cholesteric pitch P. It is worth noting that for some shapes, $|P| < 100\sigma$, suggesting that these particle models would be good candidates for (direct) simulations of cholesteric phases (under twisted boundary conditions). In Fig. 6.3**(c)**, we report cases in which the handedness of the cholesteric phases depends on the thermodynamic state of the system. For these peculiar helical shapes, a left-handed twist is preferred at the isotropic-cholesteric transition. However, upon increasing packing fraction, the cholesteric pitch P becomes longer and longer, and passing via an achiral state (infinite P), eventually changes sense of twist. The packing fraction at which inversion occurs depends on the particle shape, and in general the inversion occurs at higher density for larger p and r. Comparing these results with a recent study [245] that reported pitch inversion for long

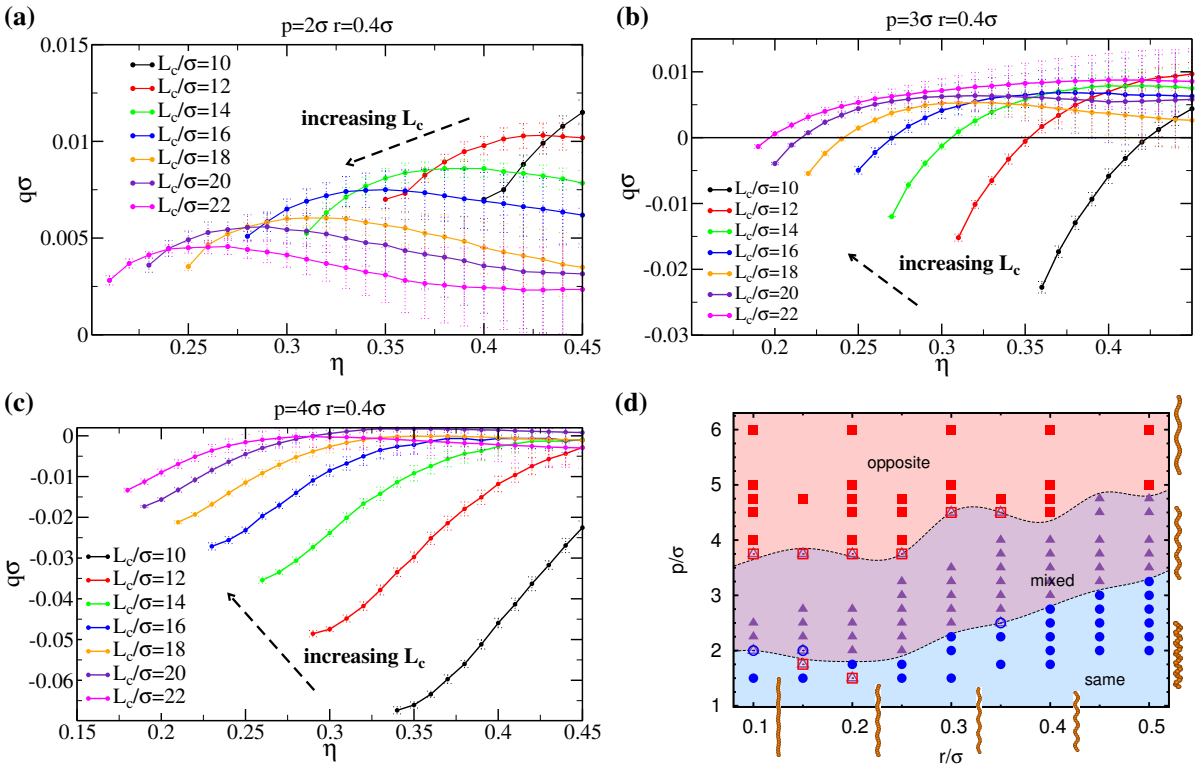

Figure 6.4: Density dependence of the cholesteric wave vector q for helices of fixed radius $r = 0.4\sigma$ and different contour lengths L_c ($N_s = \frac{3}{2}L_c/\sigma$) with particle pitches **(a)** $p = 2\sigma$ **(b)** $p = 3\sigma$ **(c)** $p = 4\sigma$. **(d)** Radius r - pitch p state diagram for helices with contour length $L_c = 20\sigma$ and $N_s = 30$, with regions indicating the same, mixed, and opposite handedness regimes. Boundaries are shifted (upwards) with respect to the state diagram presented in Fig. 6.3**(d)**.

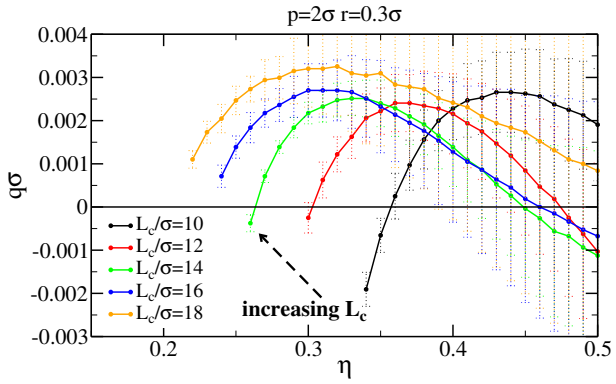

Figure 6.5: Cholesteric wave vector q as a function of packing fraction η for helices with fixed geometry ($p = 2\sigma$, $r = 0.3\sigma$) and different contour length L_c ($N_s = \frac{3}{2}L_c/\sigma$), which show a double twist inversion at intermediate values of L_c. Despite the large statistical error bars for large η, we will see in Fig. 6.7**(c)** that this trend is in principle possible.

and soft (Yukawa) helices using Straley's approach, we observe that the nematic order parameter S at which the inversion occurs can be much lower for the particles in the

present study. Indeed, soft long helices [245] exhibit sense inversion only for a high degree of alignment ($S > 0.9$), whereas for our short hard helices inversion can occur very close to the isotropic-cholesteric transition ($S \sim 0.65$). If the corresponding packing fraction at which the inversion takes place becomes too high it is possible that another phase (e.g. smectic) becomes stable, thereby preventing such an inversion. To summarize our results, we report in Fig. 6.3**(d)** a state diagram using the molecular pitch p and radius r as axes of our representation. Depending on the functional behaviour of P vs η, we identify three regions that will be referred as *same*, *opposite* and *mixed*. Open symbols represent cases for which our statistical accuracy is not enough for a precise classification. Uncertain points are also found for helices with very small p and r (e.g. $p = 2\sigma$, $r = 0.1\sigma$). For these parameters, the particle shape resembles a rod with protrusions rather than a proper helix, making the computation of the excluded volume more demanding and suggesting that very small changes in the shape give rise to complicated inter-locking effects.

In Fig. 6.4 we study the dependence of the (inverse) pitch on particle contour length L_c for selected particle shapes belonging to the three different classes (same, mixed, opposite). In Fig. 6.4**(a)**, we report the cholesteric wave vector $q = 2\pi/P$ for helices of fixed geometry ($p = 2\sigma$ and $r = 0.4\sigma$) and different length. We observe that an increase in L_c corresponds to a decrease in q, therefore to a longer cholesteric pitch P and a weaker cholesteric character. Upon increasing particle length, weaker cholesteric phases are also observed for helices undergoing handedness inversion (mixed case), as reported in Fig. 6.4**(b)**. The same effect is also observed in helices stabilizing cholesteric phases with opposite handedness (see Fig. 6.4**(c)**). We notice that L_c does not only influence the magnitude of the cholesteric pitch but eventually also the sign and therefore the qualitative chiral behaviour, even if the particle geometry is fixed (cf. also discussion on inclination angle in Ref. [260]). We summarize our results for helices of $L_c = 20\sigma$ in the state diagram of Fig. 6.4**(d)**, where we indeed observe an overall upward shift to higher values of p of the boundaries delimiting the three different regimes with respect to Fig. 6.3**(d)**. Also in this case, the undulatory nature of the boundaries and the presence of unclear cases for small p and r reflect the sensitivity of the macroscopic chiral behaviour on subtle changes in particle shape. We notice that neither the theoretical results obtained for long helices [261, 263], predicting that $P \sim L^2$, nor experimental observations on coated fd viruses [208], for which $P \sim L^{-0.25}$, are consistent with our study. Indeed, the richer scenario of short helices does not allow to deduce a clear scaling relation between cholesteric pitch P and particle length L (notice that $L \propto L_c$ for fixed p, r, see Eq. (6.32)).

To further emphasize that the chiral behaviour of a system depends sensitively on the precise details of the single-particle properties, we conclude this section by speculating on a possible non-trivial cholesteric behaviour as a function of particle length. In Fig. 6.5, we show the cholesteric wave vector q as a function of packing fraction η, for helices with $p = 2\sigma$, $r = 0.3\sigma$ and various particle lengths. For $L_c = 10\sigma$ we observe the (single) handedness inversion as described above. Surprisingly, upon increasing the particle length by a few σ, a second twist inversion seems to occur at higher packing fraction. However, we notice that large statistical errors are present at large η. Upon further increasing the particle length ($L_c = 16\sigma$), the first inversion disappears. Therefore, in contrast with the previous case, the chirality inversion involves a transition from same to opposite handedness, upon increasing packing fraction. Finally, for helices with $L_c = 18\sigma$ no

inversion is present and only cholesterics with the same handedness are stable in the range of η studied. Even though the large statistical uncertainty seems to undermine the conclusiveness of our observations, we will see in the next section that this behaviour is consistent with our interpretation of the chiral order in terms of minimization of the excluded volume. However, it is not possible to exclude that another phase (e.g. smectic) would be more stable than the cholesteric at large η, preventing in particular the second inversion to occur.

6.3.2 Competition between shape and particle-particle correlations

In this section we try to interpret our results on the collective chiral behaviour in terms of a microscopic parameter. Harris, Kamien and Lubensky (HKL) proposed [263, 264] a pseudoscalar ψ_{HKL} to measure the internal chiral strength of a molecule, and showed that ψ_{HKL} is proportional to the macroscopic chiral strength K_T, defined in Eq. (6.27). The sign of ψ_{HKL} determines the handedness of the cholesteric phases. Ref. [263] (see table I therein) reports an explicit expression of ψ_{HKL} for an helix of uniform density, in the limit that the particle length is much larger than the particle radius. In our notation, it reads

$$\psi_{HKL} \propto -\frac{3r^4 L}{\left(2\pi\frac{L}{p}\right)^3}\left[1-\frac{24}{\left(\pi\frac{L}{p}\right)^2}\right], \tag{6.31}$$

where L is the Euclidean length, which is a function of the contour length L_c, the microscopic pitch p and the radius r given by

$$L = \frac{pL_c}{2\pi\sqrt{r^2+\left(\frac{p}{2\pi}\right)^2}}. \tag{6.32}$$

In Fig. 6.6, we report the state diagram for helices at fixed $L_c = 10\sigma$ and $L_c = 20\sigma$, based on the analysis of the sign of $\psi_{HKL}(r,p)$, in analogy with Figs. 6.3**(d)** and 6.4**(d)**. Clearly, the mixed region where sense inversion occurs cannot be explained by the pseudoscalar ψ_{HKL}, as it is density independent. Nevertheless, a qualitative trend can be captured with this purely geometric interpretation. We clearly find that the sign of ψ_{HKL} overestimates significantly the value of the microscopic pitch p for the boundary from same to opposite handedness, but describes correctly that this boundary shifts to higher p upon increasing L. Moreover, the pseudoscalar approach predicts that the cholesteric pitch scales as $P \propto L^2$, which we have already shown not to be always the case for short helices. We can therefore conclude that single-particle properties are not sufficient to completely describe the observed non-trivial macroscopic chiral behaviour and, as already noticed [263, 264], particle correlations must be taken into account as well.

As shown in our previous study [252], in order to explain the stability of chiral ordering we analyse the excluded volume associated to right/left-handed pairs of particles and the handedness of the resulting cholesteric phase. A pair of helices is in a right-handed configuration if $(\mathbf{r}-\mathbf{r}')\cdot(\hat{\omega}\times\hat{\omega}') > 0$. Vice versa, if the latter is negative it is in a

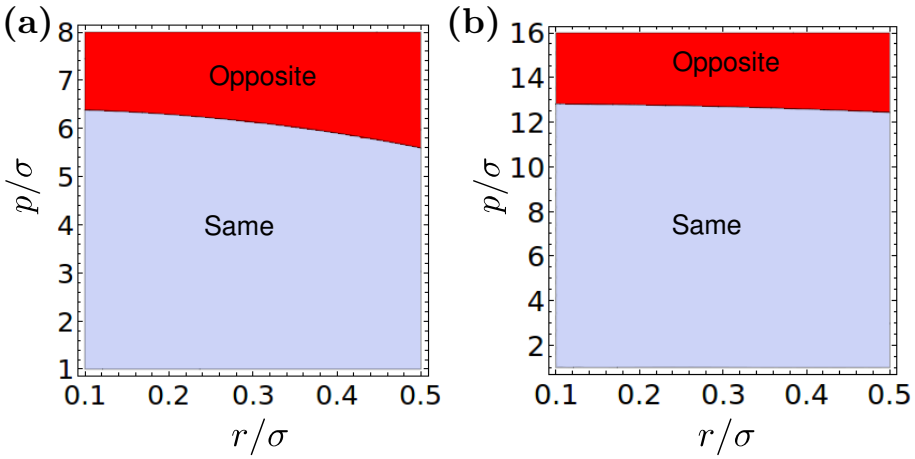

Figure 6.6: State diagrams based on the sign of the pseudo-scalar ψ_{HKL} [263, 264]. **(a)** Hard helices with fixed contour length $L_c = 10\sigma$ (cf. Fig. 6.3**(d)**). **(b)** $L_c = 20\sigma$ (cf. Fig. 6.4**(d)**). Notice the different scales of the vertical axes.

left-handed configuration. Therefore, we can define a right/left-handed excluded volume as

$$E_{\substack{R\\L}}(\hat{\omega}\cdot\hat{\omega}') = -\int d(\Delta\mathbf{r}) \int_0^{2\pi} \frac{d\alpha}{2\pi}\frac{d\alpha'}{2\pi} f(\Delta\mathbf{r},\mathcal{R},\mathcal{R}')\,\Theta(\pm\Delta\mathbf{r}\cdot(\hat{\omega}\times\hat{\omega}')), \tag{6.33}$$

with $\Theta(x)$ the Heaviside step function and α the internal angle (cf. Sec. 6.2.1). If $\Delta E \equiv E_R - E_L > 0$ a left-handed configuration is preferred, and if $\Delta E < 0$ a right-handed one. It is worth noting that ΔE is a microscopic property of a pair of helices, while ψ_{HKL} is a single-particle property. For convenience, we define a normalized $\Delta E^* = (E_R - E_L)/(E_R + E_L)$. In Fig. 6.7**(a)-(c)**, we report ΔE^* for several helical shapes (all right-handed), as a function of the angle formed by the main axis of the two helices $\gamma = \arccos(\hat{\omega}\cdot\hat{\omega}')$. In the case that ΔE^* has the same sign for all values of the angle γ, we can predict undoubtedly the handedness of the cholesteric phase. For example, in Fig. 6.7**(a)** we report helices with fixed radius $r = 0.3\sigma$ and length $L_c = 10\sigma$ and different p (moving on a vertical line in the state diagram of Fig. 6.3**(d)**). For large p, $\Delta E^* > 0$ $\forall\gamma$, consistently with the stabilization of a left-handed cholesteric (opposite case). The magnitude of the cholesteric pitch P is also qualitatively related to the magnitude of $|\Delta E^*|$. On the other hand, for helices with smaller p we observe that $\Delta E^* < 0$ for small angles γ. In this case the handedness of the liquid-crystalline phase cannot be predicted a priori. In fact, for this range of parameters we have shown (cf. Fig. 6.3**(d)**) that the cholesteric handedness depends on packing fraction, i.e. it depends on the local alignment (mixed case). The pitch inversion can be qualitatively interpreted as follows. At low packing fraction, the average angle γ between helices is relatively large and since the corresponding $\Delta E^* > 0$ an opposite-handed phase is stabilized. Increasing the packing fraction, the average γ becomes smaller and eventually $\Delta E^* < 0$, giving rise to a same-handed phase. The subtle balance between excluded volume and local alignment can also be appreciated in Fig. 6.7**(b)**, where we show results for helices with fixed internal pitch $p = 2\sigma$ but different r (horizontal line in Fig. 6.3**(d)**). Analysing the state diagram, we find upon increasing r: an (uncertain) opposite case ($r = 0.1\sigma$), mixed cases ($r/\sigma = 0.2, 0.3$),

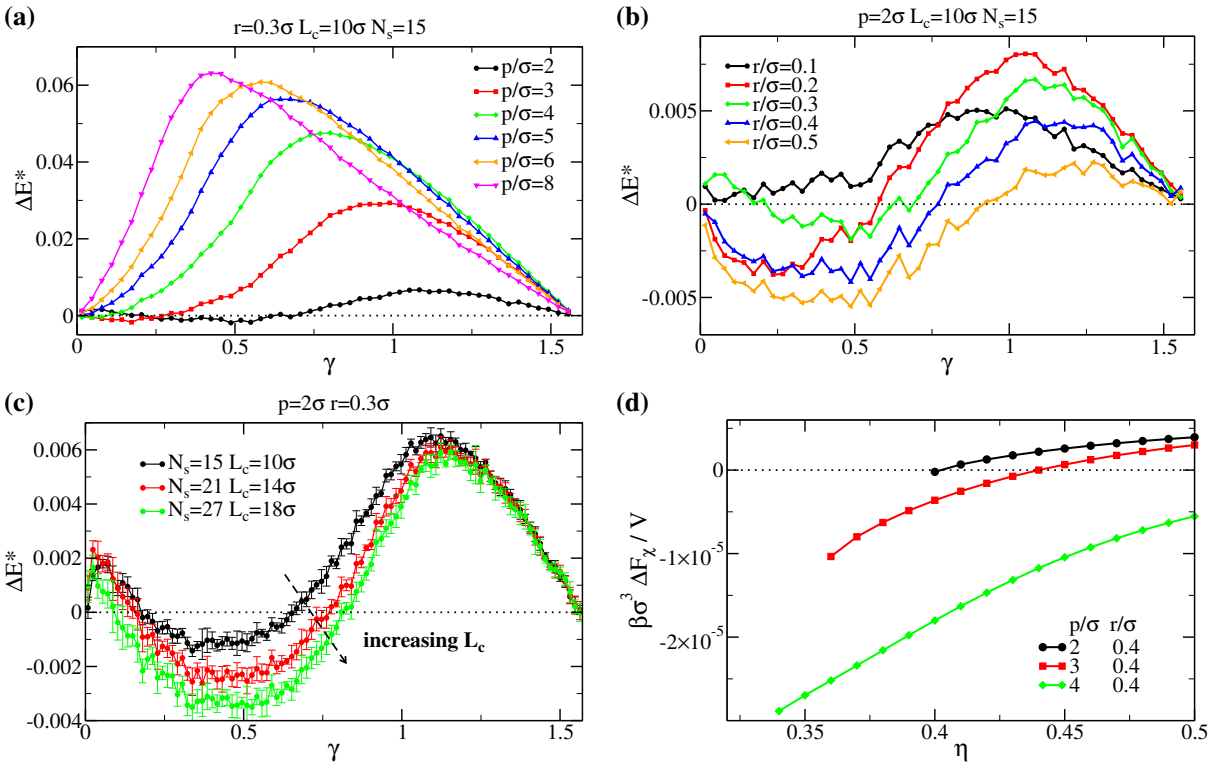

Figure 6.7: Difference in excluded volume between right- and left-handed pair configurations $\Delta E^* = (E_R - E_L)/(E_R + E_L)$ as a function of the angle between the two helices $\gamma = \arccos(\hat{\omega}\cdot\hat{\omega}')$. **(a)** Right-handed helices of length $L_c = 10\sigma$, $N_s = 15$, fixed radius $r = 0.3\sigma$ and different microscopic pitch p. **(b)** Right-handed helices of length $L_c = 10\sigma$, fixed pitch $p = 2\sigma$ and different radius r. **(c)** Right-handed helices with fixed geometry $p = 2\sigma$, $r = 0.3\sigma$ and different length L_c. Error bars are calculated over 5 independent runs of 2×10^{10} MC steps. **(d)** Thermodynamic average of the excluded volume difference ΔF_χ as a function of η for helices of length $L_c = 10\sigma$ ($N_s = 15$), $r = 0.4\sigma$ and different p. The trends of ΔF_χ match qualitatively with the density dependence of the cholesteric wave vector q (cf. Fig. 6.4).

and same-handedness cases ($r/\sigma = 0.4, 0.5$). Observing that $\Delta E^* > 0\ \forall\gamma$ for helices with $r/\sigma = 0.1$, we can confirm the opposite handedness in the state diagram. Such a behaviour seems an anomaly in the state diagram but, as already mentioned, the helical shape in this region (small p and small r) has complex features that can give rise to a non-ordinary behaviour. We notice that also in the analysis of the maximum packing fraction performed in Ref. [37] (cf. Fig. 3 therein), no clear trend can be observed for helices with small p and small r (e.g. helices with $p = 1\sigma$ $r = 0.2\sigma$ represent a local minimum in the maximum η). The angular dependence of ΔE^* for $r = 0.2\sigma$ is already described above and explains the mixed case. A double inversion seems also possible in the case of $r = 0.3\sigma$ and it will be described in detail in Fig. 6.7**(c)**. For helices with $r/\sigma = 0.4, 0.5$, we also observe two regions for ΔE^* but in these cases the range of angles γ with $\Delta E^* < 0$ is larger than the (mixed) case of $r/\sigma = 0.2$, and $\Delta E^* > 0$ is only for γ values that are so large that they are not expected to contribute to the nematic order. Moreover, ΔE^* takes also values more negative. As a consequence, the stabilized phase

has the same (right-handed) handedness of the constituent helices. The dependence of $\Delta E^*(\gamma)$ on particle length for $p = 2\sigma$ and $r = 0.3\sigma$, reported in Fig. 6.7**(c)**, is consistent with the observations made for the chiral behaviour shown in Fig. 6.5. In all cases we observe for increasing γ the sequence positive-negative-positive for ΔE^* suggesting the possibility of a double inversion for all particle lengths. However, the depth of the region in which $\Delta E^* < 0$ is larger for longer helices, and is caused by the different chiral behaviour for particles with different lengths, as already seen before. These observations manifest the intricate link between microscopic and macroscopic chirality. This indicates that although the calculation of ΔE^* is a powerful tool, and computationally faster than the full minimization, it cannot always be considered as an exhaustive analysis, which is to be expected as this type of analysis is based on geometrical two-body properties only, which do not take into account the thermodynamic state point. In order to do so, we introduce the ODF $\psi(\theta)$ to explicitly account for the local alignment in the system. We therefore *thermodynamically* average the difference in the excluded volume, introducing a quantity that mimicks the functional form of the excess second-virial free energy [252]:

$$\frac{\beta \Delta F_\chi}{V} = -\frac{n^2}{2} \oint d\hat{\omega} \oint d\hat{\omega}' \, \psi_0(\hat{\mathbf{n}}_0 \cdot \hat{\omega}) \psi_0(\hat{\mathbf{n}}_0 \cdot \hat{\omega}') \Delta E(\hat{\omega} \cdot \hat{\omega}'), \tag{6.34}$$

with $\psi_0(\hat{\mathbf{n}}_0 \cdot \hat{\omega}')$ the ODF in the achiral limit. In Fig. 6.7**(d)** we report ΔF_χ for three representative cases of helices with $L_c = 10\sigma$, $r = 0.4\sigma$ and $p = 2\sigma$ (same), $p = 3\sigma$ (mixed) and $p = 4\sigma$ (opposite). By comparing with the density dependence of q in Fig. 6.4 (black lines in panels **(a)-(c)** respectively), we observe that all the three regimes are captured by ΔF_χ, including a good agreement on the packing fraction at which the sign inversion is obtained. We can therefore conclude that a solely geometric interpretation is not sufficient to describe our results and that the degree of local alignment must be taken into account by weighting the excluded volume difference ΔE^* with the ODF.

6.3.3 Chiral order vs uniaxial order: weak chirality limit and comparison with Straley's approach

We have shown in Sec. 6.2.3 that we can recover the theory proposed by Straley [63] by expanding the full free-energy functional for small q. An interesting difference between Straley's small-q expansion with coefficients evaluated in the achiral limit ($q = 0$) and the present study involves the effect of q on the ODF which is taken into account here and ignored in Straley's approach. In Fig. 6.8, we show an example of the difference between the ODF corresponding to the achiral limit ($q = 0$) and that at $q \neq 0$ for which the free energy has actually a minimum (helices with $p = 8\sigma$, $r = 0.4\sigma$, $L_c = 15\sigma$, $N_s = 15$). We observe a more peaked ODF associated to the chiral order (N^*) than the achiral one (N). In the inset, we see that this difference becomes more pronounced upon increasing the packing fraction since the liquid crystal phase becomes more chiral (smaller $\mathcal{P}$) for this kind of helices. Even though the difference can be small, it is yet reflected in the free energy (cf. Fig. 6.2**(a)**) and in the nematic order parameter S that can differ by a few percent.

In Straley's method [63] the uniaxial ODF is then used to compute the chiral strength K_T and the twist elastic constant K_2. Subsequently, the equilibrium cholesteric wave

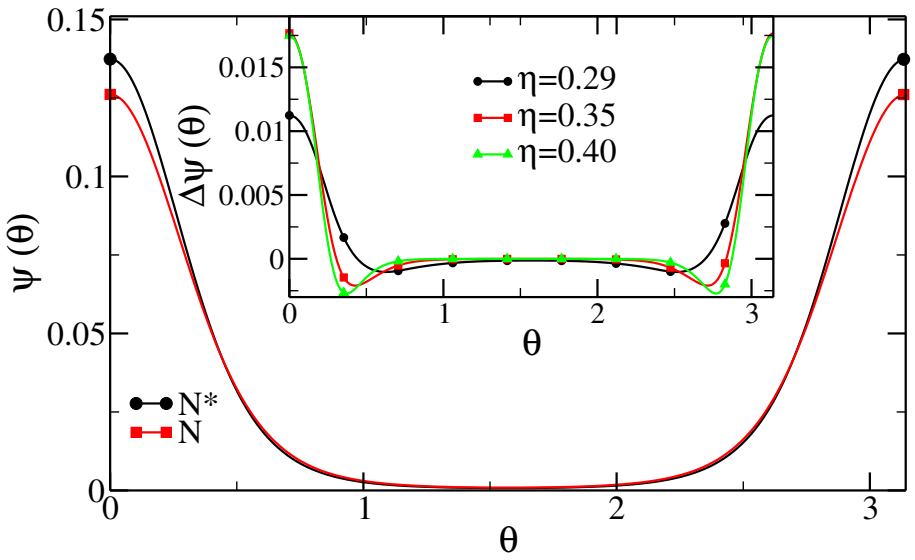

Figure 6.8: Orientation distribution function $\psi(\theta)$ for uniaxial nematic phase (N) and cholesteric (N^*) for helices with $p = 8\sigma$, $r = 0.4\sigma$, $L_c = 10\sigma$, $N_s = 15$ at the isotropic-nematic transition ($\eta \simeq 0.29$). Inset: difference $\Delta\psi(\theta) = \psi_{N^*}(\theta) - \psi_N(\theta)$ for different packing fraction.

helix	η_{N^*}	S_{IN^*}		$10^4\ K_T$		K_2		P	
	here	here	Ref. [260]	here	Ref. [260]	here	Ref. [260]	here	Ref. [260]
$r = 0.2\ p = 2$	0.300	0.699	0.64	4.27	4.83	0.199	0.154	-2990	-2008
$r = 0.2\ p = 4$	0.274	0.677	0.66	47.3	41.36	0.194	0.177	-260	-268
$r = 0.2\ p = 8$	0.258	0.690	0.68	42.3	-29.03	0.203	0.184	-310	-399
$r = 0.4\ p = 2$	0.403	0.612	0.60	-10.7	-3.83	0.160	0.153	965	2509
$r = 0.4\ p = 4$	0.340	0.622	0.61	110	98.35	0.150	0.152	-93	-97
$r = 0.4\ p = 8$	0.282	0.619	0.61	115	110.13	0.136	0.159	-90	-90

Table 6.1: Comparison between the method described here and Straley's approach as implemented in Ref. [260]. Our results are obtained by averaging 16 runs of 10^{10} MC steps for the excluded volume integration (only significant digits are reported). K_T and K_2 are calculated using Eqs. (6.27) and (6.28), and the cholesteric pitch P by minimizing the full functional. All the quantities are in reduced units with $k_BT = 1$ and $\sigma = 1$.

vector in the second-order expansion approximation is obtained via $q_{II} = -K_T/K_2$. In our case, from the calculated free energy landscape, by using Eqs. (6.27) and (6.28), we are able to obtain the density dependence of these two constants. In Fig. 6.9 we assess quantitatively Straley's method by plotting q_{II} obtained from second-order expansion and q obtained by the minimization of the full functional, for selected helical shapes (the ones studied in Ref. [260]). We observe that for the helices in Fig. 6.9**(a)** the difference is very small. Since the macroscopic chiral behaviour for these particles is very weak (cf. Sec. 6.3.1) we expected that a second-order approximation would not be too off. However, in case of cholesterics with shorter pitch we find an appreciable difference, as can be observed from Fig. 6.9**(b)** in which we report the case for helices with $p = 8\sigma$, $r = 0.4\sigma$. Since the higher-order terms can be positive or negative (without any clear correlation

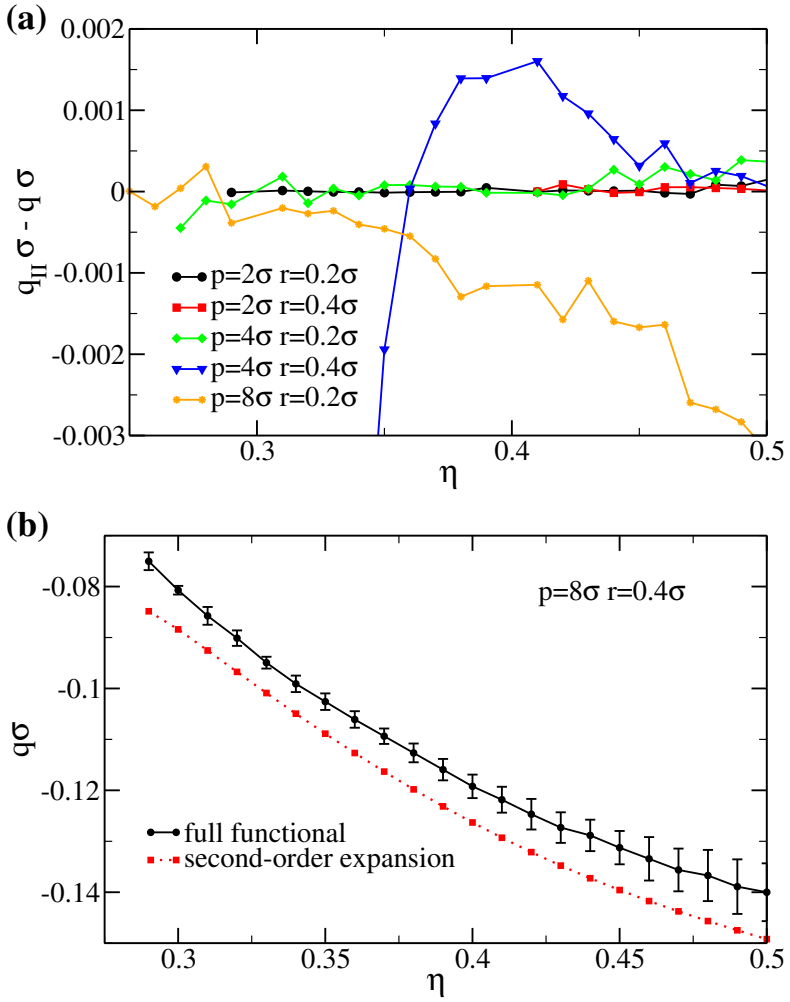

Figure 6.9: **(a)** Difference in the cholesteric wave vector $q_{II} - q$ as a function of η obtained by expansion of the free-energy functional q_{II} (see Eqs. (6.27) and (6.28)) and by minimization of the full functional q, for selected helices of length $L_c = 10\sigma$ and varying microscopic pitch p and radius r. **(b)** The cholesteric wave vector q as a function of η for helices with $p = 8\sigma$, $r = 0.4\sigma$, $L_c = 10\sigma$.

with the chiral behaviour), we cannot conclude that Straley's method under/overestimate the results systematically. In Tab. 6.1, we compare our results with Ref. [260], in which a sophisticated implementation of Straley's method was used. We can thus confirm that the overall scenario seems to be well captured by Straley's approach, even we can not exclude that subtleties in the numerical implementation of both approaches could lead to quantitative discrepancy for the value of the cholesteric pitch P in some particular cases.

We conclude our analysis, by noting that in the limit of weakly chiral long helices, several studies predicted various scaling relations for the main quantities regulating the chiral liquid-crystalline behaviour. Despite the relatively small η-regime of interest here, much smaller than a decade, which limits the meaning of exponents, we briefly discuss these scalings anyway for comparison with our results. For example, in his original work [63]

Straley proposed that $K_2 \sim \eta^2$, resulting in a cholesteric pitch $P \propto 1/S^2$. However, experiments often show a different density dependence of the elastic constant (for example in the thermotropic PBLG, [212] $K_2 \sim \eta^{0.36}$). Subsequently, Odijk [262] suggested that $P \sim \eta^{-1}$ for rigid hard helices, and $P \sim \eta^{-5/3}$ for flexible hard helices. Scaling relations are also measured in experiments, for example some fd viruses [208] show $P \sim \eta^{-1.45}$, while $P \sim \eta^{-1.8}$ is observed for PBLG [212]. In contrast, we find that none of these relations apply uniquely to the short hard helices studied here. Indeed, in Fig. 6.10**(a)**, where we plot K_2 as a function of η for several helical shapes, we observe that the functional form of the twist elastic constant K_2 computed from Eq. (6.28), depends on the different helical shape considered and cannot be described by a simple power law relation, at least not for the present parameter set. Analogously, in Fig. 6.10**(b)**, we plot P vs η for very weakly chiral helices ($p = 20\sigma$) along with the best fits of the expected power laws in these regimes. Due to the poor mutual agreement of the exponents, we tend to conclude that also the density dependence of the cholesteric pitch P of short helices does not obey any general power law.

6.4 Towards softer colloids

In this section, we modify the particle model to study the effect of an additional soft interaction on the macroscopic chiral behaviour. The helical shape is still described by the parameters N_s, L_c, p and r (see Sec. 6.3.1), but spheres of different helices now attract or repel each other via the following short-range potential (cf. cartoon in Fig. 6.11**(a)**):

$$\beta U(r_{1i2j}) = \begin{cases} \infty & r_{1i2j} < \sigma \\ \beta\epsilon & \sigma \leq r_{1i2j} < r_{soft} \\ 0 & r_{1i2j} \geq r_{soft} \end{cases} \tag{6.35}$$

where r_{1i2j} is the distance between sphere i of helix 1 and sphere j of helix 2, and r_{soft} determines the range of the potential. For $\beta\epsilon > 0$ (< 0) we obtain a repulsive square shoulder (attractive square well) potential, whereas for $\beta\epsilon = 0$ we recover the hard-core potential studied above. Even though the computation of the excluded volume coefficients becomes more expensive, we are still able to obtain reliable results (cf. error bars in Fig. 6.11) using the simple procedure described in Sec. 6.2.4.

In Fig. 6.11**(a)**, we report the density dependence of q for helices with $p = 8\sigma$, $r = 0.2\sigma$, which interact via a very short-ranged potential ($r_{soft} = 1.5\sigma$) that can be either attractive or repulsive. We observe that the effect of an additional attraction (repulsion) enhances (reduces) the macroscopic chiral behaviour with respect to the purely hard helices. In fact, upon increasing the attractive well from $\beta\epsilon = 0$ (hard case) to $|\beta\epsilon| = 0.07$, the cholesteric pitch can be decreased by hundreds of σ, depending on η as well. The opposite effect is obtained when the soft interaction is repulsive, as can als be observed in Fig. 6.11**(b)**. In this case ($p = 8\sigma$, $r = 0.4\sigma$), the soft repulsion with a range of $r_{soft} = 1.5\sigma$ masks partially the molecular chiral features producing an effective shape that resembles more achiral rods. In Fig. 6.11**(c)**, we study at fixed interaction strength $\beta\epsilon = 0.03$ the effect of the interaction range of the repulsion r_{soft} for the same helices. Analogously, increasing the interaction range produces a longer cholesteric pitch, whose equilibrium value depends

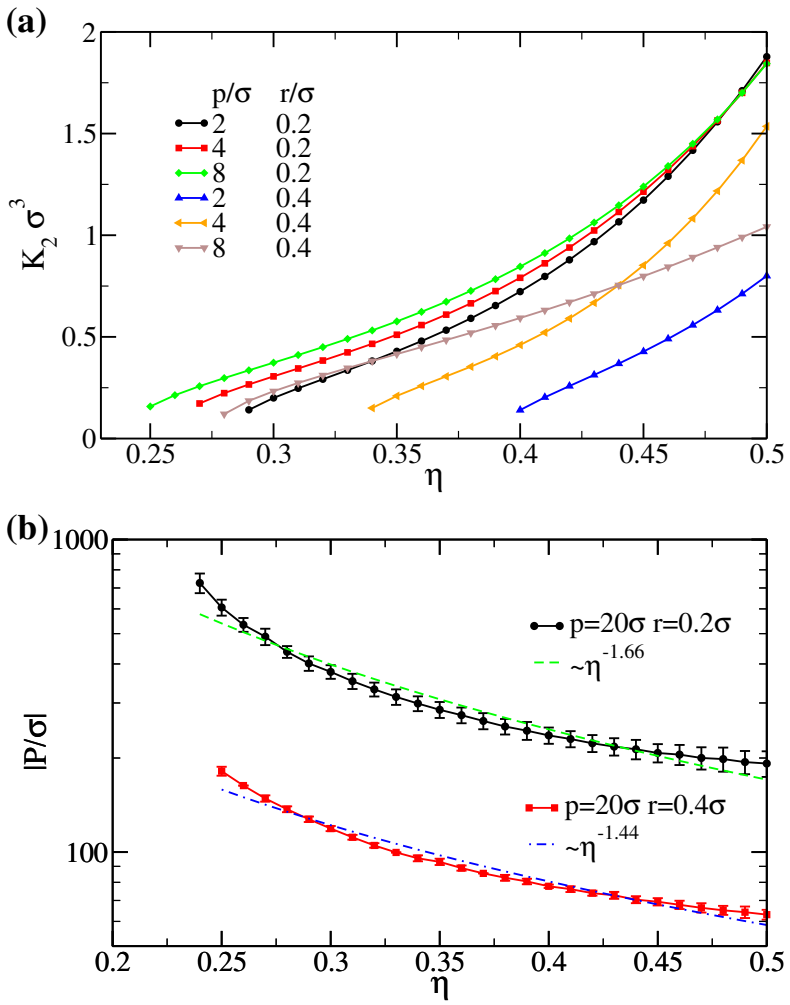

Figure 6.10: **(a)** Density dependence of the twist elastic constant K_2, calculated by using Eq. (6.28), for selected helices of length $L_c = 10\sigma$. **(b)** Log-Lin plot of absolute value of the cholesteric pitch P for helices of length $L_c = 10\sigma$ and very long internal pitch $p = 20\sigma$. Lines are best fits of the power laws indicated in the legend.

less sensitively on the density. Such an effect is also observed for helices manifesting both right- and left-handed phases (mixed case), as reported in Fig. 6.11**(d)**. In this particular case ($p = 3\sigma$, $r = 0.4\sigma$), the transition between the two types of cholesterics becomes less abrupt for increasing interaction range, eventually making it hard to identify within our statistical accuracy.

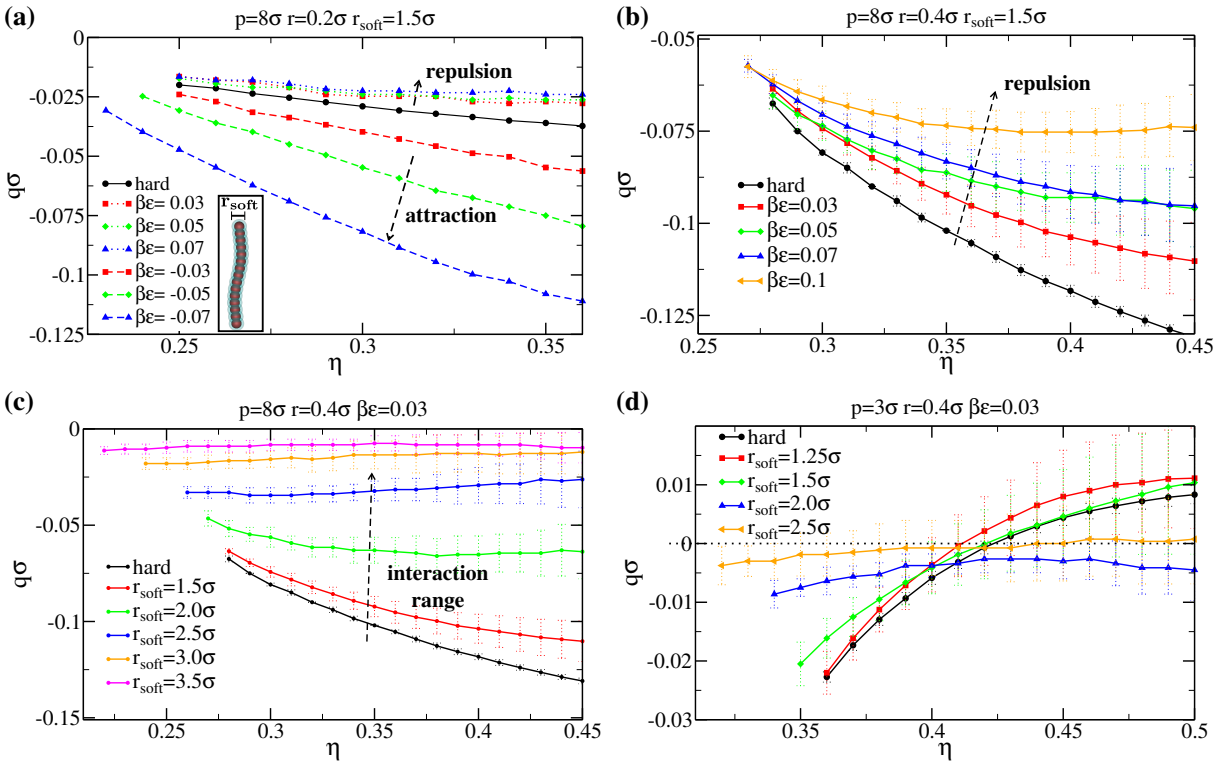

Figure 6.11: Density dependence of the cholesteric wave vector q for selected cases of short-ranged soft helices of length $L_c = 10\sigma$. **(a)** Effect of attraction ($\beta\epsilon < 0$, dashed lines) and repulsion ($\beta\epsilon > 0$, dotted lines) with respect to the hard case (full line) of helices with a microscopic pitch $p = 8\sigma$, radius $r = 0.2\sigma$ and interaction range $r_{soft} = 1.5\sigma$. Inset: cartoon of the particle model. **(b)** Effect of interaction strength $\beta\epsilon$ for short-range ($r_{soft} = 1.5\sigma$) repulsive helices. **(c)** Effect of interaction range r_{soft} for helices with $p = 8\sigma$, $r = 0.4\sigma$ and interaction strength $\beta\epsilon = 0.03$ stabilizing an opposite-handed cholesteric. **(d)** Effect of interaction range r_{soft} on helices ($p = 3\sigma$, $r = 0.4\sigma$, $\beta\epsilon = 0.03$) exhibiting handedness inversion.

6.5 Cholesteric order in binary mixtures

A straightforward application of the theory presented here is the study of (binary) mixtures of chiral particles. In particular it is possible to study the chiral behaviour of a mixture of right- and left-handed particles and the doping of an achiral system. In Fig. 6.12 we report some exemplary phase diagrams to illustrate some of the possible combinations. The fact that hard helices stabilize cholesteric phases with different handedness and their non-trivial dependence on the density enriches tremendously the possibility of tuning the sense and the magnitude of the cholesteric pitch. The phase diagrams are obtained by minimizing the free-energy functional for a binary mixture with species $i = 1, 2$, that has the additional mixing entropy term (compared with Eq. 6.22), the orientationl free energy for both species and an excluded volume term extended to a binary mixture:

$$\begin{aligned}\frac{\beta\mathcal{F}_q[\psi_1,\psi_2]}{V} = n(\log\mathcal{V}n - 1) \; + \; n\sum_{i=1}^{2} x_i \log x_i \; + \\ + \; 4\pi^2 n \sum_{i=1}^{2} x_i \int_{-1}^{1} d\cos\theta \, \psi_i(\theta) \; \log\psi_i(\theta) \; + \\ + \; \frac{n^2 G(\eta)}{2} \sum_{i=1}^{2}\sum_{j=1}^{2} x_i \, x_j \sum_{l,l'=0}^{\infty} \psi_{il} \, \psi_{jl'} \, E^{ij}_{ll'}(q) \; , \end{aligned} \quad (6.36)$$

with x_i composition of species i, $E^{ij}_{ll'}(q)$ excluded-volume coefficients between species i and j depending as before on the imposed cholesteric wave vector q, and ψ_{il} expansion coefficients of the orientation distribution $\psi_i(\theta)$. Subsequently, by computing the Gibbs free energy (per particle) $g(x, P) = G/N = F/N + PV/N$, with F the (minimum) free-energy, P the pressure and V the volume, one can straightforwardly determine the phase coexistence by equating the chemical potential of both species and the pressure in the two coexisting phases. All results are based on a discrete grid for q, as in the single-component case.

From Fig. 6.12(a)-(b)-(c), we observe that racemic mixtures, i.e., mixtures with equal amount of enantiomers (right- and left-handed particles) form an achiral state (uniaxial nematic), as predicted earlier [35]. This also implies that chirality alone cannot drive phase separation in hard-particle systems, and (large) size asymmetry is also required [170], similarly to what was predicted for softer chiral systems in Ref. [247]. Such an asymmetry in the shape/potential can also be enhanced by the addition of depletants, as observed for mixtures of fd-viruses with different lengths, which stabilize cholesteric phases with different handedness [231]. However, in the case that the single component system exhibits a sense inversion of the cholesteric arrangement, mixtures of these left- and right-handed particles will stabilize both handedness for composition different from $x = 0.5$ as shown in Fig. 6.12(c). Also in this case, the dependence on the system density/pressure is crucial. In general, the macroscopic chiral behaviour can be finely tuned by changing radius and pitch of the helices (e.g. in Fig. 6.12(d)) or keeping them fixed and changing particle lengths to tune the composition at which the achiral nematic phase is formed (e.g. in Fig. 6.12(f)). Also the doping of an achiral phase, composed for example of linear rigid hard chains, can be predicted and presents counter-intuitive aspects. For example, when

only right-handed dopants that form right-handed cholesterics in the single-component case are added in a small quantity to the achiral phase, a left-handed (opposite sense of the dopants) can be stabilized (e.g. in Fig. 6.12(e)). Once more, these results are evidences of a non-trivial dependence between micro- and macro-chirality that is difficult to predict a priori by just looking at the particle shape.

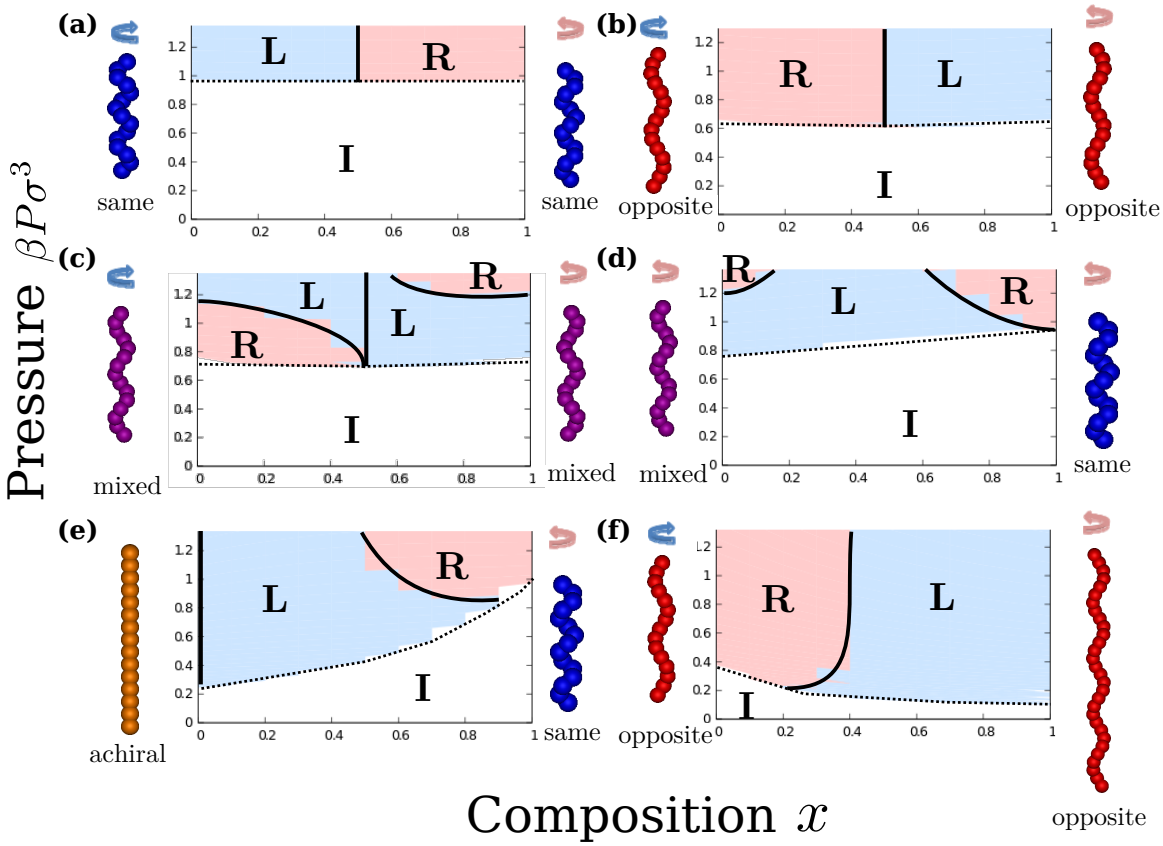

Figure 6.12: DFT predictions for cholesteric ordering in binary mixtures of hard (chiral) rods. The phase diagrams are presented in the pressure $\beta P\sigma^3$ - composition x plane. Cartoons on the x-axis represent the particles forming the binary mixture and they are drawn on the side of the diagram where they are in a single-component system. The arrow on top of the cartoons represents the handedness of the particle (blue=left-handed, red=right-handed). Labels below the particle cartoons and colors of the cartoons represent the behaviour in the single-component limit: blue particles have a shape that stabilizes cholesterics with same handedness; purple particles belong to the mixed region; red to the opposite-handedness region; the orange linear chain is an achiral particle. Regions in the phase diagrams are colored and labelled corresponding to the handedness of the cholesteric phase: red and letter R for a right-handed phase, blue and letter L for left-handed phase; white regions (I) correspond to the isotropic phase. Solid lines in the phase diagrams indicate where a uniaxial achiral nematic phase is expected. Dotted lines indicate where the isotropic-nematic/cholesteric transition occurs. All results are based on a numerical method based on a finite grid, therefore approximate. Binary mixtures studied are **(a)** left/right-handed helices with $p = 2\sigma, r = 0.4\sigma, L_c = 10\sigma$; **(b)** left/right-handed helices with $p = 8\sigma, r = 0.4\sigma, L_c = 10\sigma$; **(c)** left/right-handed helices with $p = 3\sigma, r = 0.4\sigma, L_c = 10\sigma$; **(d)** right-handed helices with $p = 3\sigma$ or $p = 2\sigma$, and $r = 0.4\sigma, L_c = 10\sigma$; **(e)** achiral linear chain with $L_c = 10\sigma$ and right-handed helices with $p = 2\sigma, r = 0.4\sigma, L_c = 10\sigma$; **(f)** left/right-handed helices with $p = 8\sigma, r = 0.4\sigma$ and $L_c = 10\sigma$ or $L_c = 20\sigma$.

6.6 Concluding remarks

We have developed a second-virial density functional theory for the chiral order in nematic phases. We set up a theoretical framework to obtain the equilibrium cholesteric pitch, eliminating (some) of the assumptions of Straley's approach [63]. The use of MC integration as numerical method for the calculation of the effective excluded volume renders the theory fast, easy to implement and suitable for a wide range of particle models. We apply our theory to study the cholesterics of short hard helices, an apparently simple colloidal model that displays a richer chiral behaviour than expected when considering long weakly chiral helices. In particular, we focus on the handedness of the cholesteric phase and we find a non-trivial dependence on particle shape and length, leading to a possible double sense inversion in some cases. We interpret our results as a competition between the geometric properties and the tendency of local alignment, resulting in a thermodynamic average of the difference in the excluded volume associated to right- and left-handed pairs. We also provide a quantitative comparison with Straley's theory, confirming that the most important features of the macroscopic chiral behaviour can be captured with that method as well. Our results provide new insights on the role of entropy in the link between micro- and macro-chirality, suggesting that entropy should not be overlooked in experiments on colloidal liquid crystals since most of the unexpected chiral phenomena could be ascribed to entropic effects only. However, the limited aspect ratio of our particles and the lack of other important features, for example flexibility, have to be considered to fully analyse the phase behaviour of some fd viruses [273, 279–282]. By incorporating short-range soft interactions into the hard helix model, we have shown that it is possible to assess the macroscopic chiral behaviour also beyond non purely hard-core colloids. However, it is likely that in order to deal with more complex inter-particle potentials, a more sophisticated implementation of MC integration should be considered.

The theoretical description of the chiral phase can also be improved. Since the biaxial order is expected to be strongly coupled to the chiral order [263, 264, 283, 284], future studies based on an orientation distribution function that explicitly accounts for the local biaxial arrangement, would provide new insights into the problem. Additionally, introducing local biaxiality would allow us to better understand the competition in systems of hard helices between the cholesteric phase and the recently discovered screw-like phase [37, 266]. Furthermore, our theory can easily be extended to mixtures, addressing other fundamental questions such as the doping of achiral nematic phases and the chiral behaviour of racemic mixtures. Finally, the recent progresses in chemical synthesis and in controlling the colloidal self-assembly processes, resulting in chiral superstructures, suggest that the number and variety of chiral building blocks will be soon enlarged [285–292]. Our approach will be useful to describe the macroscopic chiral behaviour of these new colloids.

6.7 Appendix: Computer simulations of a cholesteric phase formed by hard helices

An extensive computer simulation study on the phase behaviour of hard helices was performed by Kolli *et al.* [37, 265, 266, 293] and revealed interesting effects related to the chiral (and in some cases more specifically to the helical) shape on the macroscopic self-organisation. However, they did not explicitly obtain the isotropic-cholesteric transition in computer simulations but relied on the theoretical predictions (based on Straley's theory that are consistent with our results) to associate the uniaxial nematic phase that they obtained in their simulations with the cholesteric phase [293]. Furthermore, they showed that other phases, e.g. so-called screw-like nematic and different smectic phases, are stabilized and can compete with the cholesteric phase, and in some cases pre-empt the region of stability of the cholesteric phase. Clearly, the region of nematic/cholesteric stability is dependent on the particle aspect ratio, as already evidenced in the study of hard spherocylinders [118]. Therefore, longer helices would have a larger regime for which the cholesteric phase is stable (and phenomena like sense inversion could occur), at the price that longer helices implies longer cholesteric pitches (see Fig. 6.4), that eventually are not accessible with computer simulations of ordinary system sizes. Nevertheless, here we show that already in the case of hard helices with $L_c = 10\sigma$ ($N_s = 15$), $p = 8\sigma$, $r = 0.4\sigma$, for which we predict a quite short pitch close to the isotropic-cholesteric transition ($|\mathcal{P}| \simeq 90\sigma$), a cholesteric phase can be obtained by performing Monte Carlo simulations of 2100 particles between two hard smooth walls in the NVT ensemble. In Refs. [37, 265, 266, 293], 900 up to 2000 particles and standard periodic boundary conditions were employed since the focus was not on the cholesteric phase. Furthermore, we observe that a long run ($> 6 * 10^6$ MC steps) was needed to reach an equilibrated configuration. Because of the strong coupling between rotation and translation in the dynamics of helical particles (as noted also in the study of Refs. [37, 266]), as well as the existence of a screw-like nematic phase makes it particularly challenging to simulate this system. In Fig. 6.13(a) we show a time series of snapshots taken from a simulation run with an aligned achiral state used as initial configuration. Particles are colored according to the orientation of their main axis and the corresponding nematic director profile along the direction perpendicular to the two walls is depicted by the orientations of the rod-like segments. After long equilibration a spontaneous left-handed twist is propagated throughout the system. Interestingly, when a right-handed twisted configuration was used as initial configuration the system spontaneously twisted back (Fig. 6.13(b)) whereas when started from a left-handed, the sense remains the same (but changes in magnitude when the system is fully relaxed, see Fig. 6.13(c)), proving that hard helices with $L_c = 10\sigma$, $p = 8\sigma$, $r = 0.4\sigma$ stabilize indeed a cholesteric phase with opposite handedness (see Fig. 6.3(d)). The final cholesteric pitch seems also to be in agreement with the theoretical predictions ($|\mathcal{P}| \sim 70\sigma$) but in this thesis we did not investigate further the hard-helix system. On the other hand, in the next chapter, we will introduce a novel hard chiral particle model that we used to obtain by computer simulations (chronologically) the first evidence of a cholesteric phase purely stabilized by entropic interactions and we will discuss several aspects on how to study the cholesteric order in computer simulations.

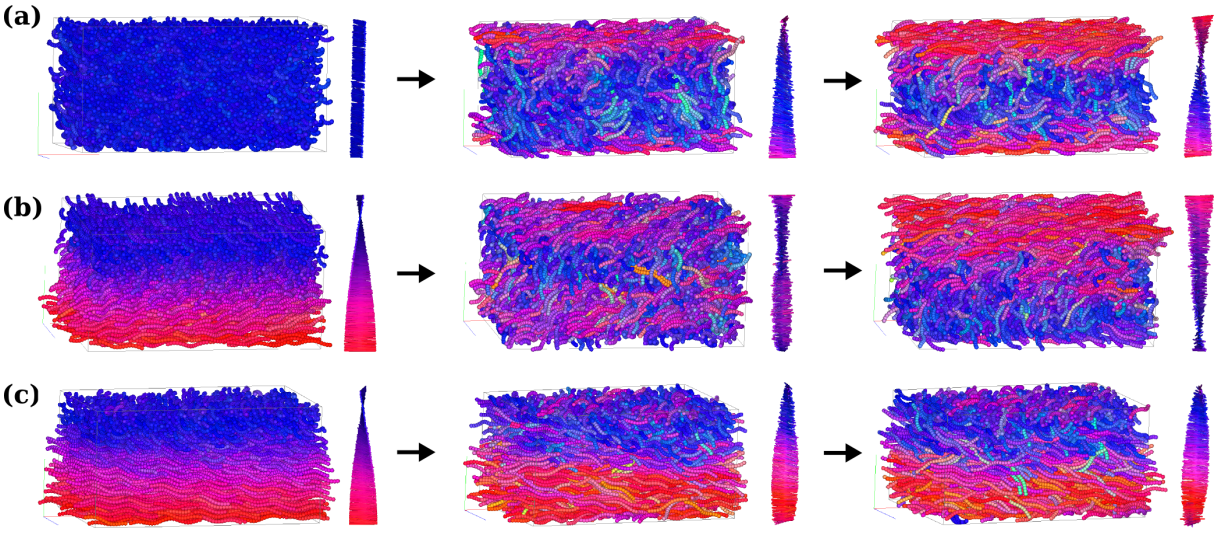

Figure 6.13: Simulation snapshots of cholesterics of hard helices with $p = 8\sigma$, $r = 0.4\sigma$, $L_c = 10\sigma$, obtained by NVT-Monte Carlo simulations of 2100 particles at a packing fraction $\eta \simeq 0.319$ and confined between two smooth hard walls. Particles are colored according to the orientation of their main axes and the corresponding nematic director profile along the direction perpendicular to the two walls is depicted by the orientation of the rod-like segments. (a) Time-series of configurations starting from an achiral state taken at time zero, after $4 * 10^6$ MC steps and after $9 * 10^6$ MC steps. The system spontaneously twists in a left-handed cholesteric. (b) Starting from a right-handed configuration, snapshots taken at time zero, after $3 * 10^6$ MC steps and after $6 * 10^6$ MC steps. The system twists back. (c) Starting from a left-handed initial configuration, snapshots taken at time zero, after $3 * 10^6$ MC steps and after $6 * 10^6$ MC steps. The left-handed twist is preserved but the magnitude of the cholesteric pitch changes upon system relaxation.

Acknowledgments

Some of the results presented in this chapter are part of a collaboration with Simone Belli, who originally developed the density functional theory under the supervision of René van Roij at the Institute for Theoretical Physics (UU). We thank SURFsara (www.surfsara.nl) for the support in using the Lisa Compute Cluster. We thank Mike Allen and Jon Doye for useful correspondence and discussions.

7

Twisted polyhedra: entropy-driven formation of prolate and oblate cholesteric phases by computer simulations

Predicting the macroscopic chiral behaviour of cholesteric liquid crystals from the microscopic chirality of the particles is highly non-trivial, even when the chiral interactions are purely entropic in nature. Here we introduce a novel chiral hard-particle model, namely particles with a twisted polyhedral shape and obtain, for the first time, a stable fully-entropy-driven cholesteric phase by computer simulations. By slightly modifying the triangular base of the particle, we are able to switch from a left-handed prolate to a right-handed oblate cholesteric using the same right-handed twisted particle model. Furthermore, we find qualitative agreement with an Onsager-like theory, suggesting that the latter can be used as a quick tool to scan the huge parameter space associated to the microscopic chirality. Our results unveil how the competition between particle biaxiality and chirality is reflected into the nematic self-organization and new theoretical challenges on the self-assembly of chiral particles can be undertaken.

7.1 Introduction

Since Onsager's prediction of a purely entropy-driven phase transition from an isotropic fluid of infinitely long hard Brownian rods to an orientationally ordered nematic phase [30], hard particles have served as paramount models in condensed matter studies. The seminal work on crystallization of hard spheres revealed the crucial role of computer simulations in proving that order can be induced by entropy alone [23, 24]. The macroscopic structure obtained by self-assembly of colloidal particles is often directly linked to the shape of the constituent building blocks [64, 294]. As soon as we move away from spherical particles a bewildering variety of thermodynamically stable structures with increasing complexity arises [64, 65]. As a result, a concurrent increase of simulation studies on hard particles show that entropy can be the sole driving force in the formation of crystals featuring different symmetries, plastic crystals, liquid crystals, and even quasi-crystals [31, 32, 64–67, 195, 266, 295, 296].

Shape anisotropy is the essential ingredient to form liquid crystals (LC), phases featuring long-range orientational order but no or only partial positional order [35]. Hard bodies have been extensively employed also in the field of LCs [52]. Thirty-five years after Onsager's prediction, the first entropy-stabilized nematic phase was observed in computer simulations of hard ellipsoids [31]. In the nematic liquid-crystalline phase, the particles are on average aligned along a preferred direction, identified by the nematic director $\hat{\mathbf{n}}$, but the positions are homogeneously distributed in the system. Additionally, hard spherocylinders were employed in simulations to demonstrate the thermodynamic stability of an entropy-driven smectic phase [32], in which the particles are orientationally ordered and arranged in smectic layers. This system has become a popular hard-particle model system to study LC phase behaviour [118, 120]. By introducing biaxiality in the hard-particle shape, the long-searched biaxial nematic phase has also been simulated [194, 195]. Furthermore, many other LC phases have been observed in simulations, which are entropy-driven, including a cubic gyroid phase [38] and a twist-bend nematic phase [36].

Surprisingly, from this long list of entropic LC and non-LC phases, a simulation evidence of a cholesteric phase made of hard particles is still missing, despite the facts that it was the first LC phase experimentally discovered [215] and that an entropic cholesteric phase was already theoretically predicted forty years ago [63]. A cholesteric phase displays an helical chiral arrangement of the director field, $\hat{\mathbf{n}}(z) = \left\{\cos\left(\frac{2\pi}{\mathcal{P}}z\right), \sin\left(\frac{2\pi}{\mathcal{P}}z\right), 0\right\}$, with z the axis of the macroscopic twist (chiral director) and $\mathcal{P}$ the cholesteric pitch that determines the typical length scale associated to the helical periodicity (see also Fig. 6.1). Several theoretical studies have been dedicated to better understand the link between microscopic and macroscopic chirality. A unified picture has still yet to be achieved since it is clear that the cholesteric pitch $\mathcal{P}$ depends in a non-trivial way on both the single-particle properties and the thermodynamic state of the system (for example see [63, 223, 247, 252, 263, 264]). The microscopic origin of chirality has also been the focus of experimental studies on colloidal systems [208, 219, 223], and of computer simulation studies based on strongly chiral attractive interactions [246, 250, 297].

The main reason that a cholesteric phase of hard bodies has never been observed in simulations is due to the fact that the cholesteric pitch length is on the order of hundreds or thousands times the particle length, and that huge system sizes, beyond

our computational limits, are needed to accomodate the cholesteric pitch. Recently, hard helices have been introduced as a simple particle model, but the formation of a cholesteric phase has never been addressed in simulations as the focus of these studies was more on the intriguing chiral phases that occur at high densities [266, 293] (see also Sec. 6.7). Hence it is still unsettled if and how a twist in the particle shape gives rise to the cholesteric order and several questions, that have been addressed by computer simulations for the achiral nematic phase, like nucleation, wetting etc... [120, 123], remained so far unexplored for the cholesteric phase.

7.2 A novel chiral hard particle model

Here, we show the first fully-entropy-driven cholesteric phase obtained by computer simulations of hard twisted polyhedral shaped particles. As we explain below, this particle model presents several shape features that can be easily tuned, e.g. aspect ratio, convexity, biaxiality, handedness, degree of twist (or molecular pitch), number of polyhedral faces. A systematic study of how these properties, some of which are intuitively associated to microscopic chirality and liquid-crystalline behaviour, affect the self-assembly of many of such particles, can be efficiently carried out by perfoming computer simulations. In particular, here we study the nematic phase behaviour of the simplest shape of this class, i.e., twisted triangular prisms (TTP). Our particle is obtained by twisting one base of an elongated triangular prism of height h, which is the distance between the two triangular bases, by an angle α relative to the other base and by adding additional edges to ensure flat faces (see Fig. 7.1). Remarkably, depending on the choice of which vertices are connected by these additional edges, it is possible to build both concave and convex chiral particles. The triangular base has fixed perimeter $\pi\omega$, such that in the limit of infinite number of sides (circle) the width ω coincides with particle diameter. In this study we consider concave TTPs with either equilateral or isosceles triangular bases defined by the base angle γ. When the top triangular base is rotated clockwise the twist angle α is positive and *it is tempting to call the TTP right-handed*. We return to this definition of particle handedness when we discuss our results for the oblate (discotic) cholesteric phases. We note that α should be less than or equal to the smallest angle of the base to avoid self-intersection of the particle shape. For convenience, we also introduce the vectors $\mathbf{u}$, $\mathbf{v}$, and $\mathbf{w}$ describing the TTP as shown in Fig. 1, which allow us to define the long, medium, and short dimensions of the TTP by their length $|\mathbf{u}|$, $|\mathbf{v}|$, and $|\mathbf{w}|$, whereas the particle frame is described by the long, medium, and short particle axis denoted by the unit vectors $\hat{\mathbf{u}}$, $\hat{\mathbf{v}}$, and $\hat{\mathbf{w}}$. Note that the height h coincides with $|\mathbf{u}|$. To detect overlaps between particles, i.e., the key ingredient in Monte Carlo (MC) simulations aimed to study the self-assembly of hard particles, we use an algorithm based on triangle-triangle intersection detection [57], which is also suitable for concave shapes. Analogously to spherocylinders (and other hard-rod models), the nematic phase can be stabilized at sufficiently high aspect ratio (h/ω) [118], whereas the particle chirality can be tuned by changing the twist angle α that also changes the molecular pitch $p \simeq 2\pi h/\alpha$. Additionally, by further modifying the particle shape (changing the base) we

study how the competition between biaxiality and chirality propagates from microscopic (single-particle) to macroscopic (self-assembled structure) level.

Nematic phases formed by biaxial particles can be distinguished in prolate (calamitic) N_+, oblate (discotic) N_- and biaxial N_b phases, depending on which particle axes feature long-range orientational order. By introducing a shape parameter based on the dimensions of the particle $\nu = |\mathbf{u}|/|\mathbf{v}| - |\mathbf{v}|/|\mathbf{w}|$, the type of nematic phase can roughly be predicted [62, 195] (cfr. Chap. 5): For $\nu > 0$, a prolate N_+ phase is expected, in which the long axes $\hat{\mathbf{u}}$ of the particles are aligned in the nematic phase along a common director, whereas for $\nu < 0$ an oblate N_- phase is predicted, where the short particle axes $\hat{\mathbf{w}}$ display long-range orientational order. When $\nu \sim 0$ a biaxial phase is predicted to be stable, in which both the short and long particle axes show long-range orientational order, provided that other conditions that are strongly shape-dependent are also satisfied (for example for rounded board-like particles considered in Ref. [195] there is an additional condition of $|\mathbf{u}|/|\mathbf{w}| \geq 9$).

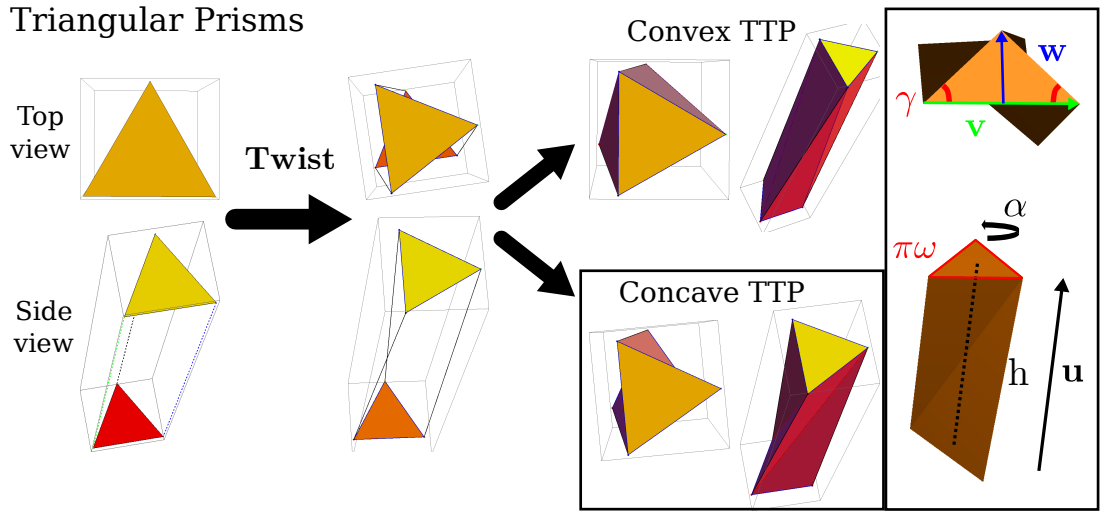

Figure 7.1: A twisted triangular prism (TTP) is constructed from an elongated prism of height h with (isosceles) triangular bases, determined by the angle γ, and perimeter $\pi\omega$. The width ω is used as the unit of length. To introduce chirality, one triangular base is twisted by an angle α relative to the other one and additional edges are constructed to obtain flat faces. The orientations of the main axes are described by the unit vectors $\hat{\mathbf{u}}$ (long), $\hat{\mathbf{v}}$ (medium) and $\hat{\mathbf{w}}$ (short).

7.3 Methods

For TTP with $\gamma \lesssim 1.10715$, $|\mathbf{v}| = \pi\cos\gamma/(1+\cos\gamma)$ and $|\mathbf{w}| = \pi\sin\gamma/(2+2\cos\gamma)$, such that the shape parameter $\nu = h(1+\cos\gamma)/\pi\cos\gamma - 2/\tan\gamma$, where $h = |\mathbf{u}|$ is the height of the particle (cfr. Sec. 5.2). The volume of the particle is calculated by using standard formulas for orientable polyhedra that requires the knowledge of face normals and vertices positions. Overlaps between particles are detected by checking intersections between triangular faces using the RAPID library [57].

Thousands of particles are simulated using standard MC simulation methods in either the NVT or NPT ensemble. In the former, MC moves consist in either single-particle translation or rotation whereas in the latter also volume-change moves (both isotropic and anisotropic scaling) are employed. Several millions of MC steps are performed both in the equilibration and production runs, where one MC step is defined as N moves, with N the number of particles. Different boundary conditions and initial configurations are used, as specified in the text. In the case of hard walls (located at $z = 0$ and $z = L_z$), the overlap detection between particles and walls is performed by checking if any vertices of the polyhedra have coordinates $z < 0$ or $z > L_z$. For the implementation of twisted boundary conditions we refer to [253]. To obtain the equilibrium equation of state we combined results obtained by starting from an isotropic configuration, from a dilute lattice and from a dense aligned lattice (constructed by first obtaining the closest packing of a few particles in an orthogonal cuboidal box). States equilibrated at close pressures are also used as initial configurations to avoid kinetic traps. To determine the transitions between different thermodynamic phases, we have calculated several order parameters in both the NPT and NVT ensembles. Using equilibrated configurations we also set up long (more than 6×10^6 MC steps) NVT simulations to accurately measure the cholesteric pitch $\mathcal{P}$. After dividing the system in slabs, by diagonalizing the tensor $\mathcal{Q}^{\hat{\mathbf{u}}}_{\alpha\beta} = (\sum_i 3\hat{\mathbf{u}}_{i\alpha}\hat{\mathbf{u}}_{i\beta} - \delta_{\alpha\beta})/2n$, where $\alpha, \beta = x, y, z$ and $i = 1, ..., n$ with n the number of particles in the slab, we compute the nematic director $\hat{\mathbf{n}}_{\hat{\mathbf{u}}}$ and the associated nematic order parameter $S^{\hat{\mathbf{u}}}$. The same procedure is repeated for the medium particle axis $\hat{\mathbf{v}}$ and the short axis $\hat{\mathbf{w}}$. We obtain $S^{\hat{\mathbf{v}}}$ and $S^{\hat{\mathbf{w}}}$, which are the largest eigenvalues of $\mathcal{Q}^{\hat{\mathbf{v}}}_{\alpha\beta} = (\sum_i 3\hat{\mathbf{v}}_{i\alpha}\hat{\mathbf{v}}_{i\beta} - \delta_{\alpha\beta})/2n$ and $\mathcal{Q}^{\hat{\mathbf{w}}}_{\alpha\beta} = (\sum_i 3\hat{\mathbf{w}}_{i\alpha}\hat{\mathbf{w}}_{i\beta} - \delta_{\alpha\beta})/2n$. Again, the nematic directors $\hat{\mathbf{n}}_{\hat{\mathbf{v}}}$ and $\hat{\mathbf{n}}_{\hat{\mathbf{w}}}$ are the associated eigenvectors. Note that we neglect here the polar nature of the particle along the axis $\hat{\mathbf{n}}_{\hat{\mathbf{w}}}$ as we assume up-down symmetry $\hat{\mathbf{n}}_{\hat{\mathbf{w}}} = -\hat{\mathbf{n}}_{\hat{\mathbf{w}}}$. However, we checked that it did not affect our results. Averaging the profiles $S(z)$, the bulk values are obtained for each state point.

For each configuration we calculate $\cos(\theta(z)) \equiv \hat{\mathbf{n}}_{\hat{\mathbf{u}}}(z) \cdot \hat{\mathbf{n}}_{\hat{\mathbf{u}}}(z = 0)$ and we bypass the up-down symmetry by taking the absolute value $|\cos(\theta(z))|$. After averaging hundreds of such profiles, we perform a one-parameter fit using $|\cos(2\pi z/\mathcal{P})|$ to extract the cholesteric pitch $\mathcal{P}$. In addition, orientational pair-correlation functions, as introduced in Ref. [250], are calculated along the chiral director (parallel to the z-axis).

$$\mathcal{S}^{\hat{\mathbf{u}}}_{220}(z) = \langle 3/2(\hat{\mathbf{u}}_i \cdot \hat{\mathbf{u}}_j)^2 - 1/2 \rangle \tag{7.1}$$

describes the nematic order between two particles i and j separated by distance $z = z_{ij}$, with $\langle . \rangle$ indicating an average over all the particles and different configurations. The distance between the maximum and the minimum of $\mathcal{S}^{\hat{\mathbf{u}}}_{220}(z)$ corresponds to half the cholesteric pitch length.

$$\mathcal{S}^{\hat{\mathbf{u}}}_{221}(z) = \langle [(\hat{\mathbf{u}}_i \times \hat{\mathbf{u}}_j) \cdot \hat{\mathbf{z}}_{ij}](\hat{\mathbf{u}}_i \cdot \hat{\mathbf{u}}_j) \rangle \tag{7.2}$$

describes the chiral organization between the two particles i and j along the z-axis. Analogously, the functions $\mathcal{S}^{\hat{\mathbf{w}}}_{220}(z)$ and $\mathcal{S}^{\hat{\mathbf{w}}}_{221}(z)$ refer to the short axis $\hat{\mathbf{w}}$.

The simulation results are compared with those obtained using a second-virial classical density functional theory that is extensively described in Chap. 6 and in Refs. [252, 298]. The input of such a theory is the pitch-dependent Legendre-expanded excluded-volume

between two particles with orientation $\mathcal{R}, \mathcal{R}'$ separated by a distance $\mathbf{r}$:

$$E_{ll'}(q) = -\int d\mathbf{r} \oint d\mathcal{R}\, d\mathcal{R}' f(\mathbf{r}, \mathcal{R}, \mathcal{R}') P_l(\hat{\mathbf{n}}_q(z) \cdot \hat{\mathbf{u}}) P_{l'}(\hat{\mathbf{n}}_q(0) \cdot \hat{\mathbf{u}}') \tag{7.3}$$

with P_l the normalized Legendre polynomial of grade l=0, 2,...,20 (only even coefficients are considered), $q = 2\pi/\mathcal{P}$ the chiral wave vector, $\hat{\mathbf{n}}_q(z) = \hat{\mathbf{x}} \sin qz + \hat{\mathbf{y}} \cos qz$ the nematic director profile and f the Mayer function that assumes a value -1 if particles overlap and 0 otherwise. The coefficients $E_{ll'}(q)$ are calculated using a MC integration scheme. Once these coefficients are calculated, the orientation distribution function $\psi(\theta)$, with θ the polar angle with respect to the local nematic director, is obtained by minimizing a Parsons-Lee-Onsager-like free-energy functional [30, 124, 125] yielding the following equation:

$$\psi(\cos\theta) = \frac{1}{Z} \exp\left\{ -n\, G(\eta) \sum_{l,l'=0}^{\infty} \frac{E_{ll'}(q)}{4\pi^2} \frac{1}{2} \left[\mathcal{P}_l(\cos\theta)\psi_{l'} + \mathcal{P}_{l'}(\cos\theta)\psi_l \right] \right\}, \tag{7.4}$$

with n the number density, $G(\eta)$ the Parsons-Lee correction, ψ_l the expansion coefficients of $\psi(\cos\theta)$ and Z the normalization factor. Finally, the equilibrium pitch $\mathcal{P}$ is obtained by inserting back $\psi(\theta)$ into the functional and identifying the minimum of the free energy.

7.4 Formation of the cholesteric phase

To investigate whether or not the twist in the particle shape is transmitted at a macroscopic level, we perform MC simulations of thousands of TTPs using different initial configurations and boundary conditions, finding consistent results. In this section we present results from MC simulations using standard periodic boundary conditions (PBC) in the NPT ensemble, i.e., at fixed number of particles N, pressure P, and temperature T, and we investigate the kinetic pathways for the formation of a *prolate* cholesteric phase.

Left-handed cholesteric phase

We first consider 2000 TTPs with a strong particle twist $\alpha = 0.7$, and with an aspect ratio $h/\omega = 5$ with an almost equilateral base ($\gamma = 1.0$), yielding $\nu \simeq 3.25 > 0$. We start from an isotropic phase (I) and perform a compression by fixing the pressure $\beta P\omega^3 = 1.5$ with $\beta = 1/(k_B T)$ and k_B Boltzmann's constant. Fig. 7.2(a) clearly demonstrates the formation of a prolate nematic phase (N_+^*) with a spontaneous macroscopic *left-handed* twist upon increasing the density. The resulting structure has been characterized using appropriate order parameters as shown in Fig. 7.3 and described in detail in the following section. We notice here that the *opposite* handedness of the cholesteric phase with respect to the particle twist is consistent with theoretical predictions [63, 252, 263, 298] for chiral particles with a large molecular pitch p, in this case $p/\omega \simeq 44.8$. The phase transformation from I to N_+^* is driven first by nematic fluctuations due to the anisotropy of the overall particle shape, and subsequently, the nematic phase becomes twisted as a result of the finer details of the chiral particle shape. Additionally, we confirm the stability of the N_+^* phase by starting from a uniaxial nematic state. We observe that the achiral order is clearly unstable since a twist starts to propagate slowly throughout the whole system. Our simulations show that a stable prolate cholesteric phase is found for a large range of twist angles, i.e., $0 \lesssim \alpha \lesssim \gamma$, and base angles $0.55 \lesssim \gamma \lesssim \pi/3$.

Kinetic pathways

We now investigate in more detail the kinetic pathways leading to N_+^* in case of short chiral rods. To this end, we focus on large systems of TTPs with aspect ratio $h/\omega = 5$, an isosceles base with angle $\gamma = 0.75$ and a particle twist angle $\alpha = 0.7$, yielding a shape parameter $\nu \simeq 1.62 > 0$. First, we determine the pressure $\beta P\omega^3$ and nematic order parameters S associated to the three main axes $\mathbf{u}, \mathbf{v}, \mathbf{w}$ as a function of packing fraction η as shown in Fig. 7.3(b). From the equation of state, we find that the IN_+^* transition occurs at a pressure $\beta P\omega^3 \simeq 1.25$, and the transition from a cholesteric phase to a higher ordered one, that we generically denote as chiral smectic (Sm^*), takes place at a pressure $\beta P\omega^3 \simeq 2.6$ (see Fig. 7.4 for more details). A closer look to the formation of the cholesteric phase reveals that for sufficiently high supersaturation of the isotropic phase ($\beta P\omega^3 = 1.9$), the transformation proceeds via spinodal decomposition, in analogy with achiral short spherocylinders [120], see Fig. 7.2(b). We clearly observe that the system is unstable as immediately many small nematic clusters with different orientations are formed throughout the system, which subsequently start to twist. Interestingly, the

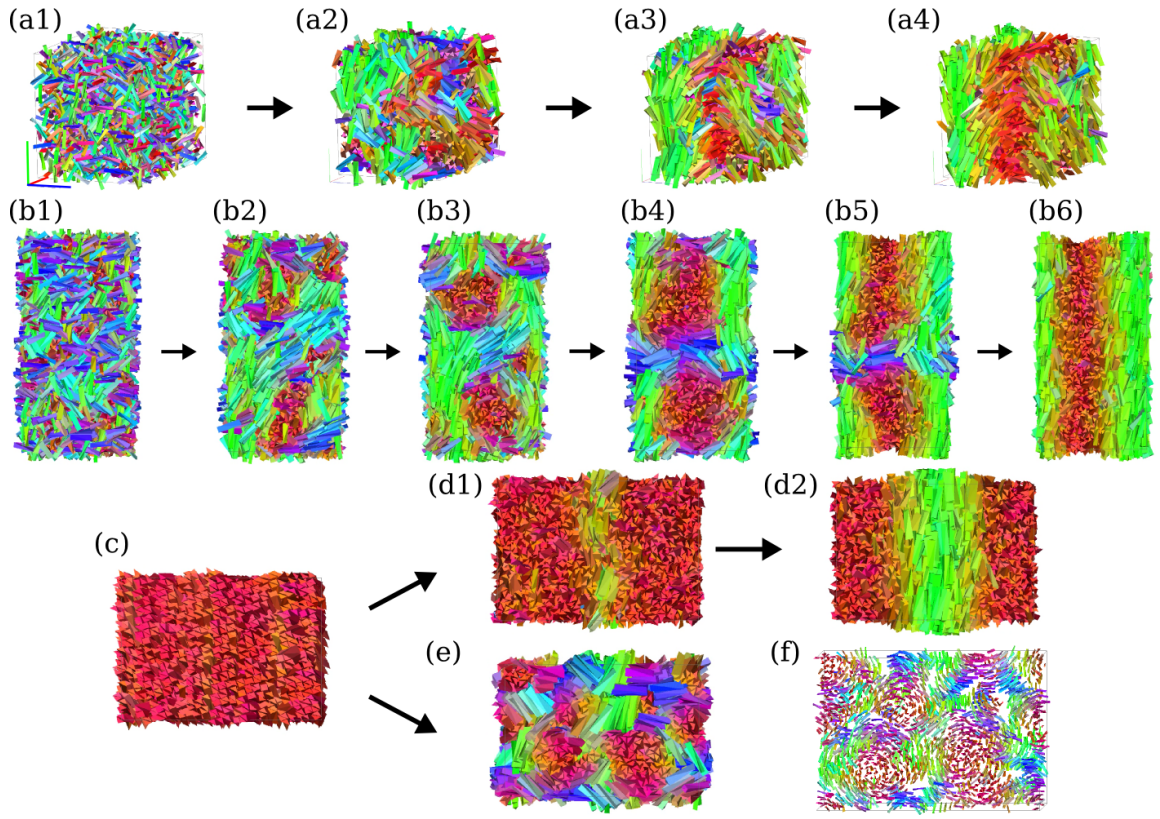

Figure 7.2: Kinetic pathways for the formation of a prolate cholesteric phase from MC simulations in the NPT ensemble under standard periodic boundary conditions. The particles are colored according to the orientation of their main axis $\hat{\mathbf{u}}$. **(a)** Snapshot time series of 2000 TTP with aspect ratio $h/\omega = 5$, base angle $\gamma = 1.0$, and particle twist angle $\alpha = 0.7$, starting from an isotropic state (a1) and imposing a pressure $\beta P\omega^3 = 1.5$. Evolution in time corresponds to an increase of the system packing fraction. The resulting phase (a4) is a *left-handed* cholesteric. **(b)** Snapshot time series of 3200 TTP with $h/\omega = 5$, $\gamma = 0.75$, and $\alpha = 0.7$, starting from an isotropic state (b1) and imposing $\beta P\omega^3 = 1.9$. In this case a spinodal instability is observed: chiral nematic domains are first formed, resembling a blue phase (b3), and slowly merge into a cholesteric defect-free phase. **(c)** Dense aligned state of 2304 TTP with $h/\omega = 5$, $\gamma = 0.75$, and $\alpha = 0.7$ used as initial configuration for expansion runs. **(d)** At pressure $\beta P\omega^3 = 2.1$ the twist slowly propagates from the center of the system (d1) to the entire system (d2) and also in this case a cholesteric phase is formed. **(e)** At higher pressure ($\beta P\omega^3 = 2.9$) an instability with respect to nematic orientational fluctuations as well as smectic layering fluctuations is observed, resulting into a *metastable* state of chiral domains composed of highly aligned particles, which bears close resemblance to a blue phase. See also panel **(f)** where the particle size is reduced.

intermediate phase looks remarkably similar to a blue phase [35, 297], but after a long equilibration time the twisted nematic domains start to merge and the system relaxes to a cholesteric phase. Finally, we also study the phase transformation starting from a dense aligned phase. We perform NPT-MC simulations both at a pressure $\beta P\omega^3 = 2.1$ corresponding to a stable N_+^* phase, and at $\beta P\omega^3 = 2.9$, where the Sm^* phase is expected to be stable. For $\beta P\omega^3 = 2.1$, we indeed find that the director field immediately starts

to twist in the aligned phase of TTPs, resulting into a cholesteric phase as shown in Fig. 7.2(c)-(d). On the other hand, at $\beta P\omega^3 = 2.9$, the system is unstable with respect to both nematic orientational fluctuations as well as smectic layering fluctuations as seen in Fig. 7.2(e), and again the final structure bears close resemblance to a blue phase, which probably corresponds to a metastable (kinetically arrested) state as the Sm^* phase is expected to be the stable state. However, this suggests an intriguing competition between packing and chirality at high pressures that will be further investigated in future studies.

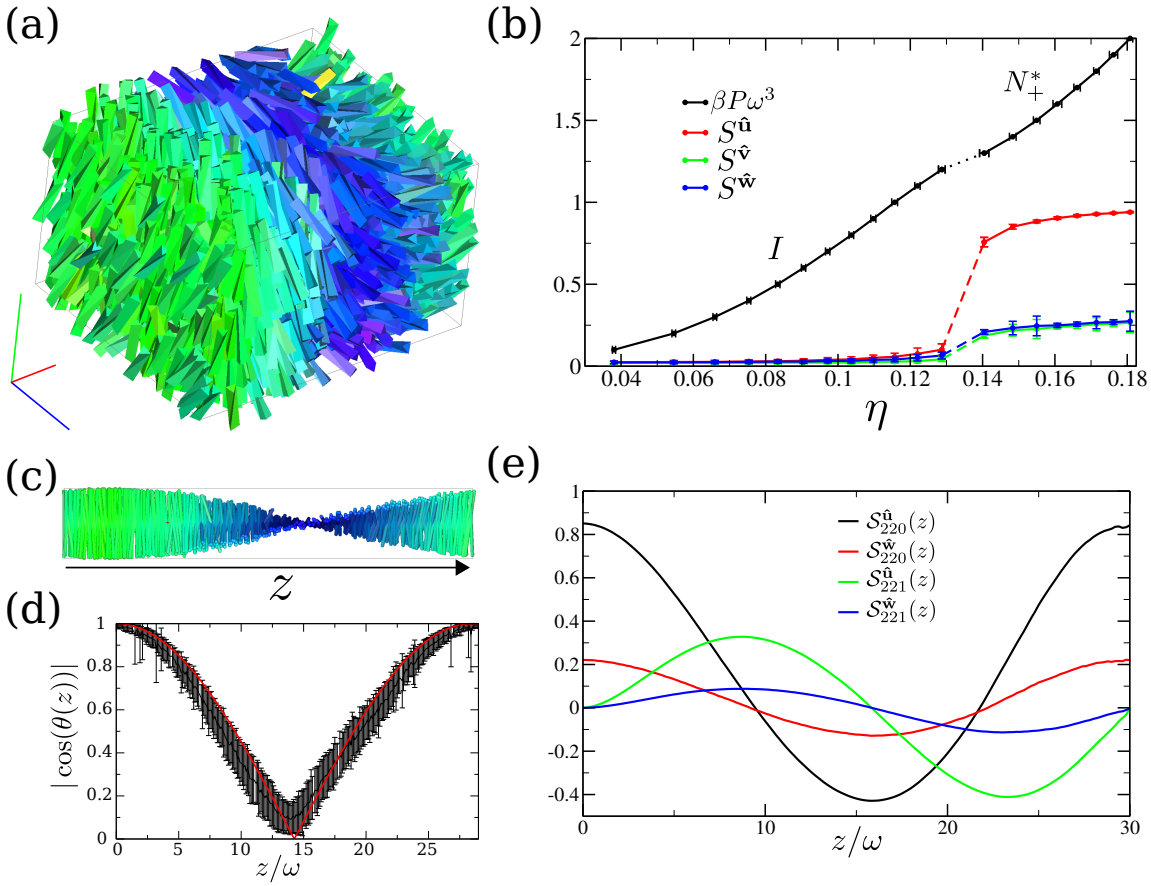

Figure 7.3: **(a)** Typical configuration as obtained from simulations of a prolate cholesteric phase of TTPs with aspect ratio $h/\omega = 5$, twist angle $\alpha = 0.7$, and base angle $\gamma = 0.75$ using PBC. Particles are colored according to the orientation of their main axis $\hat{\mathbf{u}}$. **(b)** Equation of state and nematic order parameters S associated to the particle main axis $\mathbf{u}$,$\mathbf{v}$,$\mathbf{w}$, as a function of the packing fraction η. **(c)** Nematic director profile $\hat{\mathbf{n}}_{\hat{\mathbf{u}}}$ depicted by using rods color-coded according to their orientation. **(d)** The twist is quantified by averaging hundreds of such profiles after measuring $|\cos(\theta(z))|$, with θ the twist angle along the z-direction that identifies the chiral director. The fit used to extract the cholesteric pitch $\mathcal{P}$ is indicated with a red line. **(e)** Orientational pair-correlation functions (see Sec. 7.3) calculated along the chiral director (z-direction), confirming the helical cholesteric structure and the left-handed sense of twist.

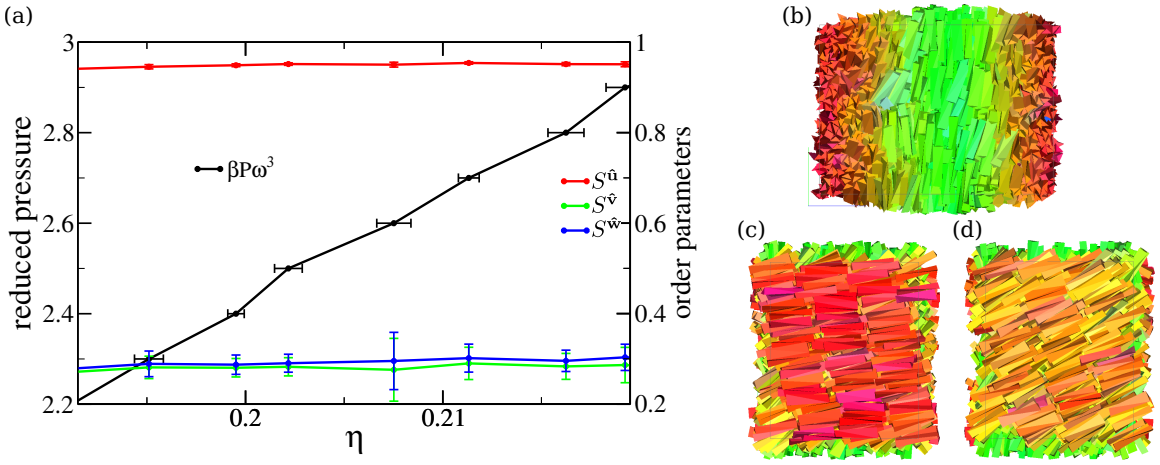

Figure 7.4: (a) The pressure $\beta P\omega^3$ (left y-axis) and nematic order parameters S (right y-axis) as a function of packing fraction η as obtained by MC simulations in the NPT ensemble with PBC for TTPs with aspect ratio $h/\omega = 5$, base angle $\gamma = 0.75$, and particle twist angle $\alpha = 0.7$. Snapshots in (b)-(c)-(d) are taken from a typical configuration at $\beta P\omega^3 = 2.9$. At this pressure the helical structure is still mantained (side view in panel (b)) but in the direction perpendicular to the chiral director the particles form smectic layers (panels (c) and (d) show cuts through the sample), corresponding to a chiral smectic phase generically denoted as Sm^*. Due to the small number of layers and particles in each slabs of the system the use of ordinary translational smectic order parameter does not locate accurately the transition from the cholesteric to Sm^*, that is therefore estimated by visual inspection of the configurations. The exact identification of the phase, that is more likely a twisted grain boundary chiral smectic A, and its stability, are beyond the scope of this chapter.

7.5 Equilibrium cholesteric pitch

We now turn our attention to the helical structure of the cholesteric phase. We want to determine the equilibrium cholesteric pitch $\mathcal{P}$ and study how boundary conditions and finite-size effects influence this quantity, that ultimately is the parameter quantifying the macroscopic chirality. To this end, we analyse the spatial dependence of the nematic director by dividing the system in slabs [246, 297] along the axis of the macroscopic twist, also called chiral director, which is oriented along the z-axis. We then compute the nematic director $\hat{\mathbf{n}}_{\hat{\mathbf{u}}}(z)$ corresponding to the long particle axis $\hat{\mathbf{u}}$, an example of such a profile is depicted in Fig. 7.3(c), and the associated nematic order parameter $S^{\hat{\mathbf{u}}}$ as displayed in Fig. 7.3(b). The same procedure is repeated for the medium particle axis $\hat{\mathbf{v}}$ and the short axis $\hat{\mathbf{w}}$ to obtain $S^{\hat{\mathbf{v}}}$, $S^{\hat{\mathbf{w}}}$ (see Fig. 7.3(b)), and $\hat{\mathbf{n}}_{\hat{\mathbf{v}}}$, $\hat{\mathbf{n}}_{\hat{\mathbf{w}}}$ (not shown).

The equilibrium pitch $\mathcal{P}$ is calculated by performing a one-parameter fit on $|\cos(\theta(z))|$ that quantifies the twist in the system (see Sec. 7.3 for details). Although our procedure removes the (small) intrinsic drift of the system occurring over different configurations, the statistical error on $\mathcal{P}$ is still on the order of several ω. The cholesteric helical structure and the sense of twist are further confirmed by orientational pair-correlation functions, shown in Fig. 7.3(e).

It is important to note that in the case of PBC the nematic director should be the same at the edges of the simulation box, i.e., $\cos(\theta(z = L_z)) = 1$ in Fig. 7.3(d) with L_z the box length in the z-direction. As a consequence, the cholesteric pitch $\mathcal{P}$ must be commensurate with L_z, i.e., L_z should be at least $\sim \mathcal{P}/2$ to observe a twist in the nematic phase [250]. By allowing the box shape to relax, either by performing NPT simulations or NVT simulations using a variable box shape, we expect the accuracy of the equilibrium pitch measurement to improve, but by repeating our simulations for different system sizes, we still observed a dependence on the initial box size (see Fig. 7.5(a)).

In order to circumvent the commensurability problems with pitch and box size, we embed the system between two planar hard walls in such a way that the nematic director can freely choose its orientation at both walls, and we perform simulations in the NVT ensemble. As can be observed from Fig. 7.6(a)-(b), the nematic director profile is indeed not commensurate anymore with L_z thereby allowing for a full relaxation of the macroscopic chiral twist. Since we simulate sufficiently large system sizes at state points that are well inside the stable region of the cholesteric phase, we expect that surface effects, such as pronounced layering or increased biaxiality [123, 299], should be negligible. We indeed observe that the walls only affect the structure at distances smaller than $\sim$ one particle diameter from the wall (see Fig. 7.7). In order to support this, we determine the equilibrium pitch $\mathcal{P}$ using different system sizes (different number of particles and different box dimensions), but at fixed packing fraction η. Panels (b) and (c) of Fig. 7.6 show indeed consistent results for the nematic director profile as well as for the value of $\mathcal{P}$. We thus regard this method to be the most convenient and reliable way for calculating the equilibrium pitch $\mathcal{P}$, in analogy with the conclusions of Ref. [246].

Finally, we perform simulations using twisted boundary conditions (TBC) [253]. We find good equilibration of our cholesteric phases of TTPs, as evidenced in Fig. 7.5(b) by the much smaller errror bars on the nematic director profile and the difference of $\pi/2$ in the θ angle at the edges of the box as imposed by the TBC. However, the use of TBC

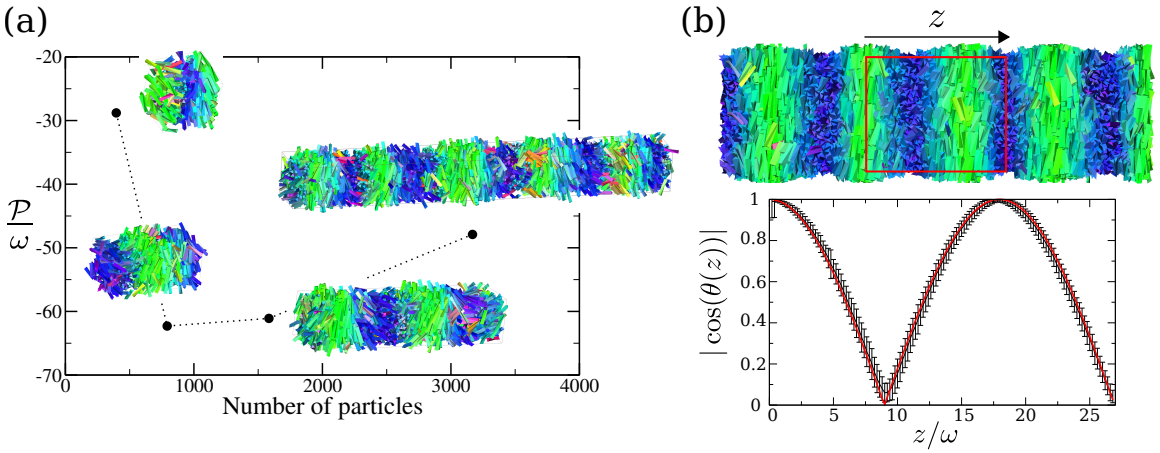

Figure 7.5: **(a)** Cholesteric pitch $\mathcal{P}$ as a function of number of particles N as obtained from MC simulations in an NVT ensemble, but allowing the simulation box to change side dimensions while keeping the volume fixed (packing fraction $\eta \simeq 0.18$). TTP with aspect ratio $h/w = 5$, twist angle $\alpha = 0.7$, and base angle $\gamma = 1.0$. Standard periodic boundary conditions (PBC) are employed, which results in a strong dependence on the initial box size. System sizes correspond to 2,4,8 times the smallest size considered. **(b)** Simulations of the same TTPs, but using twisted boundary conditions. The snapshot shows the boundaries of the simulation box in red and the first periodic images. The macroscopic twist $|\cos(\theta(z))|$, with θ the twist angle along the z-direction corresponding to the chiral director. The fit used to extract the cholesteric pitch $\mathcal{P}$ is indicated with a red line (see main text for more details). Note the difference of $\pi/2$ in the θ angle at the edges of the simulation box as imposed by the twisted boundary conditions [253].

may result into an over- or undertwisted cholesteric phase, and only by measuring the pressure tensor, which is unfortunately not straightforward for hard particles, it would be possible to extract the equilibrium value of $\mathcal{P}$ [254]. This procedure is based on a quadratic approximation around the free-energy minimum [254] and TTPs will be a suitable system to test this approach.

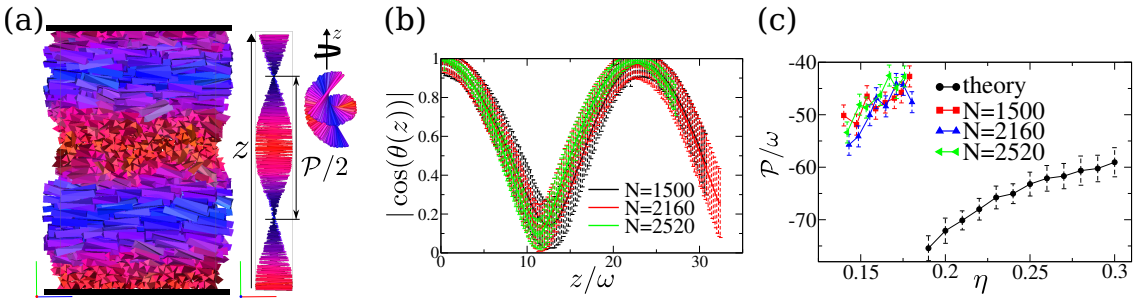

Figure 7.6: **(a)** Typical left-handed cholesteric along with cartoons of $\hat{\mathbf{n}}_{\hat{\mathbf{u}}}$ as obtained from NVT-MC simulations on systems of TTPs with aspect ratio $h/\omega = 5$, twist angle $\alpha = 0.7$, and base angle $\gamma = 0.75$ confined between two planar hard walls (in the z-direction). The particles are colored according to the orientation of their main axis $\hat{\mathbf{u}}$. **(b)** Local director profiles $\theta(z)$ obtained by simulations using varying number of particles N and varying box sizes but at fixed packing fraction $\eta \simeq 0.16$. **(c)** Cholesteric pitch $\mathcal{P}$ versus packing fraction η as obtained from simulations (using hard walls) and a second-virial density functional theory [252, 298].

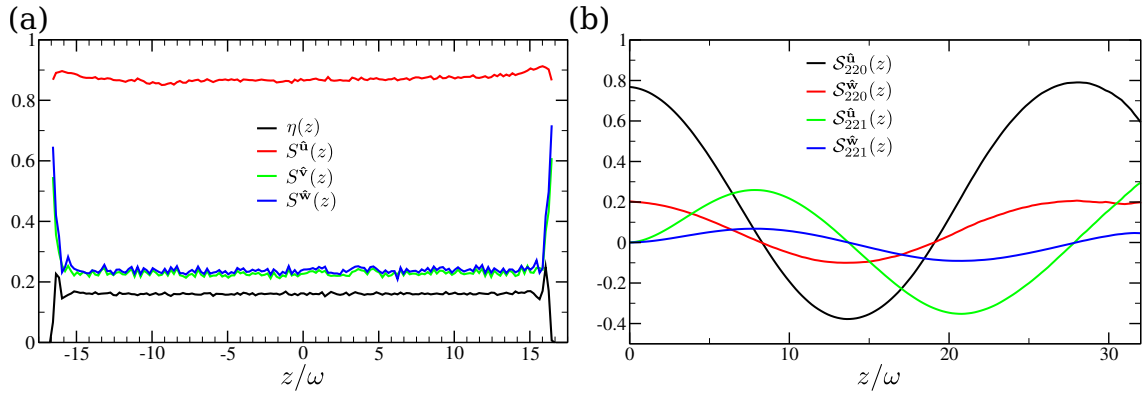

Figure 7.7: **(a)** Packing fraction $\eta(z)$ and nematic order parameter profiles $S(z)$ for TTPs with $h/\omega = 5$, $\alpha = 0.7$ $\gamma = 0.75$ between two hard walls (situated in the z-direction) obtained by simulations in NVT ensemble ($N = 2160$, $\eta \simeq 0.16$). **(b)** Orientational pair-correlation functions for the same system (cfr. Fig. 7.3(e)). The helical structure is maintained but it does not need to be commensurate with the box size.

7.6 Comparison with second-virial theory

The availability of cholesteric phases obtained from particle-based simulations provides a new testing ground for the theoretical framework describing the chiral organization in liquid crystals. We apply our recently developed second-virial density functional theory (DFT) [252, 298] (cfr. Chap. 6) to systems of TTPs and calculate the density dependence of $\mathcal{P}$. Our DFT is an extension of Onsager's theory [30] corrected with a Parsons-Lee (PL) prefactor to deal with the finite size of the particles [124, 125]. It represents an advancement over Straley's approach [63] as it does not consider the chirality in a perturbative way and it is combined with a MC integration to make it suitable for a wide range of particle models [298]. A detailed description can be found in Refs. [252, 298]. In Fig. 7.6(c) we present our results as obtained from simulations along with the DFT predictions. We plot $\mathcal{P}$ as a function of η in the range where the cholesteric phase is stable. We observe that the theory correctly captures the twist handedness, the magnitude and the trend of $\mathcal{P}$ as a function of η. In addition, we study the effect of particle shape on the cholesteric pitch $\mathcal{P}$. In Fig. 7.8(a), we present simulation results for the pitch $\mathcal{P}$ as a function of η for varying twist angle α and base angle γ. Comparing the results for $\alpha = 0.6$ (red curve) with $\alpha = 0.7$ (green) at fixed $\gamma = 0.75$, or $\alpha = 0.7$ (blue) with $\alpha = 0.8$ (yellow) at $\gamma = 1.0$, reveals that $|\mathcal{P}|$ decreases upon increasing α, i.e., increasing the microscopic chirality of the particle, as expected. Analogously, by decreasing the base angle γ, the surface associated with the longer side of the base gets larger, which effectively increases the particle chirality, thereby yielding a smaller pitch $|\mathcal{P}|$. This trend can be appreciated by comparing the results for $\gamma = 1.0$ (blue) with $\gamma = 0.75$ (green) at fixed $\alpha = 0.7$ or $\gamma = 0.9$ (red) with $\gamma = 0.75$ (black) at fixed $\alpha = 0.6$. Despite an overall little underestimation of the macroscopic twist, Fig. 7.8(b) shows that all these trends are well-captured by our DFT calculations: increasing the particle chirality, by either twisting the particle more (increasing α) or increasing the particle biaxiality (by decreasing γ), results indeed in a smaller cholesteric pitch $|\mathcal{P}|$. However, we notice that

the effect of decreasing γ on particle chirality is overestimated by the DFT with respect to the results obtained from simulation of the many-particle system. Nevertheless, the DFT can be used as a reliable and quick tool for predicting the macroscopic chiral behaviour from the microscopic chiral particle properties. We therefore use our theory to study the effect of TTPs with multiple twists on the cholesteric pitch P. Our DFT calculations as shown in Fig. 7.9(b) reveal that upon decreasing the microscopic pitch length p/ω, the sense of the macroscopic twist changes from opposite to same handedness with in between a regime where a twist inversion occurs with packing fraction, which is analogous to previous results on hard helices [252, 298] (cfr. Chap. 6). In the conclusions we will discuss possible improvements for the theoretical framework.

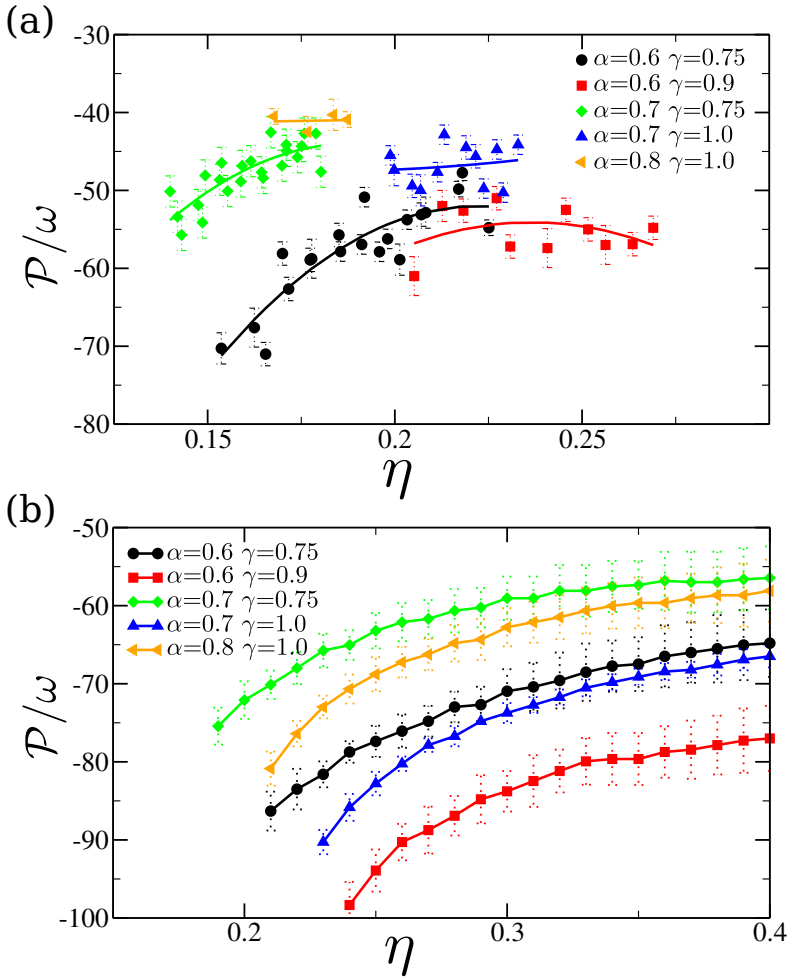

Figure 7.8: **(a)** Cholesteric pitch $\mathcal{P}$ versus packing fraction η as obtained by MC simulations (using hard walls) for TTPs with varying twist angles α and base angles γ as labelled. Lines are polynomial fits used as guides to the eye. **(b)** Theoretical predictions for the same particle models obtained by second-virial DFT [252, 298]. An increase in the twist angle α while keeping fixed the base angle γ corresponds to a shorter cholesteric pitch $|\mathcal{P}|$. Analogously, keeping fixed α and decreasing γ enhance the particle chirality and a corresponding shorter $|\mathcal{P}|$. However, this effect seems to be overestimated by theory resulting in a slightly different chiral ranking for the models considered here. In Fig. 7.9(a) the same results are shown by using the nematic order parameter instead of the packing fraction and similar conclusions are drawn.

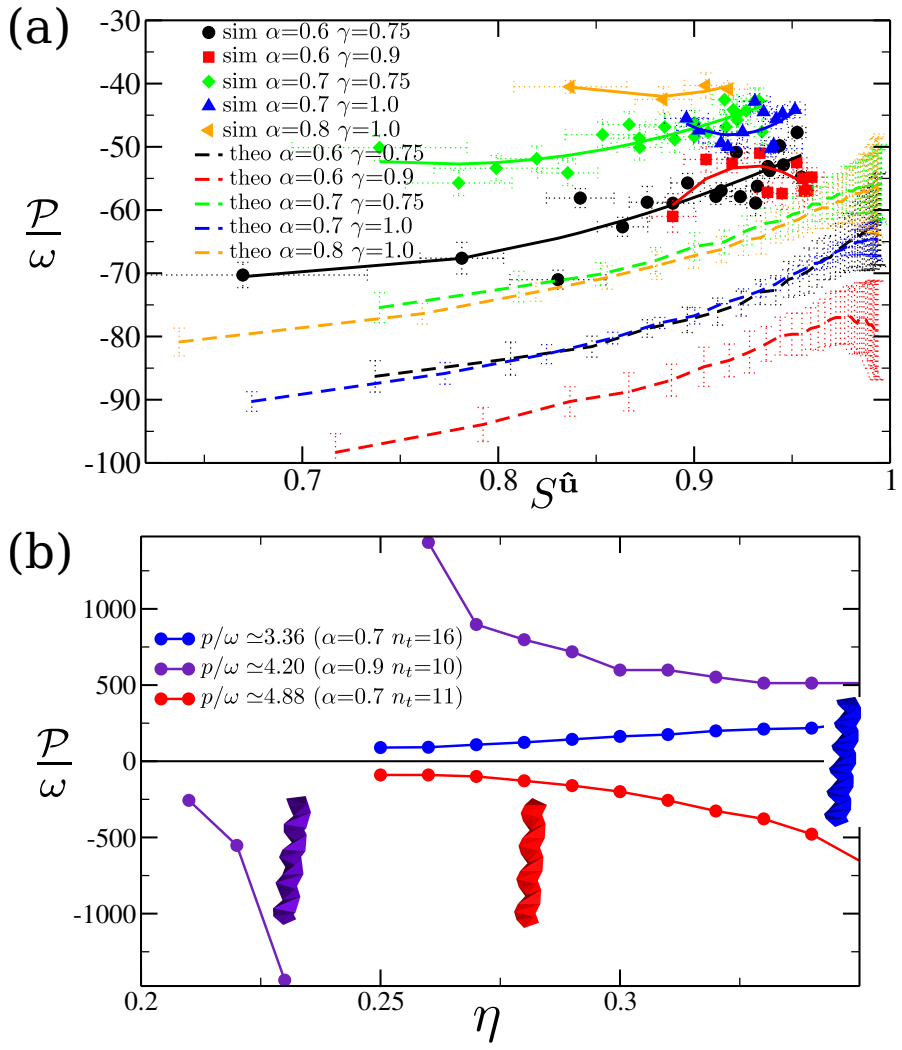

Figure 7.9: **(a)** Comparison between simulations (symbols and solid lines used as guides to the eye) and theoretical results (dashed lines) for the cholesteric pitch $\mathcal{P}$ as a function of the nematic order parameter $S^{\hat{\mathbf{u}}}$ associated to the particle long axis for the same particle models considered in Fig. 7.8. **(b)** Theoretical predictions for the cholesteric pitch $\mathcal{P}$ as a function of packing fraction η for TTPs with multiple twists (*triple hard helices*) with aspect ratio $h/\omega = 6$, and an equilateral triangular base ($\gamma = \pi/3$) and varying α and number of twists n_t such that the molecular chiral pitch $p/\omega \simeq 2\pi h/(n_t \alpha \omega)$ varies as indicated in the legend. Depending on p, the cholesteric pitch $\mathcal{P}$ can be positive (right-handed), negative (left-handed) or changing sign upon varying the packing fraction η (sense inversion), analogous to previous findings for hard helices [252, 298].

7.7 Right-handed oblate cholesteric phase

Finally, we further modify the particle shape by decreasing the base angle γ while keeping the aspect ratio $h/\omega = 5$ fixed. In this way, we construct TTPs with shape parameter $\nu < 0$, which should stabilize an oblate nematic phase. Indeed, our simulations reveal the formation of an oblate nematic phase (N_-^*) with a helical chiral arrangement of the local nematic director field corresponding to the short particle axis $\hat{\mathbf{w}}$ as exemplarily shown in Fig. 7.10 for TTPs with $h/\omega = 5$, $\gamma = 0.4$, $\alpha = 0.4$, yielding $\nu \simeq -1.41$. We observe that the orientation of the long particle axis $\hat{\mathbf{u}}$ is isotropic whereas the nematic director $\hat{\mathbf{n}}_{\hat{\mathbf{w}}}$ associated to the short axis $\hat{\mathbf{w}}$ displays the expected helical structure. Surprisingly, the macroscopic twist is now *right-handed* in contrast with the left-handed twist as observed for the prolate cholesteric phase of the same particle model but with a different α and γ (Fig. 7.3), which seems to be counter-intuitive. However, this can be explained as follows. Despite the fact that the twist angle $\alpha > 0$, meaning that the particle is twisted in a right-handed fashion along the long particle axis $\hat{\mathbf{u}}$, it also corresponds to a left-handed twist in the short particle axis $\hat{\mathbf{w}}$. As only the short particle axes show orientational order in an oblate nematic phase, and the particles are weakly chiral, we expect a macroscopic twist that is opposite to that of the short axis, i.e., a right-handed macroscopic twist, as indeed observed in our simulations. The equation of state and order parameters in Fig. 7.10(c) shows that the I-N_-^* phase transformation is specular to that of the prolate cholesteric phase. The cholesteric structure and the sense of twist are further confirmed by the orientational pair-correlation functions (see Fig. 7.10(d)).

7.8 Conclusions

In conclusion, we have shown by computer simulations of twisted triangular prisms that entropy alone can stabilize both oblate and prolate chiral nematic phases. Our results showcase once more that attributing uniquely a value to the microscopic chirality is not trivial. In this simple model we need to combine the value of the twist angle α, shape parameter ν and the microscopic pitch p to predict the sense of the twist. A more complicated competition between biaxiality and chirality is expected when $\nu \sim 0$ and a biaxial nematic phase should occur. Since a double twist cannot be space-spanning, it is interesting to investigate if the macroscopic chirality disappears or another stabilization mechanism comes into play. Twisted polyhedra are useful models to address this and other fundamental questions. For example, simulations on mixtures of particles with different handedness (see Fig. 7.11) show that racemic mixtures form achiral nematic phases, as expected from theory [35] (see also Sec. 6.5), indicating that chirality alone is not enough to drive phase separation in systems of hard particles and size asymmetry is required. By considering also depletant particles it will be possible to gain novel insights in experiments where entropy, chirality and depletion are the dominant forces [231, 300].

In addition, our simulations show qualitative agreement with theoretical predictions from an Onsager-like DFT, thereby providing confidence that the theory yields reliable results and can thus serve as a guide for future studies. For example, to study nucleation and growth of cholesteric phases, addressing questions like how the chirality changes the

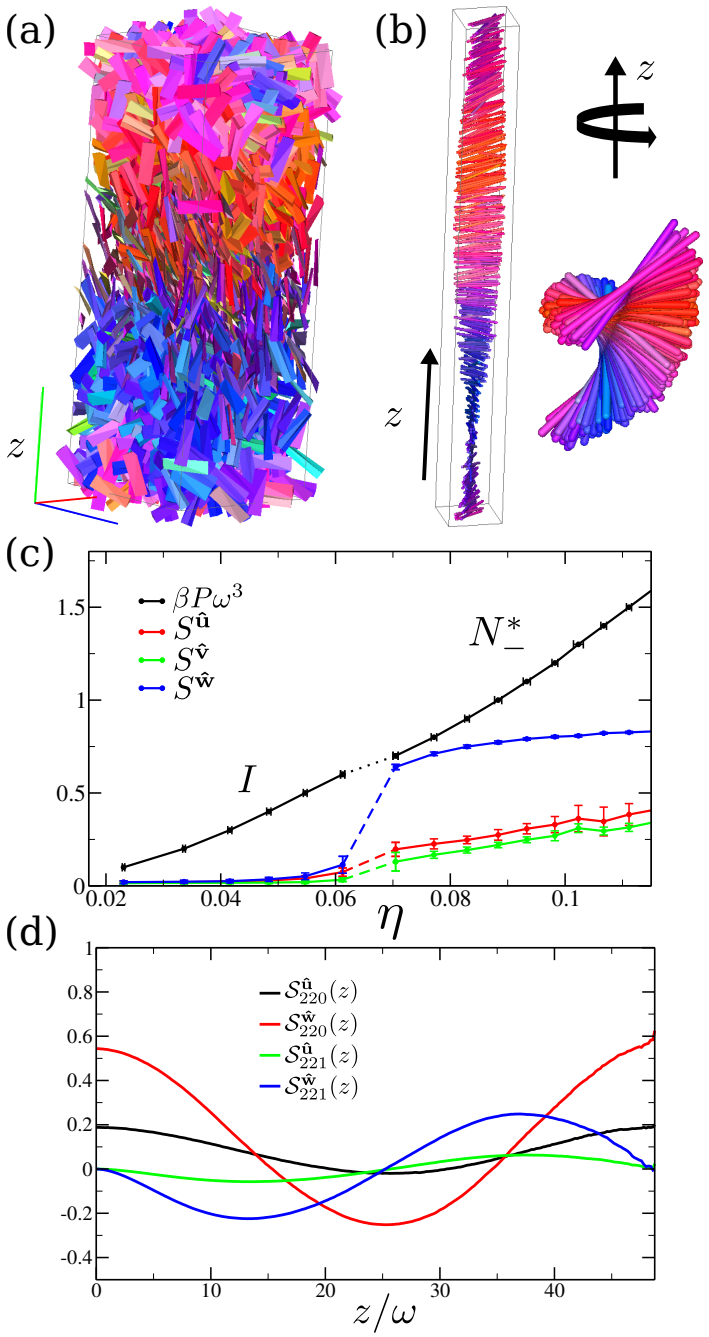

Figure 7.10: **(a)** Oblate cholesteric phase of TTPs with $h/\omega = 5$, $\alpha = 0.4$, $\gamma = 0.4$ as obtained from NPT-MC simulations ($\beta P\omega^3 = 1.0$) using PBC. Particles are colored according to the orientation of their *short* axes $\hat{\mathbf{w}}$. **(b)** Cartoon of the nematic director $\hat{\mathbf{n}}_{\hat{\mathbf{w}}}$ exhibiting a *right-handed* twist. **(c)** Equation of state and nematic order parameters $S^{\hat{\mathbf{u}}}$, $S^{\hat{\mathbf{v}}}$, $S^{\hat{\mathbf{w}}}$ as a function of packing fraction η, confirming that the transition is specular to the isotropic-prolate cholesteric phase transition (cfr. Fig. 7.3(b)). **(d)** Orientational pair-correlation functions calculated along the z-direction, confirming the helical cholesteric structure associated to the short axis $\hat{\mathbf{w}}$ and the right-handed sense of twist (opposite trend of the functions $\mathcal{S}_{221}(z)$ with respect to the one shown in Fig. 7.3(e)).

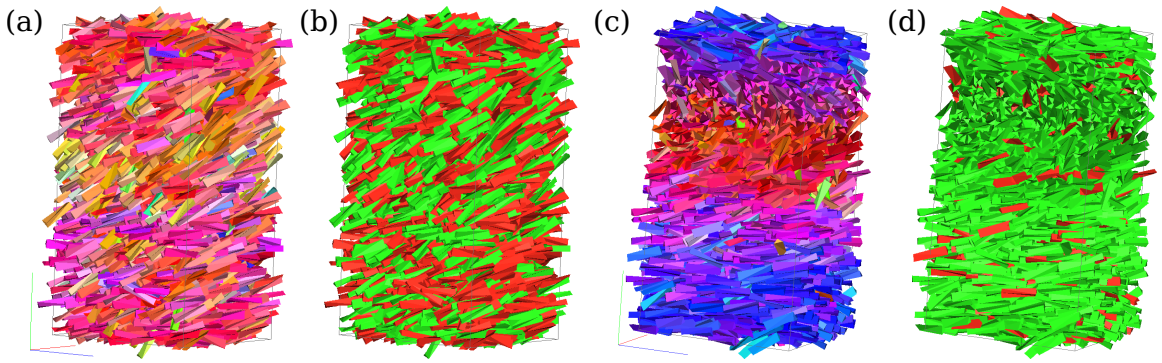

Figure 7.11: Typical configurations of mixtures of $N = 3200$ right-handed and left-handed TTPs with aspect ratio $h/\omega = 5$, base angle $\gamma = 0.75$, and twist angle $\alpha = \pm 0.7$ as obtained from MC simulations in the NPT ensemble ($\beta P \omega^3 = 1.5$) using PBC. (a) Racemic (50:50) mixture with particles colored according to the orientation of the long particle axis **u**. Note that racemic mixtures form uniaxial *achiral* nematic phases as expected from theory [35]. (b) Same racemic mixture with particles colored according to their handedness (red=right-handed, green=left-handed). Chirality alone is not enough to drive a demixing transition in a system of hard chiral particles. (c) In the case of a small fraction of right-handed enantiomers ($x = N_{right}/N = 0.1$) the expected right-handed macroscopic twist is observed. (d) Note that the right-handed TTP (red particles) are homogeneously distributed in the system.

shape of the nematic nucleus, longer particles are needed [120] for which $\mathcal{P}$ is expected to be larger and therefore a careful choice of the shape is essential. However, it is also evident that the Parsons-Lee (PL) correction does not rescale the packing fraction of twisted polyhedra accurately enough and overestimates the IN* transition. This may be remedied by a better rescaling factor than the PL correction, or by a more accurate microscopic theory such as fundamental measure theory (cfr. Chap. 5). The DFT also overestimates $\mathcal{P}$ compared to simulations, i.e., it underestimates the macroscopic chiral twist of a N* phase. A similar conclusion was also drawn in previous work on attractive chiral spherocylinders [246].

Finally, recent advancements in chemical synthesis of nanocrystals with polyhedral shape [70] and the use of polarized light to introduce chirality in the shape [301], brings optimism on the possibility of achieving control over more and more particle features, including chirality, at the microscopic level. It is worth mentioning that the twisted prisms resemble the twisted nanoribbons as synthesized in Refs.[301, 302]. We hope that our study motivates further theoretical efforts in the directions of chiral particles. Computer simulations of hard particles will be helpful in the shape design of future building blocks.

Acknowledgements

We thank SURFsara (www.surfsara.nl) for the support in using the Lisa Compute Cluster. We thank John Edison, René van Roij, Simone Belli, Laura Filion, Nick Tasios and Anjan Gantapara for useful discussions. Wessel Vlug and Gerhard Blab are sincerely thanked for providing 3D-printed models of twisted triangular prisms.

8

Towards design rules for colloidal liquid crystals?

How far are we from a complete understanding of the effect of shape on the colloidal liquid crystal behaviour? Do we already have all the necessary theoretical tools to discriminate between the different (nematic) phases? What novel nematic behaviour can we look for? In this chapter we address these issues by focusing on a couple of open questions and by reporting state-of-the-art computer simulations on chiral nematic phases of hard particles.

8.1 Introduction

We have seen that nematic phases with different symmetries are formed when the constituent particles do not have uniaxial symmetry. In a uniaxial nematic phase, the elastic deformations, namely splay, twist and bend (cfr. Sec. 3.3), cost free energy. However, chiral particles can give rise to cholesteric phases, in which the stable order features a certain degree of twist. It is then possible to imagine the existence of other modulated nematic phases, in which the thermodynamically stable state features a combination of the elastic modes. In particular, twist-bend nematic phases have been recently discovered [241, 242]. In the first part of this chapter, we try to understand what ingredients are needed to extend our second-virial theory to twist-bend nematic phases. Subsequently, we investigate the possibility of spontaneous chiral symmetry breaking in systems consisting of simple particle models. Finally, we present an extended computer simulation study to show how the competition between particle biaxiality and particle chirality is transmitted into the nematic phase behaviour.

8.2 Towards a theory for twist-bend nematics: heliconical order

Cholesteric order is the simplest chiral arrangement for a nematic phase, in which the twist axis is perpendicular to the local nematic director. In general, the local nematic director can be inclined by an angle δ with respect to the chiral director (see Fig. 8.1**(a)**), leading to the following functional dependence of the director field:

$$\hat{\mathbf{n}}_q(y) = \hat{\mathbf{x}}\,\sin\delta\sin qy + \hat{\mathbf{y}}\,\cos\delta + \hat{\mathbf{z}}\,\sin\delta\cos qy \tag{8.1}$$

In analogy with Chap. 6, in Eq. (8.1) we keep on assuming the y-axis to be the chiral director. When $0 < \delta < \pi/2$, the nematic director exhibits an heliconical arrangement that was initially attributed to be the microscopic order of a recently discovered nematic phase that was termed twist-bend [241, 242]. This phase could even display additional hexatic order [239] that will not be taken into account here. The case of the simpler cholesteric is recovered for $\delta = \pi/2$, whereas for $\delta = 0$ we have an achiral uniaxial nematic. By inserting Eq. (8.1) (instead of Eq. (6.20)) into the expression for the excluded volume coefficients (Eq. (6.21)), our theory can be used to discriminate between cholesteric and heliconical phases. By implementing a 2D grid for the chiral wave vector q and the angle δ, we compute the excluded volume coefficients and calculate the free-energy landscape, that now depends on an additional parameter, the angle δ (cf. Fig. 8.1**(b)**). In analogy with the cholesteric case, we are able to locate the free-energy minima in the $\eta - q - \delta$ space and obtain the equilibrium chiral properties characterizing the nematic phase. We apply our theory to the hard-helix particle model described in Chap. 6. In Fig. 8.1**(c)**, we report the results for helices of contour length $L_c = 10\sigma$, $r = 0.4\sigma$ and $p/\sigma = 2, 3, 4$. We recover the three regimes for the cholesteric handedness (same, mixed, opposite) and we find that the angle $\delta = \pi/2\ \forall\eta$, indicating that for these helical shapes the cholesteric order is stable with respect to the heliconical one. We have to remark that evidences of a conical phase, as originally termed, were reported in experiments on colloidal helical

flagella [221]. Moreover, a screw-like nematic phase has been observed in simulations of hard helices [37] that differs from the heliconical phase proposed here since the chiral arrangement refers to the short axis of the particles. Such a screw-like nematic phase seems to be consistent with the experimental observations and to be stable for appropriate pressures/densities with respect to the cholesteric phase formed by hard helices [37, 293]. Finally, a recent work of Greco and Ferrarini [36] shows that by taking into account both the biaxiality and the polarity of both the nematic phase and the constituent particles, it is possible to formulate an Onsager-like DFT that successfully describes the twist-bend nematic order. Such a theory was applied to hard crescent-shaped particles and, with the additional support of computer simulations, clearly shows that the formation of a twist-bend nematic phase can be entropy-driven [36]. Nevertheless, the study of the twist-bend order in nematic phases and the intricate mechanisms governing liquid crystals formed by bent-core particles are still active topics of research, that have also been extended to the colloidal domain [303–307].

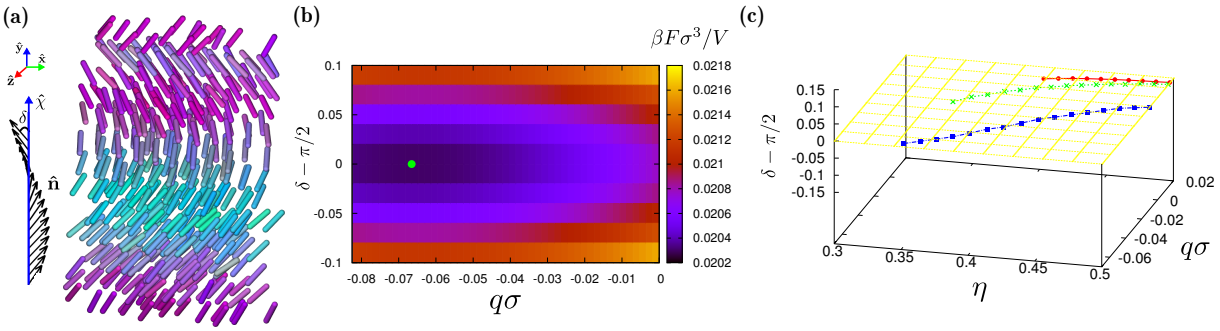

Figure 8.1: **(a)** Schematic of a twist-bend nematic phase. The local nematic director $\hat{\mathbf{n}}$ twists around the chiral director $\hat{\chi}$ with a fixed bending angle δ. **(b)** Free-energy landscape in $\delta - q$ plane, at fixed packing fraction $\eta = 0.35$ for helices with $p = 4\sigma$, $r = 0.4\sigma$ and $L_c = 10\sigma$. The green circle indicates the free-energy minimum. **(c)** Minima of free energy in $\eta - q - \delta$ space for helices of length $L_c = 10\sigma$, $r = 0.4\sigma$ and $p = 2\sigma$ (red circles), $p = 3\sigma$ (green crosses), $p = 4\sigma$ (blue squares). All the lines belong to the plane $\delta = \pi/2$, indicating that bending is not favourable.

8.3 Searching for a spontaneous chiral symmetry breaking in cholesteric phases

In his famous book on liquid crystals [35], de Gennes explained the difference between cholesteric and achiral nematic phases in terms of minima in the free energy F associated to the twist q in the system by using the analogy with magnetic systems (see Fig. 8.2). He suggested that in addition to systems forming achiral nematic phases and the ones forming cholesteric phases, a third class of systems could exist. Indeed, he suggested that 'steric interactions of dumbbell-like molecules (as in Fig. 8.2) would tend to give rise to two symmetrical minima in $F(q)$ and he also remarked that "at the present stage no helices of this kind have been found in liquid crystals". It is interesting to remark that

a spontaneous chiral symmetry breaking also occurs in twist-bend nematic phases, since indeed achiral particles can form both right- and left-handed domains [36]. However, as mentioned in the previous section, polarity and biaxiality are key elements to be taken into account to describe twist-bend nematics. On the other hand, the particles proposed by de Gennes are clearly apolar and uniaxial, and if spontaneous chiral symmetry breaking occurs, it should give rise to both right- and left-handed cholesteric phases. The theory introduced in Chap. 6 allows us to compute numerically the free energy F as a function of the wavenumber q of the chiral twist, for a given thermodynamic state of the system (e.g. at given density). We can therefore distinguish between a stable achiral nematic phase, for which the minimum of $F(q)$ is at $q = 0$, a stable cholesteric phase, for which the minimum of $F(q) = q^* \neq 0$, and a spontaneous breaking of the chiral symmetry, for which two symmetrical minima are found. Analogously, finding $K_2 \propto \frac{d^2F(q)}{dq^2} < 0$ would also be an indication that the system exhibits a spontaneous chiral symmetry breaking. Such a theory is applied in the next sections to the purely-steric particle model proposed by de Gennes and to hard spherocylinders with a uniaxial charge distribution, which, following the same reasoning, could also exhibit spontaneous chiral symmetry breaking.

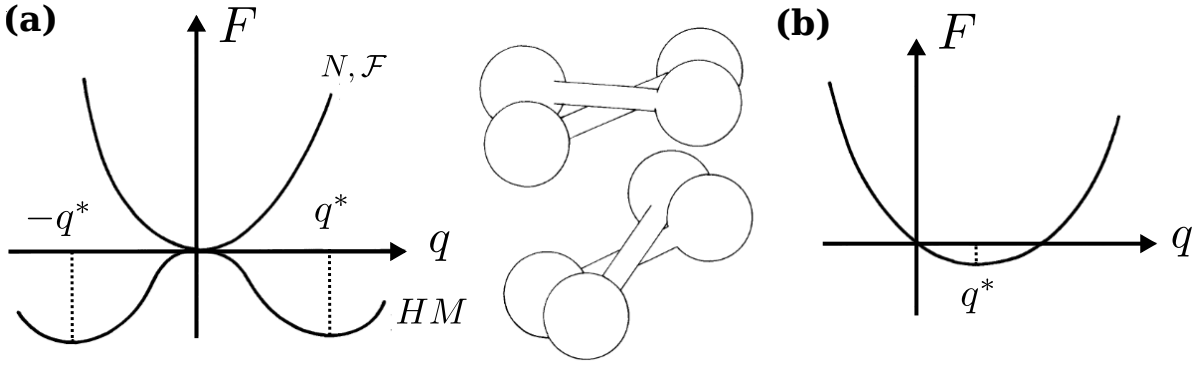

Figure 8.2: Adapted from Ref. [35]. The original caption reads: Variation of the free energy with twist for various physical systems. **(a)** Systems that do not distinguish right and left. The curve labelled $N, \mathcal{F}$ applies to a nematic or a ferromagnet (minimum of energy at zero twist). The curve labelled HM applies to a helimagnet, or to the dumbbells of the inset. **(b)** Systems distinguishing right from left such as actual cholesterics.

8.3.1 Elongated hard dumbbells

We study the nematic behaviour of hard elongated dumbbells defined by the cylinder length L, the cylinder diameter D, and the sphere diameter σ_s, as shown in Fig. 8.3(a). We use reduced units $L^* = L/D$ and $\sigma_s^* = \sigma_s/D$ and we apply our DFT (see Chap. 6) to a large number of systems: $L^* = 5, 6, 7$ and $\sigma_s^* = 1.1, 1.2, 1.25, 1.3, 1.4, 1.5, 2.0, 3.0$; $L^* = 10$ and $\sigma_s^* = 2, 3, 4, 5, 6$; $L^* = 20$ and $\sigma_s^* = 2, 3, 4, 5, 6, 7, 8, 9, 10$; $L^* = 40$ and $\sigma_s^* = 4, 6, 8, 10, 12, 14, 16$. In Fig. 8.3(a), we report the nematic order parameter S as a function of the packing fraction $\eta = \rho v_0$, with ρ the number density and $v_0/D^3 \simeq 2\frac{\pi}{6}\sigma_s^{*3} + \frac{\pi}{4}(L^* - \sigma_s^*)$ the (approximate) particle volume, for some of the systems studied.

We observe that particles with the same "effective" aspect ratio L/σ_s roughly display the jump of S, which indicates the occurrence of the isotropic-nematic phase transition, at similar packing fractions η. Notice that in some cases such a packing fraction is quite high and more ordered phases, that are not taken into account in the theory, could be more stable than the nematic phase. In Fig. 8.3(b), we plot the difference in free energy between the achiral nematic $F(q=0)$ and a cholesteric phase $F(q)$ as a function of the chiral wave number q, for dumbbells with $L^* = 20$ and $\sigma_s^* = 4$ and different packing fractions η. The isotropic-nematic transition occurs around $\eta = 0.40$. We always observe that the minimum of the free energy corresponds to $q = 0$, which is the achiral nematic phase. Notice that the apparent maxima at $|q| \simeq 0.12$ for $\eta = 0.41$ correspond to the maximum twist for which we can obtain a nematic phase by minimizing our free-energy functional. Beyond $|q| \simeq 0.12$ we obtain only isotropic orientation distribution functions that have anyway a higher free energy than the achiral nematic phase. In all the systems studied, we do not find any evidence of a spontaneous chiral symmetry breaking within the numerical accuracy of our second-virial theory. This raises the question if such as an effect can be observed when higher-order particle-particle correlations are considered. Computer simulations will address this question and hopefully will shed new light on the spontaneous chiral symmetry breaking in systems of (de Gennes) hard dumbbells.

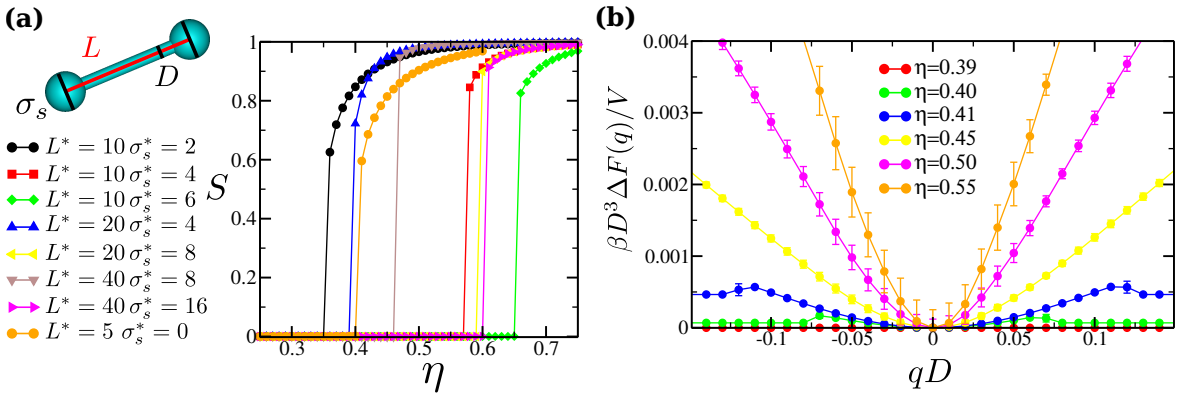

Figure 8.3: **(a)** Cartoon of the particle model and nematic order parameter S as a function of packing fraction η. The elongated hard dumbbells are defined by the cylinder length L, the cylinder diameter D and the spheres diameter σ_s (in the cartoon $L^* = L/D = 10$, $\sigma_s^* = \sigma_s/D = 3$). **(b)** Free-energy difference $\Delta F(q) = F(q) - F(q=0)$ as a function of chiral wave number qD for different packing fractions η, and for hard elongated dumbbells with $L^* = 20$ and $\sigma_s^* = 4$. We use reduced units with $\beta = 1/k_B T$, with k_B the Boltzmann constant and T the temperature, and V is the system volume. The error bars are calculated by averaging over 10 independent runs of 10^{10} MC steps. Notice that different q-grids have been investigated as well.

8.3.2 Hard rods with uniaxial charge distribution

For charged rod-like colloids in the Onsager limit (infinite aspect ratio), it is possible to find parameter regimes with a coexistence between two nematic phases, besides the expected isotropic-nematic transition [308]. The existence of a second, more aligned,

nematic phase can be explained in terms of the twisting effect. The Frank elastic constants (cfr. Sec. 3.3) have been computed in the limit of infinitely long rods, to see if the twist elastic constant K_2 can become negative, which would indicate the possibility of a spontaneously forming cholesteric phase. Although the twisting effect reduces K_2, it always remains positive [308]. In this section we investigate if spontaneous chiral symmetry breaking can occur when considering finite rods.

For this purpose, we apply our DFT to a simple model of colloidal uniaxially-charged rods. In analogy with Ref. [309], the colloids are modelled as hard spherocylinders (HSC) of diameter D and length L. The total charge on the rods Z is fixed by embedding N_s spheres interacting via a hard-core Yukawa potential (HY). The N_s spheres (with N_s odd) are evenly distributed along the backbone of the rod: they are separated by a distance $\delta = \frac{L}{N_s - 1}$ such that two spheres are always at the extremities of the spherocylinder. The total pair potential between two charged rods is given by

$$U_{12}(\mathbf{r}, \hat{\omega}, \hat{\omega}') = U_{HSC}(\mathbf{r}, \hat{\omega}, \hat{\omega}') + \sum_{i=1}^{N_s} \sum_{j=1}^{N_s} U_{HY}(r_{ij}) \,, \tag{8.2}$$

where U_{HSC} is the hard-core potential between spherocylinders

$$U_{HSC}(\mathbf{r}, \hat{\omega}, \hat{\omega}') = \begin{cases} \infty & d_{min}(\mathbf{r}, \hat{\omega}, \hat{\omega}') \leq D \\ 0 & d_{min}(\mathbf{r}, \hat{\omega}, \hat{\omega}') > D \end{cases} \,, \tag{8.3}$$

with $d_{min}(\mathbf{r}, \hat{\omega}, \hat{\omega}')$ the minimum distance between two HSCs with center-of-mass separation $\mathbf{r}$ and orientations $\hat{\omega}, \hat{\omega}'$; whereas the sphere-sphere interaction is described by a (truncated) hard-core Yukawa potential:

$$\beta U_{HY}(r_{ij}) = \begin{cases} \infty & r_{ij} < D \\ \beta\epsilon \frac{\exp[-\kappa D(r_{ij}/D - 1)]}{r_{ij}/D} & D \leq r_{ij} < r_{cut} \\ 0 & r_{ij} \geq r_{cut} \end{cases} \tag{8.4}$$

where i, j indicates spheres belonging to rods $1, 2$ respectively. The parameters $\beta\epsilon$ and N_s are related by $\beta\epsilon = \left(\frac{Z}{N_s}\right)^2$, so N_s is simply a parameter that can be varied until convergence is reached. As previously shown [309], this model with $N_s \geq 13$ is in excellent agreement with analytic results for the excluded volume of finite aspect-ratio rods with an effective linear charge distribution. Accordingly, we choose $N_s = 15$, which should guarantee a good agreement between the discrete-sphere and the linear-charge model. In the numerical integration we use a cut-off $r_{cut} \sim 1 - 2\ L$. The hard aspect ratio L/D, the total charge on the rod Z and the inverse of the Debye screening length κD are the physical independent parameters. We investigate a few combinations of aspect ratio L/D and total charge Z on the rods, as reported in Fig. 8.4. In Fig. 8.4(a), we show the free-energy difference $\Delta F(q) = F(q) - F(q = 0)$ as a function of the chiral wavenumber q, for $L/D = 10$, $Z = 1.0$, and two different packing fractions $\eta = 0.28, 0.32$. In some cases, we employ different q-grids to check that our results are consistent. However, within our numerical accuracy no evidence of a double minimum at $q = \pm q^* \neq 0$ has been observed for the entire set of parameters studied. From the second-derivative of $\Delta F(q)$ it is possible to calculate K_2 as a function of packing fraction η, as shown in Fig. 8.4(b) for $L/D = 10$

and two values of total charge $Z = 0.05$ and $Z = 1.0$. We see that K_2 increases with packing fraction and that the numerical uncertainty increases as well. In Fig. 8.4(c), we show the twist elastic constant as a function of η for aspect ratio $L/D = 40, 20, 10, 5$ and different values of total charge Z on the rods. Due to the large numerical uncertainties (not shown) at large packing fraction, quantitative conclusions about the actual dependence of K_2 on charge should be drawn carefully. However, as mentioned before, there are no indications that K_2 becomes negative. In addition, we show results for charged rods in the Onsager limit [308]. We see that the general trend of K_2 is similar to that of the largest aspect ratio $L/D = 40$, but, as expected, Onsager theory become less accurate as the aspect ratio becomes smaller. In conclusion, just as in the case of infinite rods, we do not find any evidence that a linear charge distribution can induce a spontaneous chiral symmetry breaking in uniaxially-charged colloidal rods of finite length. Therefore, a uniaxial charge distribution alone seems not enough to break chiral symmetry, at least not within a second-virial type of theory. Again, it is interesting to investigate whether or not a third-virial term (which includes three-body correlations) is able to predict a spontaneous chiral symmetry breaking of uniaxial rods, which may stabilize a cholesteric phase.

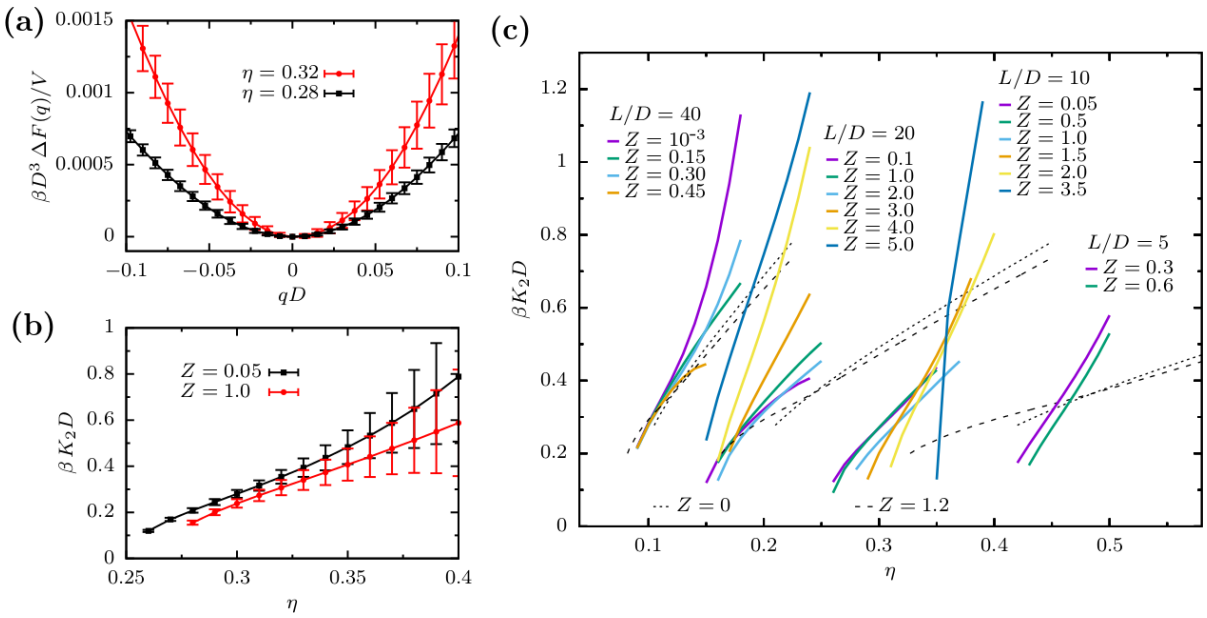

Figure 8.4: **(a)** Free-energy difference $\Delta F(q) = F(q) - F(q = 0)$ as a function of chiral wavenumber qD for two different packing fractions η, and for rods with aspect ratio $L/D = 10$, total charge on rods $Z = 1.0$ divided over $N_s = 15$ spheres, screening parameter $\kappa D = 0.2$, and cut-off $r_{cut}/D = 20$. The error bars are calculated by averaging over 10 independent runs of 10^{10} MC steps. **(b)** Twist elastic constant $\beta K_2 D$ calculated from the second derivative of $F(q)$ as a function of packing fraction η for $Z = 0.05$ and $Z = 1.0$ (for the same N_s, r_{cut}, and κD as in (a)). **(c)** Twist elastic constant $\beta K_2 D$ as a function of packing fraction η for fixed screening parameter $\kappa D = 0.2$, with different aspect ratios L/D, and with different total charges Z. The solid lines are results from the MC method for finite rods and the dashed lines are results from theory in the Onsager limit for $Z = 0$ and $Z = 1.2$, which are shown for aspect ratios $L/D = 40, 20, 10$ ($L/D = 5$ is outside of the plotted range).

8.4 Towards design rules for hard chiral particles from computer simulations

In this section, we extend our simulation study on systems of triangular twisted prisms (TTPs), introduced in Chap. 7, in order to explore the possibility of rationalising the nematic behaviour of chiral particles. Here, we consider TTPs with height $h/\omega = 5$, and study the nematic phase behaviour for different values of the base angle γ and twist angle α. In Fig. 8.5(a) we show our results in the γ-α plane. As reference, we also report results for $\alpha = 0$, corresponding to achiral triangular prisms. Some of them are also presented in Chap. 5, where however we mainly focused on the regions where $\nu \simeq 0$, with ν the shape parameter (see Chaps. 5, 7).

We observe that by tuning the shape chirality, i.e., changing α, and the shape biaxiality, i.e., changing γ, several phases can be formed upon compression from an isotropic phase (under standard periodic boundary conditions). In particular, a prolate (calamitic) chiral nematic $\mathcal{N}_+^*$ phase is observed when $\nu > 0$ (light-blue region), as already shown in Chap. 7. However, the nematic state can also change upon increasing the packing fraction. For instance, TTPs with a relatively high twist α (and $\nu > 0$) undergo a transition from a $\mathcal{N}_+^*$ phase to a phase that is reminiscent of the blue phase ($\mathcal{BP}$), as shown in Fig. 8.5(d). Indeed, the $\mathcal{BP}$ exhibits no long-range orientational order as evidenced by a vanishing nematic order parameter, but the particles are strongly aligned with respect to their neighbouring particles, which poses the question whether this $\mathcal{BP}$ may actually be a twisted grain boundaries phase with very small smectic-like domains. Interestingly, for TTPs with the strongest twist α (dark-blue region) the $\mathcal{BP}$ is observed directly from the isotropic phase without an intervening nematic phase. The $\mathcal{BP}$ seems to be surprisingly stable as even upon increasing the pressure further this phase remains. On the other hand, for $\nu < 0$ an oblate (discotic) $\mathcal{N}_-^*$ chiral nematic phase is formed, in which the short particle axes display long-range orientational order (orange and yellow regions). It is worth noting that there are two regions where the $\mathcal{N}_-^*$ phase is stable, i.e., for sufficiently small or sufficiently large base angle γ. However, in the case that the triangular base is extremely flat (when γ is very small, and thus also ν) an additional splay deformation is formed in the nematic director field $\hat{\mathbf{n}}_{\hat{\mathbf{w}}}$ corresponding to the short particle axis $\hat{\mathbf{w}}$, therefore forming a twist-splay nematic $\mathcal{N}_-^{st}$ (yellow region) when compressing from an isotropic phase, as shown in Fig. 8.5(g). Such a deformation is not generic for chiral particles but seems to be specific to triangular prisms, which is corroborated by the fact that for the achiral particle with same γ, an achiral nematic phase is observed with also a splay deformation, i.e., a $\mathcal{N}_-^s$ phase, as shown in Fig. 8.5(f). Further studies on the stability of this deformation are required but could be interpreted as another modulated nematic phase.

Finally, we focus on the region where $\nu \simeq 0$ (red region). Interestingly, we clearly observe the formation of biaxial nematic phases for both achiral and chiral triangular prisms in which both the short $\hat{\mathbf{w}}$ and long $\hat{\mathbf{u}}$ particle axes show long-range orientational order. We find that in the case of twisted triangular prisms, only one of the nematic directors show a chiral helical arrangement. To be more specific, we find at low densities that a biaxial nematic phase is formed in which only the nematic director corresponding

to the short particle axis show a helical arrangement, resulting in a $\mathcal{N}^*_{b-}$ phase as shown in Fig. 8.5(b). Upon increasing the density, this biaxial chiral nematic $\mathcal{N}^*_{b-}$ phase transforms into a (biaxial) chiral nematic $\mathcal{N}^*_{(b)+}$ phase with a helical arrangement of the nematic director associated to the long particle axes. As the orientational order of the short particle axes is very weak, we could not identify if the chiral nematic phase is uniaxial $\mathcal{N}^*_+$ or biaxial $\mathcal{N}^*_{b+}$. A transition from $\mathcal{N}_{b-}$ to $\mathcal{N}_{b+}$ is consistent with the simulations on hard board-like particles [195] and our results presented in Chap. 5, where the achiral biaxial phases were characterized by the particle axis with the highest orientational order. It is tempting to speculate that indeed only the nematic director of the particle axis that shows the strongest alignment becomes chiral in a biaxial nematic phase, as it seems unlikely that both director fields twist simultaneously and remain space-filling. However, it is impossible to rule out such a scenario of double twist as the cholesteric pitch of one or both director fields can easily exceed the system sizes that are at present accessible in simulations.

In conclusion, we have mapped out the nematic phase behaviour in the shape biaxiality-shape chirality parameter space and we have shown how the observed nematic phases can be rationalized: (i) The shape parameter ν can be used to predict which of the two particle axes exhibits long-range orientational order, resulting in a discotic $\mathcal{N}_-$ nematic phase for $\nu < 0$ or a calamitic $\mathcal{N}_+$ nematic phase when $\nu > 0$. For $\nu \sim 0$, a biaxial phase may be present, provided that other conditions that depend on the exact particle shape are satisfied. This was already demonstrated in a simulation study on hard board-like particles [195] and shown in Chap. 5 for achiral hard prisms, where the particle aspect ratio needs to be larger than a threshold value to observe a biaxial nematic phase. (ii) Furthermore, we find that in the case that the triangular base is extremely flat, the nematic phase displays a splay deformation for both chiral as well as achiral particles upon compressing from an isotropic phase. (iii) In addition, we find that for highly twisted particles or at high pressures "blue phases" can be stabilized. (iv) Our results also reveal that the coupling between particle biaxiality and chirality is highly non-trivial as the prolate nematic phases are left-handed, whereas the oblate nematic phases are right-handed using the same right-handed particle model. We have to remark that to assess the thermodynamic stability and the corresponding phase boundaries of all of these phases, accurate free-energy techniques to apply in computer simulations and an extended density functional theory that takes in account all of these effects at the same time, are needed but not yet developed.

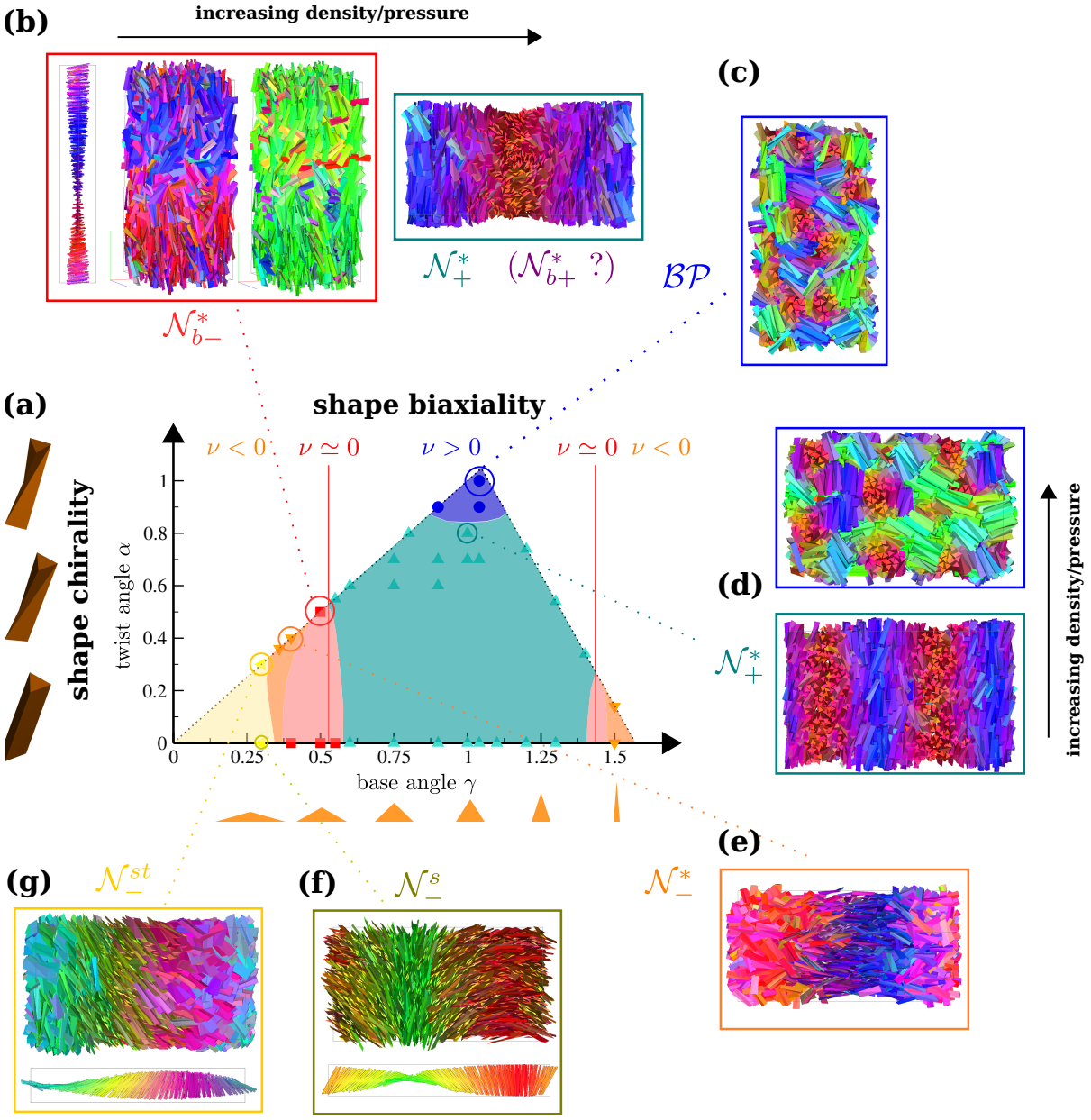

Figure 8.5: **(a)** Nematic phase behaviour for twisted triangular prisms of height $h/\omega = 5$ in the twist angle α - base angle γ representation. Regions are colored according to the type of nematic phase that is found stable (white corresponds to unphysical parameters), see text for a detailed description. **(b)** Left (red) box: $\mathcal{N}_{b-}^*$ phase with nematic director profile $\hat{\mathbf{n}}_{\hat{\mathbf{w}}}$, a configuration with particles colored according to $\hat{\mathbf{w}}$ and according to $\hat{\mathbf{u}}$. Right (cyan) box: $\mathcal{N}_{(b)+}^*$ phase with configuration of nematic phase at higher pressure, and particles colored according to $\hat{\mathbf{u}}$. **(c)** (purple) box: $\mathcal{BP}$ phase, particles colored according to $\hat{\mathbf{u}}$. **(d)** $\mathcal{N}_+^*$ and $\mathcal{BP}$ (at higher pressure) with particles colored according to $\hat{\mathbf{u}}$. **(e)** $\mathcal{N}_-^*$ with particles colored according to $\hat{\mathbf{w}}$. **(f)** $\mathcal{N}_-^s$ with particles colored according to $\hat{\mathbf{w}}$ and corresponding nematic director profile of $\hat{\mathbf{n}}_{\hat{\mathbf{w}}}$. **(g)** Snapshot of $\mathcal{N}_-^{st}$ with particles colored according to $\hat{\mathbf{w}}$ and corresponding profile of $\hat{\mathbf{n}}_{\hat{\mathbf{w}}}$.

8.5 Outlook and conclusions

In conclusion, there is a clear need for a density functional theory that is able to describe splay, twist, and bend deformations together with phase polarity and biaxiality, and therefore able to identify which kind of order amongst all possible combinations exhibits the thermodynamic stable phase. Several recent theoretical advancements suggest that such a framework will be available in the near future, at least within the second-virial approximation, at least for nematic phases. It will therefore just a matter of computational resources to scan different particle shapes and to identify the key features responsible for the various thermodynamic nematic phase. Extending such a framework to smectic phases is in principle also possible. More quantitative reliable theories should probably rely on more sophisticated approaches, such as fundamental measure theory, for which we have seen in Chap. 5 that a good agreement with simulation results is obtained in case of already quite complex shaped particles. The straightforward test for such theories will be the comparison against computer simulations. As shown in the previous section, it is already possible to directly observe very complex nematic order. However, free-energy calculation techniques for such phases are not well developed yet, especially if compared with the well established methods to determine the equilibrium crystal structures or the gas-liquid coexistence [10]. Progress in this direction will be then also important. Nevertheless, many entropy-driven phase transitions, several of them already discussed in this thesis, have been studied and clear indications on how the shape of the particles alone stabilizes the different thermodynamic phases have been identified. Yet, some puzzling issues remain, e.g. the question of whether or not a system of hard elongated dumbbells can exhibit a spontaneous chiral symmetry breaking is still open, see Sec. 8.3. In this case, a second-virial density functional theory gives a negative answer, but it is not clear what the outcome will be if higher-order virial contributions are included in the theory or perhaps we will find that in this case shape, at least the one proposed by de Gennes, is not enough to stabilize a chiral nematic phase? This question needs to be addressed.
Finally, our results, together with the exhaustive literature on hard particles, also pose the intriguing question if *any* thermodynamic phase featuring long-range order can be stabilized by entropy alone. Several shape features have been identified as responsible for the stabilization of different thermodynamic phases and therefore design rules for novel building blocks start to take shape.

Acknowledgments

Simone Belli is thanked for pointing us to the intriguing pages of de Gennes book and for starting our speculation on the spontaneous chiral symmetry breaking. Tara Drwenski is acknowledged for her work on the uniaxially-charged colloidal rods in the Onsager limit, performed under the supervision of René van Roij at the Institute for Theoretical Physics (UU). I acknowledge a conversation with Alberta Ferrarini (University of Padova) at the European Conference on Liquid Crystals (Manchester 2015) about theories for twist-bend nematics.

I sincerely thank John Edison, Simone Belli, Anjan Gantapara, Nick Tasios, Tara Drwenski, and René van Roij, for the many stimulating discussions about chirality, polyhedral (and non) shapes, theory and simulation methods, related to this chapter and more generally to this thesis.

References

[1] A. D. McNaught. *IUPAC compendium of chemical terminology.* Blackwell Science Inc. (Hoboken), 2nd edition, 1997.

[2] T. Graham, *Liquid diffusion applied to analysis.* Phil. Trans. R. Soc. London, 151:183, 1861.

[3] R. Brown, *A brief account of microscopical observations made in the months of June, July and August 1827 on the particles contained in the pollen of plants; and on the general existence of active molecules in organic and inorganic bodies.* Phil. Mag., 4:161, 1828.

[4] W. Sutherland, *A dynamical theory of diffusion for non-electrolytes and the molecular mass of albumin.* Phil. Mag., 9:781, 1905.

[5] A. Einstein, *Über die von der molekularkinetischen theorie der wärme geforderte bewegung von in ruhenden flüssigkeiten suspendierten teilchen.* Ann. Phys. (Leipzig), 17:549, 1905.

[6] J. Perrin, *Mouvement Brownien et réalité moléculaire.* Ann. Chim. Phys., 18:5, 1909.

[7] J. Perrin. *Les atomes.* Alacan (Paris), 1st edition, 1913.

[8] G. M. Whitesides and B. Grzybowski, *Self-assembly at all scales.* Science, 295:2418, 2002.

[9] Editorial. *Assembling insight.* Nat. Mater. Vol. 14 Issue 1, 2015.

[10] D. Frenkel and B. Smit. *Understanding molecular simulation: from algorithms to applications.* Academic Press, 2002.

[11] A. Yethiraj and A. van Blaaderen, *A colloidal model system with an interaction tunable from hard sphere to soft and dipolar.* Nature, 421:513, 2003.

[12] S. C. Glotzer and M. J. Solomon, *Anisotropy of building block and their assembly into complex structures.* Nat. Mater., 6:557, 2003.

[13] A. van Blaaderen and P. Wiltzius, *Real-space structure of colloidal hard-sphere glasses.* Science, 270:1177, 1995.

[14] A.-P. Hynninen, J. H. J. Thijssen, E. C. M. Vermolen, M. Dijkstra, and A. Van Blaaderen, *Self-assembly route for photonic crystals with a bandgap in the visible region.* Nat. Mater., 6:202, 2007.

[15] J. F. Galisteo-López, M. Ibisate, R. Sapienza, L. S. Froufe-Pérez, A. Blanco, and C. López, *Self-assembled photonic structures.* Adv. Mater., 23:30, 2011.

[16] P. Podsiadlo, G. V. Krylova, A. Demortière, and E. V. Shevchenko, *Multicomponent periodic nanoparticle superlattices.* J. of Nanopart. Res., 13:15, 2010.

[17] F. X. Redl, K.-S. Cho, C. B. Murray, and S. O'Brien, *Three-dimensional binary superlattices of magnetic nanocrystals and semiconductor quantum dots.* Nature, 423:968, 2003.

[18] S. Mühlig, A. Cunningham, J. Dintinger, T. Scharf, T. Bürgi, F. Lederer, and C. Rockstuhl, *Self-assembled plasmonic metamaterials.* Nanophotonics, 2:211, 2013.

[19] D. Frenkel, *Entropy-driven phase transitions.* Physica A, 263:26, 1999.

[20] R. Clausius, *Ueber verschiedene für die Anwendung bequeme Formen der Hauptgleichungen der mechanischen Wärmetheorie.* Ann. Phys. (Leipzig), 125:353, 1865.

[21] D. Frenkel, *Order through entropy.* Nat. Mater., 14:9, 2015.

[22] M. Planck, *Ueber das Gesetz der Energieverteilung im Normalspectrum.* Ann. Phys. (Leipzig), 309:553, 1901.

[23] B. Alder and T. Wainwright, *Phase transition for a hard sphere system.* J. Chem. Phys., 27:1208, 1957.

[24] W. Wood and J. Jacobson, *Preliminary results from a recalculation of the monte carlo equation of state of hard spheres.* J. Chem. Phys., 27:1207, 1957.

[25] J. E. Kirkwood. *Phase transformations in solids.* edited by R. Smoluchowski, J. E. Mayer, W. A. Weyl (Wiley, New York), 1951.

[26] J. K. Percus (ed.). *The many-body problem.* Interscience, 1963.

[27] P. N. Pusey and W. Van Megen, *Phase behaviour of concentrated suspensions of nearly hard colloidal spheres.* Nature, 320:340, 1986.

[28] R. Piazza, T. Bellini, and V. Degiorgio, *Equilibrium sedimentation profiles of screened charged colloids: A test of the hard-sphere equation of state.* Phys. Rev. Lett., 71:4267, 1993.

[29] R. Piazza, *Settled and unsettled issues in particle settling.* Rep. Prog. Phys., 77:056602, 2014.

[30] L. Onsager, *The effects of shape on the interaction of colloidal particles.* Ann. N. Y. Acad. Sci., 51:627, 1949.

[31] D. Frenkel, B. M. Mulder, and J. P. McTague, *Frenkel nematic.* Phys. Rev. Lett., 287:52, 1984.

[32] D. Frenkel, H. N. W. Lekkerkerker, and A. Stroobants, *Thermodynamic stability of a smectic phase in a system of hard rods.* Nature, 332:822, 1988.

[33] J. A. C. Veerman and D. Frenkel, *Phase behavior of disklike hard-core mesogens.* Phys. Rev. A, 45:5633, 1992.

[34] A. Kloczkowski and J. Stecki, *A molecular model for the smectic A phase.* Mol. Phys., 55:689, 1985.

[35] P.-G. de Gennes and J. Prost. *The Physics of Liquid Crystals.* Oxford University Press, 1993.

[36] C. Greco and A. Ferrarini, *Entropy-driven chiral order in a system of achiral bent particles.* Phys. Rev. Lett., 115:147801, 2015.

[37] H. B. Kolli, E. Frezza, G. Cinacchi, A. Ferrarini, A. Giacometti, and T. S. Hudson, *From rods to helices: evidence of a screw-like nematic phase.* J. Chem. Phys., 140:081101, 2014.

[38] L. J. Ellison, D. J. Michel, F. Barmes, and D. J. Cleaver, *Entropy-driven formation of the gyroid cubic phase.* Phys. Rev. Lett., 97:237801, 2006.

[39] G. Oster, *Two-phase formation in solutions of tobacco mosaic virus and the problem of long-range forces.* J. Gen. Physiol., 33:445, 1950.

[40] S. Fraden, G. Maret, D. J. D. Caspar, and R. B. Meyer, *Isotropic-nematic phase transition and angular correlations in isotropic suspensions of tobacco mosaic virus.* Phys. Rev. Lett., 63:2068, 1989.

[41] Z. Dogic and S. Fraden, *Smectic phase in colloidal suspensions of semiflexible virus particles.* Phys. Rev. Lett., 78:2417, 1997.

[42] Z. Dogic and S. Fraden, *Ordered phases of filamentous viruses.* Curr. Opin. Colloid In., 11:47, 2006.

[43] F. Livolant and A. Leforestier, *Condensed phases of DNA: Structures and phase transitions.* Prog. Polym. Sci., 21:1115, 1996.

[44] Y. Maeda and S. Hachisu, *Schiller layers in β-ferric oxyhydroxide sol as an order-disorder phase separating system.* Colloids Surf., 6:1, 1983.

[45] H. Maeda and Y. Maeda, *Liquid crystal formation in suspensions of hard rodlike colloidal particles: direct observation of particle arrangement and self-ordering behavior.* Phys. Rev. Lett., 90:018303, 2003.

[46] M. P. B. van Bruggen, J. K. G. Dhont, and H. N. W. Lekkerkerker, *Morphology and kinetics of the isotropic-nematic phase transition in dispersions of hard rods.* Macromolecules, 32:2256, 1999.

[47] O. Pelletier, P. Davidson, C. Bourgeaux, and C. Livage, *The effect of attractive interactions on the nematic order of V_2O_5 gels.* Europhys. Lett., 48:53, 1999.

[48] F. M. van der Kooij, K. Kassapidou, and H. N. W. Lekkerkerker, *Liquid crystal phase transitions in suspensions of polydisperse plate-like particles.* Nature, 406:868, 2000.

[49] A. Kuijk, A. van Blaaderen, and A. Imhof, *Synthesis of monodisperse, rodlike silica colloids with tunable aspect ratio.* J. Am. Chem. Soc., 133:2346, 2011.

[50] A. Kuijk, D. V. Byelov, A. V. Petukhov, A. van Blaaderen, and A. Imhof, *Phase behavior of colloidal silica rods.* Faraday Discuss., 159:181, 2012.

[51] C. Zannoni, *Molecular design and computer simulations of novel mesophases.* J. Mater. Chem., 11:2637, 2001.

[52] L. Mederos, E. Velasco, and Y. Martinez-Raton, *Hard-body models of bulk liquid crystals.* J. Phys.: Condens. Matter, 26:463101, 2014.

[53] C. Vega and S. Lago, *A fast algorithm to evaluate the shortest distance between rods.* Comp. and Chem., 18:55, 1994.

[54] D. Eberly. *Intersection of convex objects: The method of separating axes.* http://www.geometrictools.com/, 2008.

[55] E. Gilbert, D. Johnson, and S. Keerthi, *A fast procedure for computing the distance between complex objects in three-dimensional space.* Robotics and Automation, IEEE Journal of, 4:193–203, 1988.

[56] G. van den Bergen, *A fast and robust GJK implementation for collision detection of convex objects.* Journal of Graphics Tool, 4:7, 1999.

[57] GAMMA Research Group at the University of North Carolina. *RAPID - Robust and Accurate Polygon Interference Detection.* http://gamma.cs.unc.edu/OBB/, 1997.

[58] M. P. Allen and D. J. Tildesley. *Computer simulation of liquids.* Clarendon Press, 1989.

[59] R. Evans, *The nature of the liquid-vapour interface and other topics in the statistical mechanics of non-uniform, classical fluids.* Adv. Phys., 28:143, 1979.

[60] R. van Roij. *Lecture notes: Soft condensed matter theory*, 2012.

[61] L. Cademartiri, K. J. M. Bishop, P. W. Snyder, and G. A. Ozin, *Using shape for self-assembly.* Phil. Trans. R. Soc. A, 370:2824, 2012.

[62] J. P. Straley, *Ordered phases of a liquid of biaxial particles.* Phys. Rev. A, 10:1881, 1974.

[63] J. P. Straley, *Theory of piezoelectricity in nematic liquid crystals, and of the cholesteric ordering.* Phys. Rev. A, 14:1835, 1976.

[64] P. F. Damasceno, M. Engel, and S. C. Glotzer, *Predictive self-assembly of polyhedra into complex structures.* Science, 337:453, 2012.

[65] M. Dijkstra, *Entropy-driven phase transitions in colloids: from spheres to anisotropic particles.* Adv. Chem. Phys., 156:35, 2015.

[66] U. Agarwal and F. A. Escobedo, *Mesophase behaviour of polyhedral particles.* Nat. Mater., 10:230, 2011.

[67] S. Torquato and Y. Jiao, *Dense packings of the platonic and archimedian solids.* Nature, 460:876, 2009.

[68] J. Gong, G. Li, and Z. Tang, *Self-assembly of noble metal nanocrystals: Fabrication, optical property, and application.* Nano Today, 7:564, 2012.

[69] L. Zhang, W. Niu, and G. Xu, *Synthesis and applications of noble metal nanocrystals with high-energy facets.* Nano Today, 7:586, 2012.

[70] Y. Xia, Y. Xiong, B. Lim, and S. Skrabalak, *Shape-controlled synthesis of metal nanocrystals: Simple chemistry meets complex physics?* Angew. Chem. Int. Ed., 48:60, 2009.

[71] F. C. Frank, *Supercooling of liquids.* Proc. R. Soc. Lond. A Math. Phys. Sci., 215:43, 1952.

[72] J. H. Conway and N. J. A. Sloane. *Sphere Packings, Lattices and Groups.* Springer-Verlag, New York, 1998.

[73] J. T. McGinley, I. Jenkins, T. Sinno, and J. C. Crocker, *Assembling colloidal clusters using crystalline templates and reprogrammable DNA interactions.* Soft Matter, 9:9119, 2013.

[74] D. R. Nelson and B. I. Halperin, *Pentagonal and icosahedral order in rapidly cooled metals.* Science, 229:233, 1985.

[75] P. J. Steinhardt, D. R. Nelson, and M. Ronchetti, *Bond-orientational order in liquids and glasses.* Phys. Rev. B, 28:784, 1983.

[76] J. P. K. Doye and D. J. Wales, *The structure and stability of atomic liquids: From clusters to bulk.* Science, 271:484, 1996.

[77] N. C. Karayiannis, R. Malshe, M. Kröger, J. J. de Pablo, and M. Laso, *Evolution of fivefold local symmetry during crystal nucleation and growth in dense hard-sphere packings.* Soft Matter, 8:844, 2012.

[78] J. D. Bernal and J. L. Finney, *Random close-packed hard-sphere model. II. Geometry of random packing of hard spheres.* Discuss. Faraday Soc., 43:62, 1967.

[79] B. O'Malley and I. Snook, *Crystal nucleation in the hard sphere system.* Phys. Rev. Lett., 90:085702, 2003.

[80] P. G. Bolhuis, D. Frenkel, S.-C. Mau, and D. A. Huse, *Entropy difference between crystal phases.* Nature, 388:235, 1997.

[81] A. L. Mackay, *A dense non-crystallographic packing of equal spheres.* Acta Cryst., 15:916, 1962.

[82] S. C. Hendy and J. P. K. Doye, *Surface-reconstructed icosahedral structures for lead clusters.* Phys. Rev. B, 66:235402, 2002.

[83] Y. Wang, S. Teitel, and C. Dellago, *Melting of icosahedral gold nanoclusters from molecular dynamics simulations.* J. Chem. Phys., 122:214722, 2005.

[84] H. Hubert, B. Devouard, L. A. J. Garvie, M. O'Keeffe, P. R. Buseck, W. T. Petuskey, and P. F. McMillan, *Icosahedral packing of B_{12} icosahedra in boron suboxide (B_6O).* Nature, 391:376, 1998.

[85] J. P. K. Doye and F. Calvo, *Entropic effects on the structure of Lennard-Jones clusters.* J. Chem. Phys., 116:8307, 2002.

[86] J. Lacava, B. P., and T. Kraus, *Nanoparticle clusters with Lennard-Jones geometries.* Nano Lett., 12:3279, 2012.

[87] H. Hofmeister, *Forty years study of fivefold twinned structures in small particles and thin films.* Cryst. Res. Technol., 33:3, 1998.

[88] M. R. Langille, J. Zhang, M. L. Personick, S. Li, and C. A. Mirkin, *Stepwise evolution of spherical seeds into 20-fold twinned icosahedra.* Science, 337:954, 2012.

[89] J. Tang, X. Zhou, D. Zhao, G. Q. Lu, and C. Yu, *Hard-sphere packing and icosahedral assembly in the formation of mesoporous materials.* J. Am. Chem. Soc., 129:9044, 2007.

[90] J. P. K. Doye and D. J. Wales, *Thermally-induced surface reconstructions of Mackay icosahedra.* Z. Phys. D: At., Mol. Clusters, 40:466, 1997.

[91] G. Meng, N. Arkus, M. P. Brenner, and V. N. Manoharan, *The free-energy landscape of clusters of attractive hard spheres.* Science, 327:560, 2010.

[92] D. J. Wales, *Surveying a complex potential energy landscape: Overcoming broken ergodicity using basin-sampling.* Chem. Phys. Lett., 584:1, 2013.

[93] A. Fortini and M. Dijkstra, *Phase behaviour of hard spheres confined between parallel hard plates: manipulation of colloidal crystal structures by confinement.* J. Phys.: Condens. Matter, 18:L371, 2006.

[94] H. Löwen, E. C. Oguz, L. Assoud, and R. Messina, *Colloidal crystallization between two and three dimensions.* Adv. Chem. Phys., 184:225, 2012.

[95] F. Smallenburg. *Clustering and self-assembly in colloidal systems.* PhD thesis, Utrecht University, 2012.

[96] D. C. Rapaport, *The event-driven approach to N-body simulation.* Progr. Theoret. Phys. Suppl., 178:5, 2009.

[97] T. Schilling and F. Schmid, *Computing absolute free energies of disordered structures by molecular simulation.* J. Chem. Phys., 131:231102, 2009.

[98] T. Schilling and F. Schmid, *A method to compute absolute free energies or enthalpies of fluids.* Physics Procedia, 4:131, 2010.

[99] F. Romano, E. Sanz, P. Tartaglia, and F. Sciortino, *Phase diagram of trivalent and pentavalent patchy particles.* J. Phys.: Condens. Matter, 24:064113, 2012.

[100] M. Marechal and M. Dijkstra, *Stability of orientationally disordered crystal structures of colloidal hard dumbbells.* Phys. Rev. E, 77:061405, 2008.

[101] P. R. ten Wolde, M. J. Ruiz-Montero, and D. Frenkel, *Numerical calculation of the rate of crystal nucleation in a Lennard-Jones system at moderate undercooling.* J. Chem. Phys., 104:9932, 1996.

[102] W. G. Hoover and F. H. Ree, *Melting transition and communal entropy for hard spheres.* J. Chem. Phys., 49:3609, 1968.

[103] A. Cacciuto, S. Auer, and D. Frenkel, *Onset of heterogeneous crystal nucleation in colloidal suspensions.* Nature, 428:404, 2004.

[104] B. de Nijs. *Towards crystals of crystals of nanocrystals.* PhD thesis, Utrecht University, 2014.

[105] B. de Nijs, S. Dussi, F. Smallenburg, J. D. Meeldijk, D. J. Groenendijk, L. Filion, A. Imhof, A. van Blaaderen, and M. Dijkstra, *Entropy-driven formation of large icosahedral colloidal clusters by spherical confinement.* Nat. Mater., 14:56, 2015.

[106] M. I. Bodnarchuk, M. V. Kovalenko, H. Groiss, R. Resel, M. Reissner, G. Hesser, R. T. Lechner, W. Steiner, F. Schäffler, and W. Heiss, *Exchange-coupled bimagnetic wüstite/metal ferrite core/shell nanocrystals: Size, shape, and compositional control.* Small, 5:2247, 2009.

[107] A. van Blaaderen and A. Vrij, *Synthesis and characterization of colloidal dispersions of fluorescent, monodisperse silica spheres.* Langmuir, 8:2921, 1992.

[108] J. Farges, M. F. De Feraudy, B. Raoult, and G. Torchet, *Noncrystalline structure of argon clusters. II. Multilayer icosahedral structure of Ar_N clusters* $50 < N < 750$. J. Chem. Phys., 84:3491, 1986.

[109] H. Friedrich, C. J. Gommes, K. Overgaag, J. D. Meeldijk, W. H. Evers, B. de Nijs, M. P. Boneschanscher, P. E. de Jongh, A. J. Verkleij, K. P. de Jong, A. van Blaaderen, and D. Vanmaekelbergh, *Quantitative structural analysis of binary nanocrystal superlattices by electron tomography.* Nano Lett., 9:2719, 2009.

[110] A. van Blaaderen and P. Wiltzius, *Real-space structure of colloidal hard-sphere glasses.* Science, 270:1177, 1995.

[111] W. H. Evers, B. de Nijs, L. Filion, S. Castillo, M. Dijkstra, and D. Vanmaekelbergh, *Entropy-driven formation of binary semiconductor-nanocrystal superlattices.* Nano Lett., 10:4235, 2010.

[112] D. Wang. Private Communication, 2015.

[113] L. Filion. *Self-assembly in colloidal hard-sphere systems.* PhD thesis, Utrecht University, 2011.

[114] M. Dijkstra, R. van Roij, and R. Evans, *Phase diagram of highly asymmetric binary hard-sphere mixtures.* Phys. Rev. E, 59:5744, 1999.

[115] V. N. Manoharan, M. T. Elsesser, and D. J. Pine, *Dense packing and symmetry in small clusters of microspheres.* Science, 301:483, 2003.

[116] E. Lauga and M. P. Brenner, *Evaporation-driven assembly of colloidal particles.* Phys. Rev. Lett., 93:238301, 2004.

[117] F. Bai, D. Wang, Z. Huo, W. Chen, L. Liu, X. Liang, C. Chen, X. Wang, Q. Peng, and Y. Li, *A versatile bottom-up assembly approach to colloidal spheres from nanocrystals.* Angew. Chem. Int. Ed., 46:6650, 2007.

[118] P. Bolhuis and D. Frenkel, *Tracing the phase boundaries of hard spherocylinders.* J. Chem. Phys., 106:666, 1997.

[119] S. C. McGrother, D. C. Williamson, and G. Jackson, *A re-examination of the phase diagram of hard spherocylinders.* J. Chem. Phys., 104:6755, 1996.

[120] A. Cuetos and M. Dijkstra, *Kinetic pathways for the isotropic-nematic phase transition in a system of colloidal hard rods: A simulation study.* Phys. Rev. Lett., 98:095701, 2007.

[121] R. Ni, S. Belli, R. van Roij, and M. Dijkstra, *Glassy dynamics, spinodal fluctuations, and the kinetic limit of nucleation in suspensions of colloidal hard rods.* Phys. Rev. Lett., 105:088302, 2010.

[122] A. Patti, D. El Masri, R. van Roij, and M. Dijkstra, *Collective diffusion of colloidal hard rods in smectic liquid crystals: Effect of particle anisotropy.* J. Chem. Phys., 132:224907, 2010.

[123] M. Dijkstra, R. van Roij, and R. Evans, *Wetting and capillary nematization of a hard-rod fluid: A simulation study.* Phys. Rev. E, 63:051703, 2001.

[124] J. D. Parsons, *Nematic ordering in a system of rods.* Phys. Rev. A, 19:1225, 1979.

[125] S. D. Lee, *A numerical investigation of nematic ordering based on a simple hard rod model.* J. Chem. Phys., 87:4972, 1987.

[126] R. van Roij, *The isotropic and nematic liquid crystal phase of colloidal rods.* Eur. J. Phys., 26:S57, 2005.

[127] F. C. Frank, *I. Liquid crystals. On the theory of liquid crystals.* Discuss. Faraday Soc., 25:19, 1958.

[128] A. Poniewierski and R. Holyst, *Density-functional theory for systems of hard rods.* Phys. Rev. A, 41:6871, 1990.

[129] S.-D. Lee and R. B. Meyer, *Computations of the phase equilibrium, elastic constants, and viscosities of a hard-rod nematic liquid crystal.* J. Chem. Phys., 84:6, 1985.

[130] S.-D. Lee, *Density-functional approach to curvature elasticity in a liquid-density nematic system.* Phys. Rev. A, 39:3631, 1989.

[131] R. Wittmann, M. Marechal, and K. Mecke, *Elasticity of nematic phases with fundamental measure theory.* Phys. Rev. E, 91:052501, 2015.

[132] M. P. Allen and D. Frenkel, *Calculation of liquid-crystal Frank constants by computer simulations.* Phys. Rev. A, 37:1813, 1988.

[133] B. Tijpto-Margo, G. Evans, M. P. Allen, and D. Frenkel, *Elastic constants of hard and soft nematic liquid crystals.* J. Phys. Chem., 96:3942, 1992.

[134] J.-P. Hansen and I. R. McDonald. *Theory of simple liquids.* Academic Press, 3rd edition, 2006.

[135] M. Kröger and P. Ilg, *Derivation of Frank-Ericksen elastic coefficients for polydomain nematics from mean-field molecular theory for anisotropic particles.* J. Chem. Phys., 127:034903, 2007.

[136] M. Marechal, M. Hermes, and M. Dijkstra, *Stacking in sediments of colloidal hard spheres.* J. Chem. Phys., 135:034510, 2011.

[137] S. Auer and D. Frenkel, *Prediction of absolute crystal-nucleation rate in hard-sphere colloids.* Nature, 409:1020, 2001.

[138] K. K. Kobayashi, *On the theory of translational and orientational melting with application to liquid crystals.* Phys. Lett. A, 31:125, 1970.

[139] W. L. McMillan, *Simple molecular model for the smectic a phase of liquid crystals.* Phys. Rev. A, 4:1238, 1971.

[140] M. Cifelli, G. Cinacchi, and L. De Gaetani, *Smectic order parameters from diffusion data.* J. Chem. Phys., 125:164912, 2006.

[141] M. Marechal, A. Patti, M. Dennison, and M. Dijkstra, *Frustration of the isotropic-columnar phase transition of colloidal hard platelets by a transient cubatic phase.* Phys. Rev. Lett., 108:206101, 2012.

[142] W. Lechner and C. Dellago, *Accurate determination of crystal structures based on averaged local bond order parameters.* J. Chem. Phys., 129:114707, 2008.

[143] R. van Roij, P. Bolhuis, B. Mulder, and D. Frenkel, *Transverse interlayer order in lyotropic smectic liquid crystals.* Phys. Rev. E, 52:R1277, 1995.

[144] M. Fasolo and P. Sollich, *Equilibrium phase behavior of polydisperse hard spheres.* Phys. Rev. Lett., 91:068301, 2003.

[145] S.-E. Phan, W. B. Russel, J. Zhu, and P. Chaikin, *Effects of polydispersity on hard sphere crystals.* J. Chem. Phys., 108:9789, 1998.

[146] S. Auer and D. Frenkel, *Suppression of crystal nucleation in polydisperse colloids due to increase of the surface free energy.* Nature, 413:711, 2001.

[147] T. H. Zhang, B. W. M. Kuipers, W. Tian, J. Groenewold, and W. K. Kegel, *Polydispersity and gelation in concentrated colloids with competing interactions.* Soft Matter, 11:297, 2015.

[148] E. Zaccarelli, C. Valeriani, E. Sanz, W. Poon, M. E. Cates, and P. N. Pusey, *Crystallization of hard-sphere glasses.* Phys. Rev. Lett., 103:135704, 2009.

[149] E. Zaccarelli, S. M. Liddle, and W. C. K. Poon, *On polydispersity and the hard sphere glass transition.* Soft Matter, 11:324, 2015.

[150] E. van den Pol, D. M. E. Thies-Weesie, A. V. Petukhov, G. J. Vroege, and K. Kvashnina, *Influence of polydispersity on the phase behavior of colloidal goethite.* J. Chem. Phys., 129:164715, 2008.

[151] S. Belli, A. Patti, M. Dijkstra, and R. van Roij, *Polydispersity stabilizes biaxial nematic liquid crystals.* Phys. Rev. Lett., 107:148303, 2011.

[152] M. A. Bates and D. Frenkel, *Nematic-isotropic transition in polydisperse systems of infinitely thin hard platelets.* J. Chem. Phys., 110:6553, 1999.

[153] M. A. Bates and D. Frenkel, *Influence of polydispersity on the phase behavior of colloidal liquid crystals: A monte carlo simulation study.* J. Chem. Phys., 109:6193, 1998.

[154] T. Biben, J. P. Hansen, and J. L. Barrat, *Density profiles of concentrated colloidal suspensions in sedimentation equilibrium.* J. Chem. Phys., 98:7330, 1993.

[155] S. Savenko and M. Dijkstra, *Sedimentation and multiphase equilibria in suspensions of colloidal hard rods.* Phys. Rev. E, 70:051401, 2004.

[156] A. Kuijk. *Fluorescent colloidal silica rods - Synthesis and phase behavior.* PhD thesis, Utrecht University, 2012.

[157] T. Besseling. *Self-assembly of colloidal spheres and rods in external field.* PhD thesis, Utrecht University, 2014.

[158] A. Kuijk, A. Imhof, M. H. W. Verkuijlen, T. H. Besseling, E. R. H. van Eck, and A. van Blaaderen, *Colloidal silica rods: material properties and fluorescent labeling.* Part. Part. Syst. Charact., 31:706, 2014.

[159] T. H. Besseling, M. Hermes, A. Kuijk, B. de Nijs, T. S. Deng, M. Dijkstra, A. Imhof, and A. van Blaaderen, *Determination of the positions and orientations of concentrated rod-like colloids from 3D microscopy data.* J. Phys.: Condens. Matter, 27:194109, 2015.

[160] H. N. W. Lekkerkerker and G. J. Vroege, *Liquid crystal phase transitions in suspensions of mineral colloids: new life from old roots.* Phil. Trans. R. Soc. A, 371:20120263, 2013.

[161] M. Adams, Z. Dogic, S. L. Keller, and S. Fraden, *Entropically driven microphase transitions in mixtures of colloidal rods and spheres.* Nature, 393:349, 1998.

[162] M. Adams and S. Fraden, *Phase behavior of mixtures of rods (tobacco mosaic virus) and spheres (polyethylene oxide, bovine serum albumin).* Biophys. J., 74:669, 1998.

[163] Y. Nagaoka, T. Wang, J. Lynch, D. LaMontagne, and Y. C. Cao, *Binary assembly of colloidal semiconductor nanorods with spherical metal nanoparticles.* Small, 8:843, 2012.

[164] S. Lago, A. Cuetos, B. Martínez-Haya, and L. F. Rull, *Crowding effects in binary mixtures of rod-like and spherical particles.* J. Mol. Recogn., 17:417, 2004.

[165] G. Cinacchi and L. De Gaetani, *Diffusion in the lamellar phase of a rod-sphere mixture.* J. Chem. Phys., 131:104908, 2009.

[166] L. Wu, A. Malijevský, G. Jackson, E. A. Müller, and C. Avendaño, *Orientational ordering and phase behaviour of binary mixture of hard spheres and hard spherocylinders.* J. Chem. Phys., 143:044906, 2015.

[167] G. Cinacchi, E. Velasco, and L. Mederos, *Entropic segregation in smectic phases of hard-body mixtures.* J. Phys. Condens. Matter, 16:S2003, 2004.

[168] A. Cuetos, B. Martínez-Haya, S. Lago, and L. F. Rull, *Use of Parsons-Lee and Onsager theories to predict nematic and demixing behavior in binary mixtures of hard rods and hard spheres.* Phys. Rev. E, 75:061701, 2007.

[169] Z. Dogic, D. Frenkel, and S. Fraden, *Enhanced stability of layered phases in parallel hard spherocylinders due to addition of hard spheres.* Phys. Rev. E, 62:3925, 2000.

[170] R. van Roij, B. Mulder, and M. Dijkstra, *Phase behavior of binary mixtures of thick and thin hard rods.* Physica A, 261:374, 1998.

[171] S. K. Lai and X. Xiao, *Phase diagram of colloid-rod system.* J. Chem. Phys., 132:044905, 2010.

[172] S. Varga, K. Purdy, A. Galindo, S. Fraden, and G. Jackson, *Nematic-nematic phase separation in binary mixtures of thick and thin hard rods: Results from Onsager-like theories.* Phys. Rev. E, 72:051704, 2005.

[173] S. Varga, E. Velasco, L. Mederos, and F. J. Vesely, *Stability of the columnar and smectic phases of length-bidisperse parallel hard cylinders.* Mol. Phys., 107:2481, 2009.

[174] T. Koda, M. Numajiri, and S. Ikeda, *Smectic-A Phase of a Bidisperse System of Parallel Hard Rods and Hard Spheres.* J. Phys. Soc. Jpn., 65:3551, 1996.

[175] Y. Martinez-Ratón, G. Cinacchi, E. Velasco, and L. Mederos, *Depletion effects in smectic phases of hard-rod-hard-sphere mixtures.* Eur. Phys. J. E, 21:175, 2006.

[176] S. D. Peroukidis, A. G. Vanakaras, and D. J. Photinos, *Liquid crystalline phases and demixing in binary mixtures of shape-anisometric colloids.* J. Mater. Chem., 20:10495, 2010.

[177] D. Antypov and D. J. Cleaver, *Orientational and phase-coexistence behaviour of hard rod-sphere mixtures.* Chem. Phys. Lett., 377:311, 2003.

[178] D. Antypov and D. J. Cleaver, *The role of attractive interactions in rod-sphere mixtures.* J. Chem. Phys., 120:10307, 2004.

[179] N. Urakami and M. Imai, *Dependence on sphere size of the phase behavior of mixtures of rods and spheres.* J. Chem. Phys., 119:2463, 2003.

[180] F. J. Vesely, *Smectic phases in hard particle mixtures: Koda's theory.* Mol. Phys., 103:679, 2005.

[181] G. H. Koenderink, G. A. Vliegenthart, S. G. J. M. Kluijtmans, A. Van Blaaderen, A. P. Philipse, and H. N. W. Lekkerkerker, *Depletion-induced crystallization in colloidal rod-sphere mixtures.* Langmuir, 15:4693, 1999.

[182] E. Grelet, *Hard-rod behavior in dense mesophases of semiflexible and rigid charged viruses.* Phys. Rev. X, 4:021053, 2014.

[183] X. Ye, J. A. Millan, M. Engel, J. Chen, B. T. Diroll, S. C. Glotzer, and C. B. Murray, *Shape Alloys of Nanorods and Nanospheres from Self-Assembly.* Nano Lett., 13:4980, 2013.

[184] N. A. M. Verhaegh and A. V. Blaaderen, *Dispersions of Rhodamine-Labeled Silica Spheres: Synthesis, Characterization, and Fluorescence Confocal Scanning Laser Microscopy.* Langmuir, 10:1427, 1994.

[185] B. Mulder, *Isotropic-symmetry-breaking bifurcations in a class of liquid-crystal models.* Phys. Rev. A, 39:360, 1989.

[186] M. J. Freiser, *Ordered states of a nematic liquid.* Phys. Rev. Lett., 24:1041, 1970.

[187] G. R. Luckhurst, *Liquid crystals: A missing phase found at last?* Nature, 430:413, 2004.

[188] K. Severing and K. Saalwächter, *Biaxial nematic phase in a thermotropic liquid-crystalline side-chain polymer.* Phys. Rev. Lett., 92:125501, 2004.

[189] L. A. Madsen, T. J. Dingemans, M. Nakata, and E. T. Samulski, *Thermotropic biaxial nematic liquid crystals.* Phys. Rev. Lett., 92:145505, 2004.

[190] B. R. Acharya, A. Primak, and S. Kumar, *Biaxial nematic phase in bent-core thermotropic mesogens.* Phys. Rev. Lett., 92:145506, 2004.

[191] R. Berardi and C. Zannoni, *Do thermotropic biaxial nematics exist? A Monte Carlo study of biaxial Gay-Berne particles.* J. Chem. Phys., 113:5971, 2000.

[192] R. Berardi, L. Muccioli, S. Orlandi, M. Ricci, and C. Zannoni, *Computer simulations of biaxial nematics.* J. Phys.: Condens. Matter, 20:463101, 2008.

[193] E. van den Pol, A. V. Petukhov, D. V. B. D. M. E. Thies-Weesie, and G. J. Vroege, *Experimental realization of biaxial liquid crystal phases in colloidal dispersions of boardlike particles.* Phys. Rev. Lett, 103:258301, 2009.

[194] P. J. Camp and M. Allen, *Phase diagram of the hard biaxial ellipsoid fluid.* J. Chem. Phys., 106:6681, 1997.

[195] S. D. Peroukidis and A. G. Vanakaras, *Phase diagram of hard board-like colloids from computer simulations.* Soft Matter, 9:7419, 2013.

[196] S. D. Peroukidis, A. G. Vanakaras, and D. J. Photinos, *Supramolecular nature of the nematic-nematic phase transitions of hard boardlike molecules.* Phys. Rev. E, 88:062508, 2013.

[197] R. Rosso, *Orientational order parameters in biaxial nematics: Polymorphic notation.* Liquid Crystals, 34:737, 2007.

[198] M. P. Allen, *Computer simulations of a biaxial liquid crystal.* Liquid Crystals, 8:499, 1990.

[199] Y. Rosenfeld, *Free-energy model for the inhomogeneous hard-sphere fluid mixture and density-functional theory of freezing.* Phys. Rev. Lett., 63:980, 1989.

[200] P. Tarazona, *Density functional for hard sphere crystals: A fundamental measure approach.* Phys. Rev. Lett., 84:694, 2000.

[201] Y. Rosenfeld, *Density functional theory of molecular fluids: Free-energy model for the inhomogeneous hard-body fluid.* Phys. Rev. E, 50:R3318, 1994.

[202] H. Hansen-Goos and K. Mecke, *Fundamental measure theory for inhomogeneous fluids of nonspherical hard particles.* Phys. Rev. Lett., 102:018302, 2009.

[203] H. Hansen-Goos and K. Mecke, *Tensorial density functional theory for non-spherical hard-body fluids.* J. Phys.: Condens. Matter, 22:364107, 2010.

[204] M. Marechal and H. Löwen, *Density functional theory for hard polyhedra.* Phys. Rev. Lett., 110:137801, 2013.

[205] P. Tarazona and Y. Rosenfeld, *From zero-dimension cavities to free-energy functionals for hard disks and hard spheres.* Phys. Rev. E, 55:R4873, 1997.

[206] M. Marechal, H. H. Goetzke, A. Härtel, and H. Löwen, *Inhomogeneous fluids of colloidal hard dumbbells: Fundamental measure theory and Monte Carlo simulations.* J. Chem. Phys., 135:234510, 2011.

[207] B. S. John, C. Juhlin, and F. A. Escobedo, *Phase behavior of colloidal hard perfect tetragonal parallelepipeds.* J. Chem. Phys., 128:044909, 2008.

[208] E. Grelet and S. Fraden, *What is the origin of chirality in the cholesteric phase of virus suspensions?* Phys. Rev. Lett., 90:198302, 2003.

[209] P. J. Collings. *Liquid Crystals: Nature's Delicate Phase of Matter.* Princeton University Press, 2002.

[210] N. Tamaoki, *Cholesteric liquid crystals for color information technology.* Adv. Mater., 13:1135, 2001.

[211] J. P. F. Lagerwall and G. Scalia, *A new era for liquid crystal research: Applications of liquid crystals in soft matter nano-, bio- and microtechnology.* Curr. Appl. Phys., 12:1387, 2012.

[212] D. B. DuPré and R. W. Duke, *Temperature, concentration, and molecular weight dependence of the twist elastic constant of cholesteric poly-γ-benzyl-L-glutamate.* J. Chem. Phys., 63:143, 1975.

[213] B. P. Huff, J. J. Krich, and P. J. Collings, *Helix inversion in the chiral nematic and isotropic phases of a liquid crystal.* Phys. Rev. E, 61:5372, 2000.

[214] L. Rossi, S. Sacanna, and K. P. Velikov, *Cholesteric colloidal liquid crystals from phytosterol rod-like particles.* Soft Matter, 7:64, 2011.

[215] F. Reinitzer, *Beiträge zur kenntnis des cholesterins.* Monatsh. Chem., 9:421, 1888.

[216] O. Z. Lehmann, *Über fliessende krystalle.* Z. Phys. Chem. (Leipzig), 4:462, 1889.

[217] G. J. Vroege and H. N. W. Lekkerkerker, *Phase transitions in lyotropic colloidal and polymer liquid crystals.* Rep. Prog. Phys., 55:1241, 1992.

[218] C. Robinson, *Liquid-crystalline structures in polypeptide solutions.* Tetrahedron, 13:219, 1961.

[219] G. Zanchetta, F. Giavazzi, M. Nakata, M. Buscaglia, R. Cerbino, N. A. Clark, and T. Bellini, *Right-handed double-helix ultrashort DNA yields chiral nematic phases with both right- and left-handed director twist.* Proc. Natl. Acad. Sci. USA, 107:17497, 2010.

[220] Z. Dogic and S. Fraden, *Cholesteric phase in virus suspensions.* Langmuir, 16:7820, 2000.

[221] E. Barry, D. Beller, and Z. Dogic, *A model liquid crystalline system based on rodlike viruses with variable chirality and persistence length.* Soft Matter, 5:2563, 2009.

[222] Z. Zhang and E. Grelet, *Tuning chirality in the self-assembly of rod-like viruses by chemical surface modifications.* Soft Matter, 9:971, 2013.

[223] F. Tombolato, A. Ferrarini, and E. Grelet, *Chiral nematic phase of suspensions of rodlike viruses: left-handed phase helicity from a right-handed molecular helix.* Phys. Rev. Lett., 96:258302, 2006.

[224] J. F. Revol, H. Bradford, J. Giasson, R. H. Marchessault, and D. G. Gray, *Helicoidal self-ordering of cellulose microfibrils in aqueous suspension.* Int. J. Biol. Macromol., 14:170, 1992.

[225] R. S. Werbowyj and D. G. Gray, *Liquid crystalline structure in aqueous hydroxypropyl cellulose solutions.* Mol. Cryst. Liq. Cryst., 34:97, 1976.

[226] K. Hiltrop. *Chirality in Liquid Crystals.* edited by H. S. Kitzerow and C. Bahr (New York: Springer), 2001.

[227] S. M. Aharoni, *Rigid backbone polymers. 2. Polyisocyanates and their liquid-crystal behavior.* Macromolecules, 12:94, 1979.

[228] T. Sato, Y. Sato, Y. Umemura, A. Teramoto, and Y. Nagamura, *Polyisocyanates and the interplay of experiment and theory in the formation of lyotropic cholesteric states.* Macromolecules, 26:4551, 1993.

[229] J. Watanabe, H. Kamee, and M. Fujiki, *First observation of thermotropic cholesteric liquid crystal in helical polysilane.* Polym. J., 33:495, 2001.

[230] T. Gibaud, E. Barry, M. J. Zakhary, M. Henglin, A. Ward, Y. Yang, C. Berciu, R. Oldenbourg, M. F. Hagan, D. Nicastro, R. B. Meyer, and Z. Dogic, *Reconfigurable self-assembly through chiral control of interfacial tension.* Nature, 481:348, 2012.

[231] P. Sharma, A. Ward, T. Gibaud, M. F. Hagan, and Z. Dogic, *Hierarchical organization of chiral rafts in colloidal membranes.* Nature, 513:77, 2014.

[232] F. C. Bawden, N. W. Pirie, J. D. Bernal, and I. Fankuchen, *Liquid crystalline substances from virus-infected plants.* Nature, 138:1051, 1936.

[233] F. Tombolato and A. Ferrarini, *From the double-stranded helix to the chiral nematic phase of B-DNA: A molecular model.* J. Chem. Phys., 122:054908, 2005.

[234] N. Katsonis, E. Lacaze, and A. Ferrarini, *Controlling chirality with helix inversion in cholesteric liquid crystals.* J. Mater. Chem., 22:7088, 2012.

[235] N. D. Mas, A. Ferrarini, P. L. Nordio, P. Styring, and S. Todd, *Prediction of pitch in twisted nematics: Puzzling cases.* Mol. Cryst. Liq. Cryst., 328:391, 1999.

[236] E. Barry, Z. Hensel, Z. Dogic, M. Shribak, and R. Oldenbourg, *Entropy-driven formation of a chiral liquid-crystalline phase of helical filaments.* Phys. Rev. Lett., 96:018305, 2006.

[237] K. Hasegawa, I. Yamashita, and K. Namba, *Quasi- and nonequivalence in the structure of bacterial flagellar filament.* Biophys. J., 74:569, 1998.

[238] R. B. Meyer, *Effects of electric and magnetic fields on the structure of cholesteric liquid crystals.* Appl. Phys. Lett., 12:281, 1968.

[239] R. D. Kamien, *Liquids with chiral bond order.* J. Phys. II, 6:461, 1996.

[240] A. Eremin and A. Jákli, *Polar bent-shape liquid crystals - from molecular bend to layer splay and chirality.* Soft Matter, 9:615, 2013.

[241] V. Borshch, Y. K. Kim, J. Xiang, M. Gao, A. Jákli, V. P. Panov, J. K. Vij, C. T. Imrie, M. G. Tamba, G. H. Mehl, and O. D. Lavrentovich, *Nematic twist-bend phase with nanoscale modulation of molecular orientation.* Nat. Commun., 4:2635, 2013.

[242] D. Chen, J. H. Porada, J. B. Hooper, A. Klittnick, Y. Shen, M. R. Tuchband, E. Korblova, D. Bedrov, D. M. Walba, M. A. Glaser, J. E. Maclennan, and N. A. Clark, *Twist-bend heliconical chiral nematic liquid crystal phase of an achiral rigid bent-core mesogen.* Proc. Natl. Acad. Sci. USA, 110:15931, 2013.

[243] G. T. Evans, *Hard body model for chiral nematic liquid crystals.* Mol. Phys., 77:969, 1992.

[244] S. Varga and G. Jackson, *A study of steric chirality: the chiral nematic phase of a system of chiral two-site HGO molecules.* Mol. Phys., 109:1313, 2011.

[245] H. H. Wensink, *Spontaneous sense inversion in helical mesophases.* EPL, 107:36001, 2014.

[246] S. Varga and G. Jackson, *Study of the pitch of fluids of electrostatically chiral anisotropic molecules: Mean-field theory and simulation.* Mol. Phys., 104:3681, 2006.

[247] H. H. Wensink and G. Jackson, *Generalized van der Waals theory for the twist elastic modulus and helical pitch of cholesterics.* J. Chem. Phys., 130:234911, 2009.

[248] H. H. Wensink and G. Jackson, *Cholesteric order in systems of helical Yukawa rods.* J. Phys.: Condens. Matter, 23:194107, 2011.

[249] G. Germano, M. P. Allen, and A. J. Masters, *Simultaneous calculation of the helical pitch and the twist elastic constant in chiral liquid crystals from intermolecular torques.* J. Chem. Phys., 116:9422, 2002.

[250] R. Memmer, *Determination of equilibrium pitch of cholesteric phases by isobaric-isothermal Monte Carlo simulation.* J. Chem. Phys., 114:8210, 2001.

[251] W. J. A. Goossens, *Molecular theory of cholesteric phase and of twisting power of optically active molecules in a nematic liquid crystals.* Mol. Cryst. Liq. Cryst., 12:237, 1971.

[252] S. Belli, S. Dussi, M. Dijkstra, and R. van Roij, *Density functional theory for chiral nematic liquid crystals.* Phys. Rev. E, 90:020503(R), 2014.

[253] M. P. Allen and A. J. Masters, *Computer simulation of a twisted nematic liquid crystal.* Mol. Phys., 79:277, 1993.

[254] D. Frenkel, *Simulations: The dark side.* Eur. Phys. J. Plus, 128:10, 2013.

[255] R. Berardi, H.-G. Kuball, R. Memmer, and C. Zannoni, *Chiral induction in nematics: A computer simulation study.* J. Chem. Soc., Faraday Trans., 94:1229, 1998.

[256] S. Varga and G. Jackson, *Simulation of the macroscopic pitch of a chiral nematic phase of a model chiral mesogen.* Chem. Phys. Lett., 377:6, 2003.

[257] M. P. Allen, *Calculating the helical twisting power of dopants in a liquid crystal by computer simulation.* Phys. Rev. E, 47:4611, 1993.

[258] P. J. Camp, *On the helical twisting power of chiral dopants in liquid crystals.* Mol. Phys., 91:381, 1997.

[259] A. V. Emelyanenko, M. A. Osipov, and D. A. Dunmur, *Molecular theory of helical sense inversions in chiral nematic liquid crystals.* Phys. Rev. E, 62:2340, 2000.

[260] E. Frezza, A. Ferrarini, H. B. Kolli, A. Giacometti, and G. Cinacchi, *Left or right cholesterics? A matter of helix handedness and curliness.* Phys. Chem. Chem. Phys., 16:16225, 2014.

[261] A. A. Kornyshev, S. Leikin, and S. V. Malinin, *Chiral electrostatic interaction and cholesteric liquid crystals of DNA.* Eur. Phys. J. E, 7:83, 2002.

[262] T. Odijk, *Pitch of a polymer cholesteric.* J. Phys. Chem., 91:6060, 1987.

[263] A. B. Harris, R. D. Kamien, and T. C. Lubensky, *Microscopic origin of cholesteric pitch.* Phys. Rev. Lett., 78:1476, 1997.

[264] A. B. Harris, R. D. Kamien, and T. C. Lubensky, *Molecular chirality and chiral parameters.* Rev. Mod. Phys., 71:1745, 1999.

[265] E. Frezza, A. Ferrarini, H. B. Kolli, A. Giacometti, and G. Cinacchi, *The isotropic-to-nematic phase transition in hard helices: Theory and simulation.* J. Chem. Phys., 138:164906, 2013.

[266] H. B. Kolli, E. Frezza, G. Cinacchi, A. Ferrarini, A. Giacometti, T. S. Hudson, C. De Michele, and F. Sciortino, *Self-assembly of hard helices: a rich and unconventional polymorphism.* Soft Matter, 10:8171, 2014.

[267] W.-K. Tung. *Group Theory in Physics.* World Scientific Publishing Company, 1985.

[268] L. Liu, P. Lu, L. Meng, W. Jin, and S. Li, *Excluded volumes of clusters in tetrahedral particle packing.* Phys. Lett. A, 378:835, 2014.

[269] N. Ibarra-Avalos, A. Gil-Villegas, and A. Richa, *Excluded volume of hard cylinders of variable aspect ratio.* Mol. Simul., 33:505, 2007.

[270] K. T. Nguyen, F. Sciortino, and C. De Michele, *Self-assembly-driven nematization.* Langmuir, 30:4814, 2014.

[271] C. De Michele, T. Bellini, and F. Sciortino, *Self-assembly of bifunctional patchy particles with anisotropic shape into polymers chains: Theory, simulations, and experiments.* Macromolecules, 45:1090, 2012.

[272] C. De Michele, L. Rovigatti, T. Bellini, and F. Sciortino, *Self-assembly of short DNA duplexes: from a coarse-grained model to experiments through a theoretical link.* Soft Matter, 8:8388, 2012.

[273] H. B. Movahed, R. C. Hidalgo, and D. E. Sullivan, *Phase transitions of semiflexible hard-sphere chain liquids.* Phys. Rev. E, 73:032701, 2006.

[274] W. H. Press, S. A. Teukolsky, W. T. Vetterling, and B. P. Flannery. *Numerical Recipes in C.* Cambridge University Press, 1992.

[275] A. J. Schultz and D. A. Kofke, *Virial coefficients of model alkanes.* J. Chem. Phys., 133:104101, 2010.

[276] A. J. Schultz and D. A. Kofke, *Fifth to eleventh virial coefficients of hard spheres.* Phys. Rev. E, 90:023301, 2014.

[277] K. M. Benjamin, J. K. Singh, A. J. Schultz, and D. A. Kofke, *Higher-order virial coefficients of water models.* J. Phys. Chem. B, 111:11463, 2007.

[278] M. Allen. Private Communication, 2014.

[279] M. Dennison, M. Dijkstra, and R. van Roij, *The effects of shape and flexibility on bio-engineered fd-virus suspensions.* J. Chem. Phys., 135:144106, 2011.

[280] M. Dennison, M. Dijkstra, and R. van Roij, *Phase diagram and effective shape of semi-flexible colloidal rods and biopolymers.* Phys. Rev. Lett., 106:208302, 2011.

[281] Z. Dogic, J. Zhang, A. W. C. Lau, H. Aranda-Espinoza, P. Dalhaimer, D. E. Discher, P. A. Janmey, R. D. Kamien, T. C. Lubensky, and A. G. Yodh, *Elongation and fluctuations of semiflexible polymers in a nematic solvent.* Phys. Rev. Lett., 92:125503, 2004.

[282] H. Fynewever and A. Yethiraj, *Phase behavior of semiflexible tangent hard sphere chains.* J. Chem. Phys., 108:1636, 1998.

[283] R. Priest and T. C. Lubensky, *Biaxial model for cholesteric liquid crystals.* Phys. Rev. A, 9:99, 1974.

[284] S. Dhakal and J. V. Selinger, *Chirality and biaxility in cholesteric liquid crystals.* Phys. Rev. E, 83:020702(R), 2011.

[285] D. Zerrouki, J. Baudry, D. Pine, P. Chaikin, and J. Bibette, *Chiral colloidal clusters.* Nature, 455:380, 2008.

[286] Y. Yin and Y. Xia, *Self-assembly of spherical colloids into helical chains with well-controlled handedness.* J. Am. Chem. Soc., 125:2048, 2003.

[287] L. Jiang, J. W. J. de Folter, J. Huang, A. P. Philipse, W. K. Kegel, and A. V. Petukhov, *Helical colloidal sphere structures through thermo-reversible co-assembly with molecular microtubes.* Angew. Chem. Int. Edit., 52:3364, 2013.

[288] G. Singh, H. Chan, A. Baskin, E. Gelman, N. Repnin, P. Král, and R. Klajn, *Self-assembly of magnetite nanocubes into helical superstructures.* Science, 345:1149, 2014.

[289] F. Smallenburg, H. R. Vutukuri, A. Imhof, A. van Blaaderen, and M. Dijkstra, *Self-assembly of colloidal particles into strings in a homogenous external electric or magnetic field.* J. Phys.: Condens. Matter, 24:464113, 2012.

[290] G. T. Pickett, M. Gross, and H. Okuyama, *Spontaenous chirality in simple systems.* Phys. Rev. Lett., 85:3652, 2000.

[291] H. B. Chen, Y. Zhou, J. Yin, J. Yan, Y. Ma, L. Wang, Y. Cao, J. Wang, and J. Pei, *Single organic microtwist with tunable pitch.* Langmuir, 25:5459, 2009.

[292] Y. Okazaki, J. Cheng, D. Dedovets, G. Kemper, M.-H. Delville, M.-C. Durrieu, H. Ihara, M. Takafuji, E. Pouget, and R. Oda, *Chiral colloids: Homogeneous suspension of individualized SiO_2 helical and twisted nanoribbons.* ACS Nano, 8:6863, 2014.

[293] H. B. Kolli, G. Cinacchi, A. Ferrarini, and A. Giacometti, *Chiral self-assembly of helical particles.* Faraday Discuss., DOI:10.1039/C5FD00132C.

[294] G. van Anders, D. Klotsa, N. K. Ahmed, M. Engel, and S. C. Glotzer, *Understanding shape entropy through local dense packing.* Proc. Natl. Acad. Sci. USA, 111:E4812, 2014.

[295] P. F. Damasceno, A. S. Karas, B. A. Schultz, M. Engel, and S. C. Glotzer, *Controlling chirality in entropic crystals.* Phys. Rev. Lett., 115:158303, 2015.

[296] A. Haji-Akbari, M. Engel, A. S. Keys, X. Zheng, R. G. Petschek, P. Palffy-Muhoray, and S. C. Glotzer, *Disordered, quasicrystalline and crystalline phases of densely packed tetrahedra.* Nature, 642:773, 2009.

[297] M. Melle, M. Theile, C. K. Hall, and M. Schoen, *Nanoconfinement-induced structures in chiral liquid crystals.* Int. J. Mol. Sci., 14:17584, 2013.

[298] S. Dussi, S. Belli, R. van Roij, and M. Dijkstra, *Cholesterics of colloidal helices: Predicting the macroscopic pitch from the particle shape and thermodynamic state.* J. Chem. Phys., 142:074905, 2015.

[299] R. van Roij, M. Dijkstra, and R. Evans, *Orientational wetting and capillary nematization of hard-rod fluids.* Europhys. Lett., 49:350, 2000.

[300] L. Kang, T. Gibaud, Z. Dogic, and T. C. Lubensky, *Entropic forces stabilize diverse emergent structures in colloidal membranes.* Soft Matter, 12:386, 2016.

[301] J. Yeom, B. Yeom, H. Chan, K. W. Smith, S. Dominguez-Medina, J. H. Bahng, G. Zhao, W.-S. Chang, S.-J. Chang, A. Chuvilin, D. Melnikau, A. L. Rogach, P. Zhang, S. Link, P. Král, and N. A. Kotov, *Chiral templating of self-assembling nanostructures by circularly polarized light.* Nat. Mater., 14:66, 2015.

[302] S. Srivastava, A. Santos, K. Critchley, K. S. Kim, P. Podsiadlo, K. Sun, J. Lee, C. Xu, G. D. Lilly, S. C. Glotzer, and N. A. Kotov, *Light-controlled self-assembly of semiconductor nanoparticles into twisted ribbons.* Science, 327:1355, 2010.

[303] P. J. Camp, M. P. Allen, and A. J. Masters, *Theory and computer simulation of bent-core molecules.* J. Chem. Phys., 111:9871, 1999.

[304] R. Memmer, *Liquid crystal phases of achiral banana-shaped molecules: a computer simulation study.* Liquid Crystals, 29:483, 2002.

[305] Y. Lansac, P. K. Maiti, N. A. Clark, and M. A. Glaser, *Phase behavior of bent-core molecules.* Phys. Rev. E, 67:011703, 2003.

[306] C. Greco, G. R. Luckhurst, and A. Ferrarini, *Molecular geometry, twist-bend nematic phase and unconventional elasticity: a generalised Maier-Saupe theory.* Soft Matter, 10:9318, 2014.

[307] Y. Yang, G. Chen, L. J. Martinez-Miranda, H. Yu, K. Liu, and Z. Nie, *Synthesis and liquid-crystal behavior of bent colloidal silica rods.* J. Am. Chem. Soc., 138:68, 2016.

[308] T. Drwenski, S. Dussi, M. Hermes, M. Dijkstra, and R. van Roij. *Phase diagrams of charged colloidal rods: can a uniaxial charge distribution break chiral symmetry?* arXiv:1512.04694. accepted in J. Chem. Phys. (2016).

[309] E. Eggen, M. Dijkstra, and R. van Roij, *Effective shape and phase behavior of short charged rods.* Phys. Rev. E, 79:041401, 2009.

Summary

In this thesis, we study entropy-driven phase transitions in suspensions of colloidal particles. Colloids are small particles, with typical sizes varying from the nanometer to the micron range, dispersed in a medium that is composed of much smaller particles (atoms or molecules). Because of this size difference, colloids experience Brownian motion that allows them to (slowly) move around the medium, exploring the microscopic configurations available, and possibly arrange themselves in ordered structures. This process is called *self-assembly* and the different structures that can be formed are analogous to those of atomic and molecular systems. For example, colloids can self-assemble into fluids (disordered arrangements of particles), liquid-crystals (partially ordered), and crystals (fully ordered). The stability of and the transitions between these phases, i.e., the *phase behaviour*, depend both on the interactions between the colloids and the properties of the whole system, which are thermodynamic parameters like temperature or density. Here, we focus on systems composed of *hard* colloidal particles: particles that do not have any interactions except for the fact that cannot overlap with each other. By using computer simulations and classical density functional theory, we show that the particle *shape is enough* for the formation of several thermodynamic phases. In other words, it is possible to obtain order in complete absence of any attraction in the system, just by increasing the density of the system. These transitions are (fully) *entropy-driven* since no change in energy is associated to the phase transition but only a change in entropy, that is a quantity related to the number of possible microscopic particle arrangements. Forming a more ordered structure corresponds to increasing the number of ways that the particles can arrange themselves, therefore increasing the entropy of the system.

Hard spheres, that have served as an indispensable model system in condensed-matter studies for more than half a century, are the first system studied in this thesis. It is well established that, under equilibrium conditions, hard spheres in bulk crystallize into a face-centered-cubic (FCC) crystal. However, in chapter 2 we show that a novel phase behaviour emerges when the system is spherically confined. Indeed, when a large number (tens of thousands) of hard spheres are compressed, while confined in a spherical cavity, they do not self-assemble into an FCC crystal but rather they form icosahedral clusters. Icosahedral symmetry, which is not compatible with truly long-range order, is found in many other systems, such as liquids, glasses, atomic clusters, quasicrystals and virus-capsids. Our computer simulations confirm that in spherical confinement the icosahedral order is thermodynamically favoured over the FCC one and corroborate real-space measurements on evaporating emulsion droplets containing colloids, that have been performed by experimentalists in our group. Moreover, by elucidating the crystallization mechanism of the icosahedral structures, we provide new insights into the interplay between confinement and crystallization.

In chapter 3, we study a system of elongated hard colloids with a spherocylindrical shape, that is a cylinder with two hemispherical caps. Shape anisotropy is the essential ingredient to form liquid-crystal phases. Hard spherocylinders have been extensively used to study uniaxial nematic and smectic (liquid-crystal) phases. In a nematic phase,

particles are on average aligned along a common direction, whereas their positions are homogeneously distributed in space. In a smectic phase, particles are aligned and form layers. The transition between an isotropic (completely disordered phase) and a nematic phase is well described by a second-virial classical density functional theory (Onsager theory). Such theory is applied in chapter 3 to spherocylinders and it is adapted to different particle models and to chiral nematic phases in the following chapters. Furthermore, we introduce a set of global and local order parameters to describe liquid crystalline order that are used in chapter 3 and in the following chapters both on simulation and experimental data. Experimentally, silica colloids with an effective spherocylindrical shape have been synthesised and studied in our group. The experimental phase behaviour of silica rods in sedimentation-diffusion equilibrium is compared against computer simulations by taking into account the effective dimensions of the experimental particles and the effect of size polydispersity on the phase behaviour. Qualitative agreement is obtained for the overall phase behaviour and quantitative agreement for packing fractions up to 40%. In chapter 4, we study liquid crystal phases formed by binary mixtures of colloidal rods and spheres, focusing in particular on the binary smectic phase, which consists of alternating layers of rods and spheres. A phase diagram of a binary mixture of silica rods and spheres, obtained by experimentalists in our group by using a quantitative real-space analysis that also relies on the order parameters introduced in this thesis, is compared with computer simulation results. We verify that the binary smectic phase observed experimentally can be stabilized by entropy alone and this opens up the possibility of combining new materials properties at different length scales, without the need to finely tune inter-particle attractions.

In chapter 5, we consider hard rod-like particles with a polyhedral shape. These colloids do not have uniaxial symmetry, like the spherocylinders, but rather are biaxial. We first simulate systems of elongated equilateral triangular prisms forming isotropic, uniaxial nematic and smectic phases and compare the phase behaviour with theoretical predictions based on fundamental measure theory, carried out by another research group, finding good agreement. We also highlight the fact that triangular prisms exhibit liquid-crystal phases at lower densities and lower particle aspect ratios with respect to spherocylinders due to the presence of flat faces in the particle shape. Next, we investigate what the necessary conditions are to form prolate, oblate and biaxial nematic phases. In fact, for biaxial particles, nematic phases can be divided into (uniaxial) prolate, (uniaxial) oblate and biaxial phases, depending on whether the long, the short, or both particle axes are aligned. We show that the general liquid-crystal behaviour can be predicted on the basis of a shape parameter that is determined by the difference between the ratios of the particle axes, as already pointed out in the literature. In particular, biaxial nematic phases are found when such a shape parameter is close to zero, i.e., the "dual" shape. However, we highlight the fact that biaxial nematic phases are only observed when the particles are sufficiently elongated. This additional criterium depends on the exact particle shape, i.e., the threshold value on the particle length becomes more extreme going from spheroplatelets to triangular prisms to cuboids.

In chapters 6, 7 and 8, we consider colloidal particles with a chiral shape. Chiral objects, like our hands, lack mirror symmetry. In the case of chiral particles, the nematic organisation is chiral as well, which implies that the direction along which the particles

are oriented twists in an helical fashion. This type of liquid-crystalline phase is termed cholesteric and features a typical length scale, called cholesteric pitch, over which the structure repeats itself. Cholesteric phases that are responsive to an external electric field and have a cholesteric pitch of the same order as the wavelength of visible light are often employed in opto-electronic applications like liquid-crystal displays (LCDs). Building a general theoretical framework to describe the microscopic origin of macroscopic chirality in (colloidal) liquid crystals is a long-standing challenge and it is the aim of chapter 6. By combining classical density functional theory with Monte Carlo calculations of virial-type coefficients, we are able to obtain the equilibrium cholesteric pitch as a function of thermodynamic state and microscopic details. Applying the theory to hard helices, we observe both right- and left-handed cholesteric phases that depend on a subtle combination of particle geometry and system density. We also predict that for particular helical shapes an inversion in the cholesteric sense of twist can occur upon increasing system density. In chapter 7, we introduce a novel chiral hard-particle model, namely particles with a twisted polyhedral shape and obtain, for the first time, a stable fully-entropy-driven cholesteric phase by computer simulations. By slightly modifying the triangular base of the particle, we are able to switch from a left-handed prolate to a right-handed oblate cholesteric using the same right-handed twisted particle model. Furthermore, we find qualitative agreement with the theoretical prediction based on the theory described in chapter 6. Our results unveil how the competition between particle biaxiality and chirality is directly transmitted at a higher level into the nematic phases. New theoretical challenges on the self-assembly of chiral particles can be now undertaken and some of them are already addressed in chapter 8. In particular, we speculate on the possible formation of novel chiral nematic phases made of hard particles and highlight some open issues in this field.

The self-assembly of colloidal particles holds a great promise of structuring matter with novel properties, in three dimensions, at different length-scales, in a bottom-up, affordable and sustainable fashion. This cannot be achieved without fundamentally understanding the key features responsible for the stabilization of the different structures, starting from the role of particle shape on the colloidal phase behaviour. Especially now that complex-shaped colloidal particles can be synthesized, design rules are needed for the building blocks of the future materials. The work presented in this thesis will, hopefully, contribute to the scientific progress along these directions.

Samenvatting

In dit proefschrift bestuderen we entropie-gedreven overgangen in suspensies van colloïdale deeltjes. Colloïden zijn kleine deeltjes, typisch een nanometer tot een micrometer groot, gedispergeerd in een medium bestaande uit veel kleinere deeltjes (atomen of moleculen). Ten gevolge van dit verschil in grootte ondergaan de colloïden Brownse beweging en bewegen ze zich (langzaam) in het medium, waarbij ze de toegankelijke microscopische configuraties verkennen en zich mogelijk verzamelen in geordende structuren. Dit proces heet zelforganisatie, waarbij de gevormde structuren analoog kunnen zijn aan de structuren die in moleculaire en atomaire systemen voorkomen. Colloïden kunnen zich bijvoorbeeld organiseren als een vloeistof (ongeordend systeem), een vloeibaar kristal (deels geordend) en als kristal (volledig geordend). De stabiliteit van en de overgang tussen deze verschillende fases, het fasegedrag, hangen af van de interacties tussen de colloïden en de thermodynamische eigenschappen van het gehele systeem, zoals temperatuur en druk. In dit proefschrift richten we ons op harde colloïden. Dit zijn deeltjes die geen interactie met elkaar hebben afgezien van het feit dat ze elkaar niet mogen overlappen. Door gebruik te maken van computersimulaties en klassieke dichtheidsfunctionaal theorie laten we zien dat de vorm van een deeltje voldoende is voor het ontstaan van verschillende thermodynamische fases. Met andere woorden, het is mogelijk om orde te verkrijgen in een systeem zonder dat er enige attracties aanwezig zijn, simpelweg door de dichtheid van het systeem te verhogen. Dit soort overgangen zijn (volledig) entropie-gedreven, omdat er alleen een verandering is in entropie en niet in energie tijdens de faseovergang. Entropie is een maat voor het aantal mogelijke microscopische configuraties waarin de deeltjes zich kunnen bevinden. Door het vormen van een geordendere structuur neemt het aantal mogelijke configuraties toe, waardoor ook de entropie van het systeem toeneemt. We beginnen met het bestuderen van een systeem dat bestaat uit harde bollen, dit is een model systeem dat van cruciaal belang is in de gecondenseerde materie. Het is algemeen bekend dat harde bollen onder evenwichtsomstandigheden kristalliseren in een vlak-gecentreerd-kristal (FCC). Echter, in hoofdstuk 2 laten we zien dat een nieuw soort fasegedrag verschijnt wanneer de deeltjes opgesloten worden in een bolvormige omgeving. Wanneer een groot aantal (tienduizenden) harde bollen worden samengedrukt in een bolvormige ruimte organiseren ze zich niet in een FCC-kristal, maar in icosaedrische clusters. Een icosaedrische symmetrie kan niet bestaan over lange afstanden en komt vooral voor in systemen zoals vloeistoffen, gassen, atomaire clusters, quasikristallen en viruscapsiden. Onze computersimulaties laten zien dat in een bolvormige ruimte de icosaedrische ordening thermodynamisch gunstiger is dan een FCC ordening en sluiten daarmee aan bij de experimentele metingen die in onze groep gedaan zijn op verdampende emulsiedruppels waarin colloïden "opgesloten" zaten. Daarnaast leidt het ophelderen van het kristallisatiemechanisme van icosaedrische structuren tot nieuw inzicht in de rol van de omgeving op het kristallisatieproces. In hoofdstuk 3, bestuderen we een systeem bestaande uit harde colloïden met een sferocilinder vorm (een cilinder met aan beide uiteinden een halve bol). De anisotrope vorm is een cruciale voorwaarde voor het vormen van een vloeibaar kristallijne fase. Harde sferocilinders worden veelal gebruikt om eenassige nematische en smectische (vloeibaar kristallijne) fases te bestuderen.

In de nematische fase zijn de deeltjes geordend langs één gemeenschappelijke richting, terwijl hun posities homogeen verdeeld zijn in de ruimte. In een smectische fase wijzen de deeltjes ook in één richting, maar zijn ze eveneens geordend in lagen. De overgang van een isotropische (ongeordende fase) naar een nematische fase kan goed beschreven worden met een tweede-viraal klassieke dichtheidsfunctionaal theorie (Onsager theorie). Dit type theorie wordt in hoofdstuk 3 toegepast op sferocilinders en aangepast naar verschillende deeltjesmodellen en de chirale nematische fase in de daaropvolgende hoofdstukken. Verder introduceren we een serie van globale en lokale ordeparameters om de vloeibare kristallijne orde te beschrijven, welke we zullen gebruiken om zowel de orde in de experimentele als de simulatie resultaten te beschrijven. Experimenteel heeft men in onze groep silica colloïden met een effectieve sferocilinder vorm gemaakt en bestudeerd. Het experimentele fasegedrag van silica staven in een gravitationeel-diffusie evenwicht is vergeleken met computersimulaties, waarbij de effectieve dimensies van de experimentele deeltjes en het effect van de polydispersiteit in deeltjesgrootte op het fasegedrag zijn meegenomen. We vinden een kwalitatieve overeenstemming voor het globale fasegedrag en een kwantitatieve overeenstemming voor volumefracties tot 40%. In hoofdstuk 4 bestuderen we de vloeibaar kristallijne fase die gevormd wordt in binaire mengsels bestaande uit bollen en staven, waarbij we ons specifiek richten op de binaire smectische fase bestaande uit alternerende lagen van staven en bollen. We hebben een experimenteel fasediagram van een binair mengsel van staven en bollen, welke is verkregen met kwantitatieve real-space analyse die berust op dezelfde ordeparameters als in deze thesis, vergeleken met de resultaten van de computer simulaties. We tonen aan dat het mogelijk is de experimentele binaire smectische fase enkel door entropie te stabiliseren. Dit maakt het mogelijk om nieuwe materialen en hun bijbehorende eigenschappen te combineren op verschillende lengteschalen, zonder dat de interacties tussen de deeltjes precies ingesteld hoeven te worden.

In hoofdstuk 5 bestuderen we harde staafachtige deeltjes in de vorm van een polyhedron. Deze colloïden hebben niet alleen een eenassige symmetrie, zoals sferocilinders, maar zijn tweeassig. We simuleren eerst systemen bestaande uit uitgerekete gelijkzijdige driehoekige prisma's die een isotropische, eenassige nematische en smectische fase vromen, en vinden dat het fasegedrage in overeenkomst is met het fasegedrag dat voorspeld is door de theoretische berekeningen van een andere groep. We laten zien dat de driehoekige prisma's al vloeibaar kristallijn gedrag vertonen bij lagere dichtheden en kortere aspect ratio's dan sferocilinders, ten gevolge van hun platte vlakkige vorm. Daarnaast bestuderen we welke condities vereist zijn voor het vormen van een prolate, oblate en tweeassige nematische fase. In het algemeen kan men de nematische fase voor tweeassige deeltjes onderverdelen in (eenassige) prolate, (eenassige) oblate en tweeassige fases, waarbij respectievelijk de lange, korte of beide assen van de deeltjes dezelfde richting op wijzen. We laten zien dat vloeibaar kristallijn gedrag kan worden voorspeld op basis van een vorm parameter, welke afhangt van het verschil in de aspect ratioâĂŹs tussen de deeltjesassen, zoals dat al eerder was beschreven in de literatuur. We benadrukken echter dat tweeassige nematisch fases alleen gevormd kunnen worden wanneer de deeltjes voldoende uitgerekt zijn. Deze voorwaarde hangt sterk af de deeltjesvorm, waarbij de minimale deeltjeslengte steeds verder toeneemt van sferoplaatjes naar drieassige prisma's naar kubusachtigen.

In hoofdstuk 6, 7 en 8, bestuderen we colloïdale deeltjes met een chirale vorm. Chirale objecten, zoals onze handen, zijn niet-spiegelsymmetrisch. Wanneer chirale deeltjes een

nematische fase vormen, is de richting waarlangs de deeltjes zich oplijnen gedraaid in de vorm van een helix. Dit type van vloeibaar kristallijne fasen wordt cholesterisch genoemd, waarbij de typische lengteschaal waarna een structuur zich herhaald de cholesterische lengte wordt genoemd. Cholesterische fases die gevoelig zijn voor elektrische velden en een cholesterische lengte hebben die vergelijkbaar is met de golflengte van zichtbaar licht, worden veelal gebruikt in opto-elektronische toepassingen, zoals LCD-schermen. Het doel van hoofdstuk 6 is om een algemene theorie te maken die de microscopische oorsprong van macroscopische chiraliteit in (colloïdale) vloeibare kristallen kan beschrijven. Met een combinatie van klassieke dichtheidsfunctionaal theorie en Monte Carlo berekeningen van viraalachtige coefficiënten verkrijgen we de evenwichts-cholesterische-lengte als functie van de thermodynamische parameters en microscopische details. Wanneer we de theorie toepassen op harde helixen, observeren we zowel rechts- als linkshandige cholesterische fases, afhankelijk van de precieze combinatie tussen de deeltjesgeometrie en de dichtheid van het systeem. Ook voorspellen we dat voor bepaalde helische vormen een inversie in de cholesterische draairichting op kan treden wanneer de dichtheid van het systeem verhoogd wordt. In hoofdstuk 7 introduceren we een nieuw chiraal harde-deeltjes-model, namelijk deeltjes met een gedraaide polyhedrische vorm en verkrijgen we gebruikmakend van computer simulaties, voor het eerst, een stabiele, volledig entropie gedreven cholesterische fase. Door de driehoekige onderzijde van het deeltje iets te modificeren kunnen we van een linkshandige prolate fase naar een rechtshandige oblate cholesterische fase overschakelen, gebruikmakend van een rechtshandig gedraaid deeltje. Daarnaast vinden we een kwalitatieve overeenkomst met de theoretische voorspelling van hoofdstuk 6. Onze resultaten laten zien hoe de competitie tussen de tweeassigheid en de chiraliteit van een deeltje zich kan uiten op een grotere lengteschaal in de nematische fase. Deze bevindingen openen de weg om nieuwe theoretische uitdagingen omtrent de zelforganisatie van chirale deeltjes aan te gaan, waarvan enkele al besproken zullen worden in hoofdstuk 8. Hierbij speculeren we over de mogelijkheid tot het vormen van nieuwe chirale nematische fasen uit harde deeltjes en bespreken we een aantal openstaande vragen uit het veld.

De zelforganisatie van colloïdale deeltjes is cruciaal bij het maken van materialen met nieuwe eigenschappen in drie dimensies, op verschillende lengteschalen, in een bottom-up, betaalbare en duurzame manier. Dit kan echter niet bereikt worden zonder fundamenteel inzicht in datgene wat de verschillende structuren stabiliseerd, beginnend met de rol van de deeltjesvorm op de uiteindelijke colloïdale fasegedrag. Gezien het feit dat men tegenwoordig colloïden in vele complexe vormen kan synthetiseren, zijn algemene regels voor de bouwstenen van nieuwe materialen noodzakelijk. Het werk dat beschreven staat in dit proefschrift draagt daar hopelijk aan bij. *

*Translated with the help of Jessi van der Hoeven

Acknowledgements

Doing a PhD is somehow similar to being on a roller coaster. The duration of the lap may vary, some tracks have more curves, the time you spend in going up or falling down is also different, the height that you reach varies, in some cases you can get excited going fast, in others you can look around and enjoy the view. In any case you have to finish the lap. Well, I finished the lap. The best was that I wasn't alone during it. I had the opportunity and the honour of spending my time with many exciting people. I will do my best to express my gratitude towards all of them: those who paid for the ticket, who were sitting close to me, or shouting in the seats in front of me, or holding my hand, who were waving from below, who suggested that this was a nice roller coaster, who continuously oils the track to ensure a smooth ride, and if I miss someone I apologize in advance, sometimes we went too fast.

Explaining how much I learned (scientifically and non) from my supervisor, Marjolein Dijkstra, is not easy, the least I can do is to thank her! Thank you, Marjolein, for your availability, your interest, your trust, your encouragement and your guidance during my PhD. I always appreciated discussing science with you during our frequent (and often very long) meetings. Thank you for not overlooking the social aspect of doing research and trying to always ensure a pleasant atmosphere in our group.

I would also like to thank Alfons van Blaaderen, Arnout Imhof and René van Roij (Institute for Theoretical Physics), who, together with Laura Filion, Marijn van Huis, Krassimir Velikov, and Patrick Baesjou, form the excellent staff of the Soft Condensed Matter (SCM) group, in which theory, experiments and simulations are combined by a great ensemble of researchers in a socially and scientifically stimulating environment. In particular, I want to thank Alfons for his impressive amount of valuable remarks and comments during the workdiscussions and other meetings, from which I clearly benefited. Analogously, thanks to René for his contagious enthusiasm and the many fruitful discussions we had.

Furthermore, thanks to Frank Smallenburg and Laura Filion for their help and their work on the icosahedral clusters project, and to Bart de Nijs who performed the great experimental work in this nice collaboration. It was a pleasure to learn from and collaborate with Simone Belli on some aspects of liquid crystals and density functional theory. On the experimental side of the liquid crystal business, I sincerely thank Thijs Besseling, Henriëtte Bakker, and Chris Kennedy for the many discussions on colloidal rods, colloidal spheres, confocal microscopy, particle tracking, and order parameters. Thanks also to Tara Drewski and to Matthieu Marechal for their intriguing research in our collaborations.

I am deeply grateful to Francesco Sciortino for introducing me to the soft matter world and pointing me to the Utrecht group. I also thank the rest of the research group at La Sapienza in Rome where I spent my master project, Emanuela Zaccarelli, Cristiano de Michele, Nicoletta Gnan, and especially Lorenzo Rovigatti who helped me to learn the

tricks of the business. It was also a pleasure to cross paths with Teun Vissers, Frank Smallenburg and Zdenek Preisler, both in Rome and in Utrecht.

I recall with pleasure the many conferences, (summer and winter) schools, workshops and so on, that I attended outside Utrecht, and I want to thank the people I went with or I met there, for sharing ideas, providing comments or just for nice chats, that definitely contributed to my PhD journey. I particularly want to thank Zvonimir Dogic, Seth Fraden, and Mike Hagan, for the exciting visit at Brandeis University and Jerome Fung for showing me around the lab. I would also like to thank Vinny Manoharan for the visit to his sparkling research group at Harvard University and Nick Schade for showing me around the lab.

But clearly within the walls of Utrecht University, I have been continuously bombarded by different scientific stimuli as well. For that, the many research groups at Utrecht University, with which we share countless (high-level) seminars, need to be thanked, but especially all the SCM colleagues deserve special acknowledgements. Thank you, Anjan, for the warm welcome at the beginning of my PhD and for sharing a lot of your experience with me. Thank you, John, for the very many (but really very many) precious discussions and suggestions and your interested way of listening and discussing science. Thanks to Anjan, Wessel, Nina, Marlous, and Henriëtte who formed the original FOCS group, in which we had many interdisciplinary discussions. Thanks also to Nick, Guido, Zdenek, Vassilis and all the simulators for the many technical discussions; and to Wessel, Ernest, Henriëtte, Thijs, Da, Jessi, Chris and all the other experimentalists who were around when I was puzzled about experimental stuff. Furthermore, thanks to Marjolein, Joep, Alexander, with whom I had many interesting meetings (together with Nick as well), during their master projects. Thanks to Gerhard Blab for the use of the 3D printer. Thanks to Wessel and Jessi for being my "paranimfen" and helping with the "samenvatting", and to Chris for polishing the back matter of this thesis. Finally, thanks to Marion, Thea and Peter for their work "behind the scenes", who helped me to efficiently deal with bureaucratic administration, technical matters and arrange/clock the workdiscussions (I was mostly on time!) and obviously thanks also to Judith, Relinde, and Chris who keep the lab running smoothly.

If acknowledging the scientific contributions to my PhD was already difficult, expressing what I have obtained in terms of human relationships during this experience is almost impossible. In these four years, I did not meet only excellent colleagues but also really nice people who became true friends. Looking back, I remember with a great pleasure several moments spent together, no matter if it was a quick greeting in the corridor or a long chat at the coffee corner. For these, thank you very much Anjan, John, Wessel, Jessi, Henriëtte, Pepijn, Nina, Wiebke, Guido, Nick, Chris, Giulia, Ernest, Tonnishtha, Sid, Da, Vats, Harini, Berend, Vassilis, Rik, Rama, Fabian, Doug, Bart, Ran, Weikai, Thijs, Johan, Jissy, Tian-Song, Marjolein, Kristina, Joost, Zdenek, Bas, Bo, Marlous, Rao, Murphy, Somil, Sina, Naveed, Anna, Frankje, Ravi, Bing, Xiaobin, Ajoy, Federico, Yang, Chang-Ming, Djamel, Simone (Belli), Thomas, Sela, Niels, Andreas, Bram, Mathijs, Jeffrey, Tara, and Giuseppe!

Thanks for all the variety of things, not necessarily work-related, that I enjoyed with you guys! Ranging from the many coffee breaks, borrels, and all the meals (of any sort)

and all the cookies (mostly Wessel) at the university; to the more dynamic activities, such as playing football in the parking lot (bike!...car!...) or more organized sport events. In particular, thanks to the "Random Walkers" running team (it was fun to run with the boss and René, being slower than the latter) and to the biking buddies, thanks (?) Nina! Of course, I appreciated very much the effort we dedicated to foosball; for that, I thank the A-league and the other random players... I can safely state that I have improved my foosball skills! Thanks to my office mates Ran (shortly), Anjan and John for making our office a lovely environment in which we could discuss all sorts of matters and where we shared a lot of good moments. I am still not sure if I have to thank Anjan for convincing me and John to get a couch for our office... anyway since then OL016 has become a reference point of (non-) scientific discussions. It was also interesting to experience a real-life phase transition when my office mates became Giulia and Toni. Thank you ladies, because it is still impossible to get bored in our office.

Thanks again, John, because despite the long time spent in the office together, you were always an extremely nice flatmate. I also enjoyed very much the Saturdays when Mr. Z joined us and you shared your "infinite wisdom". I also liked very much that we were able to host several (spicy) dinners for our SCM buddies. Thanks to Chris, who enjoyed our hospitality so much that he decided to stay as my new flatmate! I want to thank you for the uncountable enjoyable house-moments, and for introducing also weird "plant healthcare" projects and duolingo sessions... thank you!

Dear SCM friends, I had fun with you in occasion of burgers, beers (with peers), dinners, parties, board games nights, football games, artistic visits, even an international road trip and much more... thank you very much for sharing with me these really unforgettable moments.

Outside the SCM group, I would like to reserve special thanks to the players and the staff of the Tevere Hockey Club in Rome and of the MMHC Voordaan here in The Netherlands, that allow me to keep *mens sana in corpore sano*.

Un ringraziamento a tutti i miei amici (hockeyisti e non) romani, che mi hanno sempre accolto a braccia aperte durante i miei brevi ritorni, testimoniando un'amicizia che non si ferma davanti a migliaia di chilometri.

Un grazie enorme ai miei genitori, a mio fratello e al resto della mia famiglia per il loro immenso affetto e il continuo supporto.

Tot slot, lieve Jessi, dank je wel voor alles!

Simone (Utrecht, April 2016)

List of publications

Some of the results of this thesis have been part of the following publications:

- S. Belli, S. Dussi, M. Dijkstra, R. van Roij, *Density functional theory for chiral nematic liquid crystals*, Physical Review E 90, 020503(R) (2014).
- B. de Nijs/S. Dussi, F. Smallenburg, J. Meeldijk, D. Groenendijk, L. Filion, A. Ihmof, A. van Blaaderen, M. Dijkstra, *Entropy-driven formation of large icosahedral colloidal clusters by spherical confinement*, Nature Materials 14, 56 (2015).
- S. Dussi, S. Belli, R. van Roij, M. Dijkstra, *Cholesterics of colloidal helices: Predicting the macroscopic pitch from the particle shape and thermodynamic state*, Journal of Chemical Physics 142, 074905 (2015).
- T. Drwenski, S. Dussi, M. Hermes, M. Dijkstra, R. van Roij, *Phase diagrams of charged colloidal rods: can a uniaxial charge distribution break chiral symmetry?*, Journal of Chemical Physics 144, 094901 (2016).
- S. Dussi, M. Dijkstra, *Entropy-driven formation of chiral nematic phases by computer simulations*, Nature Communications 7, 11175 (2016).
- H. E. Bakker, S. Dussi, B. Droste, T.H. Besseling, C.L. Kennedy, E.I. Wiegant, B. Liu, A. Imhof, M. Dijkstra, A. van Blaaderen, *Phase diagram of binary colloidal rod-sphere mixtures from a 3D real-space analysis of sedimentation-diffusion equilibria*, manuscript submitted
- M. Marechal/S. Dussi, M. Dijkstra, K. Mecke, *Density functional theory and simulations of colloidal triangular prisms forming liquid crystals*, manuscript in preparation
- T.H. Besseling, C.L. Kennedy, S. Dussi, H.E. Bakker, M. Dijkstra, A. van Blaaderen, A. Imhof, *Experimental measurement of the equation of state of hard rods*, manuscript in preparation

Other publications by the author:

- S. Dussi, L. Rovigatti, F. Sciortino, *On the gas-liquid phase separation and the self-assembly of charged soft dumbbells*, Mol. Phys. 111, 3608 (2013).

Oral and poster presentations

Part of the work of this thesis was presented at:

- Physics@FOM 2014, Veldhoven (NL) (poster)
- NWO-CW meeting 2014, Veldhoven (NL) (oral)
- 9th Liquid Matter Conference 2014, Lisbon (PT) (oral)
- Debye Lunch Lecture 2014, Utrecht (NL) (oral)
- CHAINS conference 2014, Veldhoven (NL) (poster)
- Physics@FOM 2015, Veldhoven (NL) (oral)
- Physics@FOM 2015, Veldhoven (NL) (poster)
- MRSEC Seminar, Brandeis university (USA), June 2015, invited by S. Fraden and Z. Dogic (oral)
- Seminar Harvard university (USA), June 2015, invited by V. Manoharan (oral)
- Gordon Research Seminar on Liquid Crystals 2015, Biddeford (Maine, USA) (poster)
- Gordon Research Conference on Liquid Crystals 2015, Biddeford (Maine, USA) (oral)
- European Conference on Liquid Crystals 2015, Manchester (UK) (poster)
- Italian Physics Society Congress 2015, Roma (IT) (oral, awarded as best communication in the Structure of Matter section)
- Physics@FOM 2016, Veldhoven (NL) (poster)

About the author

Simone Dussi was born on the 12^{th} February, 1987 in Rome, Italy. After completing high school in Rome (Liceo Scientifico "Aristotele") in 2006, he began his studies in Physics at University of Rome "La Sapienza". He obtained his bachelor's degree *cum laudae* on the 28^{th} September 2009. His bachelor thesis was entitled "Electron diffraction from a surface" and the project was supervised by Prof. Maria Grazia Betti. He obtained his master's degree in Physics at the same university on the 29^{th} March 2012. The thesis project was entitled "Competition between phase separation and self-assembly: numerical study of charged soft dumbbells" and was supervised by Prof. Francesco Sciortino. From the 1^{st} July 2012 he has been a PhD student in the Soft Condensed Matter group of the Physics department at Utrecht University under the supervision of Prof. Marjolein Dijkstra. The scientific research performed during his PhD has been presented at several national and international conferences, and published in peer-reviewed journals. Part of his research also appeared on the Dutch national press (de Volkskrant and NRC) on the 1^{st} September 2014. In parallel to his studies and his research activity, Simone has been playing field hockey in Italy and in the Netherlands and he had the honour to play for the Italian national team in several international tournaments at junior and senior level.